University of Bath

UNIVERSITY OF BATH

PHD

Wear and Efficiency Mechanisms in Polyoxymethylene Spur Gears

Evans, Mike

Award date:
2017

Awarding institution:
University of Bath

[Link to publication](#)

Alternative formats

If you require this document in an alternative format, please contact:
openaccess@bath.ac.uk

Wear and Efficiency Mechanisms in Polyoxymethylene Spur Gears

Stuart Michael Evans

A thesis submitted for the degree of

Doctor of Philosophy

University of Bath
Department of Mechanical Engineering
August 2016

Contents

Table of Figures

Acknowledgements

Summary

A method has been formulated to assess the running temperature of a polymer-steel gear pair under loaded operation. The slip-roll characteristic of an involute spur gear contact is used and forms the basis for this method. It derives a power loss at the contact interface that varies through the contact and is time averaged to provide an overall efficiency of the gears. This efficiency loss results in a rise in temperature at the contact between the teeth and in turn leads to a bulk temperature rise in the gears. This is assessed with finite element and analytical models to validate the predicted temperature rise against experimental data. Good correlation was found between the modelling techniques and the experimental results.

A new mechanism of wear has also been identified for polymer gears. The mechanism is in the form of smear-shaped asperities approximately 20 μm long from which fine particulates break away at the trailing edges during loaded operation of the gears, contributing to the bulk wear of material. The smear-shaped asperities and subsequent failure modes have been identified using scanning electron microscopy techniques. Two models are presented that are used to characterise and predict the phenomenon. One model characterises the failure mode properties of the smear-shaped asperities and is formulated by the inspection of the microstructure of the polymer material. The second model predicts the volume of material worn away and finds good agreement with experimental results. The predicted worn volume was 67 mg against 77 mg measured.

Abbreviations and Nomenclature

ADC   Analogue to Digital Converter; A protocol used within the Rotork product software to convert signals from analogue to digital

ABS   Acrylonitrile Butadiene Styrene; a common engineering thermoplastic polymer

BLDC   BrushLess Direct Current – relating to motors

CAD   Computer Aided Design; A generic term covering many different software and numerical techniques implemented using a computer

CoF   Coefficient of Friction

CLA   Centre Line Average – in μin, an imperial system measurement of surface roughness.

CVA   Control Valve Actuator; An electric actuator produced by Rotork Controls that contains polymer gears which have been investigated during this research

FEA   Finite Element Analysis; A subset of Computer Aided Design dedicated to the solution of a variety of physical problems through numerical analysis

rms   Root Mean Squared

SEM   Scanning Electron Microscopy

PC   Personal Computer

PEEK   Polyetheretherketone; A semi-crystalline engineering polymer

POM   Polyoxymethylene; A semi-crystalline engineering polymer. The CVA gears are manufactured from this material

PTFE   Polytetrafluoroethylene; A synthetic fluoropolymer known for its low coefficient of friction

PV   Pressure-Velocity limit for polymers

UHMWPE   Ultra-High Molecular Weight Polyethylene

CHAPTER 1

Introduction

Toothed wheels have been put to use by civilisation for thousands of years, they are referenced in the writings of Aristotle (circa 330 BC) and the earliest machine known to have applied the mechanism of gears was the 'South Pointing Chariot'. Figure 1 shows a conjectural model built for the Science Museum in London; it uses a differential gear train with peg gears. The form of the gears has subsequently developed, but the originality and ingeniousness of the geared mechanism is impressive.

Figure 1: Chinese South pointing chariot - Science Museum (London)

The concept of the involute spur gear was originally analysed by Leonhard Euler in 1754 (Dudley, 1969), who is considered to be the father of involute gearing. The concept was later developed by Robert Willis (circa 1840) as a useful engineering mechanism for transmitting a constant angular speed and torque between two parallel shafts with the added advantage of a gear ratio reduction or increase as detailed by Dudley (1969). Over

time, this concept evolved into the Fundamental Law of Gearing and is taken for granted today in gearing design and application. Until recently, the vast majority of gears manufactured around the world have been metallic, but polymer gears are becoming more commonplace in current engineered systems as they are cheap and can be run without a lubricant. However, the wear mechanisms of polymer gears have not to date received the same level of research attention as metallic gears. As industry utilises cheaper, more easily implemented polymer gears for power applications, this knowledge will become ever more important. The following sections outline the literature and motivation behind the content of this thesis.

1.1 Industry and Academia

The cost of funding this research has been met by industry, the company being Rotork Controls Ltd, a midsized engineering firm based in Bath, UK. Rotork Controls manufacture electric valve actuators, which are industrial products used in a variety of fluid flow applications. The author is employed by Rotork and has been heavily involved with the engineering development of the Control Valve Actuator (CVA) product. Figure 2 shows a cut away view of this actuator product. The largest gear shown in white in the centre of the image is one of the Polyoxymethylene (POM) gears in the gear train. The largest POM gear and the steel pinion that drives it have been used as the base gear pair for the research undertaken. Test samples and data have also been made available by Rotork.

This product (CVA) is an electric actuator designed to be used to accurately control a process flow through a pipe valve. The actuator has the capability to sense force and output position and consists of an electrical control system, motor, gearbox and output prime mover. The product is available in a number of frame sizes and in versions for linear reciprocating output and 90° rotation. The gearbox provides a large ratio of reduction between the high speed motor rotating at around 4000 rev/min to the output, which must be slow speed but high load. There are 4-5 gearbox reduction stages and 3 of these contain POM gears.

Rotork produced its first electric actuator in 1952, led by Jeremy Fry who founded the business. Since then, the business has grown into an international company by

development of the products it sells and by acquisition of similar operations. It has developed a yearly revenue of over £500 million (rotork.com, 2016).
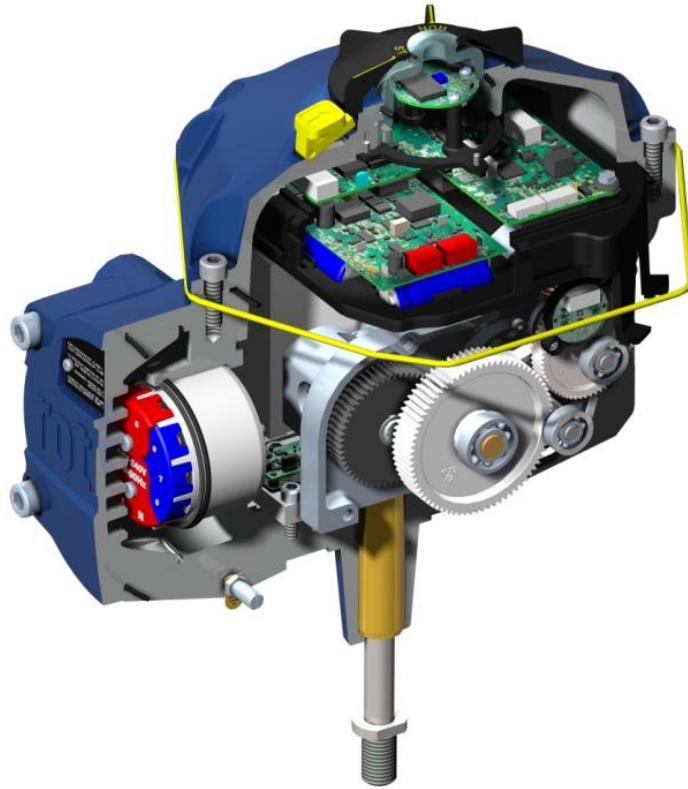
Figure 2: Rotork's Control Valve Actuator (CVA)

As the company expands, research must form part of the driving force behind new product development to ensure that it keeps ahead of the competition. Research into new areas of technology and new methods to improve engineered solutions must be at the forefront. Although the objectives of industry and academia differ subtly from one another, in this case there is sufficient overlap to perform some original research that will be of benefit to the sponsoring company. This thesis aims to make some headway into the hitherto largely un-researched area of the wear of polymer gears. It documents a new wear mechanism as well as a marked improvement in analysing the efficiency and heat rise of a pair of gears under load.

1.2 Polymer Spur Gears

A specific pair of straight cut spur gears used in the CVA product (as shown in Figure 2) has been considered throughout this thesis as they provide a convenient base on which to generalise findings. The pinion (the smaller driving gear) is manufactured from plain carbon steel (European Standard 1.5011 grade) and has 12 teeth. The gear (the larger driven gear) is made from Delrin 100, a Polyoxymethylene (POM) and has 75 teeth giving and overall reduction in speed and increase in torque to the ratio of 1:6.25. The gear material will be referred to as POM or polymer throughout this thesis. The involute geometry of the spur gears means that they transmit speed and torque from one to the other continuously and without fluctuation. There are theoretically an infinite number of different gear tooth forms as the profile of the teeth can be varied without limit, however, there are a number of different cases that have been proposed over time. The Cycloidic gear (Dudley, 1969) was used for clock designs until the involute form developed and took over as the dominant design. A recent development in gear form has been made which claims to increase the load capacity of a set of gears by subtly altering the way the teeth roll through the pitch line. This system of gearing is subject to a US patent and is called Convoloid gearing (USA Patent No. 11/016,029, 2006).

While case hardened steels are used primarily for power applications such as automotive gearboxes, there are many benefits to using polymer gears as an alternative. In the case of the pair studied during this research, the pinion is made from steel and the gear is made from a polymer. As the pinion is the smaller of the two gears, overall strength is a good reason to make this gear from steel. Strength is clearly more important with a smaller shaft and in addition to that there is less bulk material in the pinion than in the gear. Overall, a steel pinion with a polymer gear is a cost effective solution whilst maximising the mechanical properties available. It is of course possible to use the configuration of polymer pinion running against polymer gear. There are a bewildering number of polymers available to consider and a study of the others is beyond the scope of this thesis. However, commonly used polymers for gears are Nylon 66, where a lower cost is most important; Polyoxymethylene (POM), which has a reasonably high strength and is not prohibitively expensive, and Polyetheretherketone (PEEK), which is extremely wear resistant and strong, but relatively expensive being approximately 40 times the cost of POM.

1.3   Why Research Polymer Gear Wear?

For gears manufactured from case hardened steels, there are numerous resources for calculating the load capacity and resistance to wear, such as the British Standard BS ISO 6336 (2006). These are well known by gear and gearbox design engineers and can be used effectively so long as the input parameters match that expected by the standard. The standards deal with a narrow band of materials and conditions and are generated from a combination of analytical and experimental methods. They are partially empirical and if an engineer desires to use a different material outside of the parameter bounds, he/she cannot know that the outcome will always be safe and that the design will be fit for purpose. However, in terms of mechanical strength of the gear teeth, the load capacity of a gear is really only a function of geometry and material properties. Hence it is relative safe to use these resources to calculate the strength of a gear if the material does not fall within the standard set. Indeed, it is also perfectly feasible to employ traditional and computational techniques such as the Finite Element Method to determine the strength of a polymer gear tooth.

Calculation of resistance to wear is problematic because there are many more variables that combine to determine wear rates. For metallic gears, wear mechanisms have been relatively well researched in areas such as abrasion and scuffing (if the gear is grossly overloaded) or pitting and micro-pitting, which is failure by surface fatigue generally caused by improper lubrication. The conditions that must be present for these to occur in metal gears are well understood and form the basis of the standards. For a polymer gear, there is very little understanding of that fundamental wear mechanism. Does the surface undergo abrasion or adhesion? Is pitting relevant at all in a polymer? How does humidity and temperature affect the wear resistance? None of these questions are currently answered in detail sufficient to safely design a gear pair for a given load and speed using a polymeric material. This is the reason for studying the wear of polymer gears. The underlying principles of the mechanisms of wear must be understood in order to formulate a predictive model.

1.4   Research in the Open Literature

There are around 100 journal articles spanning the last 80 years that are of direct relevance to this research and they are reviewed in this section. There are other articles relating to metallic spur gears and gears made from glass reinforced polymers, but these have been set aside as less useful in the context of this thesis. Of the relevant literature there is a theme that runs from the research in the 1950s to the present and it will be shown that there is a gap in the knowledge. It is important to state that this research follows a philosophy firstly of observation with a view to identify elements that are believed to not be fully understood. Once the observation has been made it is then necessary to theorise about why that element exists. What external force or mechanism could have acted to bring it into being and can a theory be developed to explain it?

Whilst researching the literature surrounding the area of wear in polymer spur gears it has become evident that there is a missing piece to the puzzle. Work has been conducted, but much of it is concerned with the disciplines of experimentation and of empirical models of wear, building on the early work of those such as the Archard (1953) wear equation:

$$Q = \frac{KWL}{H} \tag{1}$$

where Q is the total volume worn away, W is the total normal load, H is the hardness of the softest contact surface, K is a dimensionless constant and L is the sliding distance.

Meng and Ludema (1995) provide an extensive review of the various wear models that have been developed since this original model by Archard. They describe the process of developing a wear model and state that they are all, by necessity, empirical models. The constant K in Archard's equation (1) gives the user the ability to tune the model to the specific tribological conditions without necessarily knowing the precise mechanics of what is occurring between the contacting surfaces. This approach can be very important and useful when the subject is specific, for example, in the area of medical prosthetics. In this specific case, it is important to know how long a metal-polymer contact of a specifically definable geometry will last. The actual mechanism of wear is not as crucial as knowing the durability as this has the most impact on the patient given that they must undergo serious surgery to have a prosthetic joint installed or replaced. However, to

understand how a metal-polymer contact region wears, the detail of the contact mechanism must be examined and with as much resolution as possible. Only then can a theory of the tribology of the contact be developed.

The following review is therefore grouped into four sections in line with the philosophy that has been outlined. Observation is necessary at the outset to identify any possible mechanisms of wear. Experimentation must then be performed to replicate the observed mechanism and to ensure it is created independent of external influences. Modelling techniques then provide useful information about the mechanism such as its characteristics and properties. Finally, analysis of the full model ties the other three activities together.

1.4.1   Observation

There are many techniques and many different types of equipment available to make tribological assessments of a material surface. However, Scanning Electron Microscopy (SEM) is excellent for this work as it yields very clear and unambiguous images of material surfaces with a resolution of approximately 1 μm. The images are clear and are readily interpreted by the viewer as they contain so much fine detail and good depth of field. In the early work of Kar and Bahadur (1978) and Tanaka *et al.* (1973), images are presented of the surface of a PTFE sample that has been worn using a tribometer. The surface structures can be seen clearly and although some observations of the polymer 'fibres' grouping around the wearing stylus are possible, no further analysis is given. A question that Tanaka raises is whether a film is formed over the surface of the polymer due to the heating effect of the contact between it and the metal counterface.

The work of Walton and Shi (1989), Hooke *et al.* (1996), Kukureka *et al.* (1994) and Breeds *et al.* (1993) make substantial inroads into the understanding of how spur gears run together and what the contact mechanics are for involute gear teeth. In particular, and for the first time in the literature, the action of rolling and sliding between the driven and driving gear is described. Furthermore, it is indicated how this geometry driven contact, so particular to involute spur gears, may influence the efficiency of any given gear pair as well as its resistance to wear. It should be noted that this body of work also includes investigations into gears made from glass fibre reinforced polymers as

shown by Kukureka *et al.* (1999), but this material group is outside the scope of this thesis. For the unreinforced materials, experiments are performed by driving two polymer gears together under load and SEM images are presented of the gears after the test runs. When the worn gear tooth surfaces are inspected at the high magnifications offered by the SEM it is seen that the action between the teeth is extremely complex when running a polymeric material. They also state that the wear is clearly a function of load and temperature as the formations and patterns seen on the surface appear to be made by melting of the surface. In another paper by the same group, Kukureka *et al.* (1995) describe a feature that has been formed into a flake, which could then be deformed such that pieces of the material are removed. It is a tantalisingly short comment in the paper, which is then picked up later on by Chen *et al.* (2000) as macro-transverse cracks that propagate from the surface and which then may be rolled into flakes as indicated in the Kukureka work. Abdelbary (2015) discusses lateral cracking of UHWMPE under loaded and sliding conditions and provides an electron micrograph image (after Abouelwafa, (1979)) of cracking that has developed perpendicular to the sliding direction. The cracks are described as having developed due to the cyclic loading of asperities on the surface of the polymer. These asperities are then flattened and produce high levels of stress locally which develop into subsurface cracks at their location. The features shown in the image presented are described as cracking rather than a surface feature that may have been created by the action of rolling or sliding of the metal counterface across the polymer surface. This type of feature is also described in work by others such as Kukureka *et al.* (1995) and is explained as cracking that has been generated by subsurface stresses. A detailed analysis or investigation of the features or the mechanism that creates them cannot be found in the literature and there is no further mention of this phenomenon in the literature, but how and why these features form and grow has become one of the focuses of this thesis and will be discussed in length in later chapters.

An intrinsic property of the involute spur gear is that it exhibits both rolling and sliding actions between the gear teeth as they are driven together. This property of the teeth will be investigated in depth in the next chapter, but it has been identified in the literature. Flodin (1997) investigated the slip-roll of the teeth and uses it to develop a mild wear model in combination with the Archard wear equation. This idea was also exploited by Zhang *et al.* (1999) who supposed that the slip-roll would have a detrimental effect on any surface defect. They used a finite element model to predict the propagation of cracks from a surface by the action of slip-roll; however, one impression is that the cracks were

artificially included in the model, partially to give the model something to act upon. It seems more of a case of the model driving the results rather than vice-versa, but the modelling does provide an insight into the how the slip-roll may affect the contact regime. Chen *et al.* (2000) used a twin disc machine, which is a simplified testing machine where the relative slip speed between the two discs can be controlled, to simulate the gear teeth action. They discovered that cracks could be produced. These were propagated from the surface as in the Flodin model and Chen further investigated these cracks by sectioning the discs after testing had finished. The twin disc test machine has the advantage over experimentation using real gears that the worn surfaces are visible and easily accessed. Many other techniques can also be used with this arrangement such as direct measurement of temperature, but the twin disc test machine has a deficiency as do all other gear-analogous test apparatus. In particular, the twin disc machine can be used to simulate slip only, roll only, or a combination of slip and roll, and so would seem ideal as a simplified representation of the real gear pair. However, the slip and roll components of the contact action in the twin disc machine are both in the same direction. The real gear pair in fact experiences roll and slip in opposing directions, so while the twin disc machine is a useful analogy to the real gear pair it can never accurately mimic the contact action.

The method and apparatus used for making observations is clearly of upmost importance when studying the tribological properties experienced by the running of gears and the best method should be a pair of real gears. Any disparities between the real case and the analogy are then negated. Another test method is to use a back to back apparatus with one electric motor back driving another with the gear pair in between. The driven motor acts as a generator and so provides the load. This was done by Senthilvelan and Gnanamoorthy (2009) and surface features were observed that are relevant and interesting. However, no further analysis or conclusions for wear mechanisms are given. Hooke *et al.* (1992) used a different type of machine for their investigations, a four-square rig. This machine uses a single electric motor to turn it but with two sets of spur gears contacted across two parallel shafts, one set of gears is the driving set and are case hardened steel gears. The other pair are the pair of gears to be tested and in this case are the polymer gears as performed by Mao *et al.* (2009, 2010). The load is applied to the system by a lever arm, hence is very accurately controlled and allows the load to continue to be applied even as the gears become worn. These studies were concerned with how temperature affects the wear of the gears and also how differing materials influence

matters. Acetal is used as the gear test material, which is an alternative name for POM used in this research. They conclude that the acetal material has a critical limit in terms of slip-roll beyond which complete failure of the material starts to occur due to thermal effects.

The majority of research that has been carried out in the past has focused on the action of the teeth contact with either real gears or with some design of analogous test apparatus such as the widely used pin-on-disc tribometer. This is an obvious place to begin observations, but there are other areas that may provide a broader knowledge of the physical system. For instance, very little work has been conducted on the measurement of wear from loaded gears, which could be used to validate wear models. A probable reason for the lack of work in this area is that the wear volume is a tiny percentage of the volume of the gear and so is difficult to measure with any degree of statistical significance. When glass fibres are used to reinforce the base polymer matrix, these can lead to an increased wear rate on the counterface. However, the use of carbon in place of glass fibres was shown by Giltrow and Lancaster (1967) to reduce the wear on the counterface as well as the coefficient of friction. The direction of the fibres was also found to be important as the fibres were considered to be providing point contact support between the polymer and counterface. In another piece of work by Wright and Kukureka (2001), measurement of the wear volume was done by use of a Coordinate Measurement Machine and the wear of various materials (all fibre reinforced) is plotted as function of the slip ratio of the gears as defined by their geometry. The results are thorough, but the data presented show a variation of around 70% in the wear volume measured, hence it would be difficult to draw any firm validation of a given model from these measurement data. The worn material was determined by mass, which could have been subject to variation of moisture content. An interesting conclusion from this article is that there is little work done to make a correlation between the real gear scenario and the pin-and-disc type experiments.

1.4.2   Experimentation

The coefficient of friction must be considered when embarking on experimentation into the tribological effects between two surfaces. A considerable amount of work has been published in this area, specifically with respect to polymer-steel contacts and involute gears. A study was conducted using a Bowden-Leben stick-slip machine, which

is a conventional tribometer utilising a pin sliding against a flat surface (Bowers *et al.*, 1954). For steel running against nylon (the focus of this thesis) a value of 0.37 for static friction and 0.34 for dynamic is published. This experimentation could be repeated for completeness, but there is little point in doing so as this figure is replicated in various other studies in the literature such as by Vinogradov *et al.* (1965) and Michael *et al.* (1991).

A conical indenter was drawn across various polymers including POM and measurements were taken of the quantity of material ploughed by the indenter (Lancaster (1969)). The volumes correlate with that expected by the shape and size of the indenter. The work established a relationship between the size of indenter and wear with respect to 3-body wear, which was then expanded in relation to abrasive (sand) paper. The surface roughness of the counterface was quoted as 47 μin CLA, which is approximately 1.2 Ra μm. A specific wear rate minimum for Delrin was found to be 10^{-5} cm^3/cm kg at a temperature of 160°C where the material has softened. Ploughing was not found to occur at 20°C. Abrasion of a material surface is observed as scratches, grooves or other marking that is created by either ploughing or micro-cutting of the (generally) harder material into the softer. This can be as a 2-body condition, where one surface slides against another, or as a 3-body wear situation. The 3-body case is found where a separate body is trapped between the two sliding surfaces which causes the damage. Ploughing is categorised as a feature from the harder material forcing the softer material out of the way as sliding between the two occurs. This can be a 2 or 3-body condition as summarised by Myshkin *et al.* (2005). An alternative description of the process has been shown by experiment that abrasive wear is in proportion to $1/\sigma_u\varepsilon_u$, where σ_u is the ultimate tensile stress and ε_u is the corresponding strain. This was established by Lancaster (1968) and Ratner (1964) and the correlation is referred to by their names. Lancaster noted that wear rates of polymer sliding against steel in both lubricated and unlubricated cases exhibit a minimum at approximately the softening temperature of the material.

A considerable leap forward from the basic measurement of the physical property of friction between two sliding surfaces was made by Greenwood and Williamson (1966) in their paper on the contact of nominally flat surfaces. Their work showed that the apparent area of contact between two surfaces is not the same as the real contact area. The actual contact occurs between micro asperities that are present on all surfaces and as the actual contact area due to the area of the micro-asperities is minute in comparison to the apparent contact area (to the observer), friction is independent of apparent area. Although

this work was conducted on metal-to-metal contacts, they draw conclusions about the transition from completely elastic to plastic contact based on the hardness of the softer material. Also, an experiment was designed to measure the actual surface topography and they formulated a Gaussian distribution of asperity heights across the surface. This type of first principle observation, experimental measurement and analysis yields a much better understanding of the occurrences at the contact interface and is why the paper is greatly acknowledged in the field of contact mechanics and tribology.

Clearly, the material chosen for the gears will have a large effect on the friction between them and the associated efficiency and this has been measured extensively by Walton *et al.* (2002). In this work it is seen that the efficiency ranges between 88% and 98% depending on material, load and speed. Overall, the material seems to be the driving factor in the increase or decrease of efficiency, but for ABS, there is a large increase in efficiency between 600 rev/min and 1100 rev/min suggesting that the geometry (hence slip ratio) is also important. Walton and Shi (1989) write on modelling techniques to evaluate the efficiency based on standard contact mechanics, but the paper also lists experimental data that do not correlate with this modelling. Although progress has been made in the link between the actual contact mechanism, much is still to be done to quantify it completely, even for one specific case. Indeed, for the specific case of medical prosthetics, there has been much experimentation to validate a particular geometry of ball and cup of defined materials. Fisher *et al.* (1994) found that surface roughness contributes greatly to the wear of a polymer in contact with a metal. They also concluded that the wear was not dependent on sliding velocity, however, the maximum sliding speeds used were 240 mm/s, which is lower than the sliding velocities experienced by gear teeth. This idea of surface roughness effecting the wear and efficiency of the sliding contact is corroborated by the work of Xiao *et al.* (2007) and certainly fits with logical thinking of the problem.

Investigations were made by Cooper *et al.* (1993) into the sliding of ultra-high molecular weight polyethylene against steel in hip prostheses. Their investigations showed that an increased surface roughness of the steel counterface increased the wear rate of the polymer. However, their experimentations did yield a surprising result in a hip joint such that a relatively smooth steel surface produced relatively high wear rates in the polymer. There was no conclusion on this result, however, it was felt that larger polymer asperities were deformed during contact which made surface stress concentrations that in turn developed into surface cracking and so to material removal. Cartilage explants were

obtained from bovine femoral heads to investigate the creep and stress relaxation properties of the material. Chin *et al.* (2011) use this material to make investigations with respect to polymeric materials considered in the construction of prosthetic joints building on the work of Quinn and Grodzinsky (1993). In both studies, although the onset of creep is found to be instantaneous, appreciable creep was found to occur only over a period of many hundreds of seconds. Residual shear stresses were identified and measured using a microscope and polari-scope combination by Cooper *et al.* (1994). They identified, in artificial hip joint prostheses, at least two district contact conditions were occurring. In the case where the steel femoral head was relatively rough, then heavy wear was found with little subsurface stress indicating that the ultra-high molecular weight polyethylene had been worn away by abrasion. In the second case to be investigated, where the steel surface had a significantly reduced roughness average, sub-surface stress was observed. In addition to this, subsurface cracking was also present. Their postulation is that there are two different wear mechanisms in play, abrasion and a form of pitting where sub-surface cracking causes failure of the material, which is dependent on the surface roughness of the steel counterface.

As the contact properties change due to surface texture, load and sliding speed there will be a change in the heat generated at that interface. For polymer spur gears this is of utmost importance as, if the heat generated is too great, the material could be heated above the capacity of the material. If the material melts at the contact there will be catastrophic failure of the gears at which point any model of wear is irrelevant. With this in mind, thermal considerations have been investigated and the first major contribution to this area comes in the form of the concept of a Flash Temperature between contacting surfaces. Blok (1963) presents a basic model to evaluate the instantaneous temperature rise at the contact interface based on geometry of the contact, the heat input and the sliding velocity and it is given by:

$$T_{max} = A \frac{q_{av}}{\sqrt{kc'}} \sqrt{\frac{\omega}{v}}$$

(2)

where v is the sliding velocity, ω is the width of the heat source, k is the thermal conductivity of the material, c' is the specific heat per unit volume, q_{av} is the heat input and A is the form factor. If the coefficient of friction for the material combination, speed and applied load is known, this formula (equation 2) can then be used to calculate a temperature profile for a pair of gears. The work of Blok laid the basis for the idea of a

Flash Temperature and this has been expanded and improved upon on by Barber (1970) and Samyn and Schoukens (2008). A numerical solution has been developed specifically for the application to spur gear teeth by Mao (2007), which accounts for the effects at the tooth tip as the mesh starts and finishes, but is considerably more complex than the Blok model.

The next obvious step would be to make some attempt at reducing temperature to see if that materially affects the wear rate of the gears. This has been attempted by Tsukamoto and Terashima (1986), by drilling small holes through the base of the root of the tooth to let air circulate more freely across the tooth flank. Choong (2006) and Duzcukoglu (2009) also drilled holes through the tooth along the axis of gear rotation. All three studies found that reducing the running temperature of the gears also reduces the wear rate. Little analysis is given of why this might be, but it is reasonable to suppose that the softening of a polymer that is inevitable with the application of heat is responsible. Further weight to this argument is given in a collection of papers written documenting experiments done on the PV (pressure-velocity) limits of polymers in separate tribometer type experiments and also using real gears. A PV limit presented for Polyoxymethylene (POM) is given as 560 kg/cm^2/s by Yamaguchi (1982). The value for this particular material is relevant as it is the material used in the gears studied throughout this thesis. It is also noted that the introduction of glass fibres to reinforce the polymer matrix also has the effect of reducing the running temperature of the gears as found by Senthilvelan and Gnanamoorthy (2009). This was due to the thermal transport properties of the material allowing heat to travel away from the tooth surface more easily.

Investigations have been made of the pressure-velocity (PV) limits for polymers, specifically for plain bearings by Lancaster (1971). The heat generated at the contact interface was evaluated for the specific case of a steel bar running through an acetal bearing 25 mm diameter by 25 mm long by evaluating the flash temperature at the contact. The heat generated is transmitted into the polymer and the rate of generation is evaluated against the heat capacity of the material and the softening/melting temperatures of it. The modelling of these PV limits was validated by experimental work and it was found that, for the specific case, the limit of the acetal at approximately 1 m/s was 1 MN/m^2.

An interesting idea is presented by Yi and Quinonez (2005) for experimental measurements to be taken directly from the gear tooth surface during running of the

gears. The teeth, which are metal-metal, were drilled from the back and had small thermocouple devices inserted so that the measurement end was flush with the flank of the gear. As the thermocouple device had a fast response time in comparison to other thermal measurement devices it should have been possible to take readings dynamically as the gears are driven and to get a temperature profile of a single gear tooth pass. However, they did not do this and instead assembled data on the temperature rise over a matter of minutes.

Other experimental setups include loaded running of gears for temperature measurement and wear measurement as in the work of both Yakut *et al.* (2009) and Hooke *et al.* (1992). Also, further validation of specific wear models for use in the medical prosthetics are found by Liu *et al.* (2011). In this paper an interesting conclusion is made that the larger the prosthetic joint ball, the higher the wear rate under the area of contact even though presumably the overall contact pressure is lower (although this may be driven by the weight of the person, rather than the geometry of the joint). Boissonnet *et al.* (2012) found that wear particles get into the interface of the contact and act to increase the friction coefficient. This would also presumably increase the heat generation unless the particles acted to transport heat away from the contact.

1.4.3   Modelling

The modelling of wear has a number of difficulties associated with it. The material combination, the loading, the lubrication (or lack of lubrication) are all factors in any model. However, there is a pertinent question to answer and that is: What is the sensitivity of the model to each variable as some will dominate, whilst others have little effect? Many analytical problems in engineering are difficult, but consider the analysis of a steel structure under load. Steel is an elastic material and if it is loaded below its elastic limit then it will return to its original size and shape. Therefore, to determine the stress developed in a steel structure all that is required to be known is the geometry and the modulus of elasticity of the material. With wear this is not the case. If two hardened steel surfaces are rubbed together under a heavy load it is reasonable to assume that something resembling an adhesive wear mechanism will occur. If the same hardened steel surface is rubbed against a polymer counterface under the same load, the same wear mechanism

will not be present. Perhaps there will be some adhesion between the surfaces; also ploughing may occur if the load is sufficient, in which case, the heat generated may be sufficient to locally melt the polymer. Also, although the properties of the polymer can be characterised as having both and elastic and plastic regions to the stress-strain curve, it also exhibits far higher levels of creep to that of steel. In short, how can a model be produced to describe what is happening at the metal-polymer interface before knowing what that mechanism is? The early work on wear models was conducted by Holm *et al.* (1948), Archard (1953) and Rabinowicz (1953). These were generally restricted to metal-metal contacts. However, a dimensionless constant is present in the models to account for the exact material properties. Also, the mechanism of wear hitherto was not understood. The model presented by Archard has a constant K, which is used for exactly this purpose and while this is a useful technique that can be used to create a model of a specific system (once the value of the constant K is known) it cannot be used in all circumstances. Many different wear mechanisms have been observed through experimentation and they all have their own properties, including:

- **Adhesive wear**   Asperities make contact and micro-weld, which are then torn apart as the surfaces slide with resulting debris.

- **Abrasive wear**   Ploughing of the surface as a harder material moves across a softer material and the surface asperities of the harder material cut into and remove pieces of the softer material.

- **Surface fatigue**   Associated with pitting and micro-pitting in metallic gears where the Hertzian contact stress just beneath the surface at the point of contact is too high for the material, which results in bursting of very small pieces of the material from the surface.

- **Fretting wear**   Associated with bearings but can occur where repeated cyclic loading is coupled with small surface to surface rubbing. Is characterised by red dust which is oxidised steel in fine particle form.

- **Erosive wear**   Such as might happen as a stream of particles impacts a surface, thereby removing material.

One of the main points to note concerning the development of a wear model is that when two surfaces come into contact with one another they are never completely flat and smooth no matter how thorough the machining techniques are (e.g. grinding, lapping and polishing). There will always be surface asperities present and it is the way that these asperities interact with each other that give the contact properties between the two surfaces. Greenwood and Williamson (1966) make this proposal in their paper and discuss the statistical nature of the surface asperities whilst also providing a model to predict their distribution. This model gives a much better understanding of what is happening tribologically and also explains why the coefficient of friction between any two surfaces is not a function of the apparent area, but rather the real contact area of these asperities. The Greenwood and Williamson model has been expanded upon by Tworzydlo (1998). Although it provides considerable insight into the surface contact mechanics it does not define the specific wear mechanism for a given material combination. Xie and Williams (1996) did make some progress on this front in predicting the coefficient of friction and wear between a randomly rough hard surface and a softer surface. They used the technique developed by Greenwood and Williamson and expanded it to include specific plastic micro cutting of the softer material by the harder. This work was followed up by Williams (1999) to include the idea of plastic shakedown in the softer material, which is loaded beyond its elastic limit such that, as the load is released, permanent strain occurs in the material. If the load is cyclic then the permanent strain produces a ratchet effect in terms of deformation of the material. It is noted that a predictive temperature rise and wear model is available from the British Standards (1987) and proprietary software also provides a similar function (Beerman, 2007), but these models require test data as their input as they use empirically derived wear models similar to that of Archard (1957).

Temperature rise at the contact area is also important in understanding the mechanism of wear. As previously discussed, much work has been carried out in this area and an extensive review of it is given by Bowden and Tabor (1966). They conclude that atmospheric conditions (particularly relative humidity) are crucial as to whether or not adhesion will occur and this is backed up by more recent work by Scholz (2013). Completely analytical models have been constructed that predict the heat rise around a contact area such as in the work of Vick (2001) who used Greens' functions to describe the areas of contact, one following closely behind the other. For steel running against a polymer the temperature rise will be determined by a series of variables. The increase in temperature should be such that the polymer does not exceed its softening or melting

temperature as this would clearly result in catastrophic failure of the material. This is the basis for a concept of the PV or pressure-velocity limit for a polymer and was originally proposed by Archard (1957) and later augmented by the work of Yamaguchi (1982) and Van De Velde and De Baets (1997). In a study by Unal *et al.* (2004) of extremely high pressures of steel rubbing against polymer, rather interestingly it was found that the wear rate of a polymer in this case is not strongly dependent on the pressure applied, but rather the velocity.

An obvious contemporary engineering specific tool for analysis is the Finite Element Method (FEM) as utilised by many proprietary software. Studies have been made over the years on gears and contact elements using these. However, FEM is not really suited to the dissection of micro-asperity contact between surfaces because the asperities are very small ($< 1 \ \mu m$) and the contact area of the surfaces maybe of the order of several mm^2. In this case, the element size must be very small indeed in comparison to the overall system and so the models become exorbitantly large. In a study by Walton and Shi (1994), load sharing of polymer gears was investigated. They were not concerned with the contact conditions or characteristics, but only the loading between the gear teeth. A thermo-elastic model can be created using FE and was done so by Taburdagitan (2006). The setup is of interest as it illustrates some of the difficulties associated with producing this type of model. The mesh was refined around the gears where needed and the driven gear was loaded via a torsional spring at its centre. The conclusion of this paper was that tip relief of the gear teeth is important to the temperature rise as applying it can help to reduce the slip speed as the driving gear touches down to the driven gear and hand over of load occurs. FE techniques and models have also been used in conjunction with existing analytical and empirical models to form a composite of the two and therefore gain a better understanding of the interactions. Chang (2008) produced an FE model using the Greenwood and Williamson work as its basis and concluded that asperity contacts make little impact of the efficiency of the sliding interface. A study based on the Flodin method to derive a FE model found that the load increases as cumulative wear takes place and eventually a threshold is reached beyond which fatigue failure is a risk (Lin and Kuang, 2008). An extremely detailed FE model is presented by Mulvihill *et al.* (2011) of two spherical titanium asperities coming into contact. The ratio of the relative positions of the asperities to the asperity radii (x/R) is concluded as the main factor in whether or not fracture and material removal occurs where x is the horizontal position of the upper asperity and R is the radius.

FE models can be considered as useful tools for prediction of stress and strain through a solid continuum of material. Although the advances in computational power have been immense over the last two decades, the FE technique still has limitations when it comes to describing a single body that has both large and small scale features that must be included. To this end, is there another method of modelling the contact area that will not present these limitations and will be more appropriate to the application? If the bulk properties of a material are considered it is possible to construct a predictive model based on its physical properties and research has been made on this subject. In a study made by Kar and Bahadur (1978), which was primarily about observing the material flow of PTFE, the observation was also made that 'fibres' could be seen accumulating around the stylus of the profilometer used against the substrate material. The same effect was observed in rubber and with both a stylus and a ball indenter by Briscoe (1981), which gave flake like features once applied and appear to be a function of the bulk properties of the material. The structure of a polymer varies from type to type, but in principle and for the POM material considered in this thesis, it comprises of polymer chains around 200 nm long that are interconnected by strong and weak forces between chains. This being the case, it then should be possible to construct a mathematical representation of this structure that either repeats or is infinitely variable through the solid structure geometry. The theory of random walks by Weiss (1983) indicates how one might construct such a model and was attempted, although mainly from a chemical perspective by Porter (1996).

The strong adhesion between PTFE and tungsten was investigated by Brainard and Buckley (1973) using field ion, Auger emission and scanning electron microscopy. They found that adhesion forces were very small between the two materials until they had remained under loaded contact for a number of minutes. After that time, they considered that creep had occurred in the PTFE such that the apparent area had increased and so atomic bonding had increased at the contact interface. For short periods of contact, they found no perceptible adhesion occurred suggesting that fleeting contact should not bring the onset of adhesion. Molecular modelling techniques have been used by Cheon *et al.* (2002) to describe chemical bonds between polymer chains and in a computer modelling study carried out some relative movement of the polymer chains were found by Chiu *et al.* (2011). In particular, the polymer chains bow when subjected to a force, which is of relevance to the work presented in this thesis.

1.4.4 Analysis

In the pursuit of new knowledge, physical phenomena are observed and experiments are created to ascertain fundamental sources. These experiments and mathematical models are used to validate and describe a phenomenon. Whilst carrying out these activities it is also necessary to think about what is observed and to formulate mechanisms of the cause. There are many forms of analysis that are applicable to the area of research in tribology with respect to this thesis, from FEM to traditional contact mechanics and analysis by inspection.

A friction model is presented by Bassani *et al.* (1984) that utilises a detailed analysis of the contact mechanics between steel and polytetrafluoroethylene and applies it to a statistical assessment of the asperity densities and heights. The contact analysis was developed as a sum of the shearing and ploughing components of the contact between the two material surfaces. The model was validated against experimental work and they showed that adhesion is a major contributor to wear for lower rms deviations, whilst ploughing was more important for high rms values. A wear equation that includes a number of additional material terms was developed by Kar and Bahadur (1974). It was developed from experimentation using polyoxymethelene (Delrin 500) both unfilled and 20% filled with PTFE and includes a term for surface energy. Their work makes an observation that surface energy is included in the model as wear between the counterface (steel) and the polymer is by adhesion. They also make the point that the inclusion of a filler material greatly reduces the wear rate.

Methods were attempted by Samyn and Schoukens (2007) for comparing wear rates for polymers between small and large scale experiments. The small scale experiments generated a contact pressure of around 5 MPa, whilst the large scale arrangement gave a maximum value of 150 MPa. There was a reasonably close correlation between the results using models based on one or two parameters such as normal load or contact pressure. However, it was found that models involving multiple variables such as coefficient of friction and pressure-velocity could not be correlated in the same way. A more detailed application of the wear equation was adopted by Atkins *et al.* (1984) to predict wear rates that arise from fatigue cracking in polyethersulphone. The inclusion of two empirical constants yielded very close comparison between experimental and calculated values of wear rate. However, this would seem to be another case of

empirical model generation rather than a true representation of the contact mechanics of the polymer-steel interactions.

Walton and Shi (1989) make observations of the different wear mechanisms of polymer gears. They present diagrams of what the different failure mechanisms resemble and then review the effectiveness of the different methods of analysing these failure mechanisms. The application of the Lewis equation for bending stress in gear teeth is used as the basis for the British Standard method for calculating the strength of gears. This was built upon by the research of Breeds *et al*. (1993), Walton and Shi (1994) and Li (2002) to include SEM inspection of worn gear teeth and a finite element model of the teeth with respect to bending strength. An approach can be taken to the modelling of stress and strain that treats materials as completely filling the space that they occupy. The fact that any materials do in fact have an internal structure such as atomic and molecular constituents is ignored in this continuum approach to modelling. However, FEM is extremely reliable for predicting stresses in a continuum of a material, but it has limitations when the material is not obviously a single homogenous solid. A polymer is at first glance a homogenous solid, but in reality is made up of polymer chains and maybe it can be viewed more as a composite material than a continuum. Composite material FE models have been created by Goda *et al.* (2001) to predict the contact performance of a polymer reinforced with fibres and this study also considers the fact that this occurs on the micro scale.

1.5 Aims and Objectives

The aim of this research thesis is to add to the body of scientific knowledge in the area of the operation of polymer spur gears. Gaps in this knowledge have been identified from an extensive review of the literature in terms of the wear mechanisms specific to polymer spur gears. To an extent, the aims and objectives of this research developed as time progressed. For instance, in chapter 5, various images will be shown describing a new and previously unidentified wear mechanism. Clearly, the aim of the thesis is to provide new and insightful information to the scientific community, but this discovery in particular was somewhat serendipitous. However, the following broad aims and objectives were sought by the thesis:

i.   The analysis and inspection of the involute gear tooth geometry.
ii. The investigation of efficiency of the involute gear tooth form derived from the basic geometry and material.
iii. Inspection and analysis of possible wear mechanisms present on gear teeth and to predict and characterise their behaviour by use of numerous mathematical modelling techniques.
iv. The investigation of the running temperature of a polymer-steel gear pair and if, for the specific gear pair case, temperature is a factor in their wear.

CHAPTER 2

Involute Geometry in Relation to Heat Generation and Efficiency

This chapter explains the geometry of spur gears, how the involute form is generated and how the gears move together. This information is required in order to understand the basis for sliding induced wear. It also sets out the initial modelling for later chapters in terms of slip speed calculations.

2.1 The Involute Gear Tooth Form
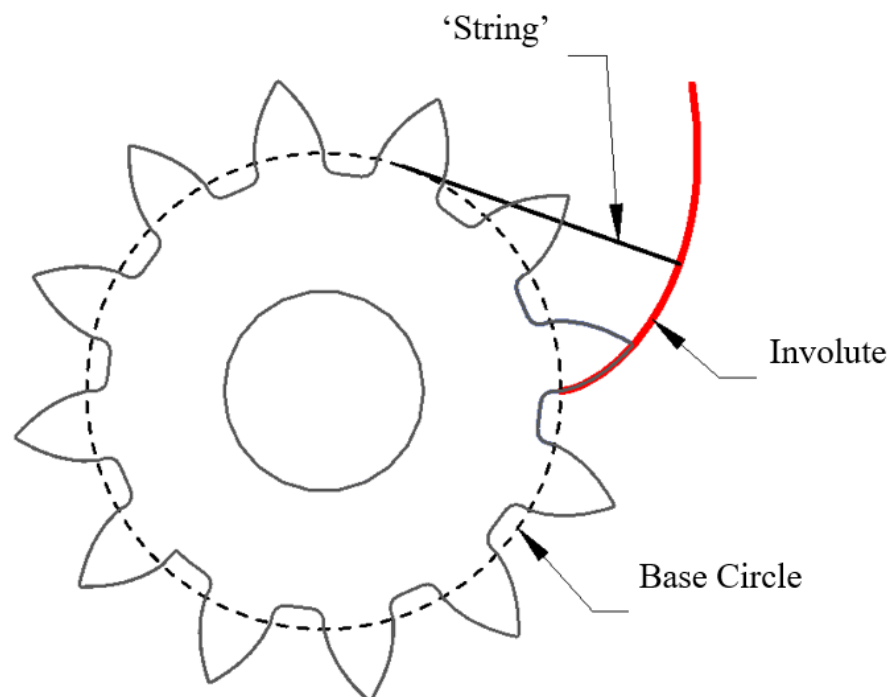
Figure 3: The geometry of involute generation for spur gears

The involute gear form is a particular profile for gear teeth that allows constant and smooth power transmission from the driving gear to the driven gear. The profile is generated by sweeping an arc from the base circle of the gear beyond the outer diameter of the gear. Figure 3 illustrates how this is done. It can be thought of as wrapping a string around a cylinder of a diameter to match the base circle. If the string is then un-wrapped from the cylinder, the path the end of the string follows generates a profile that is called an involute. This geometric arrangement provides the pure involute profile onto which can be superimposed the necessary details to produce a real manufactured gear form. The smooth transmission of movement between gears is geometrically intrinsic to the involute profile. There are a great many of published descriptions of the generation of an involute curve, Buckingham (1949) provides a detailed analysis of it along with many other aspects of gear geometry and manufacture.

2.2   Spur Gear Definition and Nomenclature
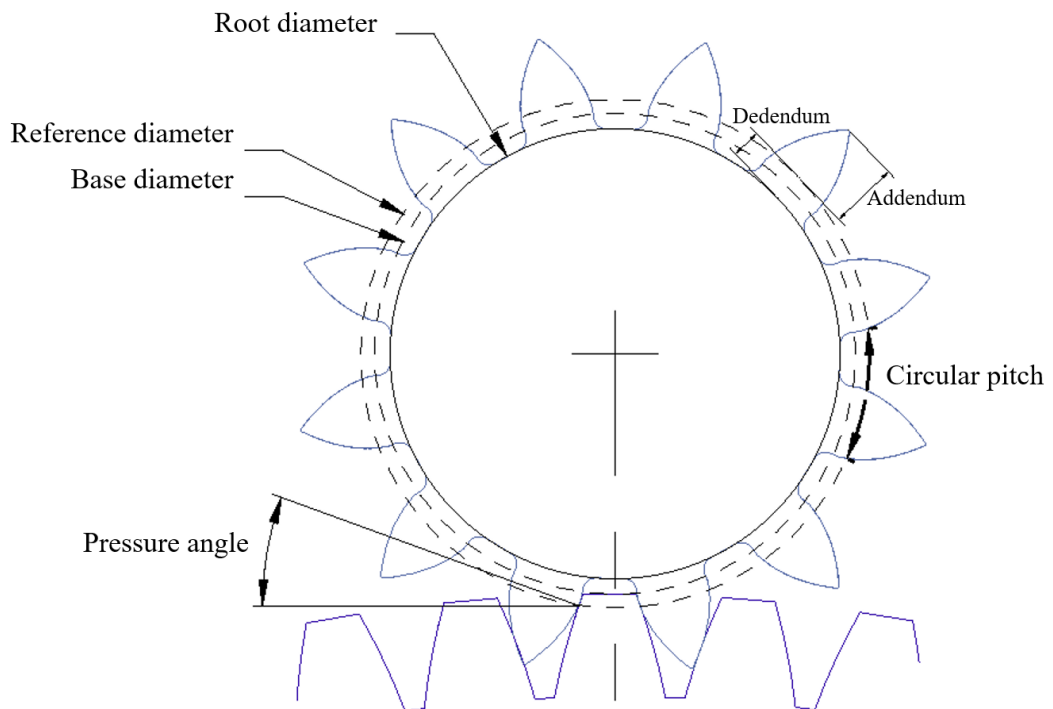
Figure 4: Spur gear definition and nomenclature

A full list of definitions and nomenclature used to completely describe the geometry, manufacturing and inspection criteria for a pair of straight cut spur gears is

extensive and can be found in The Machinery's Handbook, Olberg (2012). Figure 4 shows a diagram that illustrates the main variables and the following list describes other gear nomenclature that are relevant to this thesis:

Contact Ratio – This ratio describes how many teeth are in contact at the same time and so is an indicator of how smooth a transmission the pair will provide.

Base Diameter – The diameter from which the involute curve is struck.

Reference Diameter – The diameter at which contact between the teeth occurs when that contact point is in line with both gear centres. This is also called the Pitch Circle Diameter (PCD) or Pitch Diameter.

Pressure Angle – The angle of contact between the teeth flanks, usually 20°.

Root Diameter – The diameter at the root of the teeth.

Addendum – A measurement from the reference diameter to the outer diameter of the gear.

Dedendum – A measurement from the reference diameter to the root diameter of the gear.

Circular Pitch – The distance between two gear teeth along the Reference Diameter.

Active Face Width – The width of tooth flank actively in contact between the pinion and gear (note that the face width of the gears could be greater than this).

Backlash – The amount of clearance between flanks which results in lost motion between the pinion and gear during load reversal.

Gear Ratio – The ratio of pinion teeth to gear teeth.

Efficiency – A measure of the energy transmitted, specified as a percentage and always less than 100% due to transmission losses that are discussed in some detail throughout this thesis.

Module – The ratio of pitch diameter to number of teeth. The higher this number, the larger the teeth are.

Line of Contact – See Figure 5.

Pitch Point – The point during the contact that is in line with both gear and pinion centres.

Gear – The larger of the two gears.

Pinion – The smaller of the two gears.

2.3 Alternative Gear Types

The involute form for gear teeth is by far the most widely used as it is easy to manufacture and gives a smooth transmission of power. The involute profile is the basis of most modern gears but there are alternatives that have advantages and disadvantages. The following lists the various types of involute gear and also some alternatives:

- Spur – The gear type that is the subject of this thesis. A straight cut gear using the involute profile as its basis.
- Rack and pinion – A spur gear arrangement where the output or rack is linear to convert the rotation of the pinion into a linear motion output.
- Helical – A variation on the straight spur gear where the tooth flank is swept by an angle (commonly 15°), which makes for a smoother and quieter gear pair with slightly increased load capacity.
- Bevel – Another variation on the spur gear, although not a true involute form. The teeth are arranged at an angle to the shaft axis to give (commonly) a 90° angle between output and input shaft.
- Spiral bevel & Hypoid – A variation on the bevel gear where the teeth are swept through an angle in the same manner as the helical gear.
- Cycloidal – This is one of the oldest gear profiles and is still widely used in clock and watch movements. It does not yield a smooth transmission, but is more useful as an indexing mechanism, which is clearly and advantage for a clock or watch movement.
- Conformal – Parker (1965) - This profile geometry is constructed in such a way as the teeth flanks are concave rather than convex. This gives a much lower contact stress distribution where the two teeth touch. It was developed for some time during the 1960s and 1970s by Westland Helicopters but was eventually dropped due to the additional difficulties with manufacture that the profile presented.
- Novikov – Nacy *et al.* (2007) - A variation on the conformal gears described by Parker.
- Convoloid – Dontyne (2014) - This is a development of the involute form that includes a step at the pitch point of the gear contacts.
- Harmonic – Generally uses an involute as the base profile. The input gear is a flexible belt having fewer teeth than the output gear. The flexible input is driven by an elliptic

input cam. As the input processes around the output, the output is driven the distance equal to the difference in number of teeth giving a very high ratio in a compact form.

2.4 Studied Gear Pair
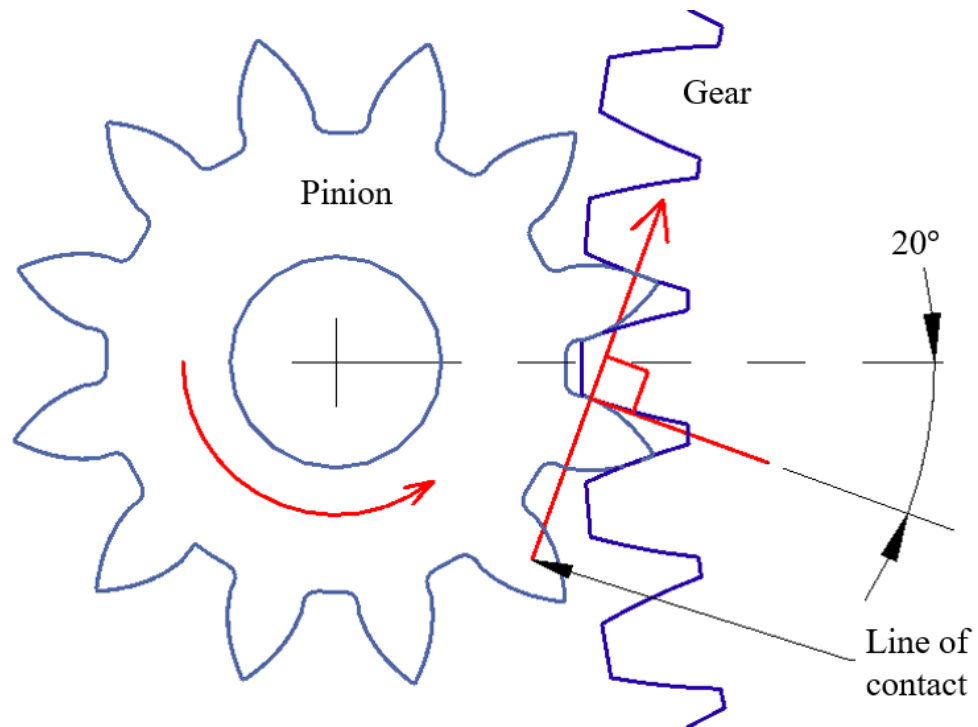
Figure 5: The studied spur gear pair geometry showing the line of contact

The research undertaken in this thesis focuses on a particular pair of gears that are manufactured for Rotork and are used within its CVA line of actuators. The gears are used to transmit power, but the prime function is in control applications. The gear geometry details are listed in Table 1 with the material properties of the two materials studied shown in Table 2. Figure 5 shows a sketch of the pinion (left) and the gear (right). The gears have a pressure angle of 20°. This means that at the point of contact, there is a force normal to the tangential contact plane at 20° from the axis between the gears. This line running normal to the contact plane is called the line of contact.

Table 1: Studied gear pair parameters

	Pinion	Gear
Number of Teeth	12	75
Torque	0.85 Nm	5.3 Nm
Speed	17.6 rad/s	2.8 rad/s
Power	15 W	<15 W
Module	1	1
Pressure Angle	20°	20°
Pitch Circle Diameter	12 mm	75 mm
Material	Steel 1.0511	POM
Profile Shift	+0.5	-0.5
Method of Manufacture	Hobbed	Hobbed
Rotork Part Number	49242	49240

Table 2: Studied gear material properties data[*]

Property	Symbol	Unit	Steel 1.0511	POM – Delrin 100
Density	ρ	kg/m3	7845	1420
Ultimate tensile strength	σ_u	MPa	620	-
Yield strength	σ_y	MPa	415	69
Modulus of elasticity	E	GPa	200	2.8
Poisson's ratio	v	n/a	0.3	0.35
Shear modulus	G	GPa	80	66
Flexural yield strength (1.3 mm/min)	σ_f	MPa	-	94
Deformation under load (13.8 MPa)	-	%	-	0.7
Coefficient of friction (DuPont)	μ	n/a	Static	0.2
			Dynamic	0.35
Deflection temperature (1.8 MPa)	-	°C	-	125
Melting temperature	-	°C	1370	177
Glass transition temperature	T_g	°C	-	-60
Specific heat capacity	c_p	J/K	486	1600
Thermal conductivity	k	W/mK	50.7	0.4

[*] DuPont (2011).

2.5 Equivalent Cylinders Analogue
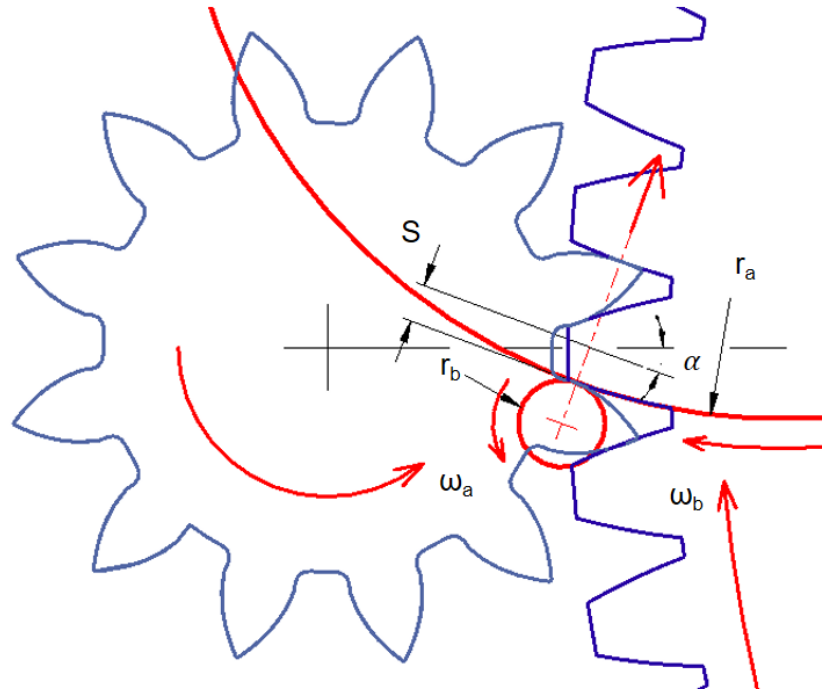
Figure 6: Equivalent cylinders geometry definition superimposed onto the studied spur gear pair.

A feature of the involute profile that is known, but not generally considered significant, is that slip occurs between the teeth flanks. This results in a reduction in efficiency of around $1 - 2$ % (Beardmore, 2013). As this slip is not large and does not impact to a great degree on efficiency it is usually ignored in many design considerations. However, it is considered in this thesis as it gives rise to thermal and tribological effects, which will be explained in further chapters. In the line diagram shown in Figure 6 it is seen that two contacting surfaces are represented by two separate cylinders of radii r_a and r_b. The inferred rotational speeds of these cylinders are equal to those of the gears, respectively. This allows a simple Hertzian contact to be evaluated at any given point in the gear teeth sweep. This technique is described by Hamrock (2004) and is used extensively when researching the characteristics of spur gears. As the two cylinders have different radii, but their speeds remain constant it is clear that there will be a varying differential slip between cylinder rotational speeds. The slip speed is

$$v = \left(r_{bg} sin\alpha + s\right)\omega_b - \left(r_{ag} sin\alpha - s\right)\omega_a \tag{3}$$

where r_{ag} is the pinion pitch radius, r_{bg} is the gear pitch radius, α is the pressure angle (rad), s is the distance of the point of contact from the centre line, ω_a is the rotational speed (rad/s) of the pinion, and ω_b is the rotational speed (rad/s) of the gear. Accordingly, $r_a = r_{ag}sin\alpha - s$ and $r_b = r_{bg}sin\alpha + s$.

2.6   Modelling and Analysis of an Accurate Involute
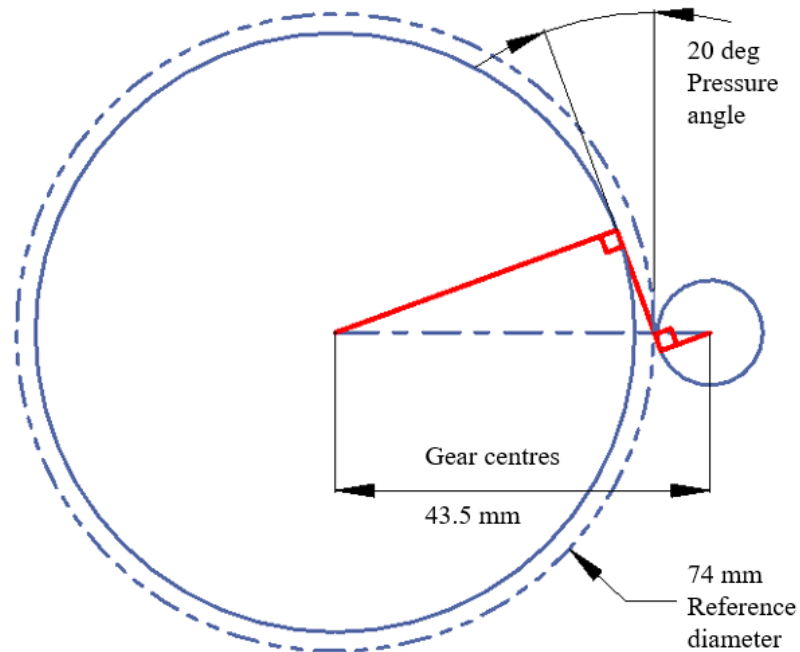
Figure 7: Base circle definition from which the involute is struck.

The geometry of a spur gear is defined by the involute curve onto which the necessary details such as root depth cut, root radii and tip radii are superimposed for the finished form. Many CAE packages are capable of producing a representation of a spur gear, but they are often not accurate and simplify the form for ease of creation and size of file. Specifically designed software such as GearTrax from Camnetics (2014) does produce a much more accurate form. In this case, however, the profile is composed of a series of flats rather than a pure involute form. To fully understand the profile a method of producing an accurate gear profile was devised and is detailed here. This accurate profile can then be analysed using a multibody dynamics software (in this case NX) as an investigation into the torque and speed transmission of the spur gear pair.

The first stage of the process is to determine the base circle of the involute, from which the involute will be struck. Figure 7 shows a sketch that has been produced to generate the base circles. The (digital file) sketch is parametric and fully constrained such that the only definable variables are the centre distance between the gear pinion (in this case 43.50 mm) and the reference diameter of the gear (74.00 mm). As the pressure angle is defined as 20.00° and the line of contact is tangent to both large and small diameter base circles, this completely defines the parameters of the sketch. In this case, the base circle for the gear is 69.54 mm and for the pinion is 12.22 mm. These diameters can also be determined through trigonometry or by a standard formula from Olberg (2012).

Once the base circle has been defined, the involute curve can be generated and is done so using trigonometry to define Cartesian coordinates for points on the involute as shown in equations (4) to (9). Figure 8 shows the trigonometry employed to do this and the equations following the figure show how the points are created based on the 'string'

length.
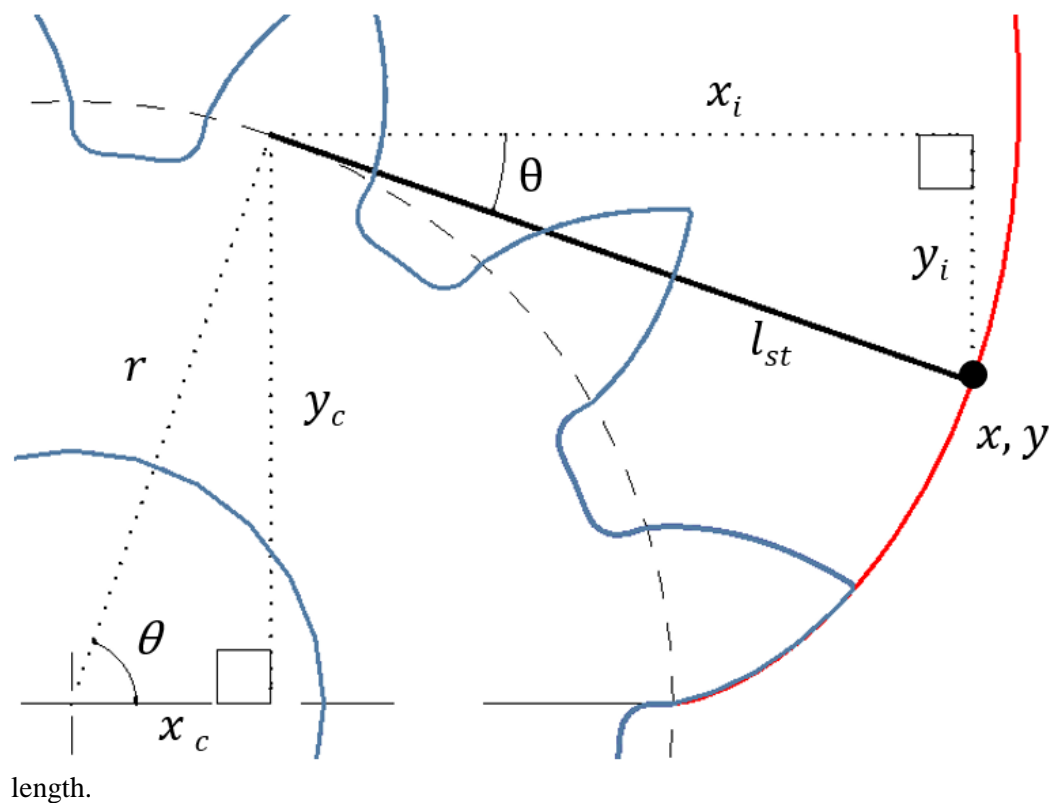
Figure 8: Cartesian coordinates for the involute

The analogy of the contact between two cylinders and the contact between the gear teeth is used extensively throughout the thesis as a means of establishing discrete points in the contact sweep to be considered for analysis and experimentation. As the gears run through their contact the relative radii of the cylinders change and these radii are directly linked to the point along the contact line 's' (Figure 6). This is a useful analogy as the geometry of the contacting surfaces can be easily determined at each discrete point though the contact sweep.

The involute curve can be generated using trigonometry with respect to the centre of the base circle (Figure 7). Firstly, the Cartesian coordinates of the base circle are calculated as x_c and y_c using the radius (r) of the base circle. Further Cartesian coordinates are then calculated from the points on the base circle as x_i and y_i with respect to the 'string' length (l_{st}). These two sets of coordinates together trace the involute curve from the base circle out beyond the outer diameter of the gear teeth:

$$x = x_c + x_i \tag{4}$$

$$y = y_c - y_i \tag{5}$$

Therefore, expanding this to include the trigonometric relationships gives:

$$x = r \cos \theta + l_{st} \cos \theta \tag{6}$$

$$y = r \sin \theta - l_{st} \sin \theta \tag{7}$$

Given that l_{st} is a function of the angle θ in relation to the full circumference of the base circle, the full expressions relating to the radius r and the angle θ are

$$x = r \cos \theta + r\theta \cos \theta \tag{8}$$

$$y = r \sin \theta - r\theta \sin \theta \tag{9}$$
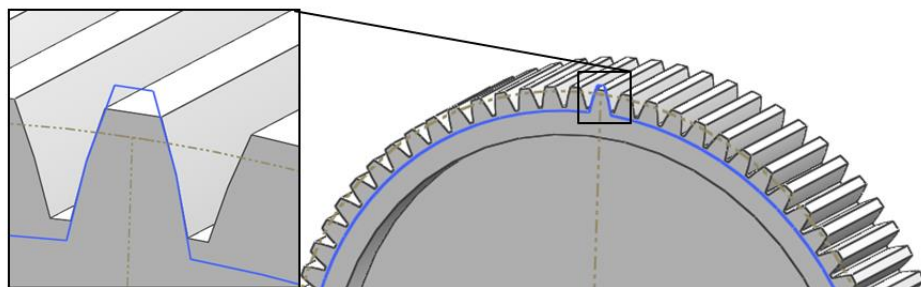
Figure 9: CAD Model of a gear

These values are evaluated over a range to output the Cartesian coordinates for the curve, which are then used to draw the involute for the gear. A data set was created for the range and was imported into NX as a smooth spline. This spline was then mirrored about the centre of the tooth, extruded to create the tooth and then patterned to complete the gear model shown in Figure 9.
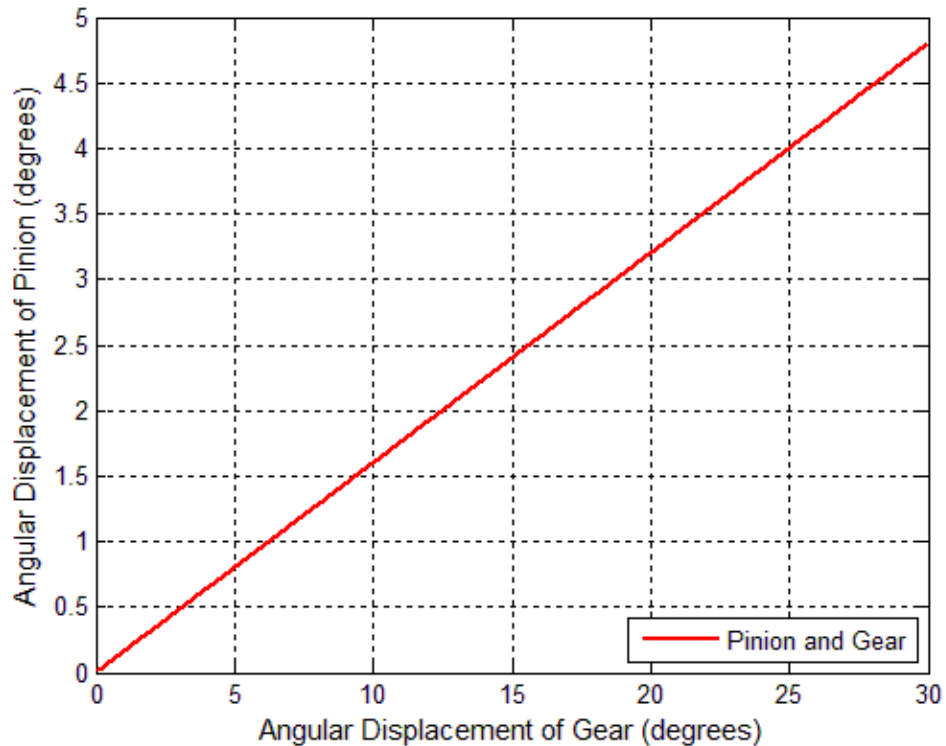
Figure 10: Results of a motion simulation of the gear model showing a smooth and linear relationship between pinion and gear

This process was followed for both pinion and gear to produce an accurate CAD model for each of the parts. The NX CAD system was then used to perform a motion simulation analysis of the two spur gears running together to confirm that they were in fact modelled correctly and with sufficient accuracy. The motion analysis output was in the form of angular displacement of each of the gears and is plotted in Figure 10. The results produce a completely straight line with no deviation from the ratio of 6.25:1 consistent with the number of teeth for each gear. It is concluded that this methodology does provide an accurate gear form and so is suitable for use during further analysis and experimentation.

2.7   Slip Speed and Efficiency

The equivalent cylinders analogy shows that a spur gear pair experiences rolling contact as the gears rotate together with a varying slip speed. This slip speed and the frictional losses associated with it account for the loss in efficiency across a gear pair. Typical spur gear efficiencies are quoted at around 95-98%, which includes losses due to the bearing and mounting arrangements as well as the sliding losses. As the two teeth are sliding with respect to one another and a loss in efficiency is seen between gears; heat is being generated at the tooth contact point. A fundamental question is: What is the temperature rise in a gear pair that is generated from the sliding action and how can it be calculated?

A mathematical model has been developed to calculate the fundamental parameters associated with a particular geometry of a gear pair, the outputs from which are used in later chapters when calculating the temperature and other contact conditions. This basic parameter model calculates the slip speed and power dissipated at the tooth contact based on load and friction. The model structure is seen in Figure 11 and is created from the information and techniques discussed in this chapter and later in Section 4.1.
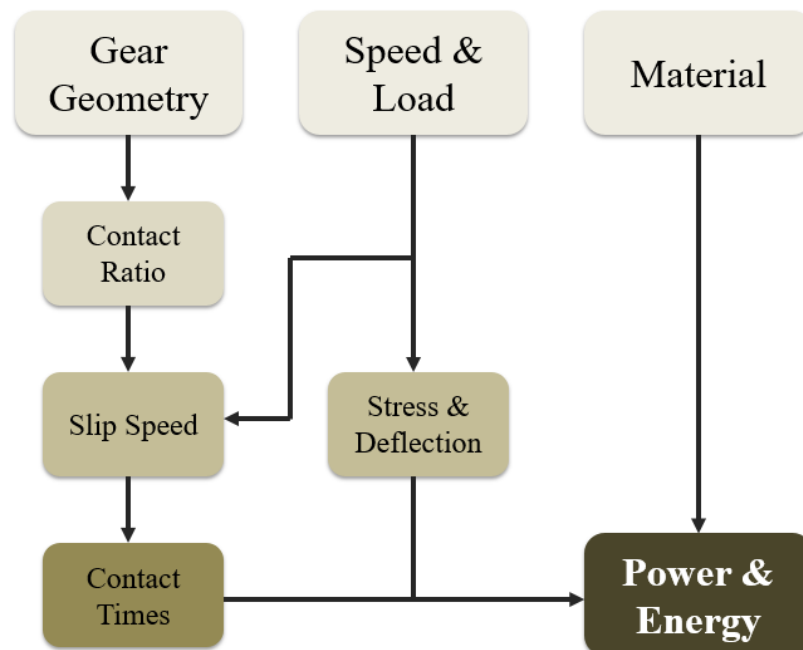
Figure 11: Gear data model structure
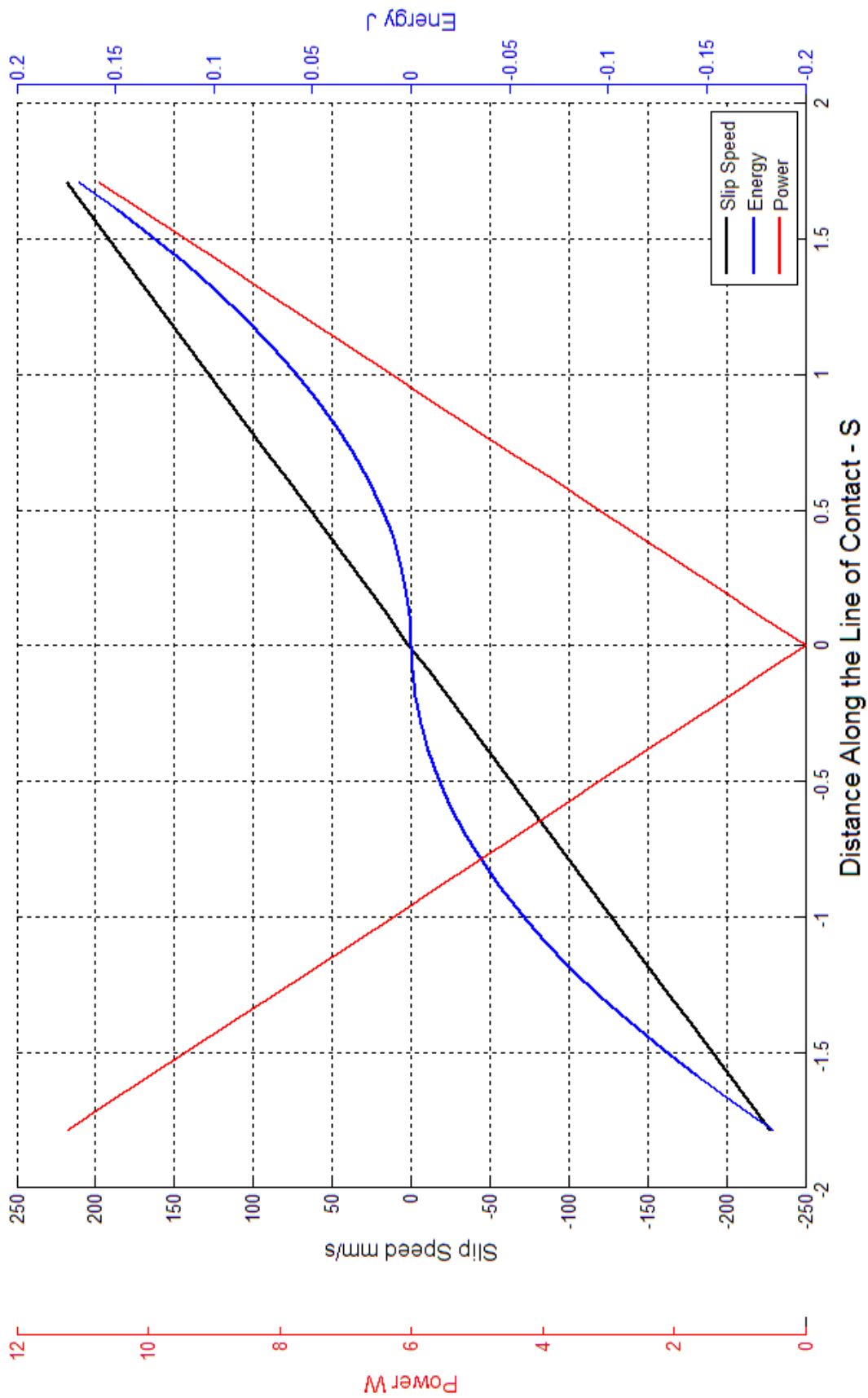
Figure 12: Gear running performance values based on the gear geometry and models developed in the previous sections of this chapter.

The model takes the basic geometry of the gears and calculates the slip speed based on equations (3), (8) and (9). It evaluates the stress and deflection experienced through the teeth contact sweep in accordance with the material, speed and load conditions (discussed in Section 4.1). It then uses a time averaging technique (detailed in Section 3.3) to evaluate the power and energy through the sweep. Figure 12 shows these data with respect to the distance moved along the line of contact or the sweep of the teeth in contact. It provides a preliminary characterisation of the gear pair in terms of slip speed and how power is dissapated at the contact which is useful in understanding the following discussions on the efficiency of the gear pair.

An important point to note about the contact characteristics between the two gears is that of the relation between the rolling and sliding action. It is evident from Figure 12 that the slip speed decreases as it reaches the point in the contact that is in line with both centres of the gears and then increases again as it moves away from it. In addition to this action, the rolling is occurring in the opposite direction.
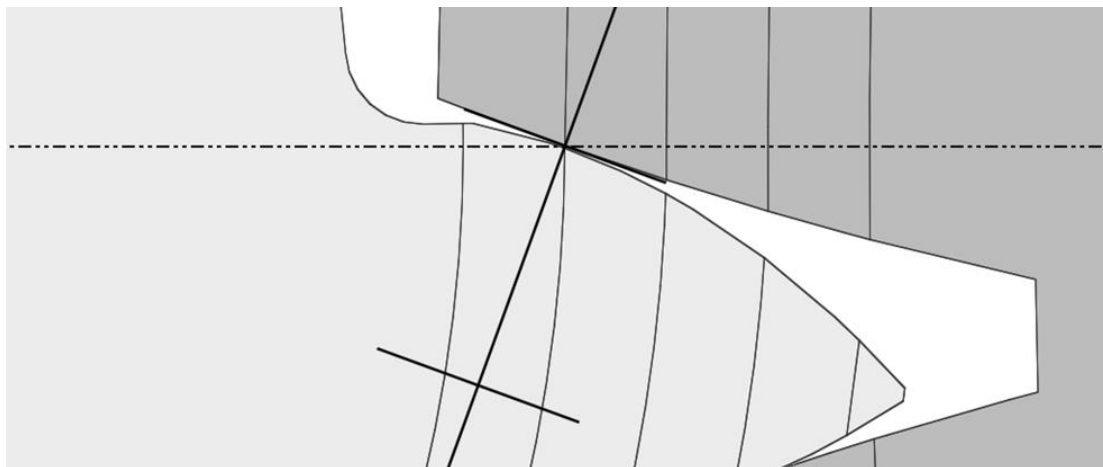
Figure 13: Zero slip between the teeth when contact is aligned with both gear axes.

Figure 13 shows the gears in contact at the zero slip position when the point of contact is in line with both gear centres (the horizontal dotted line) and $S = 0$. The driving pinion on the left is rotating in an anti-clockwise sense.
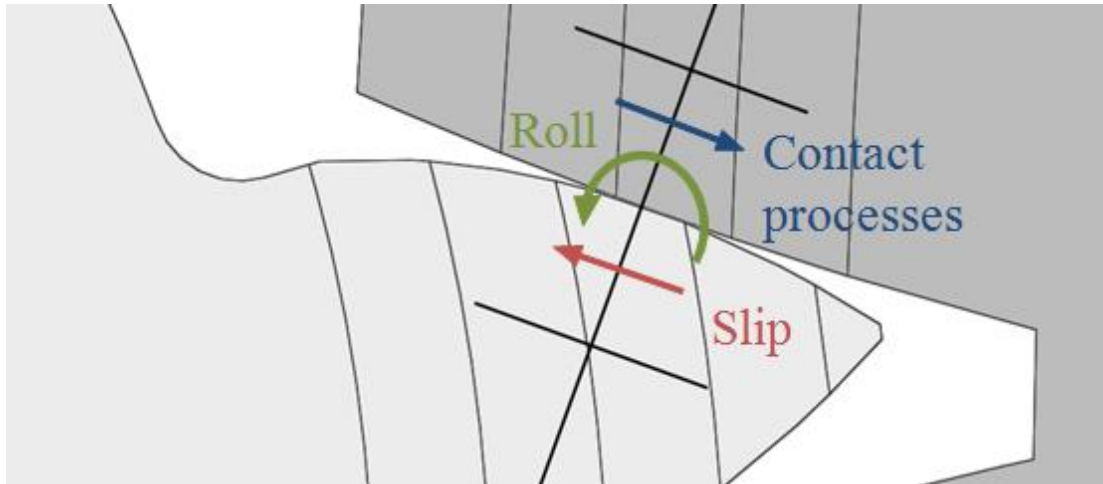
Figure 14: Slip with opposing roll between the teeth.

Figure 14 shows a point in the contact above the zero slip position. Here the driving pinion is rolling against the polymer gear face in the direction shown. Also, the two contacting surfaces experience a differential slip in the direction of the arrow shown with respect to the driving pinion on the left. It is also seen that the contact point has processed from left to right as this has occurred.
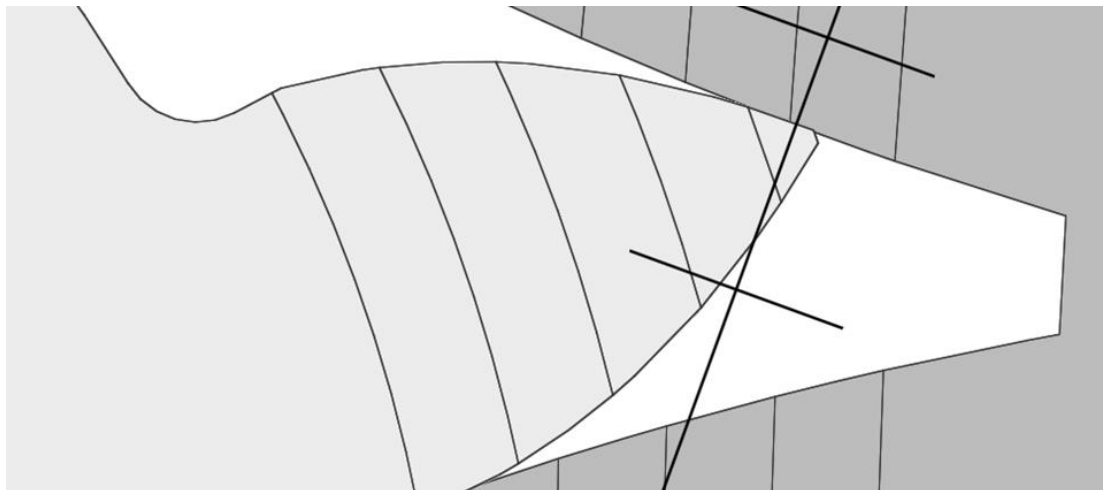
Figure 15: Maximum slip just before the pinion tooth exits the mesh.

Figure 15 shows a position just before the pinion exists the gear mesh and the slip speed here is at a maximum. Figures 13 to 15 illustrate the opposing slip and roll of the steel pinion against the polymer gear. The significance of this action will become evident in later chapters when the mechanism of wear is discussed in depth.

2.8 Consolidation of Chapter 2

This chapter has described the fundamental characteristics of the involute curve when applied to a pair of gears transmitting motion and power. A method for producing an accurate involute spur gear profile as a computer model has been developed both in terms of a three dimensional CAD model and also for use in a numerical model that calculates some of the fundamental properties of the gears. The chapter began with stating the anecdotal knowledge that a pure involute spur gear is not 100% efficient with the associated assumption that it is because of a differential slip that occurs between the teeth. Through the models and calculations that have been applied it has been proved that a differential slip that occurs between the gear teeth and the precise nature of the slip in terms of its magnitude and variability has been quantified. A study was also presented of the way the contact is made between the steel pinion and the polymer gear and the way that it changes as the pinion slides and rolls over the gear. This action is unique to spur gears and must be of utmost importance to any mechanisms of wear seen in gears operating under load. In the following chapters, this knowledge is used to formulate certain hypothesises about the heat that is generated by the slip. It will also be used to formulate a theory of a new wear mechanism in polymer spur gears.

CHAPTER 3

Experimental Investigations into Gear Running Temperatures

An involute spur gear pair is simple in concept; however, once studied in detail it is revealed as a complex mechanism in terms of surface contacts. In order to study the heat generated at the contact point between the gears it is useful to simplify the problem such that it can be more easily modelled and that the experimental method can be simplified. Pin on disc running experiments have been used extensively in tribology to study friction and wear properties between different materials, but they have also been used in studies of gears. In chapter 2, the action of the two involute forms of each gear in contact is described as a pair of cylinders of diameters relative to the point on the line of contact and the rotational speeds of the gears. This being the case, at any instantaneous point during the gear running, a set of parameters can be determined for that instant in the gear tooth contact. To do this simplifies the problem in terms of modelling and experimental requirements. Experimental hardware was designed to simulate a number of different slip speeds and points along the line of contact and an analytical model has been developed to describe it, which will be presented in this and chapter 4.

These experimental investigations were split into two sections. Firstly, a rod on axially aligned disc experiment was devised that examines the temperature at each point through the tooth sweep and the temperatures at each of these points were measured. Additionally, a second experiment has been designed that runs the real gears together under a known load and speed and teeth temperature was measured. The second real gear running experiment was then used to validate the first.

3.1 Rod on Axially Aligned Disc

Throughout this research models used to predict real physical behaviour of systems have been validated experimentally. In this case, as the mathematical models proposed represent relatively simple physical scenarios, an experiment was conceived to perform this validation. This will validate the mathematical model and will allow it to be developed further for temperature prediction in gears. This systematic approach was taken to apply a simplified experiment firstly before moving to the more complex and real condition.

3.1.1 Experiment Design

An experiment was conceived that would be capable of rotating a disc made from the same material as the studied polymer gear (POM) axially aligned against a rod made from the same material as the pinion (Steel). The following requirements were set upon the experiment design:

  i.   The design must allow for the loading of the steel rod against the polymer disc as it is rotated and also for that load to be measured dynamically.
 ii.   The hardware must accurately measure the speed of the motor and/or the disc.
iii.   The hardware was to be configurable to accept different diameters of rod on axially aligned disc.

In this way, the experiment was capable of simulating a number of different discrete points along the line contact S (Figure 5) and also measuring the speed and load of the system to accurately match it to the real gear scenario. A strain gauged load transducer was designed for this reason as it provides high accuracy both dynamically and statically.
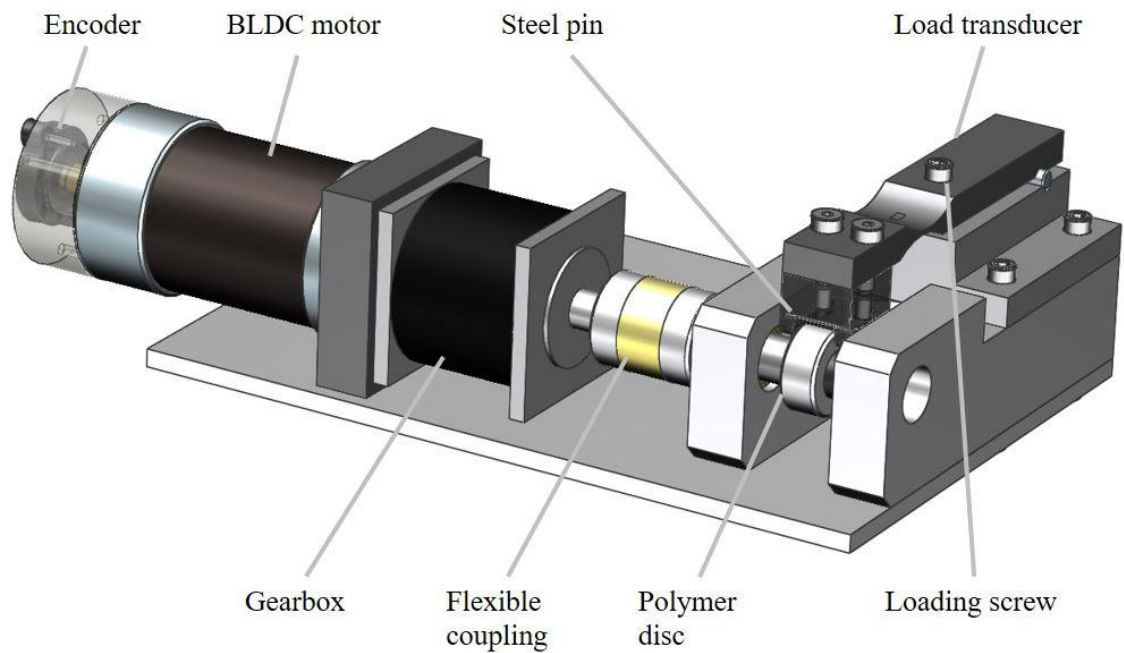
Figure 16: Rod on axially aligned disc experiment hardware design

3.1.2   Hardware Design

The experiment hardware was designed in order to evaluate the flash temperature of a steel rod rubbing against an axially aligned polymer disc. The polymer discs were made from Rotork gears to ensure that the materials used during the experiments were consistent. The experiment hardware mechanical design was performed using NX. A 3D CAD model was produced from which the 2D manufacturing drawings were created.
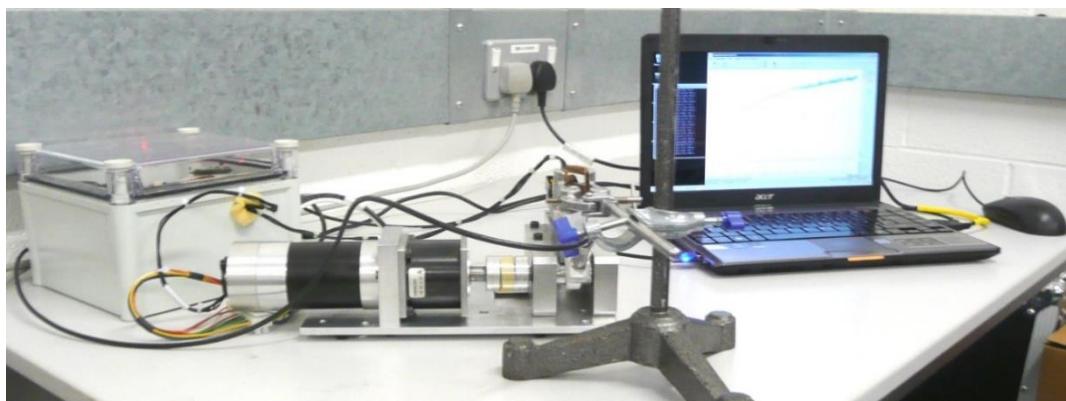
Figure 17: Rod on axially aligned disc experiment

The experiment hardware (Figures 16 and 17) consists of a 100 W brushless DC electric motor (Part Nᵒ BL5796-24V manufactured by Techtop) driving a small 5:1 reduction epicyclic gearbox. The gearbox is connected, via a flexible coupling, to a steel shaft. The polymer disc is keyed to this shaft and so could be rotated up to a maximum of 800 rev/min. An encoder is mounted to the rear of the motor and measures the motor speed by way of a Hall effect encoder sensing the angular position of the magnetic pole of a small magnet attached to the motor shaft. There is a small local amplifier PCB that converts the signal from the hall effect device into a usable signal of between 0 and 4096 counts per shaft rotation. This output is then counted with respect to time to provide a real speed of the motor shaft.

The steel rod is held by an aluminium block, which is in turn bolted to the load transducer. The load transducer is simply supported at its extent and the load between the rod and the disc is increased by tightening a screw down onto the load cell (loading screw, Figure 16). A strain gauge provides direct measurement of the strain in the transducer beam to indicate the rod load and was calibrated against a dead weight. For a given strain the control electronics returns a data count, which can be converted using a calibration graph described in the following section.
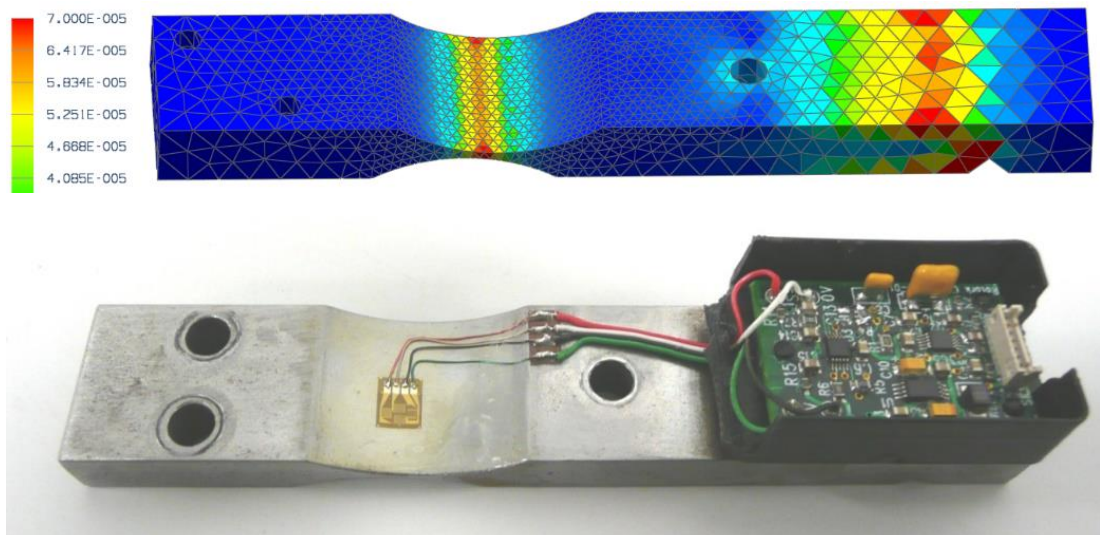
Figure 18: Load transducer design calculations and the finished load transducer.

A FE model of the load transducer (Figure 18) was produced using NX to ensure the correct strain output from it. The transducer was sized for the particular loads associated with the models presented and consists of a mild steel beam that has been machined to amplify the strain at a specific point. A full bridge strain gauge was adhered

to the steel beam in the position of the maximum strain as predicted by the FE model, which is shown in Figure 18 along with in image of the finished load transducer. The FE model was used to ensure that the strain was around 700 $\mu\varepsilon$, which is optimal for the strain gauge used. The strain gauge is a standard model produced by Vishay, details of which can be found in the appendices.

The experiment was controlled by electronics and software developed and produced to drive the CVA actuators. The motor speed was set through a PC using the Putty telnet interface (Putty version 0.60). Motor speed and load transducer data could also be read through Putty by USB connection with the electronics board. The temperature of the surface of the disc was measured using an infrared device that transfers data directly to the PC by USB interface. The sensor used was an Optris CS LT non-contact infrared thermometer. The infrared beam emitted from the device is conical in shape. It starts at a diameter of 7 mm and extends to a working range of 53 mm at a 15:1 ratio of diameter. At maximum range the device has an accuracy of ±1.5°C. Figure 19 shows how the sensor was positioned in relation to the disc surface. It is pointing directly at and is normal to the surface of the disc at approximately 5 mm distance and at an angle of 45° from horizontal. Since the output of the device is related to the mean thermal radiation of the surface, the angle of incidence of the device relative to the normal face of the disc only becomes important if a significant proportion of the signal is not collected by the sensor.
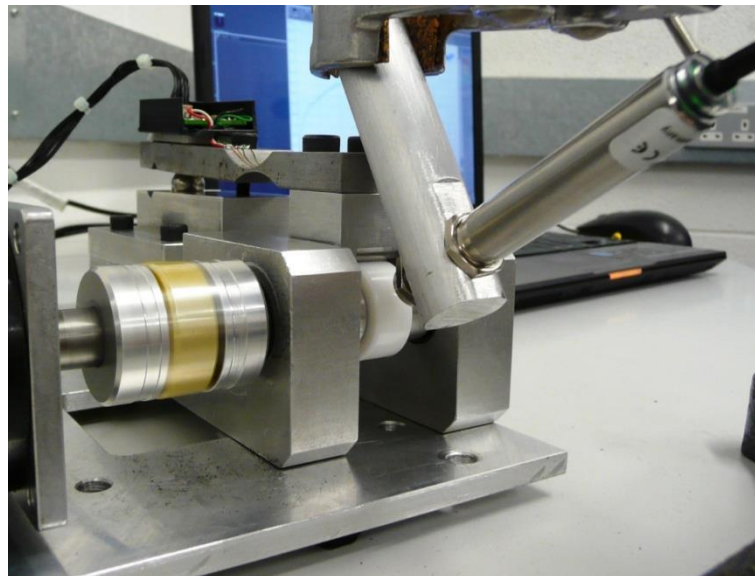
Figure 19: Positioning of the IR temperature sensor

The IR temperature sensor can be adjusted for an emissivity value of the particular material that is being measured. In this case a value of 0.91 was used for the device calibration as given by Beardmore (2013).

3.1.3   Calibration and Setup

The equipment was calibrated to ensure the correct loads and speeds were applied. To perform the calibration, the main hardware including the load transducer was turned upside down and fixed to a bench. A series of known loads were then hung from the load transducer end and the ADC (Analogue to Digital Converter) count recorded from the PC interface through the control PCB. The ADC count is an arbitrary value whose limits are from 0 to 16,000 counts and relates to the resistance change experienced by the strain gauge bridge when loaded. Figure 20 shows the data from 3 calibration runs along with an average value for the 3 data sets. The transducer shows very good linearity and also appears to be repeatable from run to run so will be accurate for the purposes of measurement of the load applied to the disc. The experiment load was 133 N as calculated in Section 4.1 and the maximum calibration load applied was 141 N. The load transducer was designed to operate as close as possible to the experiment load to maximise the sensitivity of the device, as such, the maximum calibration load was restricted to 6 % beyond the experiment load.
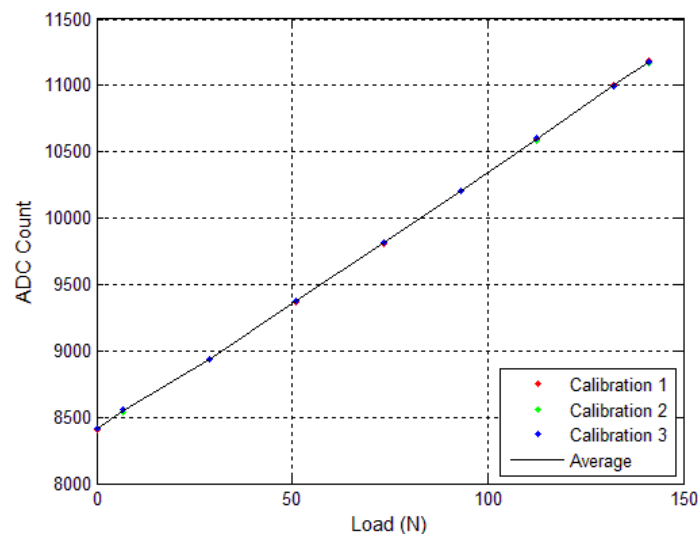
Figure 20: Rod on axially aligned disc load transducer calibration results showing three separate calibration runs with the average.

The motor speed was measured directly by an encoder mounted to the rear of the rotor, which senses a 2 pole magnet fixed onto the back end of the motor shaft. The encoder has a total number of counts of 4,096 (2^{12} bits), which defines its resolution. This figure is fed to the control board and is again converted to a digital single figure number that can be read through the PC interface. The relation between the motor speed and the ADC count is given by the expression

$$ADC = \frac{0.9\Omega}{12\pi} \times 10^{-4} \tag{10}$$

where Ω is the motor speed (rev/min).

3.1.4 Load in Relation to Temperature Fluctuation

The load applied to press the rod against the axially aligned disc cannot be perfectly constant. The build of the hardware was subject to normal manufacturing tolerances and allowance has to be made for this fact. As such, an investigation was made as to the magnitude of any fluctuations or errors that may be present in the temperature data resulting from manufacturing tolerances and build. Using the control system as detailed in the previous section, data could be acquired of the load applied to the disc and at the same time, the temperature could be measured accurately using the IR thermometer. Firstly, after a test run had been completed and the disc was up to running temperature, the disc was rotated slowly whilst the surface temperature was measured on maximum time resolution. In Figure 21 (a) the plot shows the temperature of the disc surface decaying for around 8 s at which point the disc is then slowly rotated at approximately 1 Hz. Note that the resolution of measurement of the instrument is 0.1 °C. The fluctuation in the disc temperature can be seen clearly as the bulk of the material continues to cool. Secondly, the nominal applied load can be measured dynamically from the load transducer using the PC interface. It is clear from these data that the load also fluctuates as the disc rotates, which suggests a slight out of concentricity of the disc with respect to the load transducer and rod. If the load and temperature fluctuations are plotted together as percentage errors away from their nominal values, then it is also clear that the load is indeed affecting the temperature and that the higher load results in the spike of temperature.
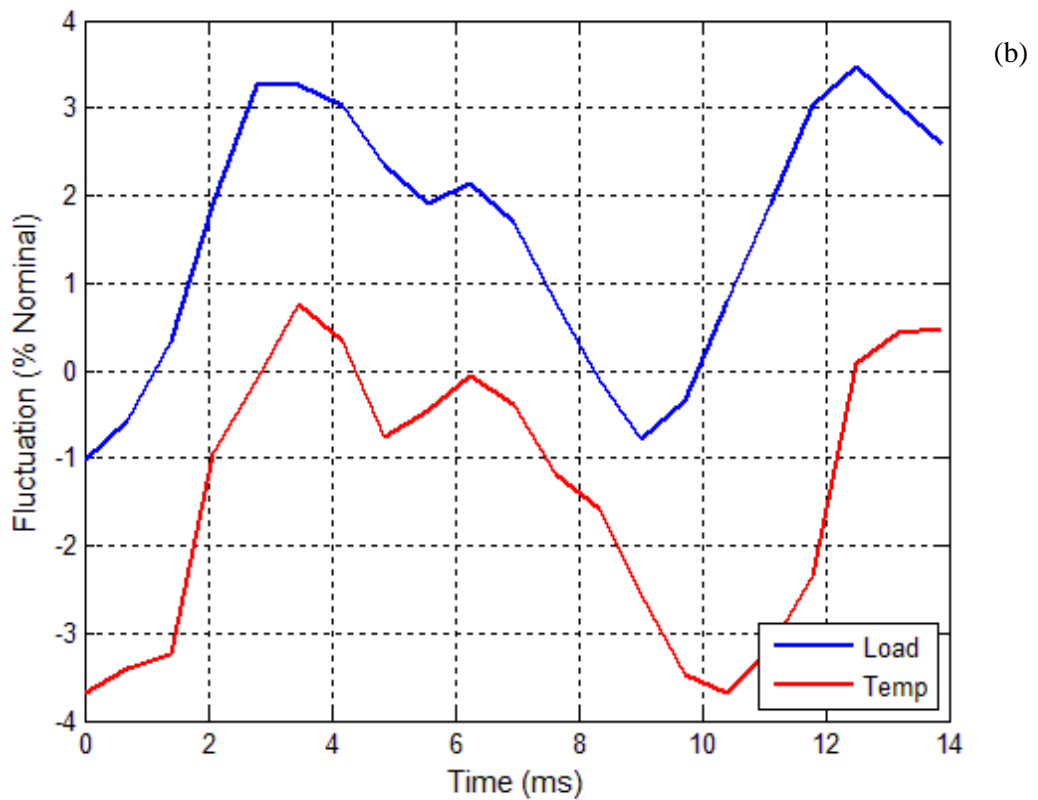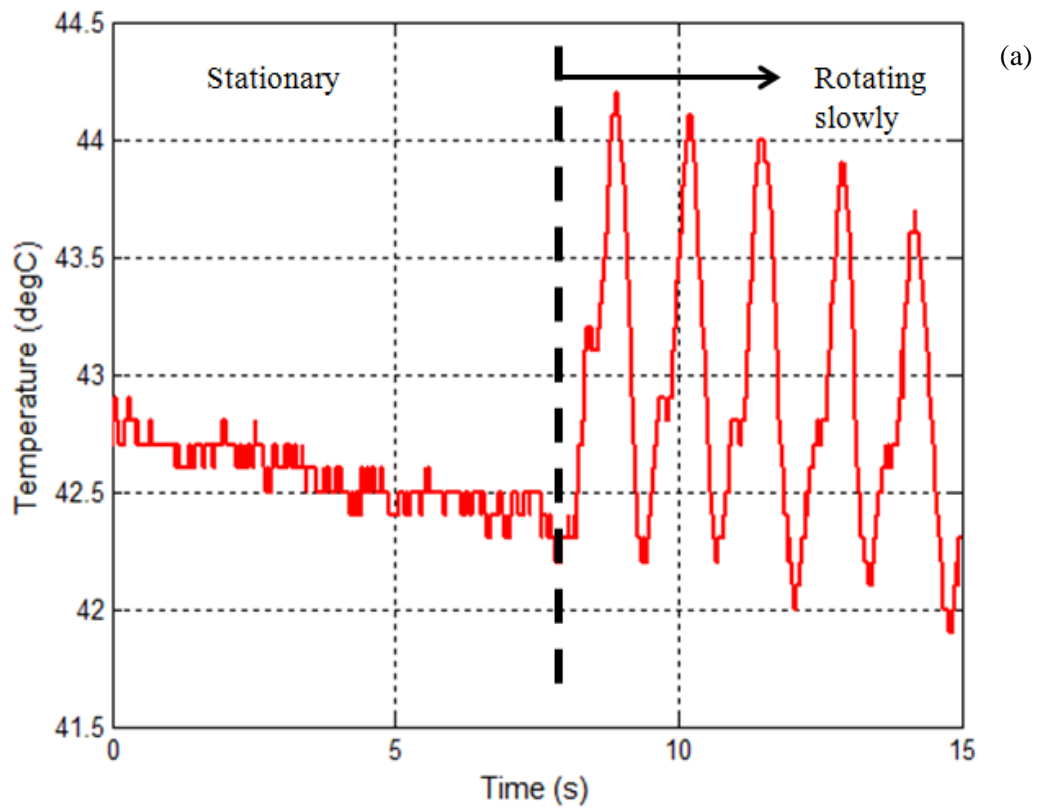
Figure 21 (a) Slow rotation disc surface temperature showing a variation in disc surface temperature around its circumference.

(b) Synchronisation of load and temperature.

On inspection of the two sets of data shown in Figure 21 (b), the curves are similar in shape and so the conclusion that the load variation has directly affected the temperature appears to be valid. Note that the data sets have been aligned on the y axis for purposes of comparison. The system therefore has a fluctuation or error in temperature measurement of around 3% due to the tolerances of the various mechanical parts. It would be possible to improve on this value by the introduction and control of suitable geometric tolerances for the shaft, disc and main housing of the experiment. However, a value of 3% is sufficiently accurate within the scope of this thesis.

3.1.5   Results

The main experimental aim was to acquire a set of results for the surface temperature rise in the disc at a variety of speeds that would correspond with a series of distances along the line of contact in a real gear pair. The set of distances and their corresponding speeds are listed in the Table 3:

Table 3: Distances along the line of contact – s (for definition of s see Section 2.5)

Distance along the Line of Contact – s (mm)	Rod on Aligned Disc Slip Speed (mm/s)	Disc Rotational Speed (rev/min)
0.1	60	45
0.2	121	91
0.3	182	138
0.4	243	184
0.6	364	275
0.9	547	414
1.1	668	505
1.4	851	643
1.6	972	735

During the initial exploratory runs of the experiment it was determined that the temperature rise in the disc was steep at the start of a run, but that the rate of temperature rise decreased as time progressed, as one would expect. However, there was also present an overall bulk increase of temperature of the experimental hardware (aluminium housing, plate, motor and gearbox). This gives rise to an additional increase in temperature of the disc surface measured.

Figure 22 shows temperature data from a trial run of the experiment at full speed and load for 1 hour. Note the increasingly wide band of temperature measurement as the experiment progresses, which can be attributed to the load fluctuation as described in the previous section. Less immediately obvious are two reasonably distinct knee points of the data. The first occurs around 12 minutes and the second at 46 minutes. The first section of the plot presents itself as temperature growth, being very steep at the outset. The second portion shows a linear increase in temperature from 95°C to 120°C. The remainder of the graph also appears to be linear but with a shallower slope. It is postulated that the first section of the graph represents a fairly isolated temperature increase experienced by the surface of the disc. After this, the structure of the experimental hardware is being heated and is in turn returning heat to the surface measurement area. There is therefore a point beyond which there is little value in continuing to take measurements as the pure heating effect of the rod rubbing on the disc is no longer observed. For this reason, a limit to the experimental time was set at 30 minutes.
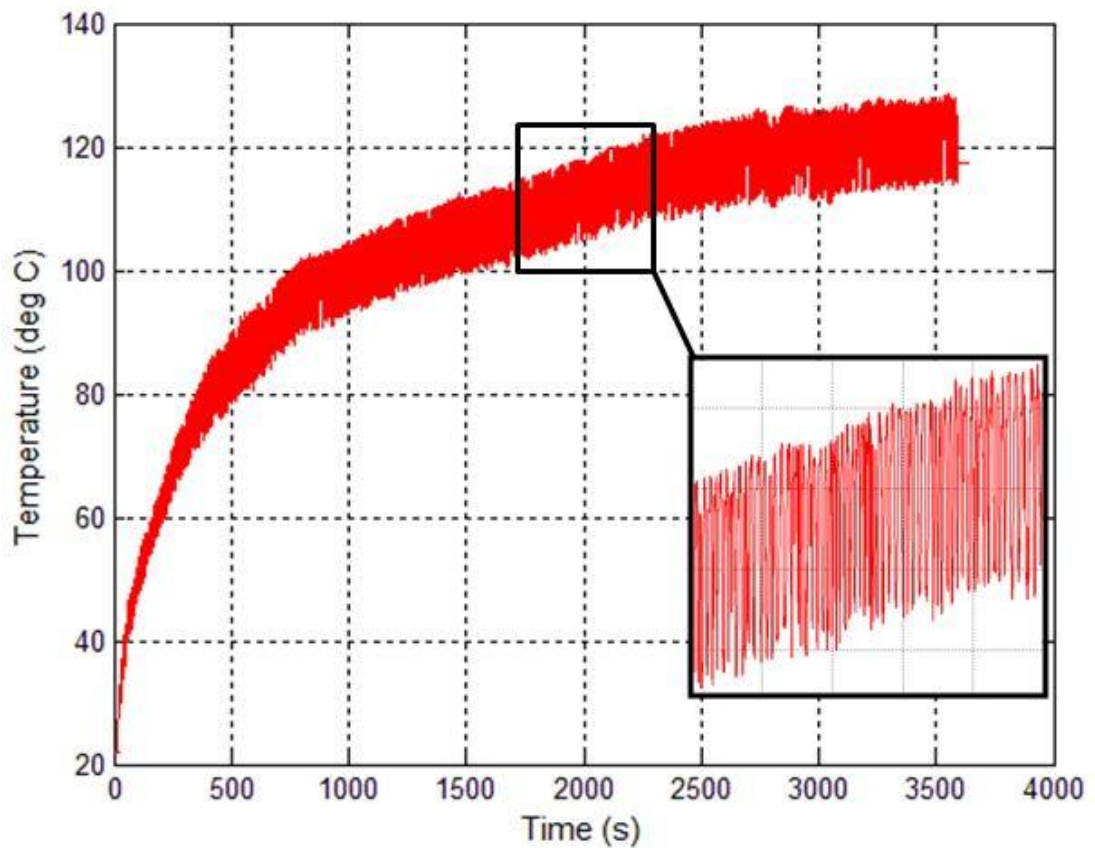
Figure 22: Trial run to determine the optimum run time

Figure 22 also shows a detailed view of a section of the data between 30 and 40 mins. The temperature fluctuation can be seen in this detailed view that has been created by the fluctuating load of the rod against the aligned disc. The band of temperature fluctuation can be seen to increase rapidly at the beginning of the experiment with the rate of change becoming reduced at the end of the data capture. This suggests that as the disc is being predominantly heated by the flash temperature source from the contact, then the temperature fluctuation is proportionate to that heat input. As heat soaks into the disc, the thermal capacity of the material accentuates the difference between the high and low temperatures. Then, as the disc reaches equilibrium with respect to the flash temperature, the differential between high and low temperatures also reaches a peak. From then on, the overall trend of temperature is to rise as the entire hardware increases in temperature.

The main experiment was then performed and a set of data produced for each of the distances along the line of contact S as previously listed in Table 3. Figure 25 shows the data for distances 0.1 mm through 1.1 mm. Ambient temperature is also measured but not plotted as it is dominated by the surface temperature series. The surface temperature of the disc increases as the slip speed increases until it is seen that the data sets for 0.9 mm and 1.1 mm overlap. Also, the 1.1 mm set exhibits a much wider band of temperature as time increases. This suggests that at the higher speeds, with a far higher flash temperature, the disc is becoming thermally saturated so that the surface temperature is no longer increased significantly by the contact flash temperature source.

When $S = 1.4$ mm and the disc is spinning relatively fast at 643 rev/min, the polymer disc became too hot and ultimately melted. However, the experiment was left to run despite this fact and, interestingly, after initial melting had occurred the system settled down again and returned to a steadily increasing temperature as with the other samples. The disc was inspected after the experiment had been completed and its surface was extremely rough, with relatively large asperities consistent with an event where the surface had become completely fluid as it melted. The reason that the experiment settled down again after the melting was a combination of the contact between the smooth rod and the melted and re-solidified disc being poor and that the disc would now be a slightly smaller diameter. This would reduce the rod force onto it. Figure 23 shows the temperature plot as this occurs and Figure 24 shows the melted disc after the experiment had been completed.
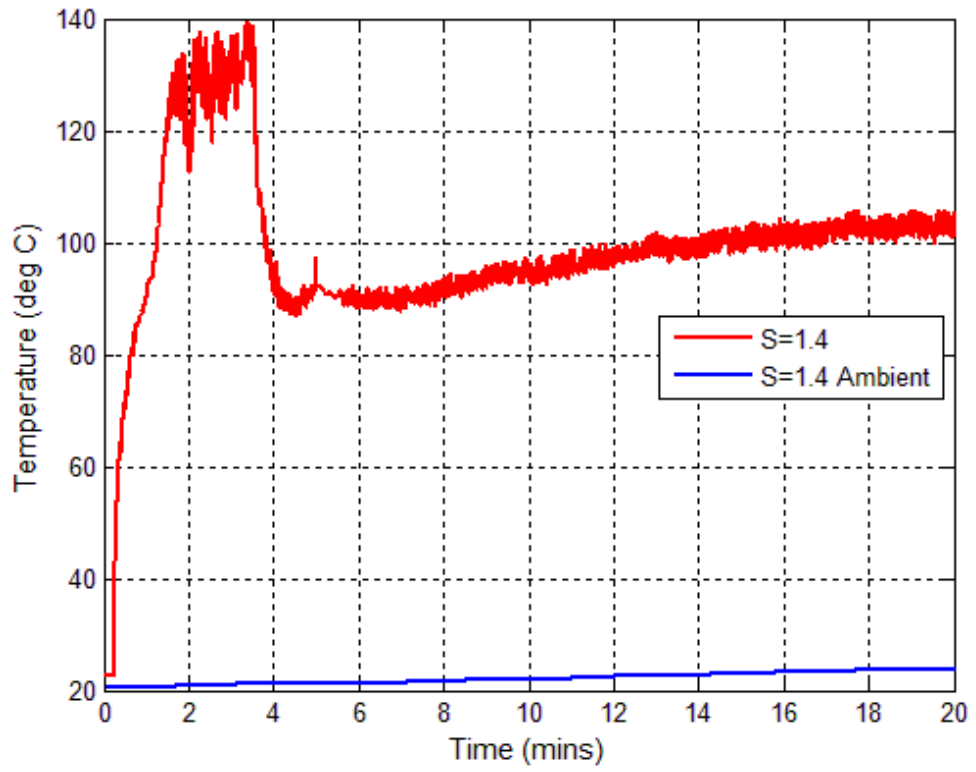
Figure 23: Temperature as the disc melts
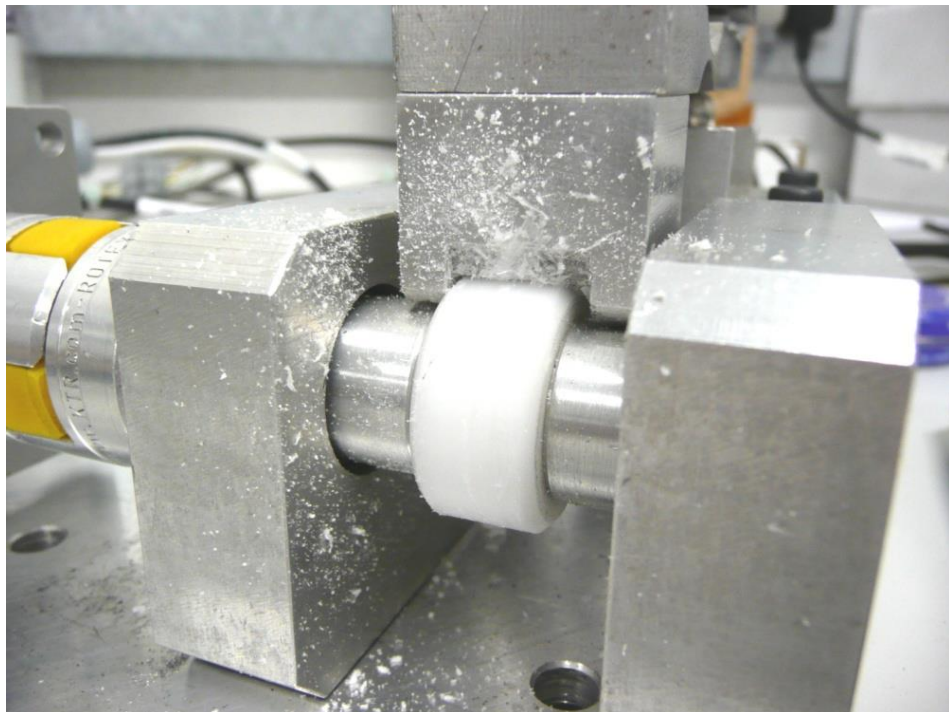
Figure 24: Melted disc post run
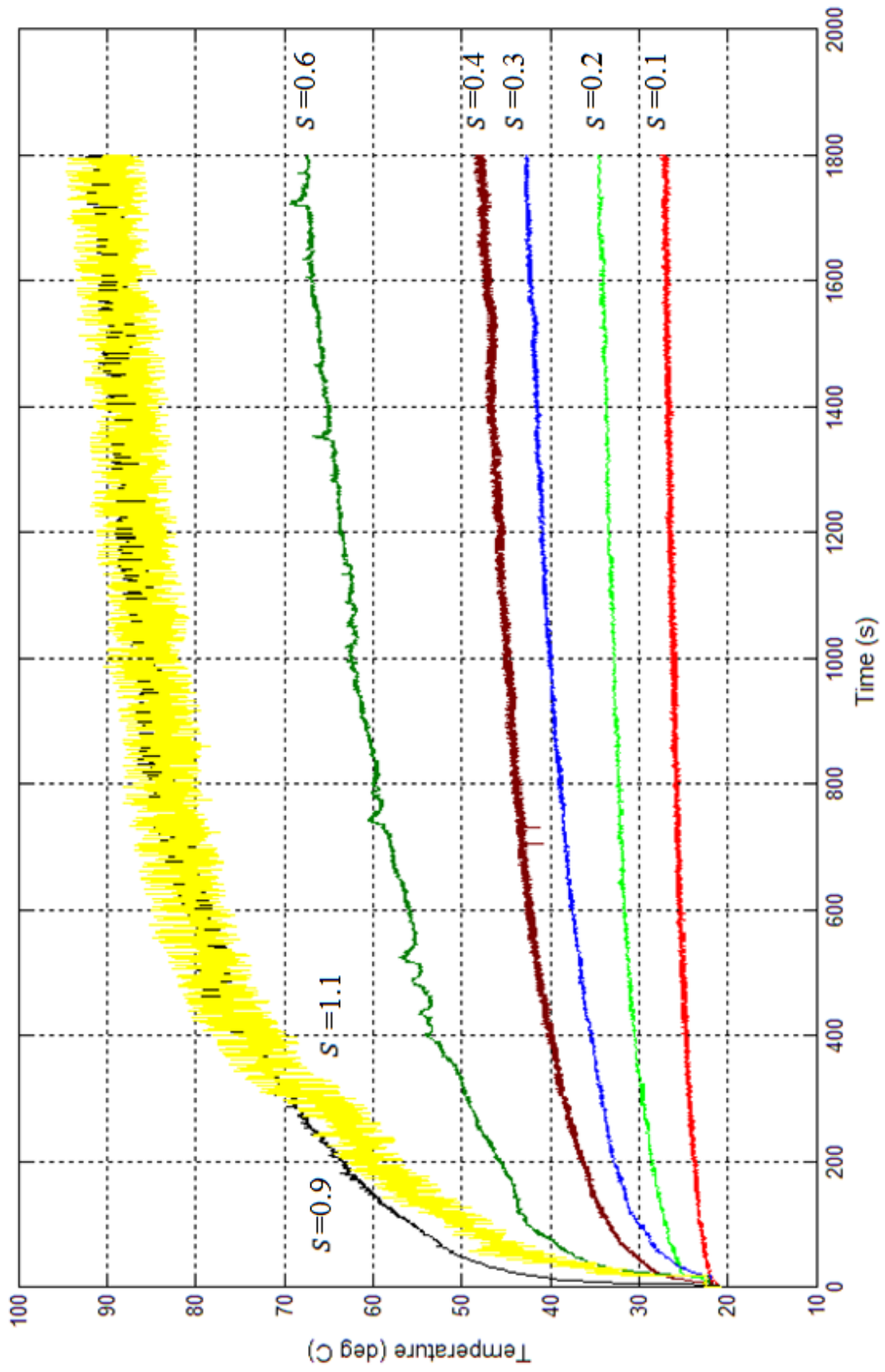
Figure 25: Rod on aligned disc running temperature results.

The blue trace shows a separate output from the thermometer of the body temperature of the device itself. It is labelled as ambient temperature and gives an indication of room temperature. However, in this case heat radiating from the hardware as the experiment progresses results in a slight rise in ambient temperature reported.

3.1.6   Discussion

When the disc melted there was an ejection of material from the disc face as it started to disintergrate. It then cooled and ceased to melt before a more gradual increase in temperature was seen similar to the data from the samples that did not melt. As the disc melted it lost material and so reduced in size. As the rod was held against the polymer disc through the load transducer, and that the load transducer is held against the disc with a screw, it is logical that the rod/disc load reduced as the disc melted. In this way, the melting occurs, the pressure reduces, the temperature drops and the disc solidifies, thus returning to a steady-state of operation.

In Figure 25 it is seen that the slightly faster slip speed generated at $S = 1.1$ mm overlaps the $S = 0.9$ mm set and that the fast slip speed set has a wider and increasing variation of temperature through the data set. The measured temperature is around 90°C for both of these data and that the deflection temperature (a standardised test to measure deformation of the material at a specified load and temperature) of the material at 1.8 MPa is 125 °C (DuPont (2011)). If the slip speed is higher it is resonable to assume that the temperature should also be higher, but this was not the case. However, if the material was just on the point of softening, the rod would be deflecting the polymer slightly more than in the previous slower run thus providing a correspondingly lower load to the polymer disc. If the load is smaller, then the temperature is also lower. The deflection temperature is approached at the $s = 1.1$ mm slip speed and as the disc rotates, the pin is constantly passing from material that is softer to material at a slightly lower temperature that is not undergoing a softening process. This situation, in conjunction with the load fluctuation shown in Figure 21, gives rise to the enlarged fluctuation band shown. It would seem therefore that the these data sets have captured the point at which the material softens dynamically.

3.2   Studied Gear Pair

Rotork gears (part numbers 49240 and 49242) were used for this experiment as a simulation of the real product application without the associated system interferences.

Polymer gear
Rotork part number 49240

Steel pinion
Rotork part number 49242

Figure 26: Rotork CVA pinion and gear, the studied gear pair.

3.2.1   Experiment Design

The product application for this pair of gears is as part of a gearbox that accurately positions an output shaft driven by a small DC brushless motor. A durability test that is performed on this product consists of a reciprocating motion through approximately 1 rotation of the large polymer gear. This reciprocation is done under a loaded condition where the load is constant and in one direction only. The test is approximately 6 million cycles. A cycle is both a forward and reverse action such that each tooth is loaded 12

million times. The aim of the experiment was to simulate the loading of the polymer gear, but without the rest of the product assembly and associated system interaction. Thus, if the same wear conditions are encountered it would be reasonable to assume that the wear pattern or mechanism is evident because of the gear geometry and materials used rather than some other system effect.
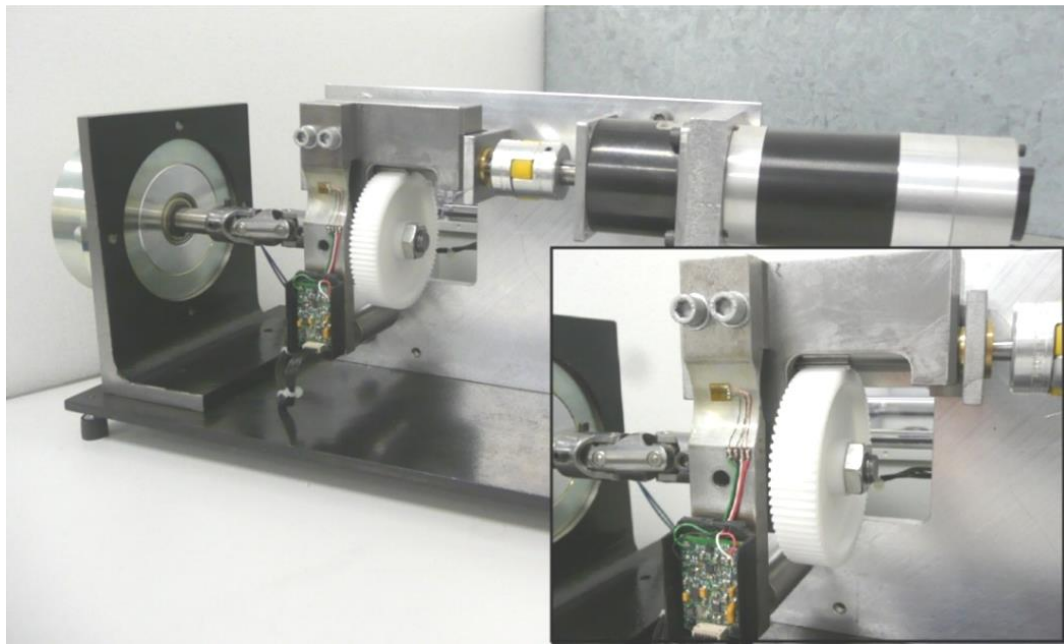
Figure 27: Gear running experiment hardware. Inset shows an enlarged view of the load transducer and support of the polymer gear.

The experiment made use of the same motor, load transducer assembly and control electronics as in the previous rod on axially aligned disc setup. This arrangement, however, drives the pair of product gears together under a constant load and speed. Figures 27 and 28 show the experiment hardware. The motor drives an inline epicyclic gearbox as before, which then directly drives the steel pinion. The pinion is supported in 2 sets of concentric bearings; the first of which allows the pinion to rotate and the second allows the frame in which the pinion is mounted to also rotate. This frame also holds the polymer gear. The output shaft from the polymer gear is connected to a magnetic particle brake (Part N° 52-OPB-80 manufactured by SG transmission). When a voltage is applied to the brake it provides a resistive load to the rotation of the output from the gear, which in turn attempts to rotate the frame. The frame is reacted against the support structure through the load transducer and so the torque generated by the output shaft from the gear

is measured directly. As in the previous experimental arrangement, the speed of the motor is measured directly at the rear of the rotor shaft.

Figure 28 shows the schematic design of the experiment hardware. The lower left view of the schematic shows the pinion bearing arrangement that allows the gear frame to pivot around the pinion axis to allow reaction of torque applied.
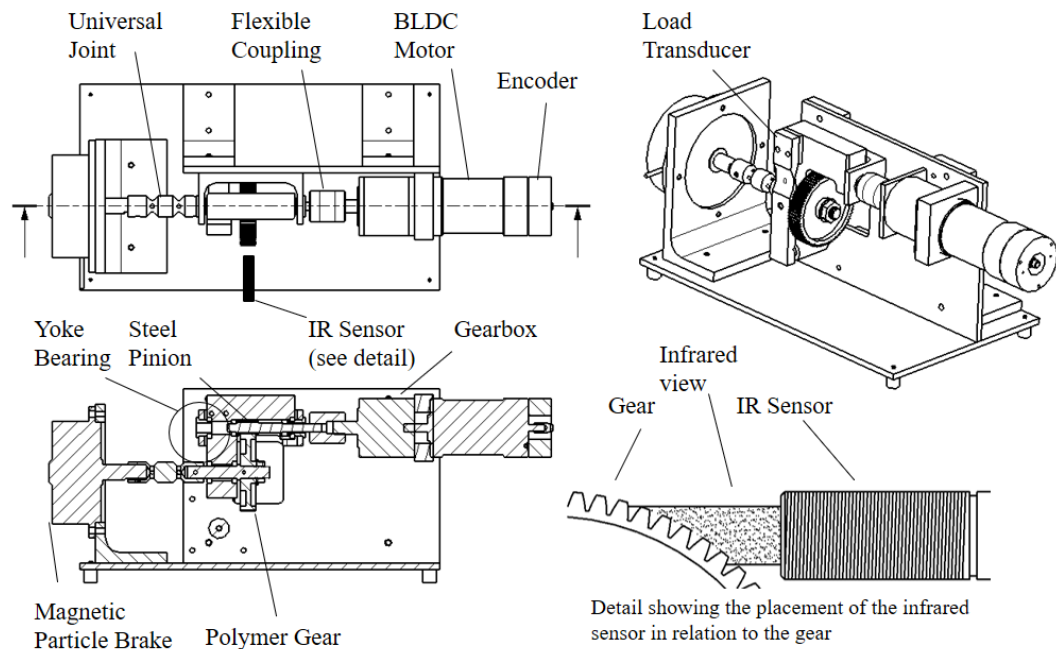
Figure 28: Gear running experiment design and positioning of the IR sensor

3.2.2 Calibration and Setup

To calibrate the experiment, the brake was removed and replaced with an arrangement that fixed an arm perpendicularly to the output of the universal joint, supported by a pair of bearings. A set of dead weights were then hung from an arm of know length to provide a definable torque on the polymer gear. In the same way as in the rod on axially aligned disc arrangement, 3 sets of measurements were taken and averaged. This average data set was used when setting the gear load during running of the experiment. The variation between data sets was +0.28% and -0.47% in relation to the average of the three data sets (Figure 29).
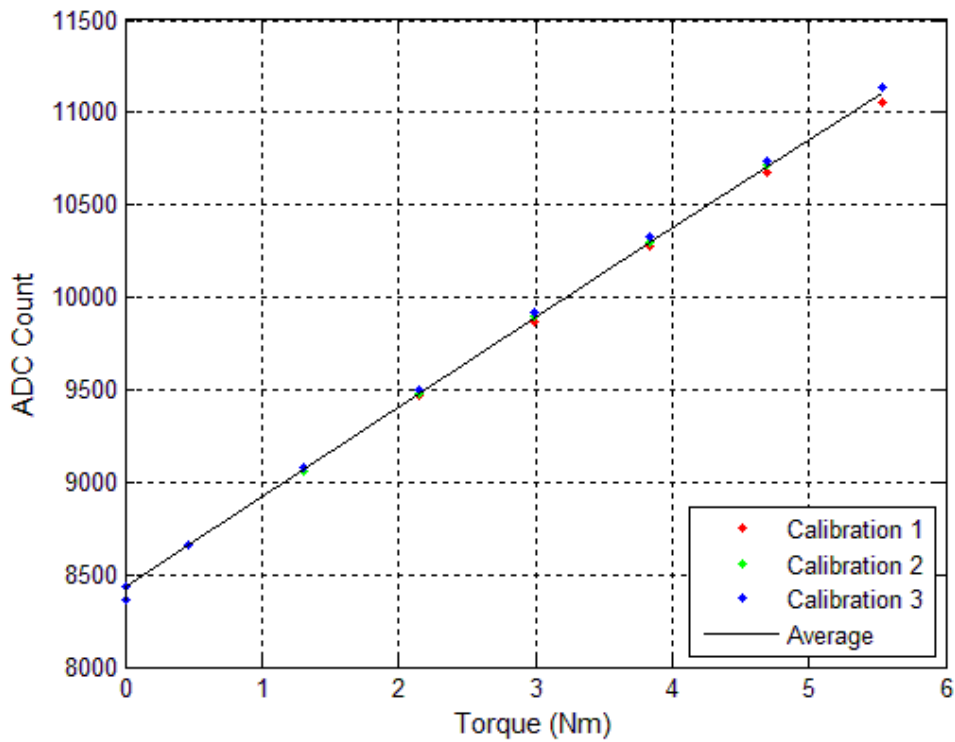
Figure 29: Gear running experiment calibration results showing three separate calibration runs with the average.

3.2.3 Results

Four temperature data sets were taken using the gear running experiment hardware. The system torque and speed were set using a trial gear and the gear was then replaced with the experiment sample and the experiment was started. Each run lasted for 1 hour to ensure that the temperature rise due to teeth contact had been captured. The temperatures continued to rise after this 1-hour period, which is discussed in the next section. Table 4 shows the running times for each data set and the time at which the data was taken; this is important to understand the results.

Table 4: Gear running times

Run	Date and Time	Time Between Runs	Data Label
1	07/09/2012 11:19	N/A	G1
2	07/09/2012 13:45	2 hrs 26 mins	G2
3	07/09/2012 14:50	1 hr 5 mins	G3
4	14/09/2012 09:09	1 week (approx)	G4
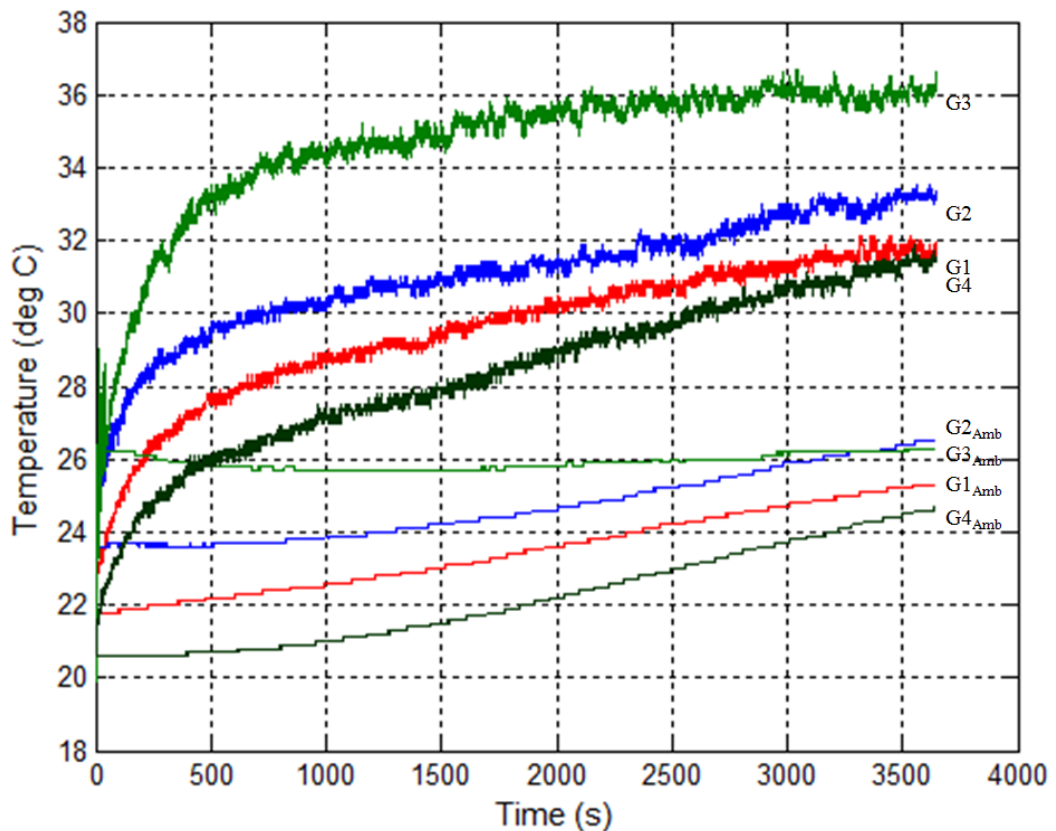
Figure 30: Gear running temperatures (4 upper series) and the IR thermometer body temperature (4 lower series).

As in the previous experiment, the same temperature sensor was used - an Optris CS infrared thermometer. This was positioned facing the teeth flanks directly as they exited from the gear mesh as the polymer gear rotates. Again, the data were logged automatically to a spreadsheet. Figure 30 shows the data as recorded during the experiment runs. G1, G2, G3 and G4 in the table relate to the data series shown in Figure 30. The subscript 'Amb' is data taken from the body of the thermometer, which is measuring the ambient temperature of the surrounding air. As discussed around Figure 25, the reported increase in ambient temperature is a result of heat radiated from the hardware as the experiment progresses. It is seen that the second data set (G2) is slightly higher by approximately 2°C than the first (G1) and the time delay between runs was around 2.5 hours. The offset in temperature between the second and third (G3) sets of data is larger at approximately 4°C and correspondingly, the time delay was shorter at just over 1 hour. The final set of data (G4) was taken after a delay of a week so that all latent heat in the system had dissipated. This data set returns a temperature just below the original set.

The infrared thermometer logs the temperature of the surface it is directed at, however, it also measures the internal temperature of the thermometer and as it is not physically connected to the rest of the system this is a good indication of the ambient temperature. These ambient data sets are also recorded and are plotted with the bulk data. Figure 31 shows the 4 data sets, but this time the ambient temperature data sets have been subtracted from the gear surface temperatures. It is seen that runs G1, G2 and G4 are coincident with a slight perturbation of G2 at around 10 minutes. However, G3, which was run with only a 1-hour gap, is shown to be approximately 4°C higher in temperature than the other runs.
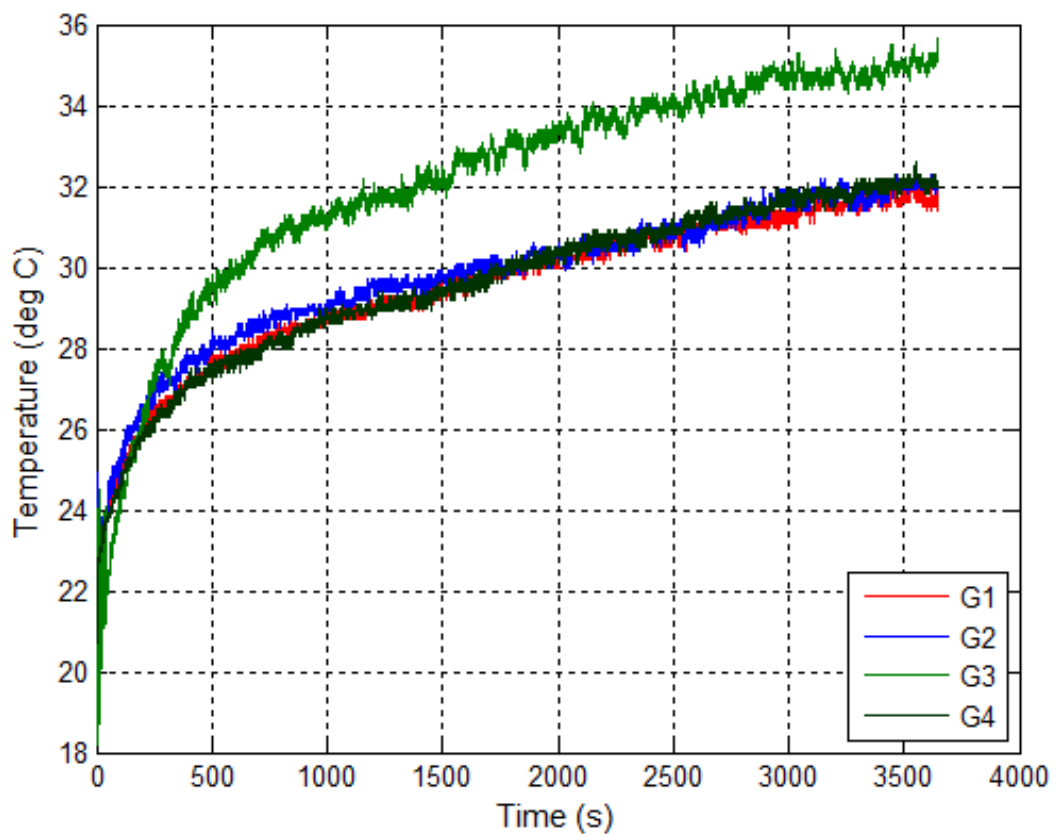
Figure 31: Gear running temperatures - adjusted for ambient

The key shown in Figure 31 is identical to that defined for Figure 30.

3.2.4 Discussion

The temperature rise measured by the infrared sensor probe was initially quite steep for the first few minutes; it then started to flatten between 10 and 20 minutes. After 20 minutes the temperature then increased fairly gradually and at a nearly linear rate. The initial high rate of temperature change can be attributed to the contact between the teeth as there is no other thermal source. The nearly linear portion is observed when thermal balance starts to occur in the gear, shaft and metal structure around it. As the heat is generated at the surface contact between the teeth it flows in towards the cooler parts of the bulk of the material. As more heat is generated at the contact a balance starts to occur between the hot tooth surface and the cool interior of the gear and it is this partial difference that is seen as a less pronounced temperature increase. After 20 minutes the experimental hardware is now becoming hot. The motor, gearbox and brake are all now hotter and, as the structure is metallic, the heat is conducted around the structure which results in both conductive and radiative heating of the gear that is not from the contact induced heating. As the focus of this experiment is to consider the thermal effect from the tooth contact it is not useful to make observations or analysis based on temperatures measured much further than the 10-20 minute point.

3.3 Discussion and Analysis of Experimental Thermal Measurements

As described in the previous sections in this chapter, two separate experiments have been devised, built and carried out to measure the temperature rise in a polymer-steel spur gear pair. The first experiment used a simplified setup whereby a rod was pressed against a rotating disc to simulate a series of points along the line of contact as the teeth sweep against each other. This simplified arrangement was developed in order to validate a model of the same arrangement. The running temperature of the real geometry (product gears) was then measured with a view to correlating the simplified experiment against the real gear running results. This correlation will be useful in the following chapter during discussion of the modelling of temperature rise in the gears.

In order to make this correlation exercise it is necessary to draw a comparison of the rod on axially aligned disc running experiment data to the data of the real gear running temperatures. The temperature data set for the rod on axially aligned disc experiment consisted of a number of separate data series and so to compare these to the real gear temperatures they must be amalgamated in some way to form a single data set. This is done by adjusting each rod on axially aligned disc data set in proportion to the amount of time it would spend at each point of the tooth sweep according to the slip speed at that point. The temperature generated at a point in the tooth contact sweep is a function of both time and distance along the line of contact

$$T_S = T(t, S) \tag{11}$$

where T_S is the temperature at the point along the line of contact S at time t. Figure 32 illustrates how this is done; the entire data series is split into discrete time steps of δt and the median instantaneous slip speed is read from the data at that point.
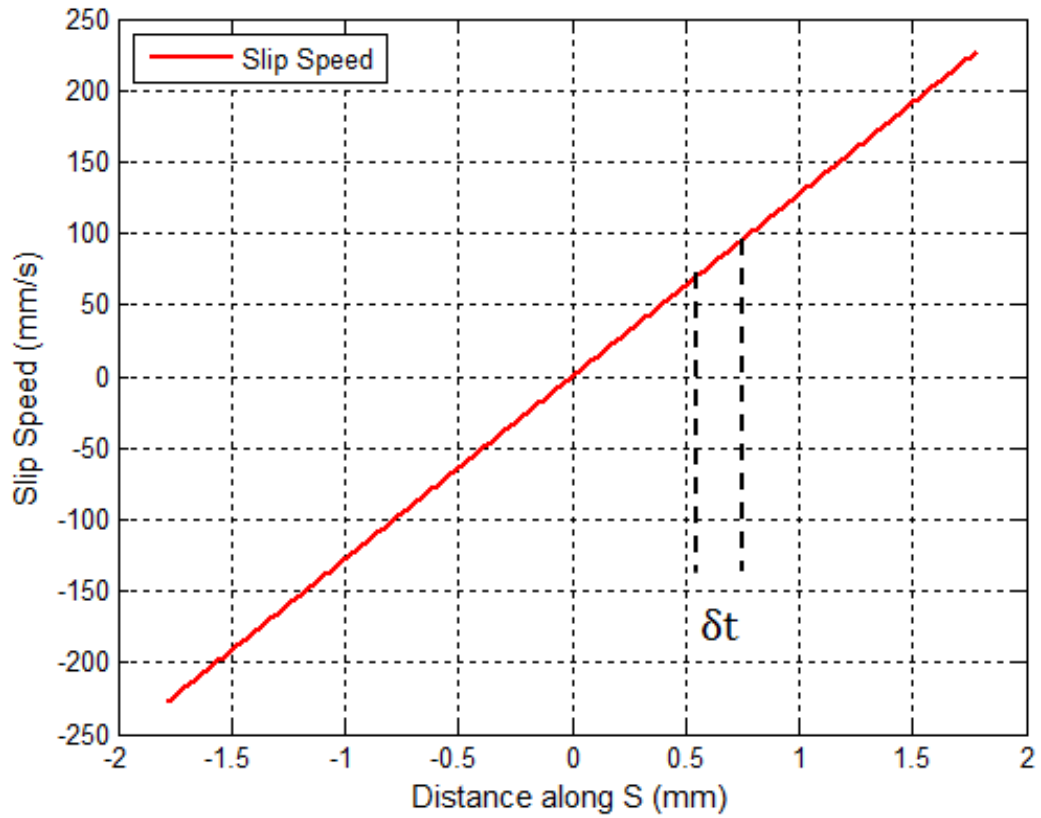
Figure 32: Time averaging discrete sample for use in time averaging of the temperature data

As the slip speed varies through the contact sweep, the time spent in contact at each discrete measurement will vary also and is given by

$$\delta t = \frac{1}{v} \delta S \qquad (12)$$

where δt is the time spent at each contact discretised position, v is the slip speed in mm/s and S is the distance along the line of contact in mm. Each rod on axially aligned disc temperature data set is then adjusted to the amount of time δt at that distance along the line of contact S

$$T_{ave}(t) = \frac{1}{S_0} \sum_{i=1}^{N} T(t, S_i) \delta S \qquad (13)$$

where T_{ave} is the sum average of all rod on axially aligned disc data sets, S_0 is the limit of travel along the line of contact S and t is the time that would be spent at this location during the sweep of the teeth in the real gears. The average temperature is the summation of the data sets.

As the gear and pinion run together there is a certain amount of sharing between teeth, which is entirely down to the particular geometry of the gear pair and is termed the contact ratio. The contact ratio is a factor equivalent to the amount that the teeth share contact through the sweep. As the teeth share contact, the heat generation will also be shared in the proportion determined by the contact ratio R_C, which is given by

$$R_C = \frac{\sqrt{\left(R_{go}{}^2 - R_{gb}{}^2\right) + \left(R_{po}{}^2 - R_{pb}{}^2\right)} - \sin \propto}{p \cos \propto}$$

(14)

where R_{go} is the outer diameter/2 of the gear, R_{gb} is the base diameter/2 of the gear, R_{po} is the outer diameter/2 of the pinion, R_{pb} is the base diameter/2 of the pinion, $\propto$ is the pressure angle of the tooth form and p is the circular pitch of the teeth. Incorporating the factor of contact ratio into the summation of the data sets gives

$$T_{ave}(t) = \frac{R_C}{S_0} \sum_{i=1}^{N} T(t, S_i) \delta S_i$$

(15)

When evaluated it is found that the data set of $S = 0.1$ mm accounts for almost all the temperature rise in this time averaged data set. In fact, the other data sets together give less than a 1 °C temperature to the face of the gear meaning that as long as a data set is taken near to $S = 0$ mm, then a temperature rise will be recorded near to that of the real gear. Figure 33 shows a sketch of the IR sensor in relation to the gear teeth as the gear temperatures are recorded.
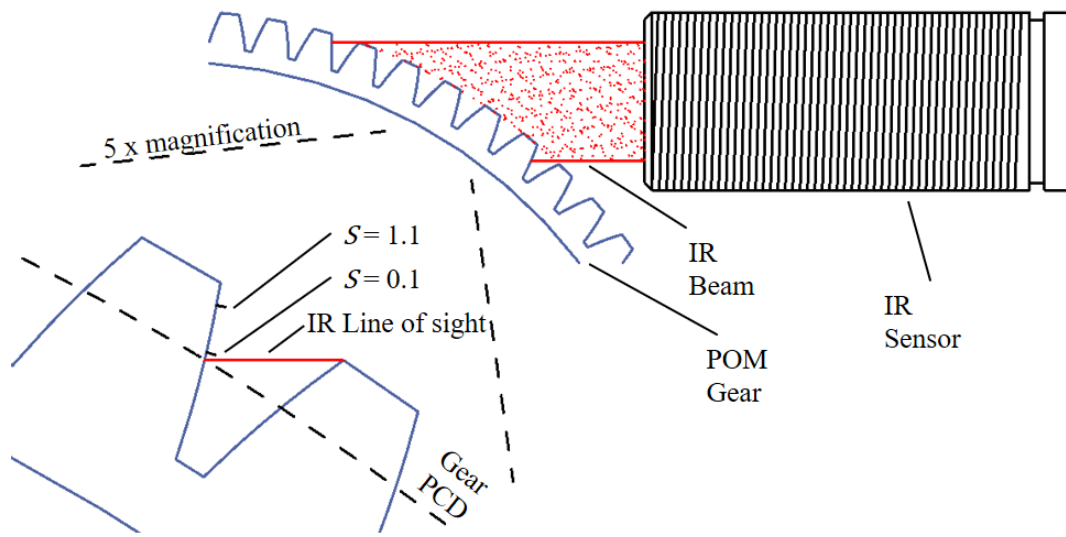
Figure 33: IR Sensor line of sight

The line of sight can be seen to be partially obscured by teeth depending on their position in relation to the sensor. The sensor, however, measures a maximum temperature recorded within the beam diameter and so long as it is pointing at one of the flank centres then the true maximum temperature will be captured.

Figure 34 shows the comparison of the summation of rod on axially aligned disc data and the gear temperature measurements. The data presented are over a 30-minute time period, which is sufficient to capture the surface temperature adequately as previously discussed. Note that the trend of each data set is similar, but that there is a small difference between the two of approximately 2.5°C.

In equation (15), the contact ratio is driven by the depth of the teeth and in the case of this real product gear and pinion combination a correction has been applied of 0.5 mm. This is a correction to the addendum and/or dedendum of the gear teeth (see Section 2.2 for definition of these features). This correction increases or decreases the tooth height and these gears a positive correction is applied to the gear and a negative correction is applied to the pinion effectively moving the contact towards the gear centre.
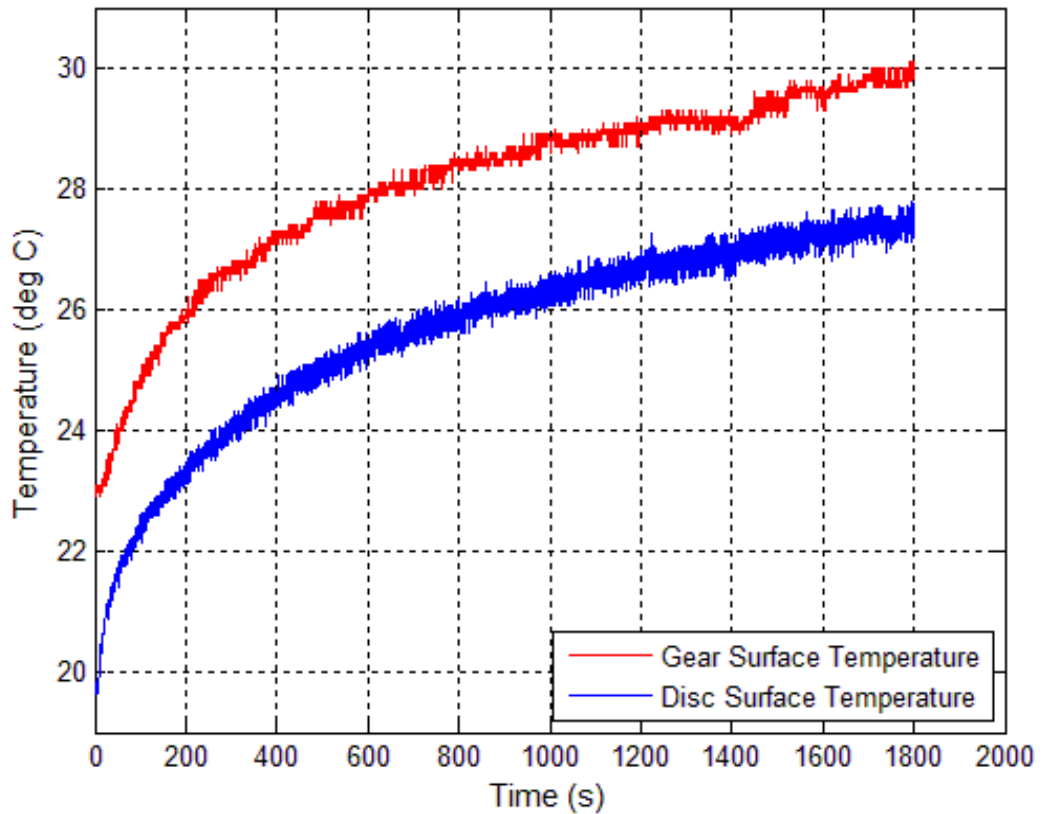
Figure 34: Comparison of temperature data

This is done to avoid undercutting and therefore weakening the tooth of the pinion. Manufacturing tolerances mean that an absolute value for any machined features may never be achieved and it is seen that the contact ratio and so the amount the teeth share during contact is particularly sensitive to the addendum and dedendum correction on the teeth. The time averaging analysis of the data was performed again, this time including a 70 μm adjustment to the correction factor. This is done by altering the values R_{go}, R_{gb}, R_{po} and R_{pb} in the contact ratio expression given in equation (14). The data comparison for this corrected analysis can be seen in Figure 35. The manufacturing drawings (see Appendix 8.5) specify a gear backlash of 0.05 mm to 0.1 mm (see Section 2.2). The radial clearance this yields for a 20 ° pressure angle is 0.135 mm. Given that the manufacturer will naturally target the nominal value and given the tolerance band applied, 70 µm is an appropriate value of variance.
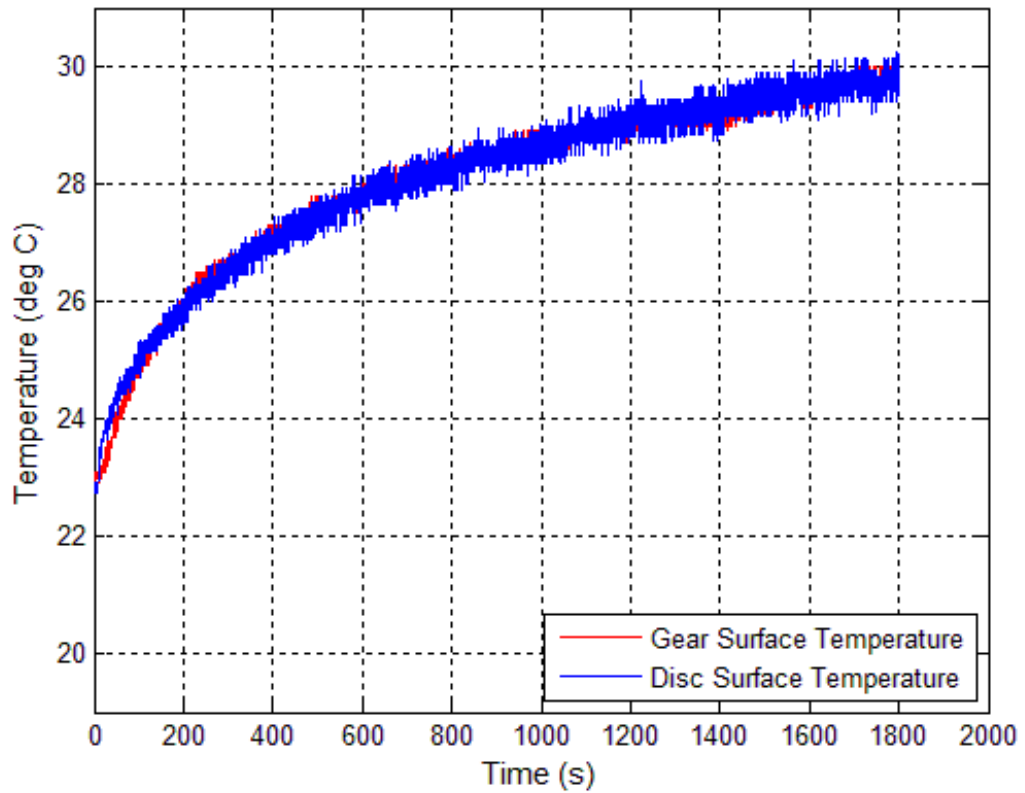
Figure 35: Comparison of temperature data with 70 μm correction

These two data sets correlate well and a manufacturing tolerance of this magnitude would not be unreasonable. It can be concluded therefore that it is possible to use the rod on axially aligned disc experiment to evaluate the likely temperature rise in a real gear pair to within a tolerance determined by the accuracy of the manufacturing process.

3.4   Consolidation of Chapter 3

In this chapter, an experiment has been devised to measure the temperature rise in a polymer disc equivalent to points along the line of contact of a polymer gear tooth. The experiment was then augmented to enable the real geometry gear pair to be run together under load and the temperature of the polymer gear to be measured dynamically.

A method has been presented to correlate the discrete measurements of the rod on axially aligned disc experiment to the real geometry gear running temperatures. This was achieved through time averaging of the rod on axially aligned disc results to adjust each data set with respect to the amount of time it spends at each discrete point in the contact sweep. The analysis of the data in this way gave a correlation between the rod on axially aligned disc experiment and the real geometry gear running experiment with a difference of 9% or 2.5°C. The temperature measured on the surface of the rod on axially aligned disc was lower than that measured on the real gear. It is proposed that the reason for this difference is due to the geometric differences between the two arrangements caused by manufacturing tolerances. An error in the correction to the teeth of 70 μm was introduced to the time averaging model which entirely aligns the two data sets.

The reason for simplifying the real gear geometry to a rod on axially aligned disc arrangement is that it is a far simpler task to calculate the temperature rise in a polymer disc through contact than it is to do the same for real gear geometry. Therefore, by validating the relationship between the two by experiment paves the way for modelling the gear temperature in a simplified way that could be used practically in an industrial design setting.

CHAPTER 4

Modelling Gear Running Temperatures

Chapter 3 details experimental work undertaken to measure the temperature rise experienced by a pair of gears where the pinion is steel and the gear is manufactured from a polymer (POM). In this chapter, models are presented that have been developed to evaluate the heat generation at the point of contact between the gear teeth and to estimate the temperature rise that results from that heat generation. The chapter begins with some calculations of basic geometry of the involute form in relation to the loads and resulting deflections. It also provides details of a methodology developed for calculating the efficiency of a pair of gears based on both their geometry and the coefficient of friction between them. An analytical model is then presented for the evaluation of temperature rise between two discs sliding together (rod on axially aligned disc). A FE model is also presented as a comparison to this analytical method and also as a method that would more probably be used in an industrial application. Finally, the chapter compares the results of the various models with the experimental data acquired in chapter 3.

For analytical reasons, only the rod on axially aligned disc arrangement has been modelled as the geometry of the real gears is complex. This simplification makes it possible to propose an overall methodology for assessing the likely running temperature of a polymer-steel gear pair. This proposal is firstly to analyse the heat rise in a polymer disc due to a contacting rod and then to compare that idealised rod on axially aligned disc case to the real gear case as discussed in chapter 3.

4.1 Forces and Deflections

Power in the form of heat dissipated into the polymer surface is a function of force and sliding velocity. Force in this case is equal to the contact force normal to the face of the contacting gear teeth multiplied by the coefficient of friction for the material combination. The normal force is given by

$$F_{cn} = \frac{\tau}{r_a} \cos \alpha \qquad (16)$$

where F_{cn} is the contact force normal to the face of the tooth, τ is the input torque, r_a is the reference radius of the pinion and α is the pressure angle of the gear teeth. When evaluated for the gears under consideration, when $\tau = 0.85$ Nm and $r_a = 6.00$ mm, the contact force between the teeth is 133.10 N. Figure 36 shows the parameters required to calculate the normal load on the tooth flank that is developed from the input torque.
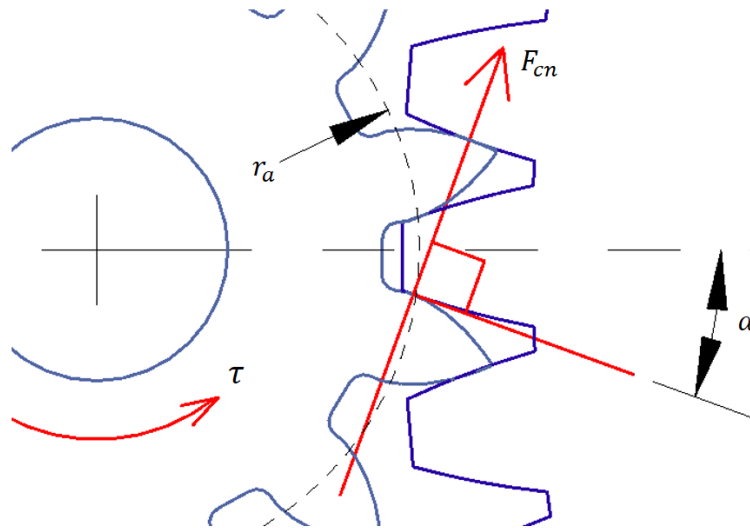
Figure 36: Normal load on the tooth flank due to tooth pressure angle.

The materials investigated are steel (European Standard 1.5011 grade) and POM. The dynamic coefficient of friction between these materials is taken as 0.35, DuPont (2011). Therefore, the power lost to heat is a function of the sliding velocity and the normal force between the steel and polymer gear teeth.

When considering a spur gear pair, it is often stated that the overall efficiency is in the region of 98%, which may be the case for hardened steel gears under a hydrodynamic lubrication regime. However, as the coefficient of friction is so much higher for the

polymer-steel pair, the efficiency is decreased. It follows that as the equivalent cylinders (Section 2.5) change to represent the contacting radii through the tooth stroke and the normal force remains constant, the penetration of the steel gear into the POM gear changes. Hence the area onto which the heat input is applied also changes. To this end, the deflection must be calculated to determine the heat flux for any given point in the contact between the teeth.
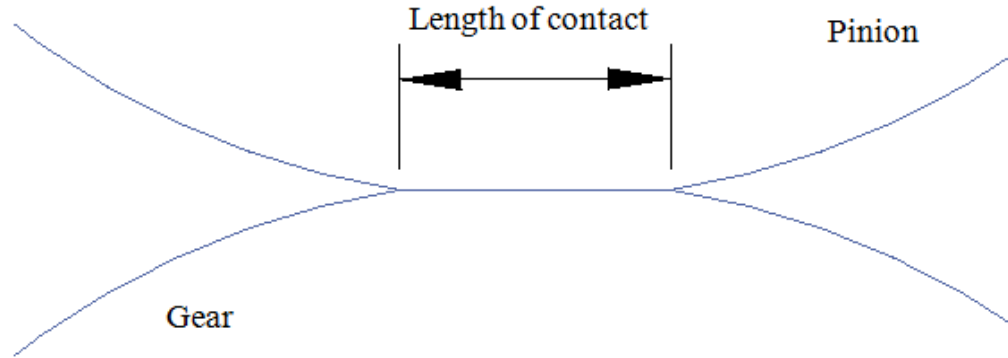
Figure 37: Length of contact due to deformation of the polymer tooth surface.

The length of contact area (as shown in Figure 37) and maximum stress for a cylinder pressing against a cylinder is given by the Hertzian contact stress formulae in Table 14.1 of Roark's Formulas for Stress and Strain (Young and Budynas, 2011). Firstly, a factor C_E is calculated to account for the two differing material properties of the rod on axially aligned disc:

$$C_E = \frac{1 - v_a^2}{E_a} + \frac{1 - v_b^2}{E_b} \tag{17}$$

where E_a is the Young's modulus for POM, E_b is the Young's modulus for steel, v_a is Poisson's ratio for POM and v_b is Poisson's ratio for steel and yields $C_E = 2.876 \times 10^{-10}$. See material data table in Section 2.4 for specific values.

The maximum Hertzian stress is

$$\sigma_{max} = 0.798 \sqrt{\frac{F_{cn}(r_a + r_b)}{2C_E w r_a r_b}} \tag{18}$$

where w is the gear teeth contact width. The length of contact due to penetration is given by

$$b = 1.6 \sqrt{\frac{2F_{cn}C_E r_a r_b}{w(r_a + r_b)}} \qquad (19)$$

Although it is not used in this analysis, for completeness, the penetration depth is given by

$$\delta = \frac{2F_{cn}C_E}{\pi w}\left[\frac{2}{3} + \ln\frac{4r_a}{b} + \ln\frac{4r_b}{b}\right] \qquad (20)$$

Therefore, the maximum stress in the material due to the contact is 72 MPa and the contact length is 0.73 mm. Given that the disc width is 10 mm, Table 5 shows evaluated variation of parameters with variation of distance along the line of contact s as the teeth move through a contact cycle.

Table 5: Contact stress at points along the line of contact S

s (mm)	0.0	0.1	0.2	0.3	0.4	0.6	0.9	1.1	1.4
σ_{max} (MPa)	74.5	73.1	71.7	70.5	69.3	67.2	64.5	62.9	60.9
b (mm)	0.73	0.73	0.73	0.72	0.72	0.71	0.71	0.70	0.69
A (mm²)	7.30	7.30	7.30	7.20	7.20	7.10	7.10	7.00	6.90
r_b (mm)	12.83	12.73	12.63	12.53	12.43	12.23	11.93	11.73	11.43
r_a (mm)	2.05	2.15	2.25	2.35	2.45	2.65	2.95	3.15	3.45
v (mm/s)	0	61	121	182	243	364	547	668	850
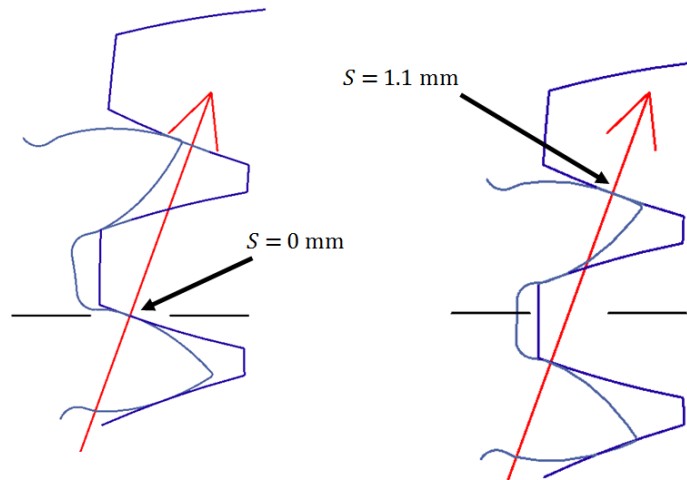
Figure 38: Relative tooth positions along the line of contact s.

Figure 38 shows the teeth as they progress along the line of contact (in red) from 0 mm at the centre line between the gear centres to 1.1 mm away from the centre. The instantaneous power that is dissipated into the polymer at each of the points along the line of contact S can be calculated:

$$P_T = F_{cn}\mu v \tag{21}$$

where F_{cn} is the normal force, μ is the coefficient of friction (0.35) and v is the sliding velocity. For $S = 0.2$ mm, P_T is evaluated as 5.64 W.

It is seen that this value of power is high (approximately 1/3 of the overall power being transmitted by the gears), but this is because of the position in the contact. The time spent at this position is a function of the slip speed and will be short. This will be dealt with in the model presented in the next section.

The heat flux generated can also be calculated simply as the power in relation to the area onto which the heat is applied

$$Q_T = \frac{F_{cn}\mu v}{A} \tag{22}$$

which may be evaluated as 0.772 W/mm² for $S = 0.2$ mm. Values for A are to be found in Table 5. This is purely the heat generated between the two contacting surfaces and takes no account for the relative proportions of that heat transport that are shared between the polymer and the steel.

4.2 Gear Data Evaluation

The equations presented in previous sections have been drawn together to assess the overall efficiency with which the gear pair transmits power. The inefficiency, or rather the power that isn't transmitted, must then be assumed to be dissipated as heat at the contact interface. The evaluation is based purely on the geometry of the gear profile, the number of teeth, the coefficient of friction between the two materials and the torque and running speed transmitted. From DuPont (2011) the dynamic coefficient of friction is 0.35. Slip speed is calculated through the contact sweep as are the equivalent cylinder diameters associated with each position. Power lost is calculated at each point in the contact sweep and is then time averaged through the whole sweep to give an overall power loss. The output from the evaluation are plots and a series of values pertaining to the characteristics of the gear pair.

The evaluation takes the basic geometry of the gears and the slip speed based on equations (8) and (9) from Section 2.7. The stress and deflection experienced through the teeth contact sweep are calculated as shown in Section 2.5. Time averaging as used in Section 3.3 and shown in equations (11) and (15), over the time spent at each step through the contact sweep is used to evaluate the power through the sweep. This evaluation of the studied gear pair is the culmination of the various techniques and equations described thus far. It gives a value for the efficiency for the gear pair as well as other information and parameters that can be used for future research and analysis of any gear pair. Figure 39 shows output data from the evaluation. The primary output from this model is the predicted efficiency of the gear mesh and is 94.8% in this case.
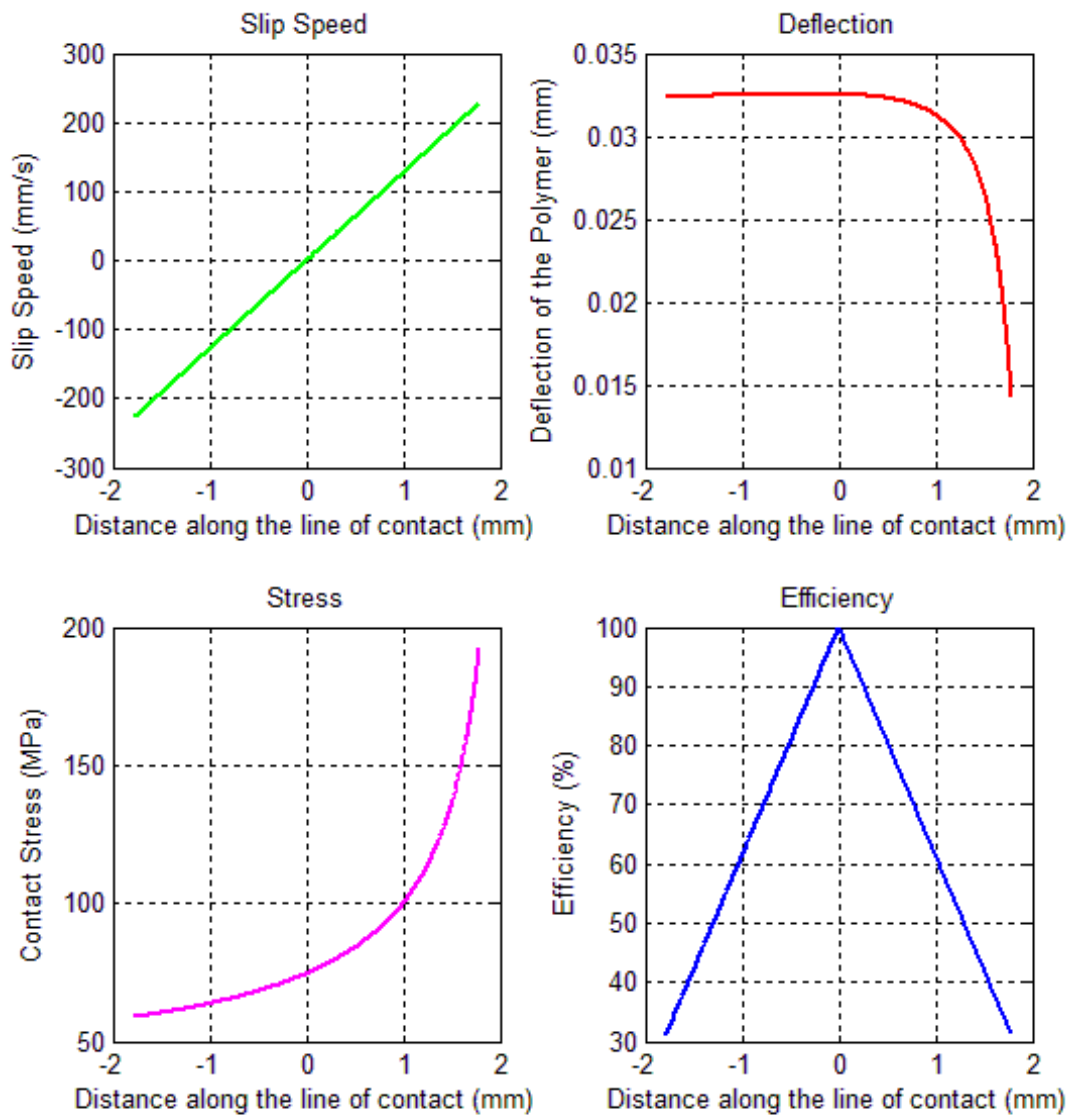
Figure 39: Gear data model output. *s* is the distance along the line of contact.

Table 6: Gear data evaluated

Maximum Deflection (mm)	**0.0325**
Maximum Slip Speed (mm/s)	**227.3**
Contact Ratio	**1.1381**
Tangential Force (N)	**133.1**
Average Efficiency (%)	**94.8**

4.3 Flash Temperature Models

Two proprietary methods have been explored for the calculation of flash temperature for the gear pair. Blok (1963) proposed that if two surfaces are rubbed together there will be heat generated at the interface. Because of the transient and constrained nature of the contact (the two surfaces are in contact so there can be no radiation or convection), there will be an instantaneous temperature rise that will be higher than expected for the load and speed conditions of that gear pair.
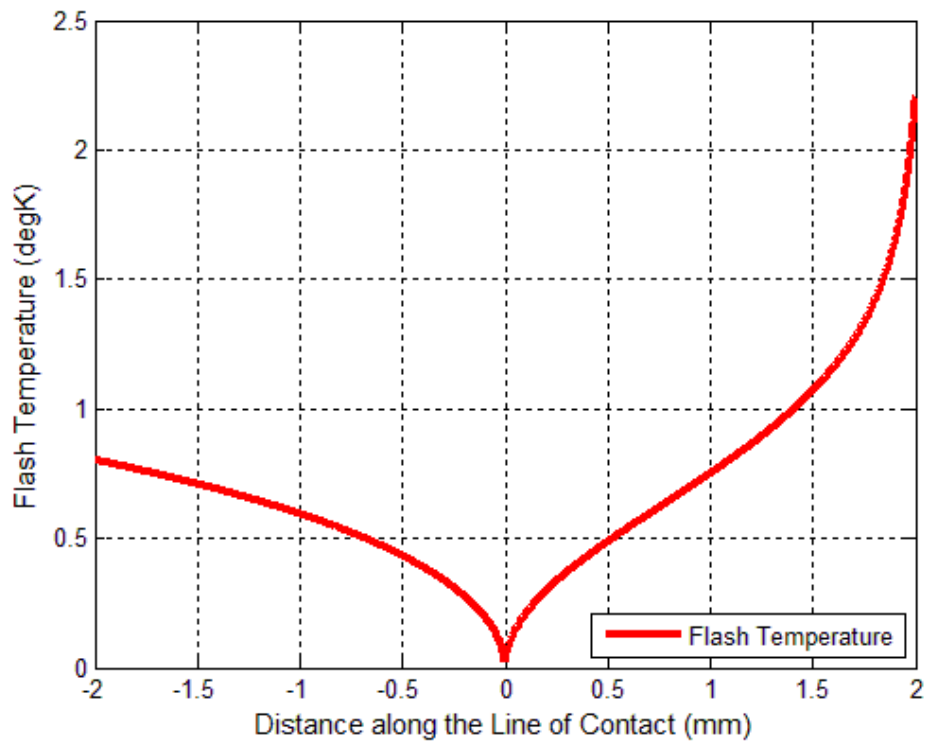
Figure 40: Flash temperature through the teeth contact sweep given by Blok

The flash temperature is given by

$$T_{max} = A \frac{q_{av}}{\sqrt{kc'}} \sqrt{\frac{\omega}{v}}$$

(23)

where v is the sliding velocity, ω is the length of the heat source, k is the thermal conductivity of the material, c' is the specific heat per unit volume, A is a form factor and

q_{av} is the heat flux input. Blok defines the heat flux as coming from the areas in contact, for this specific case of pinion and gear it is given by equation (23).

It is seen that evaluation of the Blok formula provides a curve of temperature that is a function of slip speed and contact area to a maximum of 2°C (Figure 40). This seems low in relation to previously measured gear temperatures, but the flash temperature is a transient condition and takes no account of the gradual accumulation and cyclic nature of the heat effect in the application of a continuously rotating power driven gear pair. It is useful as a concept and Figure 40 provides a good visual representation of the heat profile through the line of contact, but cannot provide the final temperature of the gears.

A British Standard (2006) on the specification of non-metallic gears gives an empirically derived formula for the running temperature expected for a gear set where one is steel and the other is a polymer:

$$T = T_0 + \frac{136 P_T \mu (1 + u)}{(z_2 + 5)} \left[\frac{1.71 \times 10^4 K_a}{f z_2 (vm)^{K_M}} + \frac{7.33 K_b}{A_G} \right] + 5 \tag{24}$$

where P_T is the transmitted power in kW, μ is the coefficient of friction, u is the gear ratio, z is the number of teeth, f is the face width in mm, v is the sliding velocity, m is the gear module in mm, A_G is the surface area of the gearbox and $K_{a,b,M}$ are lookup table constants provided by the standard.

When evaluated, the maximum running temperature is found to be 34.3°C assuming an ambient temperature of 21°C. The temperature rise due to running is 13.3°C. It does not provide much insight into what is occurring at the surface, but this formula is included for completeness and will be compared to other results at the end of the chapter.

4.4 Analytical Dynamic Thermal Model
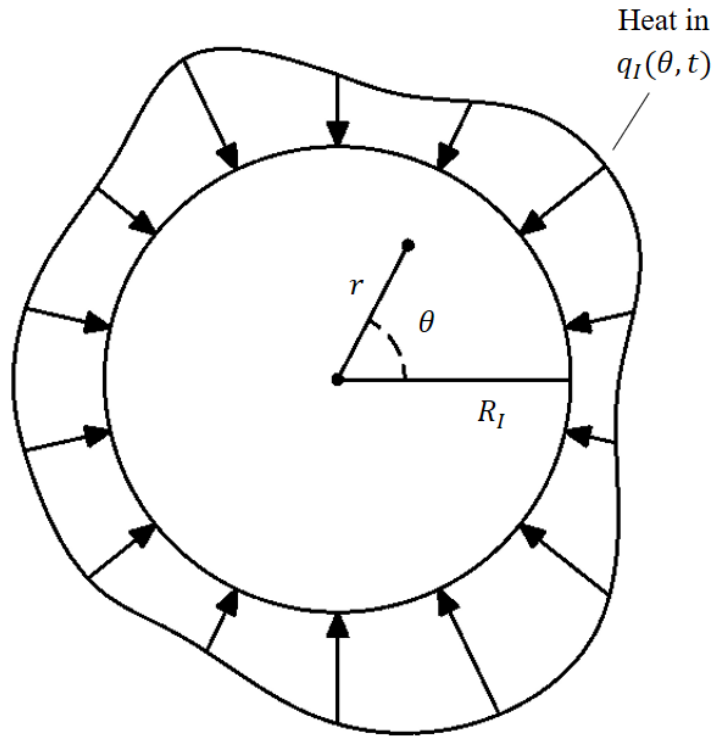
Figure 41: Geometry and coordinates associated with the polymer disc analytical dynamic thermal model.

Flash temperature predictions such as in Figure 40 indicate behaviour in the immediate vicinity of contact between the two surfaces. However, cyclical thermal response due to rotation is not predicted. Higher order analytical modelling is possible to determine temperature rise generated in magnetic bearing touchdown events as conducted by Keogh and Yong [27]. In the following model consideration is given to the interaction of the steel rod in contact with the rotating polymer disc. The model is based around the heat transfer equation in polar coordinates (Figure 41), which may be axially averaged across the width of the polymer disc:

$$\frac{\partial^2 T}{\partial r^2} + \frac{1}{r}\frac{\partial T}{\partial r} + \frac{1}{r^2}\frac{\partial^2 T}{\partial \theta^2} - \frac{1}{\alpha}\frac{\partial T}{\partial t} - \beta T = 0 \tag{25}$$

where T is the axially averaged disc temperature relative to the ambient temperature, T_a, (r, θ) are polar coordinates, and

$$\alpha = \frac{k}{\rho c_p}, \beta = \frac{2h}{Lk} \tag{26}$$

where k is the thermal conductivity of the polymer, ρ is its density, c_p is the specific heat capacity, L is the disc width, and h is the convection heat transfer coefficient. The boundary condition at the outer surface of a cylinder of radius $r = R_I$ is

$$k\frac{\partial T}{\partial r}\bigg|_{r=R_I} = q_I(\theta, t) \tag{27}$$

where $q_I(\theta, t)$ is the axially averaged circumferential heat flux into the disc. Taking the Laplace transform of (27) gives

$$\frac{\partial^2 \overline{T}}{\partial r^2} + \frac{1}{r}\frac{\partial \overline{T}}{\partial r} + \frac{1}{r^2}\frac{\partial^2 \overline{T}}{\partial \theta^2} - \frac{p}{\alpha}\overline{T} - \beta\overline{T} = 0 \tag{28}$$

where p is the Laplace transform variable. Expanding transformed temperature and heat flux as a Fourier series in the circumferential coordinate gives

$$\overline{T}(r, \theta, p) = \sum_{-\infty}^{\infty} \overline{T}_n(r, p)e^{in\theta} , \bar{q}_I(\theta, p) = \sum_{-\infty}^{\infty} \bar{q}_{In}(p)e^{in\theta} \tag{29}$$

The equation of heat conduction becomes

$$\frac{\partial^2 \overline{T}_n}{\partial r^2} + \frac{1}{r}\frac{\partial \overline{T}_n}{\partial r} - \left(\frac{n^2}{r^2} + \frac{p}{\alpha} + \beta\right)\overline{T}_n = 0 \tag{30}$$

The Bessel function solution that is finite as r tends to 0 is

$$\overline{T}_n(r, p) = A_n I_n(\lambda r) \tag{31}$$

where $\lambda = \sqrt{\frac{p}{\alpha} + \beta}$. The boundary condition of equation (29) is satisfied by

$$A_n = \frac{1}{k\lambda I_n'(\lambda R_I)}\bar{q}_{In}(p) \tag{32}$$

Hence

$$\overline{T}_n(r, p) = \frac{I_n(\lambda r)}{k\lambda I_n'(\lambda R_I)}\bar{q}_{In}(p) \tag{33}$$
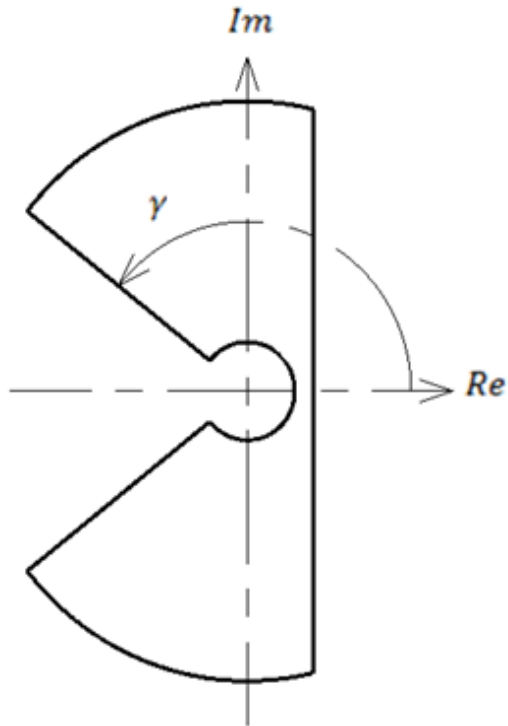
Figure 42: Completion of the inversion contour.

The following recurrence relation (Abramowitz and Stegun, 1967) applies:

$$I_n'(z) = I_{n+1}(z) + \frac{n}{z} I_n(z) \tag{34}$$

Equation (33) can then be inverted to give a solution in the time domain as

$$T_n(r,t) = \frac{1}{2\pi i} \int_{c-i\infty}^{c+i\infty} \frac{I_n(\lambda r)}{k\lambda \left(I_{n+1}(\lambda R_I) + \frac{n}{\lambda R_I} I_n(\lambda R_I) \right)} \overline{q}_{In}(p) e^{pt} dp \tag{35}$$

The temperature response may be obtained using the convolution integral

$$T_n(r,t) = \int_0^t H_n(r, t-\tau) q_{In}(\tau) dt \tag{36}$$

where

$$H_n(r,t) = \frac{1}{2\pi i} \int_{c-i\infty}^{c+i\infty} \frac{I_n(\lambda r)}{k\lambda \left(I_{n+1}(\lambda R_I) + \frac{n}{\lambda R_I} I_n(\lambda R_I) \right)} e^{pt} dp \tag{37}$$

Because $I_n\left(ve^{\pm\frac{1}{2}\pi i}\right) = e^{-\frac{1}{2}n\pi i}J_n(\mp v)$ has poles on the real axis it is appropriate to complete the contour of integration as shown in Figure 42. In general, $p = z_\gamma \alpha x^2/R_I^2$ on the angled lines where $x > 0$ and $z_\gamma = e^{i\gamma}$ on the upper line. Hence

$$dp = 2\frac{z_\gamma \alpha}{R_I^2} x dx, \quad \lambda_\gamma = \sqrt{\frac{z_\gamma x^2}{R_I^2} + \beta} \tag{38}$$

It now follows that

$$\frac{1}{2\pi i}\int_{c-i\infty}^{c+i\infty} f(\lambda)e^{pt}ds$$

$$= \frac{z_\gamma \alpha}{\pi i R_I^2}\int_0^\infty f(\lambda_\gamma)e^{\frac{z_\gamma \alpha x^2 t}{R_I^2}} x dx \tag{39}$$

$$- \frac{z_{-\gamma}\alpha}{\pi i R_I^2}\int_0^\infty f(\lambda_{-\gamma})e^{\frac{z_{-\gamma}\alpha x^2 t}{R_I^2}} x dx$$

Since the second term is the complex conjugate of the first term, it follows that

$$\frac{1}{2\pi i}\int_{c-i\infty}^{c+i\infty} f(\lambda)e^{pt}dp = Re\left(\frac{2z_\gamma \alpha}{\pi i R_I^2}\int_0^\infty f(\lambda_\gamma)e^{\frac{z_\gamma \alpha x^2 t}{R_I^2}} x dx\right) \tag{40}$$

In this expression

$$z_\gamma f(\lambda_\gamma)x = \frac{2R_I^2}{Lk} h_n(x,\rho,\gamma)$$

$$h_n(x,\rho,\gamma) = \frac{z_\gamma x I_n\left(z_\gamma^{0.5}\rho x\right)}{\left(z_\gamma^{0.5} x I_{n+1}\left(z_\gamma^{0.5}x\right) + n I_n\left(z_\gamma^{0.5}x\right)\right)} \tag{41}$$

where $\rho = r/R_I$. It now follows from equations (36) and (37) that

$$T_n = H_n(r,t)$$

$$= \frac{\alpha}{\pi i k R_I}\int_0^t\int_0^\infty \left\{h_n(x,\rho,\gamma)e^{\frac{z_\gamma \alpha x^2(t-\tau)}{R_I^2}} - h_n(x,\rho,-\gamma)e^{\frac{z_{-\gamma}\alpha x^2(t-\tau)}{R_I^2}}\right\} q_{In}(\tau)d \tag{42}$$

> 1 Rotation

2nd Rotation

10 Rotations

21.645
21.64
21.635
21.63
21.625
21.62
21.615
21.61
21.605

degC
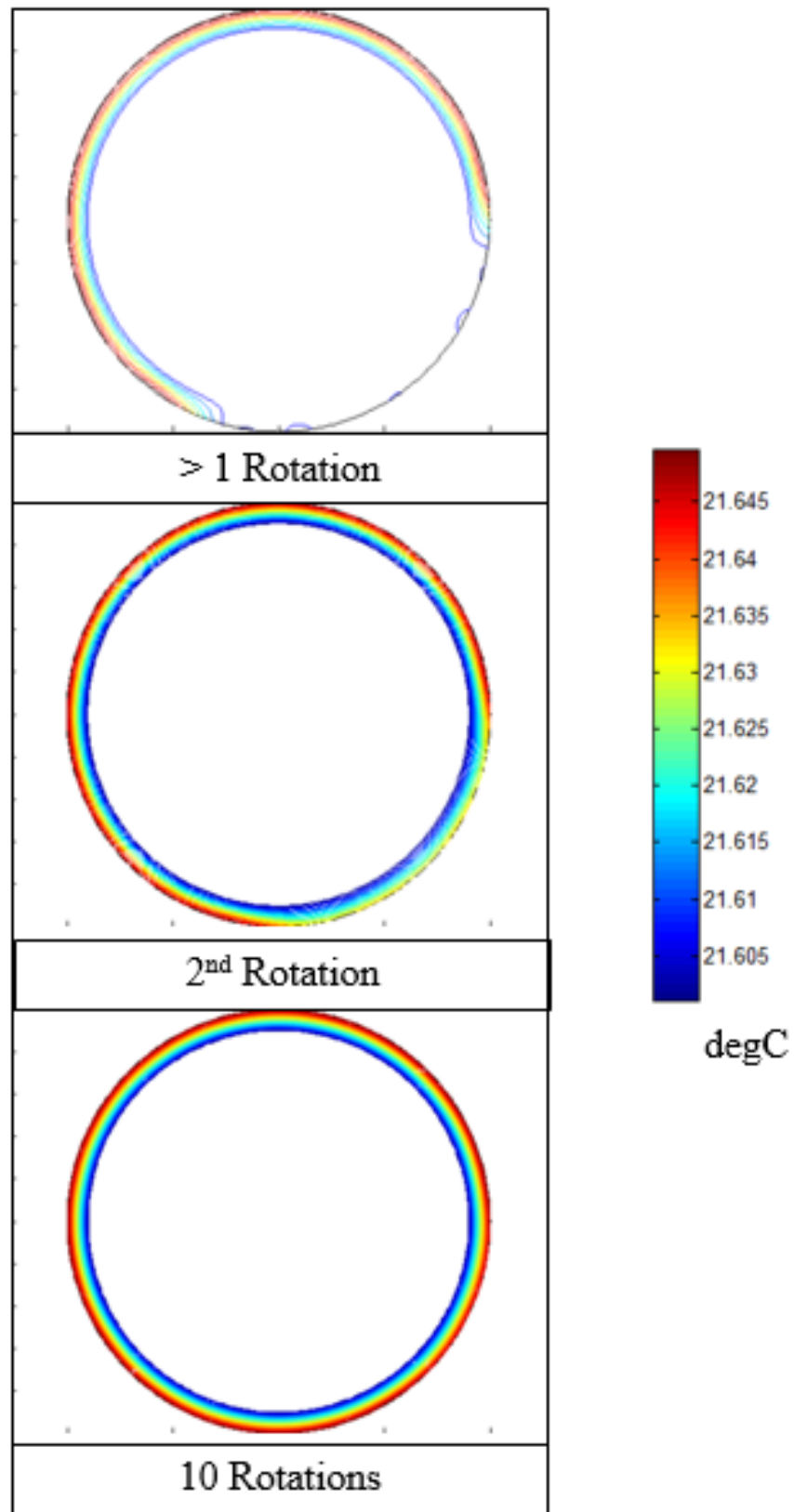
Figure 43: Model results of disc temperature contours for up to 10 rotations.

Considering the axially aligned rod and disc, the heat flux can be regarded as rotating at frequency ω about the circumference of the disc, which is considered to be stationary:

$$q_I(\theta, t) = Q_I(\theta - \omega t) \tag{43}$$

Hence

$$q_I(\theta, t) = \sum_{-\infty}^{\infty} Q_{In} e^{-in\omega t} e^{in\theta} \tag{44}$$

Then

$$q_{In}(\tau) = Q_{In} e^{-in\omega\tau} \tag{45}$$

Substituting into equation (42) and performing the time integration yields

$$T_n(r, t) = \frac{1}{2i} \left(T_{n,\gamma}(r, t) - T_{n,-\gamma}(r, t) \right) \tag{46}$$

where

$$T_{n,\gamma}(r, t) = \frac{2\alpha}{\pi k R_I} \int_0^{\infty} h_n(x, \rho, \gamma) \frac{e^{z_\gamma \alpha x^2 t / R_I^2}}{\left(z_\gamma \alpha x^2 / R_I^2 + in\omega \right)} dx \, Q_{In} \tag{47}$$

For a heat flux arising from a Hertzian pressure distribution between the aligned rod and disc, an appropriate expression for the heat flux into the polymer is

$$Q_I(\theta) = \begin{cases} Q_0 \sqrt{(\theta_0^2 - \theta^2)}, & |\theta| < \theta_0 \\ 0, & |\theta| > \theta_0 \end{cases} \tag{48}$$

where $Q_0 = \phi \mu R_I \omega$ and $2\theta_0$ is the angular extent of the contact zone. The implication of equation (48) is that the Fourier coefficients follow as

$$Q_{In} = \begin{cases} \dfrac{Q_0 \theta_0}{2n} J_1(n\theta_0), & n \neq 0 \\ \dfrac{Q_0 \theta_0^2}{2}, & n = 0 \end{cases} \tag{49}$$

The complete expression for the axially averaged disc temperature is

$$T(r, \theta, t) = \sum_{-\infty}^{\infty} T_n(r, t) e^{in\theta} \qquad (50)$$

This expression was evaluated using MatLAB (MathWorks version R2011b) for the parameters matching the case when $s = 0.2$ mm. Time dependent contour plots of the disc temperature are shown in Figure 43. The heat source moves in an anti-clockwise sense starting from the right hand side of the disc. After the second rotation it can be seen that the wall is starting to cool as the leading edge of the heat approaches the heat source for the third time. In the 10 rotation plot, the temperature is nearly uniform around the circumference of the disc. Figure 44 shows the temperature variation at a fixed point on the circumference at 45° clockwise from the top of the disc. The initial step-like variation is due to the cyclic heating as the heat source (aligned rod) passes the observation point. The steps persist, though are not resolvable on the macro scale of Figure 45.
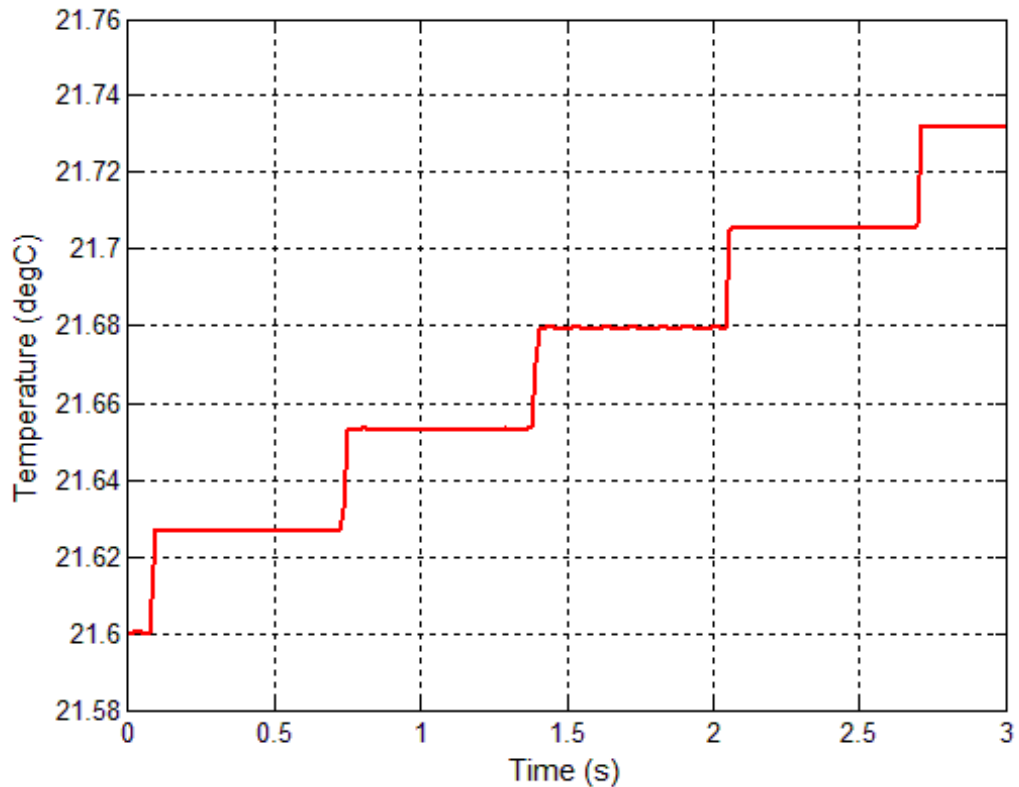
Figure 44: Fixed point temperature variation with time – high resolution.
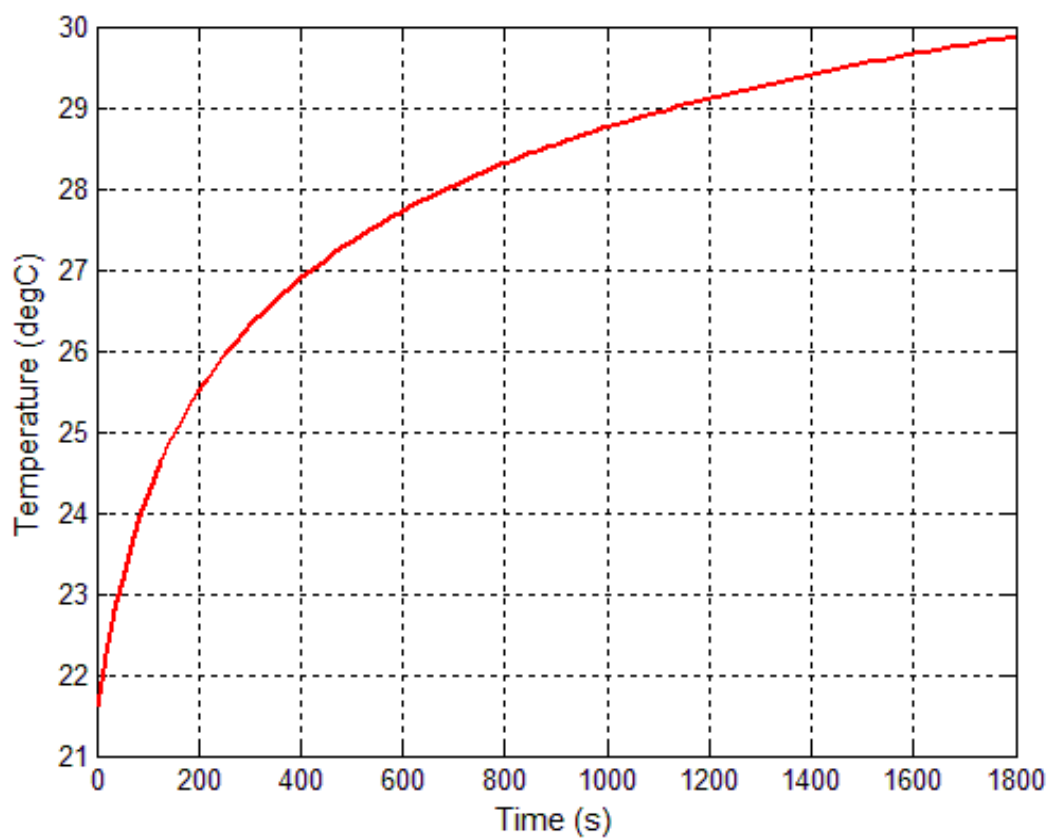
Figure 45: Fixed point temperature increase with time - complete data

4.5   Finite Element (FE) Model
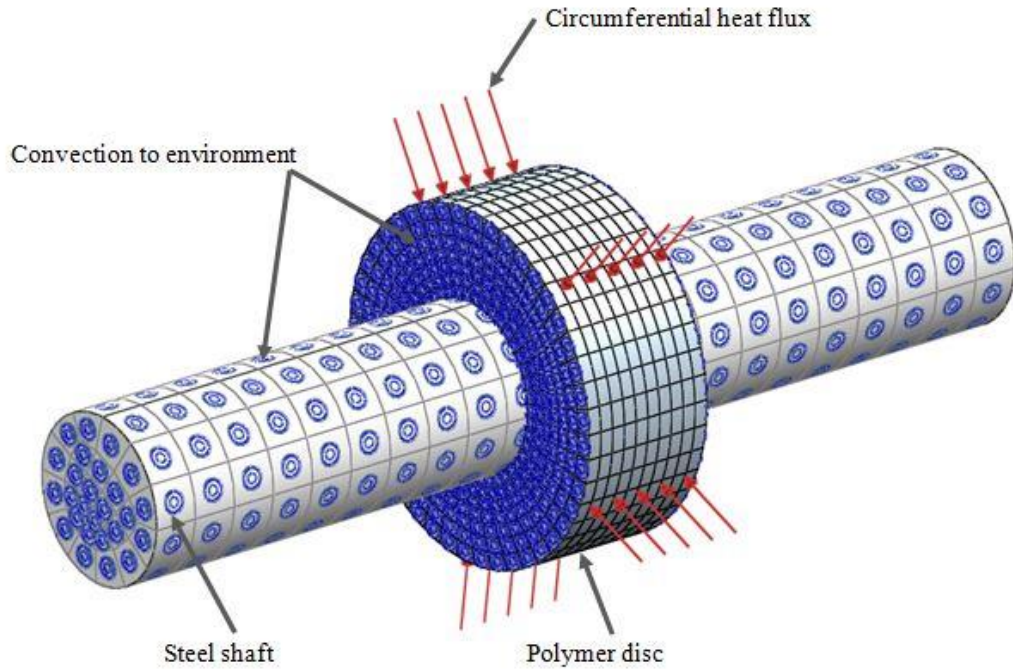
Figure 46: Circumferential heat flux FE model.

Table 7: Model parameters

	Disc	**Shaft**
Element type	20 Node Hexagonal	20 Node Hexagonal
Element number	3080	572
Element size	1 mm	3.4 mm
Element Material	POM	Steel

A solver was used and the following heat transfer coefficients were applied:

(a) 200 $W/m^2/deg$ C between the shaft and the disc

(b) 12 $W/m^2/deg$ C shaft to the environment

(c) 1.9 $W/m^2/deg$ C the disc to environment

The heat load of 0.13 W was uniformly distributed on the outer circumferential surface of the polymer disc.

The FE model of the aligned rod and disc arrangement, without rotation, was established to provide an assessment of the thermal response. Figure 46 shows the

meshed shaft and disc. The finite element model has been developed as a design environment alternative to the full analytical model described in Section 4.4. A series of these models (to represent different points along the line of contact S) should be used in conjunction with the time averaging technique described in Section 3.3 to determine the heat rise in a gear. A heat flux distribution is applied to the outer diameter of the polymer disc and convection boundary conditions to the environment were set up on the flanks of the disc and also on the external surfaces of the steel shaft. Since the model was non-rotational, an averaged heat flux was applied over the circumferential surface of the polymer disc. A heat flux from the aligned rod to the polymer disc was evaluated according to equation (22). This was then scaled to distribute it over the complete circumferential surface according to

$$Q_{FET} = Q_T \frac{A_i}{A_d} \tag{51}$$

where Q_{FET} is the heat flux value of the circumferential distribution applied in the FE model, Q_T is heat flux generated under the aligned rod (equation (22)), A_i is the area of indentation of the rod on disc, and A_d is the circumferential area of the modelled disc circumferential surface. The heat flux was applied in a step-like manner and a time dependent solution was obtained for a point on the centreline of the disc, as shown in Figure 46 . Although the general trend is similar to the experimental measurements of Figure 31, a more accurate dynamic thermal analysis from the rod heat flux is appropriate and is given in Section 4.4.

The results of the FE model are shown in Figure 48 and Figure 49 . A heat flux applied to the entire circumference of the disc is consistent with the equivalent cylinders analogue for a pair of gears in contact at a specific point in the sweep, in this case at $S = 0.2$ mm. The heat flux is applied around the disc and the maximum temperature of the disc surface reaches a value of just under 30°C after a 30-minute solution time.

Figure 47 shows the results of a sensitivity study to find the most efficient mesh density for the thermal FE solution. Temperature is shown on the y axis and although the difference between the highest reported temperature and the converged solution is only 0.6 °C, the solution converges rapidly at a mesh density of 1 element/mm^3.
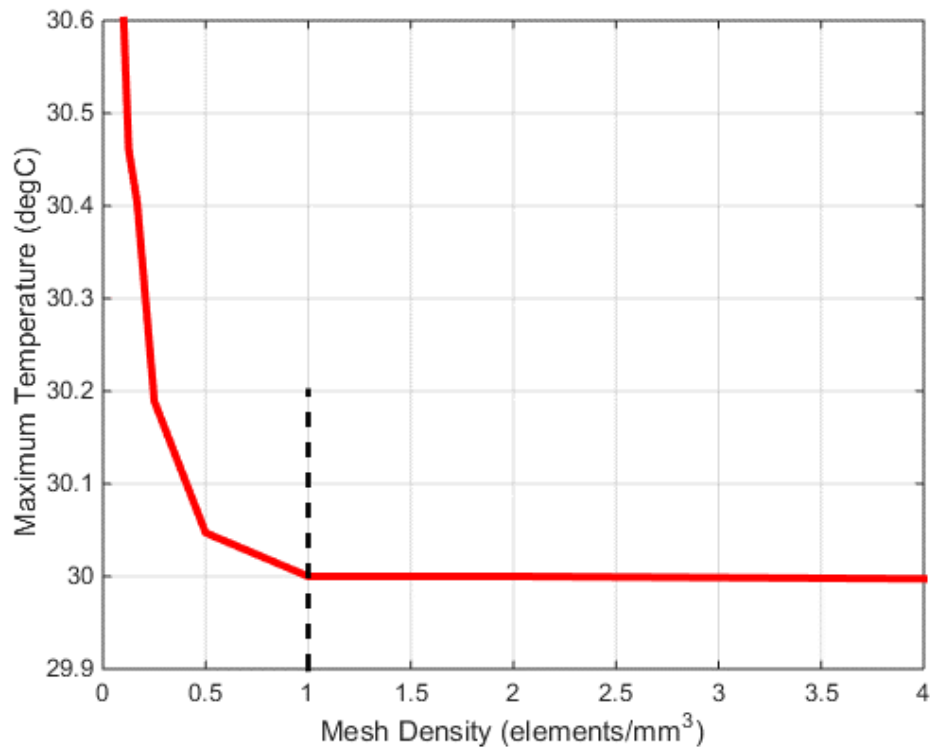
Figure 47: Solution convergence for temperature - black
dotted line shows final solution mesh density value
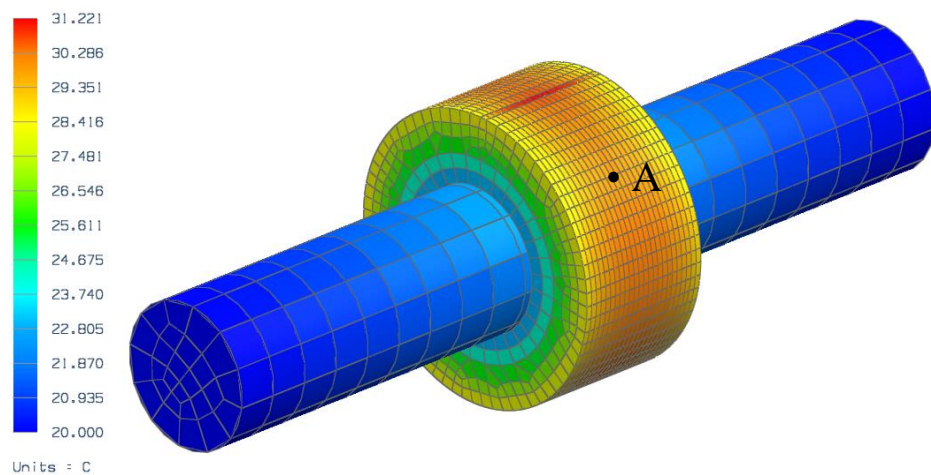
Figure 48: Circumferential heat load thermal plot

Point 'A' in Figure 48 shows the position of the element that corresponds to the experiment measurement of temperature on the disc. Figure 49 shows the temperature of that element over the 30-minute period.
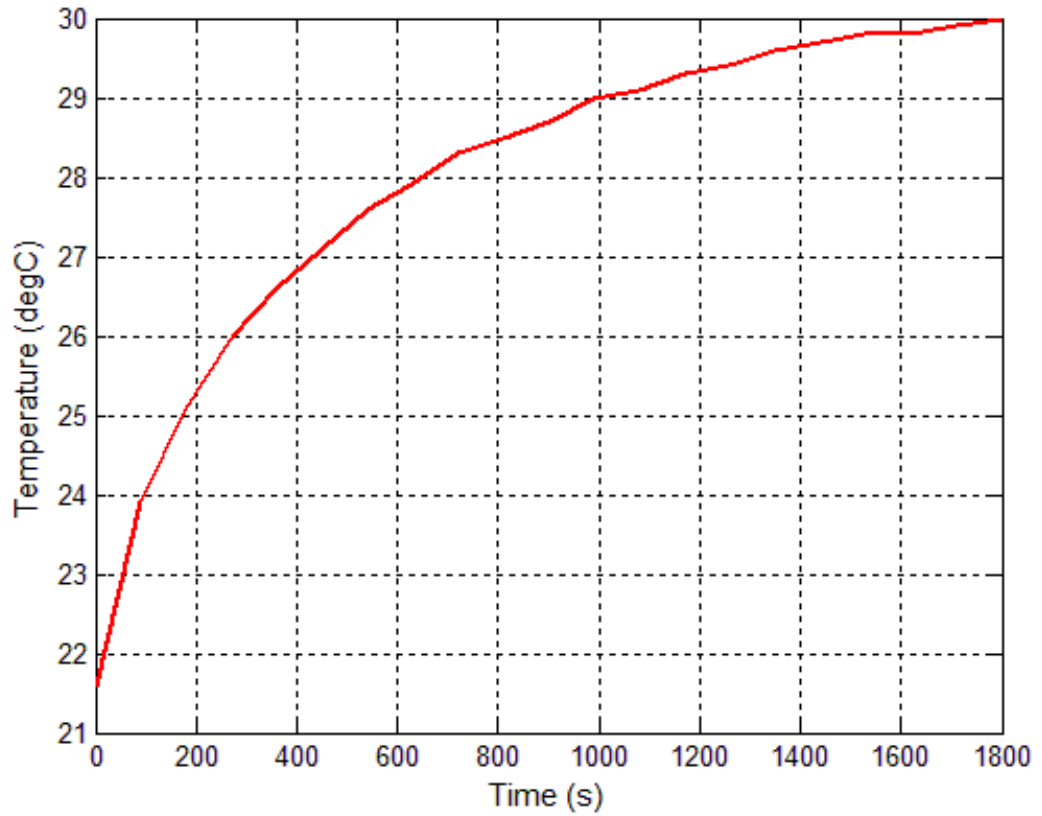
Figure 49: FE Model results – temperature at point 'A'

4.6   Comparison of Modelling Results with Experimental Results
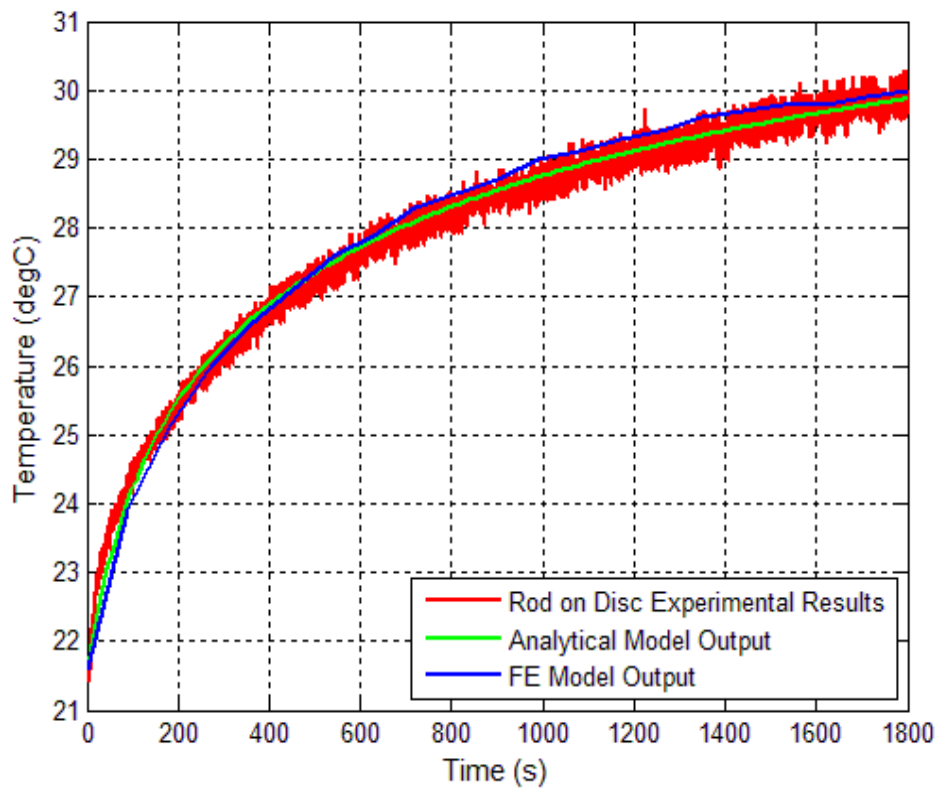
Figure 50: Comparison of rod on axially aligned disc temperatures
with the model predictions

Finally, the temperatures measured and time averaged from the rod on axially aligned disc experiment can be compared to both the analytical and finite element models that have been presented. These data are also shown in Figure 50 and good correlation exists between the three data sets. If a model were produced for a series of equivalent cylinders (either a FE or analytical model as detailed in the previous chapter) then the output of those models could be time averaged as described in Section 3.3. As shown in Figure 50, this time averaged data would correlate well with the real gear running temperatures and so could be used in this manner to predict them. This is useful and convenient because, as previously discussed, a model that accurately represents the geometry and contact conditions of a spur gear pair would be excessively complex to construct and run.

4.7   Consolidation of Chapter 4
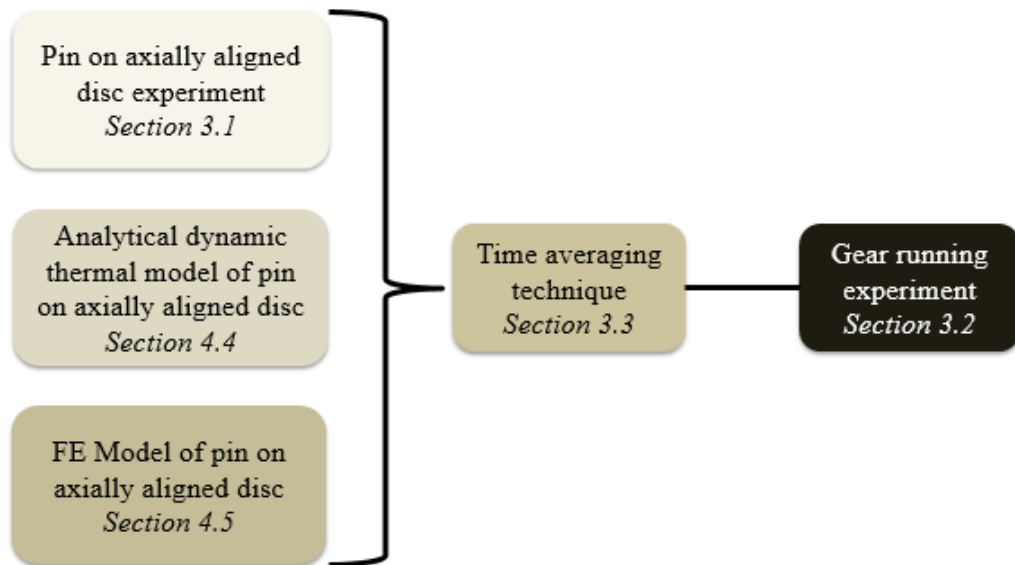
Figure 51: Multidisciplinary modelling approach

In conclusion, the approach taken for predicting the temperature rise in the gears is somewhat multi-disciplinary in nature and is outlined in Figure 51. This approach has been developed as it relies very little on assumption but rather on cross validation of techniques by experimentation and by correlation of models. Firstly, the analytical model is used to find out the heat transfer properties of the rod on axially aligned disc system. This first part of the technique has been validated against the experimental work to determine the heat transfer properties of the system. The model as described in Section 4.4 is an entirely analytical solution of the heat equation in polar coordinates and so can be considered as robust as it does not rely on assumptions to produce an accurate result. The second stage of the process is to create a finite element model of the same rod on axially aligned disc arrangement. This stage predicts the surface temperature of the disc. The third and final stage of the process is then to use the analogy of equivalent cylinders to directly liken the disc to the real gears by the process of time averaging as developed at the end of chapter 3.

CHAPTER 5

Experimental Observations of Gear Tooth Surfaces

This chapter documents the imaging of polymer gear teeth and how a Scanning Electron Microscope (SEM) was used to identify a new wear mechanism. It also groups together images taken over a 2-3 year period during which an effort was made to identify as many incidences of the mechanism as possible in product tested applications and also in duplicated laboratory conditions.

5.1   Scanning Electron Microscope

Numerous samples have been inspected using a scanning electron microscope [JEOL SEM6480LV]. The operation of a scanning electron microscope is well documented and an excellent description of the physical principles of the SEM and some techniques for successfully operating them are given by Gagnadre *et al.* (2009). The samples were run as a gear pair using the experimental hardware previously described in Section 3.2 and were then prepared for the microscope chamber. Gears were inspected that had been subjected to a variety of different running conditions. They can be split into 2 groups:

(1) Those that have been removed from a Rotork product post durability testing.

(2) Those that have been run using the equipment described in chapter 3. A full list of inspected gears is shown in Table 8.

Table 8: Gear samples imaged by the SEM

Figure Number	No of Cycles	Speed (revs /min)	Torque (Nm)	Sample Description
Figure 53	12×10^6	26.9	5.3	Initial observations using a conventional optical microscope.
Figure 54	12×10^6	26.9	5.3	Teeth cut from a CVA durability test actuator. The first set of observations made using the SEM technique.
Figure 55	12×10^6	26.9	5.3	As Figure 54.
Figure 56	12×10^6	26.9	5.3	As Figure 54 and Figure 55.
Figure 57	12×10^6	168	0.85	Steel pinion from a CVA durability test actuator for comparison with the polymer gears.
Figure 58	0	0	0	Completely unused, unworn polymer gear imaged as a benchmark comparison against the other observations.
Figure 59	10-1000	26.9	5.3	Progressive wear trials.
Figure 60	50000	26.9	5.3	Maximum test cycles achievable in one day in the laboratory.
Figure 61	10000	128	15.9 (apparent)	These test gears were thinned down to increase the contact pressure and so the apparent torque input.
Figure 62	6×10^6	128	5.3	A long term laboratory test (50% product life) run showing a large scale profile view.
Figure 63	3×10^6	128	5.3	A long term laboratory test (25% product life) run showing a large scale plan view of the wear field.
Figure 64	1.2×10^6	128	5.3	A long term laboratory test (10% product life) run showing smearing and the debris field.
Figure 65	1.2×10^6	128	5.3	As Figure 64.
Figure 66	1.2×10^6	128	5.3	As Figure 64 and Figure 65.

5.1.1 Sample Preparation

To prepare each test sample a procedure was developed to ensure that the tooth flanks of the samples were not disturbed or damaged and that a consistent methodology was followed. The following steps were undertaken:

- The gear was placed into a specially designed mandrel that held firmly the gear and includes features that allow it to be clamped in a milling machine.
- The gear was then milled using a Bridgeport milling machine (manufactured by Hardinge) from four directions to expose four legs as shown in Figure 52(a). Using a milling machine to do this ensured that each tooth flank could be exposed

(a)   (b)
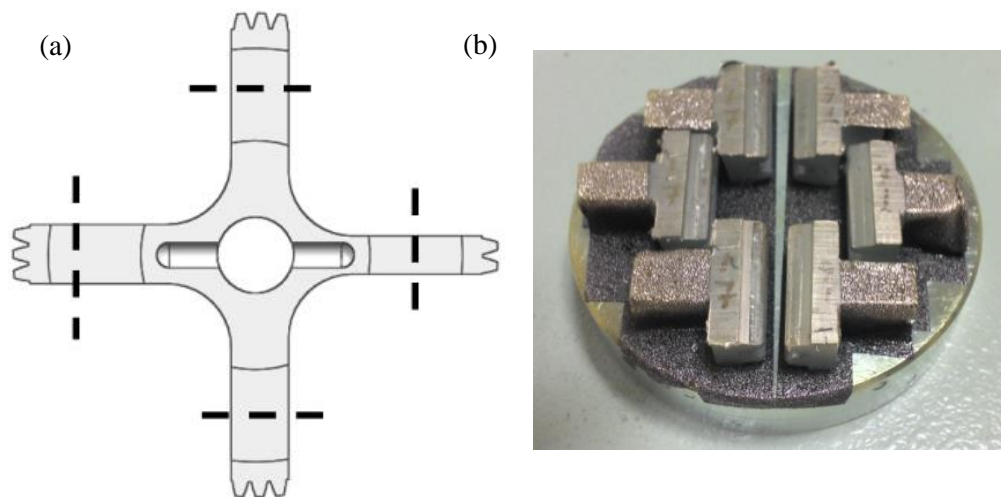
without risk of damaging its surface.

Figure 52   (a) Gear sample machining and

(b) Fully prepared sample stub for SEM imaging

- The legs were then cut at the dashed lines (Figure 52(a)) to leave samples of which two flank faces could be easily imaged. Only one exposed flank face would have been loaded for a given gear as each had been loaded in one direction only.
- The samples were fixed to an aluminium stub for mounting to the XYZ translation tables of the SEM. They were fastened down with magnetic tape and additional tape was wrapped over the top of the back of the sample to ensure electrical conductivity between the top face of the sample to the aluminium stub.

- The samples were then held for at least 24 hours in a vacuum chamber to out-gas and decontaminate them for use in the SEM chamber, which was also held under partial vacuum.
- They were then sputter coated using an Edwards S150B sputter coater with gold to ensure good conductivity with the SEM machine, which is necessary to get good imaging results. Figure 52 (b) shows the completed sample stub.

5.2 Initial Observation of Smearing
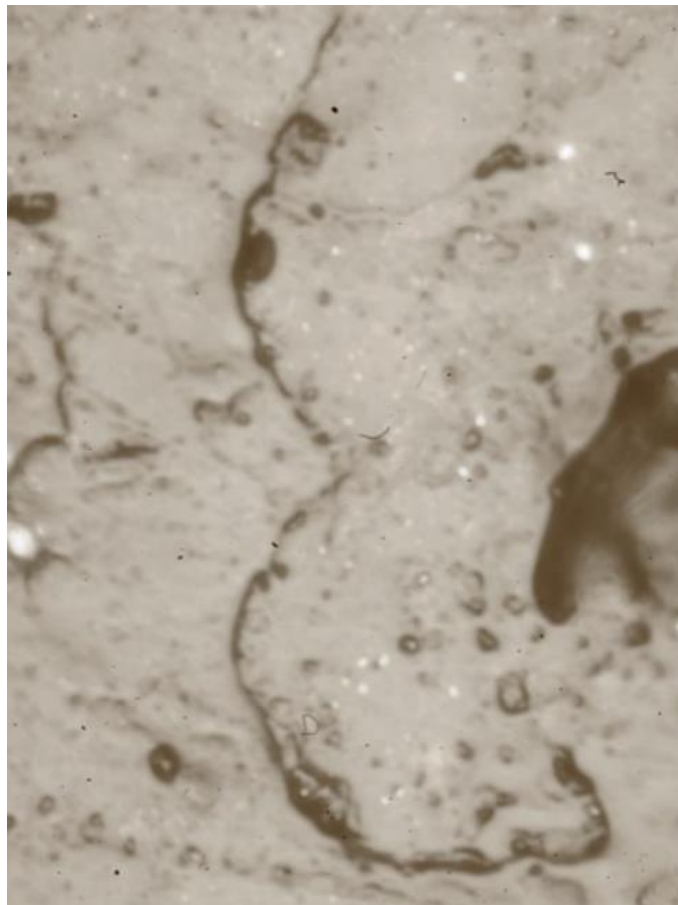
Figure 53: Optical microscope observation at a magnification of
x400 showing the first 'smear' feature found.

The magnification of the image shown in Figure 53 is approximately x600 to x800 and shows a double curved feature somewhat resembling the character epsilon ε. It was

imaged using a digital camera attached to the secondary input of a standard optical microscope. The image is not particularly clear, but it is included as it shows the first evidence for the wear mechanism. Because of this image, and a feeling that this branch of investigation may be of interest, a decision was made to pursue it further using SEM techniques.
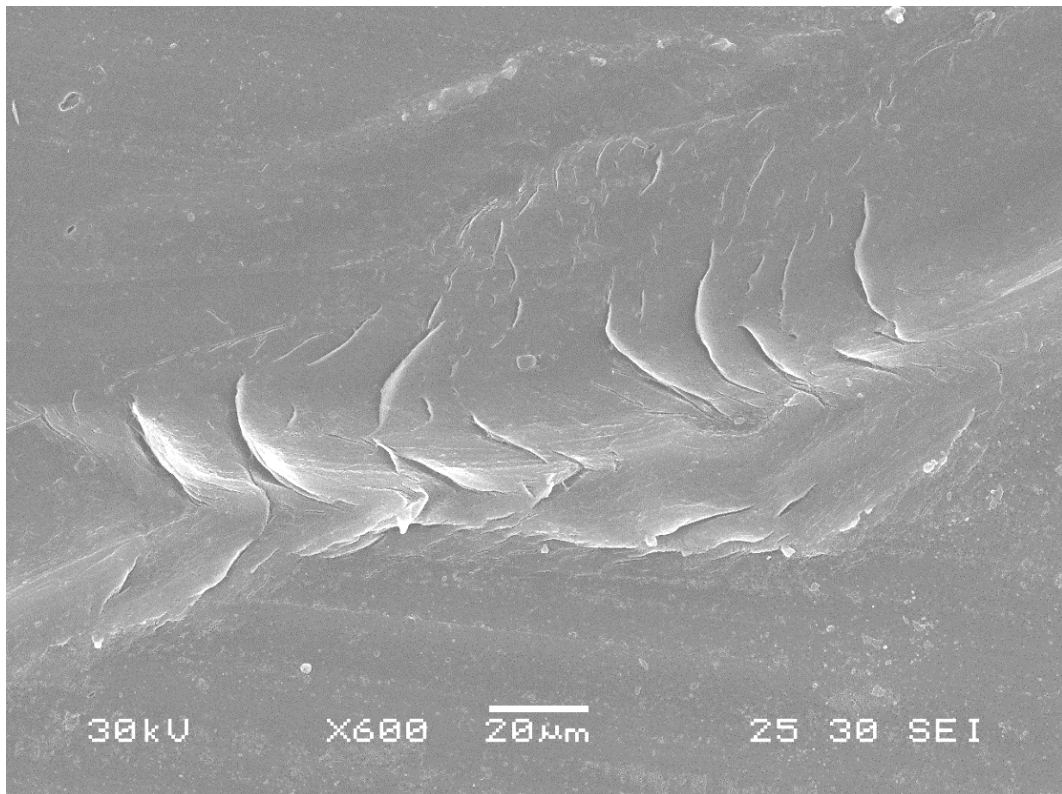
Figure 54: Smears observed on the polymer tooth surface of a CVA product durability tested gear.

The image in Figure 54 was taken of the flank of the tooth of a gear that had been used in the product durability test of a CVA actuator. The gear had experienced approximately 6 million cycles, a cycle being one forward and one reverse direction pass of one tooth loaded in one direction only. The gear may transmit around 15 W of power and the gear output torque is 5.3 Nm. The total time the product was running under this load was around one year, so this sample represents a valuable resource for studying wear. The sliding direction across the tooth flank is from right to left and a number of features are evident in the centre of the view. The features, which will be referred to as

smears, range between 20 to 60 μm in length and appear to be swept along in the direction of the sliding of the steel tooth across the polymer. The image was taken from the side at an angle of 30 degrees to give a better perspective of their form.

This image was taken during one of the first sessions using the SEM and immediately presented itself as of interest. The tribological effect shown may be due to the interaction of the steel pinion with the polymer gear. This feature became the main object of the research in two respects. Firstly, to ascertain if this was in fact caused by the teeth interaction and, secondly, if a theory could be formulated that explains the wear mechanism in the polymer gear.
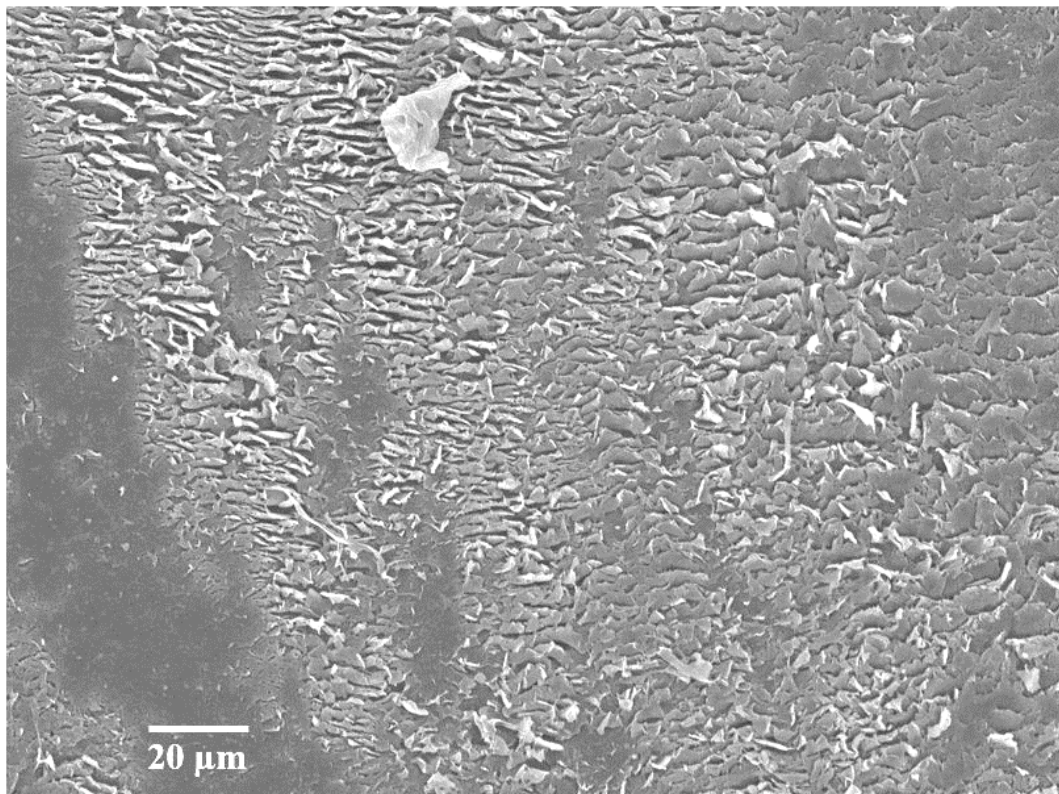
Figure 55: Smear field observed on the polymer tooth surface of a CVA product durability tested gear.

Figure 55 was taken from the same CVA actuator that had undergone one year of durability testing. The features are imaged directly normal to the surface. The smears are approximately the same size as in Figure 54, but are much more closely packed together and occur in a field of grouped features. The sliding direction in this case is vertically from the bottom to the top of the image. Note that there is an area to the bottom left of the

smear field that does not appear to have been affected in the same way as the main body of the field. In fact, during scanning of tooth flanks for areas of interest many formations ranging from obviously scored and abrasive wear to areas that were largely unaffected by the contact with the steel gear were noted. It could well be the case that, due to manufacturing tolerances of the parts, there are areas of tooth flank that are not and never come into contact at this micro level of inspection.
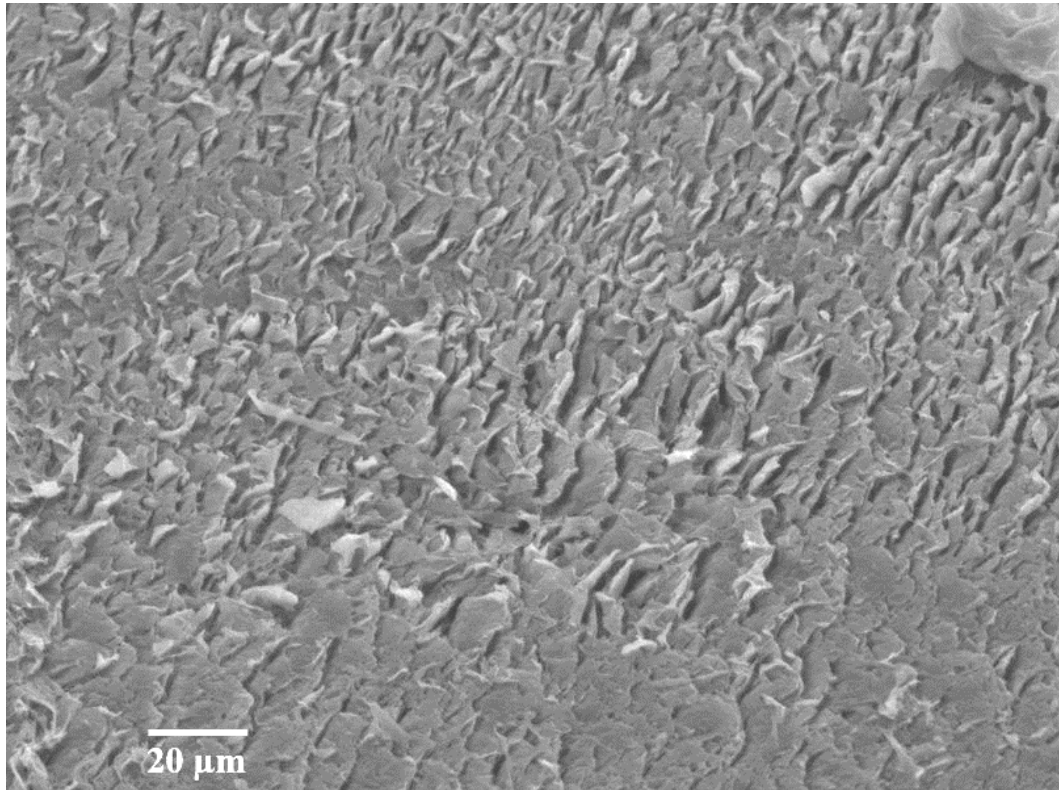
Figure 56: Smear field observed on the polymer tooth surface of a CVA product durability tested gear – angled view.

Figure 56 shows the same smear field as in Figure 55. It is from the side with the angle of the sample table set to the maximum tilt of 40 degrees, which maximises the perspective of the image to the smear formations. The smears are so pronounced in that they are overlapping and are so long and flat that it looks very much due to the action of the sliding steel over many cycles. It is at this point that a hypothesis begins to form as to the origins of these features and how they may contribute to wear of the polymer gear. If the smears form and eventually, over many cycles of loaded operations become elongated and stretched, they may reach a threshold and become detached. This would be a volume removal of material and so would represent wear by a distinct and definable mechanism.

5.3   Steel Pinion and Unworn Polymer Gear
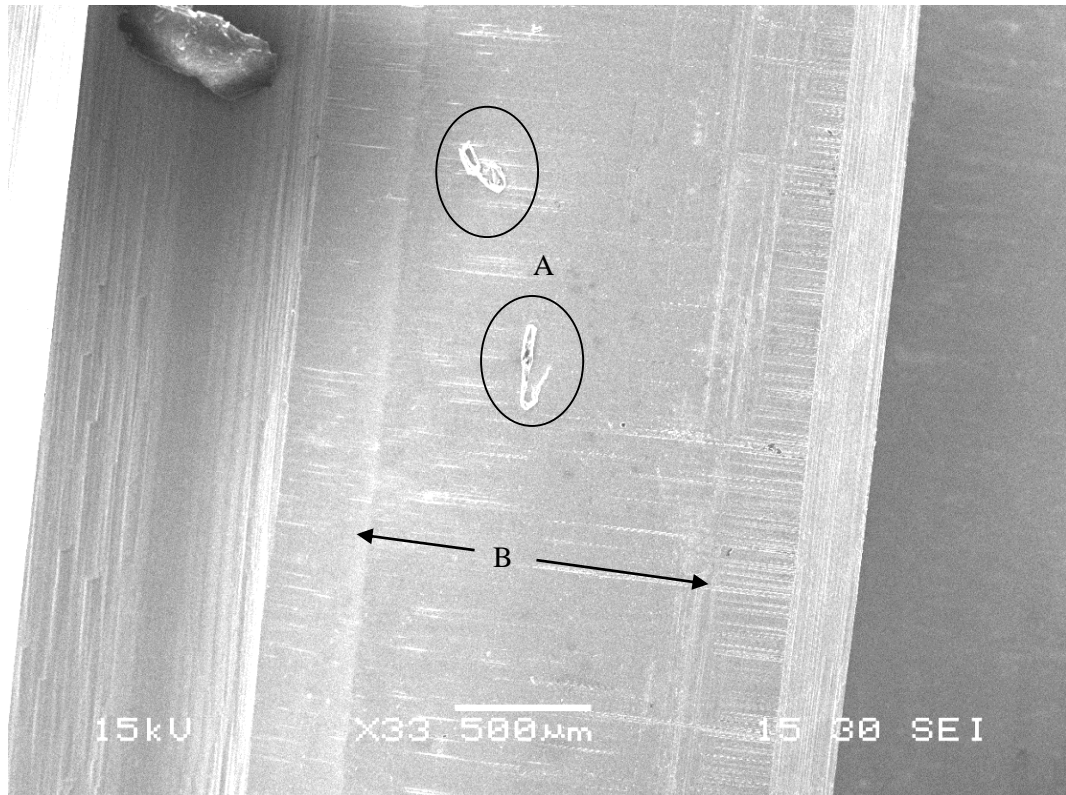
Figure 57: Steel pinion tooth showing mild wear and debris.

The image shown in Figure 57 shows a large scale view of the steel pinion that had been run with the product tested gears as listed in Table 8. The tooth flank has been largely unaffected by the loaded running of approximately 12 million cycles. Some unknown debris (A) can be seen on the tooth surface and some of the machining marks have been polished out, as evident with the area (B) in contact in the central portion of the tooth flank. Surface profile measurements were taken and are documented and discussed in Section 5.10.1. They show that the steel pinion has been largely unaffected by loaded running.
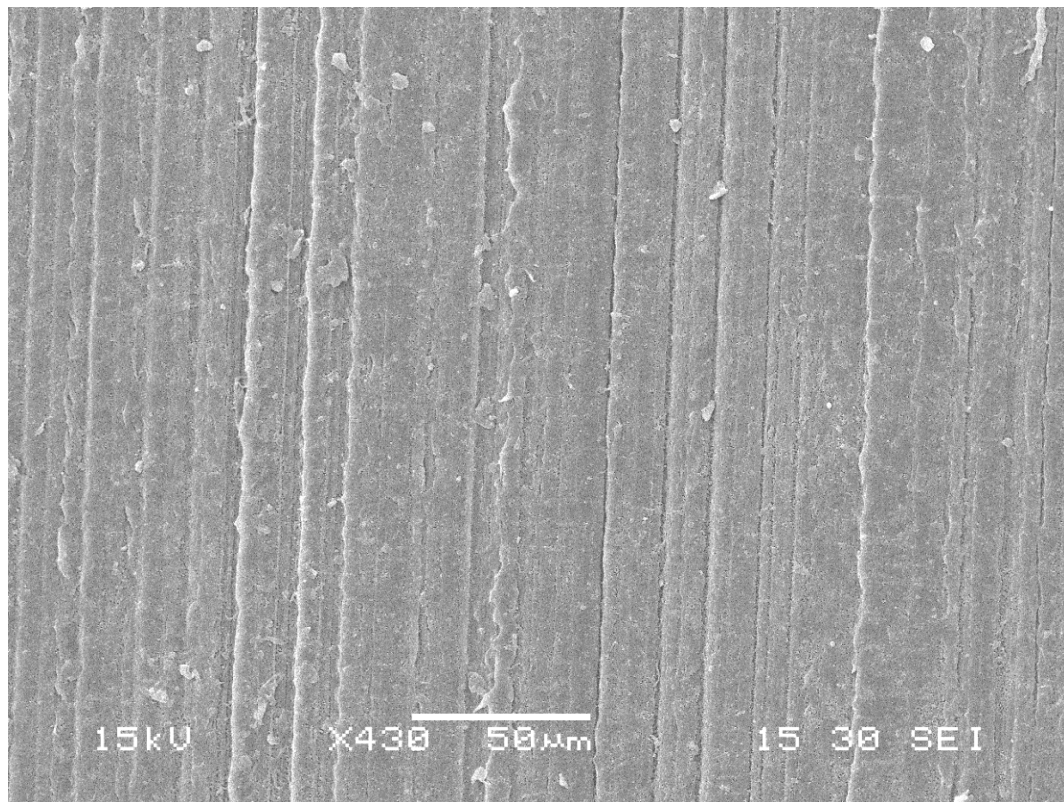
Figure 58: Unworn polymer gear tooth flank showing machining marks.

Figure 58 shows the surface of an unworn polymer gear tooth flank. This gear was completely unused and prepared for the SEM in the same way as the other gears to give four separate samples. The machining marks can be seen clearly in the image in the direction across the flanks of the tooth (top to bottom on the image). This image is a benchmark for the other images presented. A possible conjecture for the existence of the smear features seen in previous images is that they are in some way drawn from or are initiated from the machining lines as seen in the unworn flank. However, any slip during operation would be orthogonal to these lines and indeed, the smears are in the correct direction to support this theory – in the image above the sliding direction would be from right to left. However, if this were the case, smears should always be present across these lines. Note that in the Figure 55 there are plain portions of polymer that have smoothed flat by the action of the steel pinion sliding against the polymer flank. The steel pinion has in fact been in contact with the machined surface of the initially unworn polymer flank and yet it has not produced the smear features but has smoothed them flat. Also, it will be seen in later images that the smears are not of consistent pitch spacing whilst the machining marks are consistent in this respect.

5.4 Initial Scoping Runs
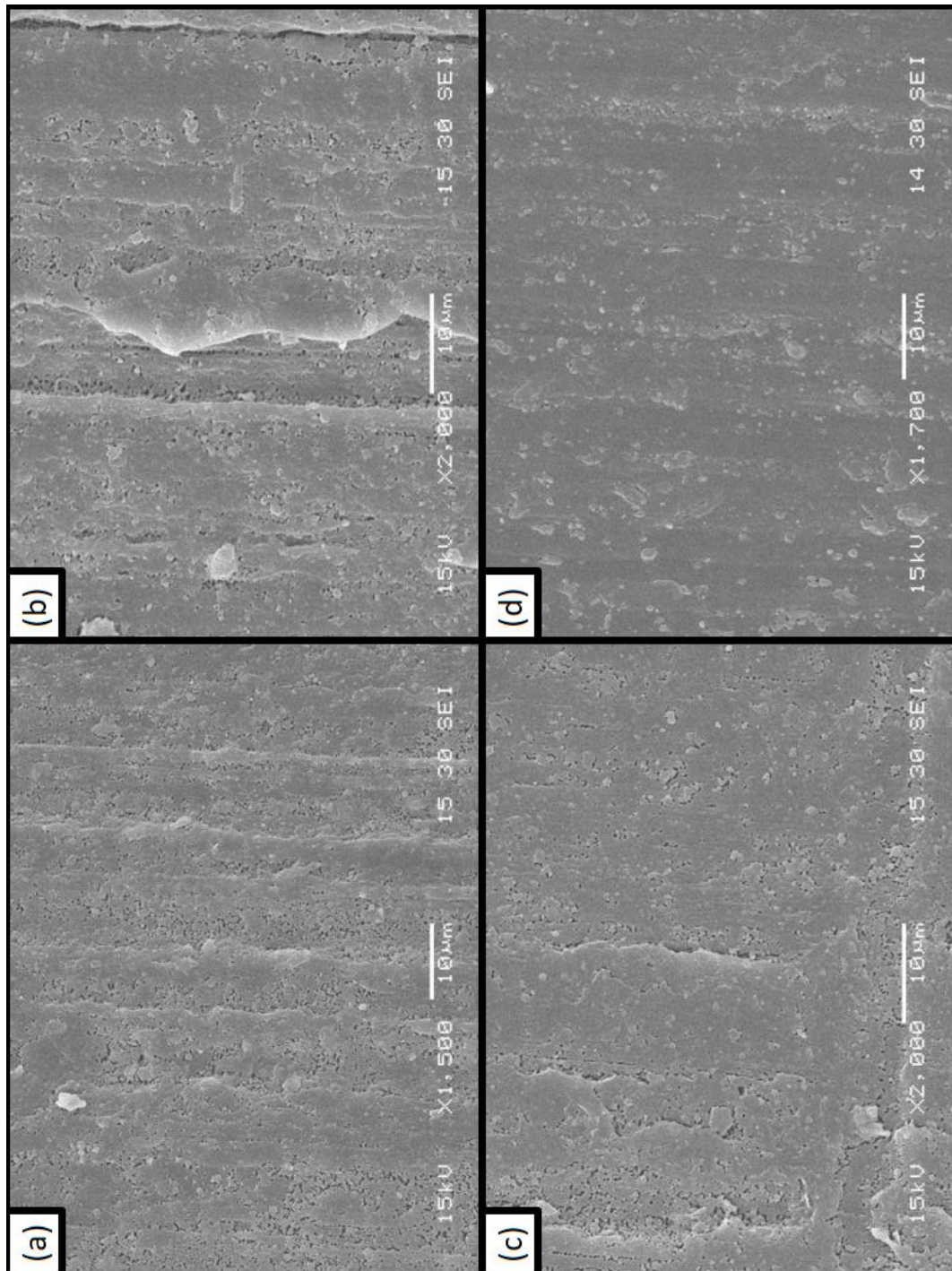
Figure 59: Wear progression over 1000 cycles

Sample numbers are shown for each sub-image

((a) = 0 cycles; (b) = 10 cycles; (c) = 100 cycles; (d) = 1000 cycles)

Figure 59 consists of a composite image showing the progression of wear of the polymer gear tooth flanks over a period over 1000 cycles. The progression runs from the un-worn Sample (a) to (b) at 10 cycles, (c) at 100 cycles and finally sample (d) at 1000 cycles. In comparison with the unworn gear image shown in Figure 58, the image of Sample (a) is at a higher magnification, but the machining marks can still be clearly seen running from side to side. This set of images were taken with a view to identifying the point at which the smearing starts to take place. There is a general smoothing of the surface as the number of cycles increases and by the time the gear flanks have seen 1000 cycles, the machining marks have been almost completely smoothed out. After 1000 cycles no smears are seen and so it is evident that this mechanism does not start until sometime after 1000 cycles and once the smoothing of the surface is complete. To run a gear for significant periods of time and then to prepare it and image it would have taken a considerable amount of time. The 12 million cycle gear from the product durability testing took one year to complete, so clearly a full range of results would take many years. However, this testing does provide the knowledge that the machining marks are in fact smoothed out of the surface of the gear flank before smearing takes place. In order to prove that surface finish of the polymer gear tooth flank does not affect the creation of smearing, an extensive trial could be made to test for this correlation. However, given the large numbers of experiments required to carrying this out satisfactorily, this course of action was not taken during this research programme.

5.5 Maximum Cycles in 1 Day
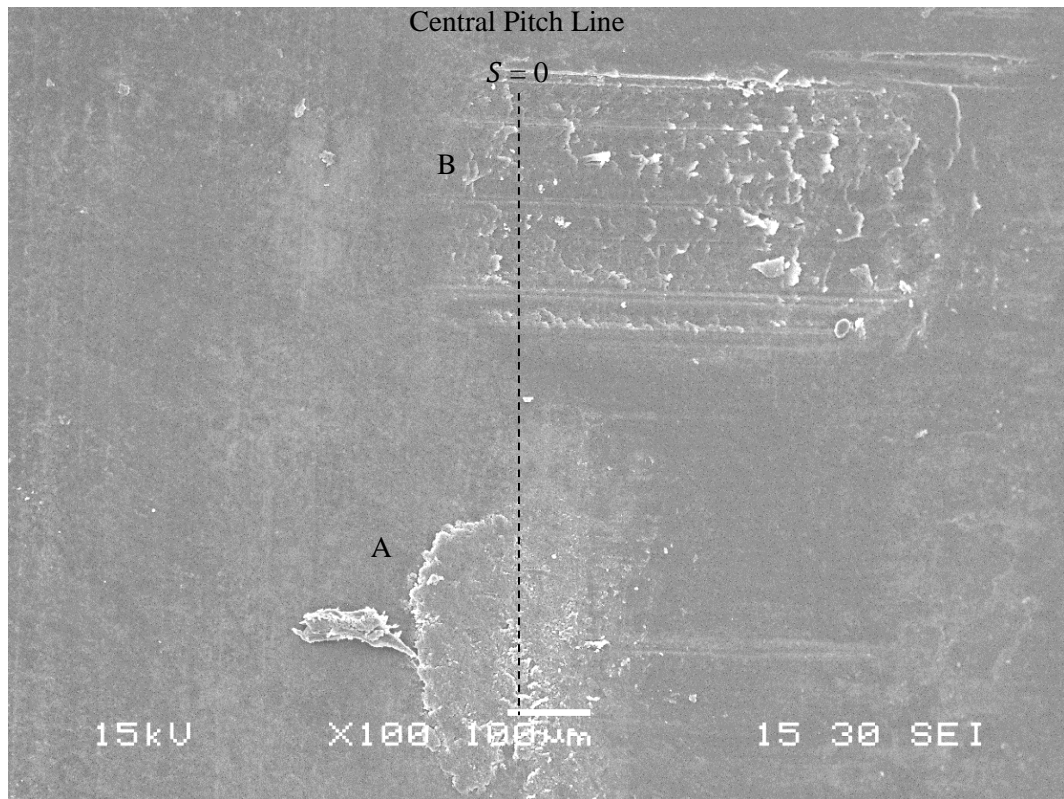
Figure 60: Polymer tooth observations at 50,000 Cycles, the maximum run in 1 day.

After the initial trial run to determine if the point at which the smearing mechanism initiates could be found, the next course of action taken was to run an experiment using the gear running experiment hardware for the maximum time allowable in a one day. This would complete a maximum of around 50,000 cycles. Figure 60 shows an image taken from this gear. The image is centred on the pitch point of the flank of the gear and shows a pair of features:

A. One is at the bottom of the image and to the left of the pitch line.
B. Another is at the top of the image and is to the right of the central pitch point.

Note that although the features are different in form, they are both pointing away from the central pitch point line. As previously discussed, the pitch line is the line on which the steel gear is in pure rolling and that the sliding reverses direction. These features illustrate this as they are pointing in different directions and so the only way they could be formed is if they were subjected to shear stresses of opposing directions. Also

worthy of note is that the feature (B) contains a number of smears, although they do not appear to be well defined. Feature (A) is larger and seems to be a macro version of the smaller smears. There is a slither of material that is almost detached from the leading edge of smear A. This is indicative of the potential wear mechanism.

5.6 Thin Gears
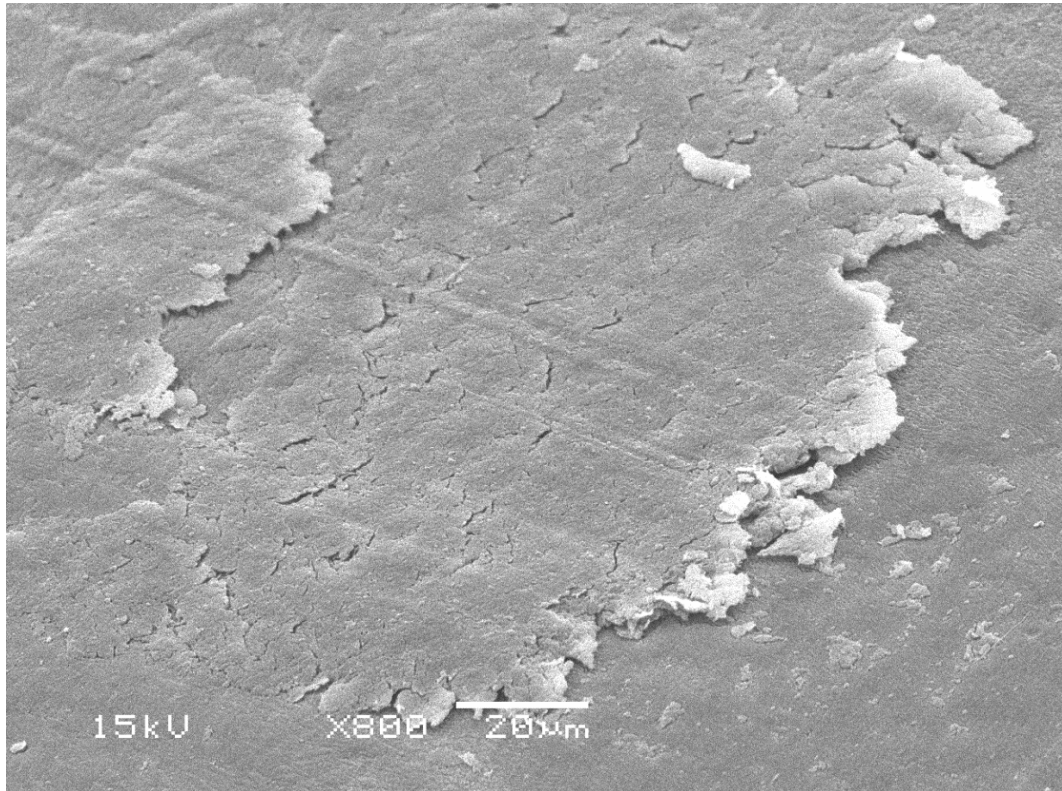
Figure 61: Thin gear tooth observations – increased pressure and speed

In an effort to accelerate the wear mechanism it was decided to thin down the polymer gears reducing them to a 1/3 of their original thickness. By using the same loading conditions as with previous experiments the resultant average pressure that the gear contact area was subjected to was therefore increased by a factor of 3. In addition to this, the speed at which the gears were run was also increased by a factor of 5.

Figure 61 shows an image of one of those thin gears; the sliding direction is from the top left to the bottom right of the image. The feature is similar in size, shape and apparent construction to smear A in the lower part of Figure 60. It is certainly not as

delicate in form as the originally observed smears (Figure 54) and is around 10 times the length with a rougher leading edge. There does appear to be material that has been removed from the leading edge.

It is clear that trying to accelerate the experiment has altered the outcome such that the smear features do not fully represent those from other experiments and from product durability testing. The original smear features seen in Figure 54 are smoother, more delicate and smaller in size to these new accelerated versions. The larger, rougher smears appear to have been constructed by a more vigorous action and it is proposed that there must be a relationship between the formation size and mechanical characteristics derived from speed and load. This may be proposed for further investigation beyond the scope of this research.

5.7   6 Million Cycles
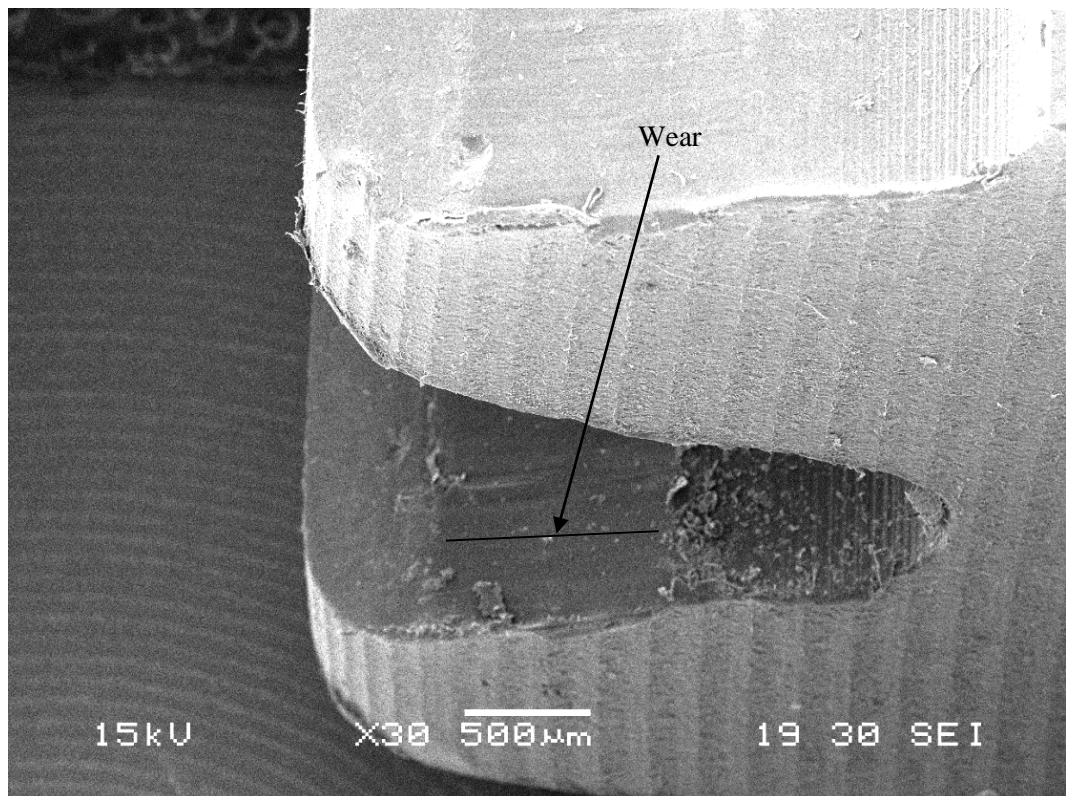
Figure 62: Large scale view showing the tooth wear pattern

The image seen in Figure 62 is included as it shows the wear pattern on the flank of a polymer gear tooth. A region approximately 1 mm long running from the centre of the tooth flank out towards the tooth tip is evident. In fact, the sliding of the steel pinion against the flank is also in this direction. Because of the high ratio between the two gears, the polymer gear has a far smaller contact region than the steel pinion. Machining marks can be seen in the root of the tooth and on the outer face of the gear. A quantity of debris is also seen in the root on the lower tooth in the image.

5.8   3 Million Cycles
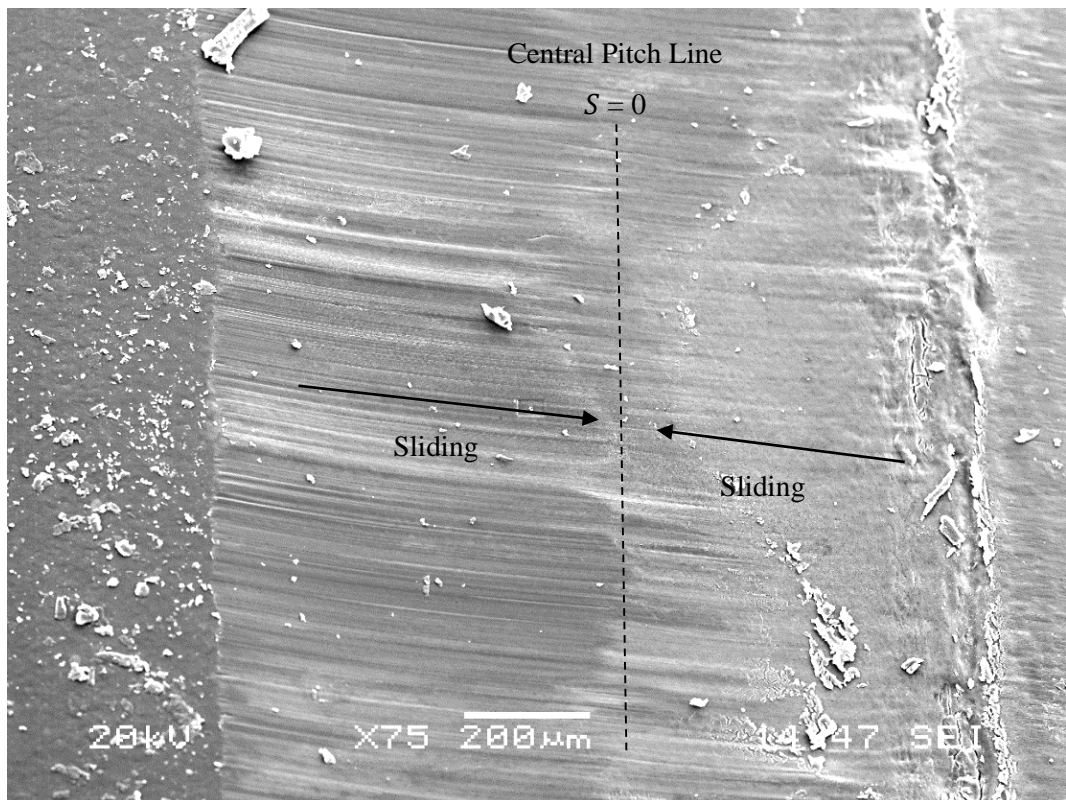
Figure 63: Whole wear field of the polymer gear showing the sliding directions and the pitch line position.

The image shown in Figure 63 is from a test gear that has completed 3 million cycles under load. It is taking from directly above the surface of the gear flank at the wear area observed in Figure 62. The rolling is from right to left, while sliding occurs towards the central pitch line. Although smeared material can be seen on the right hand side of the

wear area, debris has been ejected to the left. This ejection of the wear material is opposite to the sliding direction of the steel pinion against the polymer gear, but it is with the rolling action. From the scale of this image it appears that wear has taken place through abrasion only, however, the previous higher magnification images show that this is not the case and that material is being formed by the load and the sliding/rolling action generated by the gear teeth running together.

5.9   1.2 Million Cycles
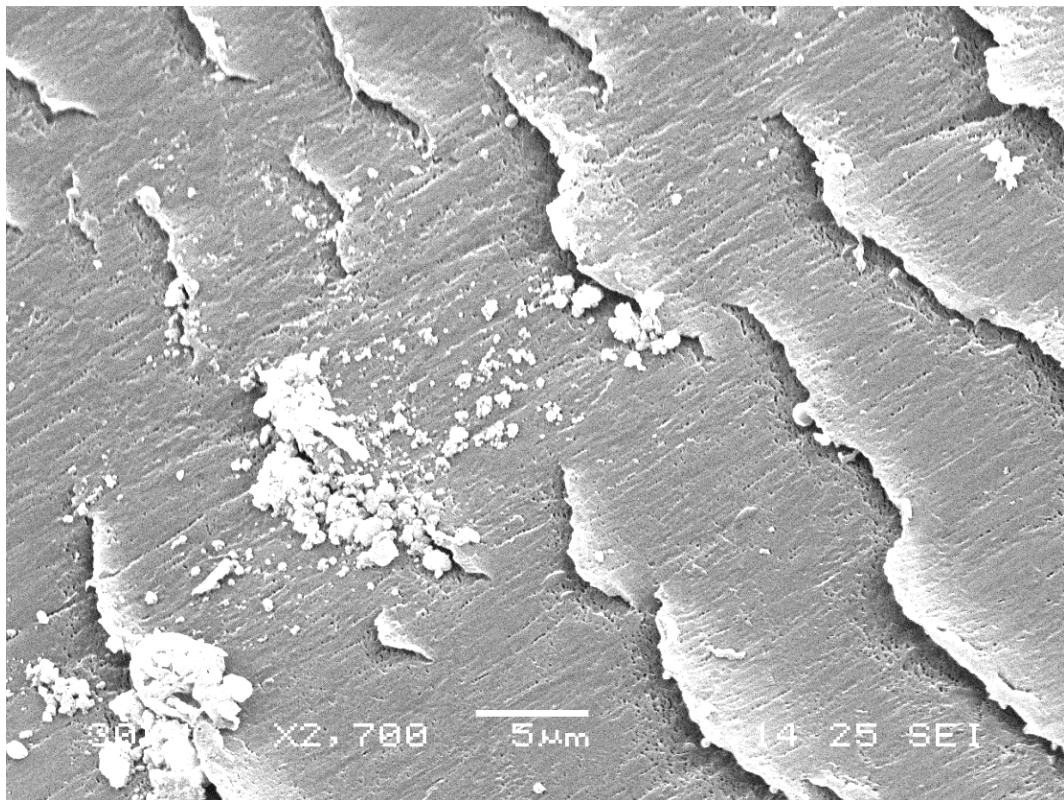
Figure 64: Debris breaks from the leading edge of a smear capturing the moment of material removal.

Figure 64 shows a number of smear features distributed on the surface of a gear tooth flank that has been subjected to 1.2 million cycles under the same load and speed regime as that of the product durability testing of Figure 54. The slip direction in this case is from the top right of the image to the bottom left. In the centre of the image a quantity of material appears to have broken away from the leading edge of the smear above and was in the process of being swept away by the mating steel gear. The event has been imaged

at a point just after the debris has detached from the leading edge of the smear but before it has been carried away by subsequent cycles of the gear. The smears are of the same order of size as the original smears, around 20 μm in length and are quite smooth and delicate as in the original (Figure 54). It would seem that the smears have been replicated by experimental methods, which reinforces the theory that they are created purely by the action of the steel pinion running against the polymer gear rather than by some other system influence.

Figure 65 shows another tooth flank from the same gear with similar smears to Figure 64. This image is particularly clear as there is no debris obscuring the features. Note that the surface texture of the material directly underneath the smear features is subtly different to elsewhere. It is proposed that this texturing of the surface sub-smear is due to the smear being forced down into contact with the material underneath it during each pass of the steel pinion. This supports the hypothesis that each smear is pressed and drawn, almost extruded, during each pass of the gear and it is this action that grows the smear and finally results in material breaking from the leading edge.
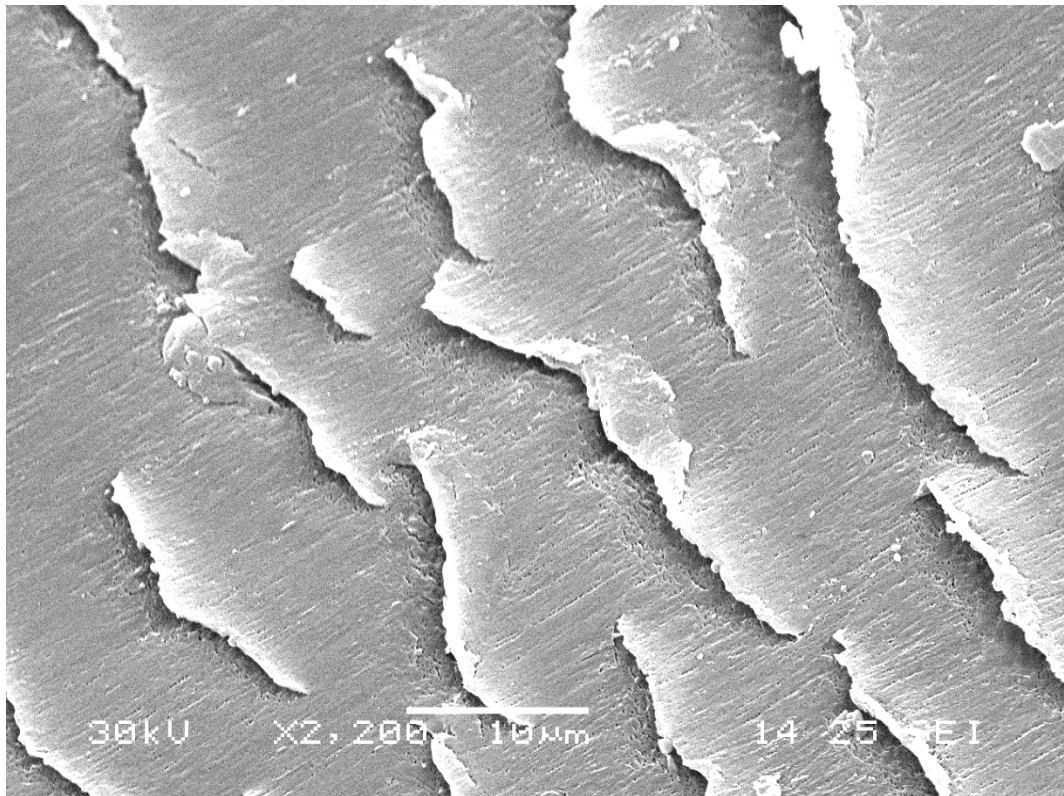
Figure 65: Smear field showing clear definition of flattened leading edges
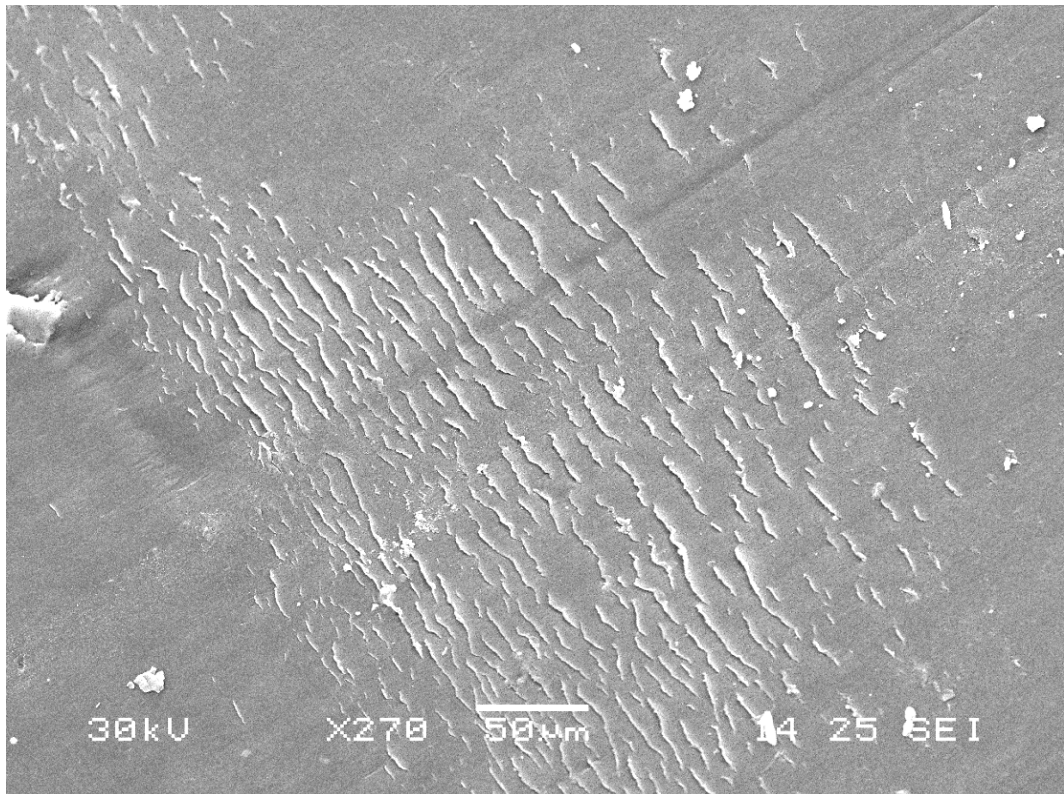
Figure 66: Smears vary in pitch as the sliding speed varies through the contact.

Finally, Figure 66 shows a larger scale view of one of the smear fields on the 1.2 million cycle gears and it allows an interesting observation. Again, the sliding direction in this image is from the top right to the bottom left and the pitch of the smear is reduced towards the bottom left. That is, the spacing between the smears in the direction of the sliding becomes smaller towards the bottom left of the view. This coincides with a decreasing slip speed to bottom left of the image.

The smears also become smaller as the slip speed decreases at the end of the contact. It is proposed that this is due to the roll angle becoming shallower as the slip speed decreases. This allows more smears to form under a larger contact area moving over the polymer with a reduced energy per unit area, thus the smears are smaller.

5.10 Profile Measurement

Gear teeth were scanned to record the exact shape and the quantity of material that had been worn away during operation of the 6 million cycle gears. This method was chosen over weighing the gears because it gives information on the worn profile, which helps in the understanding of the wear process. An additional concern with weighing is that the quantity of worn material will be very small in comparison to the full gear. Also, the use of gravitometric methods are susceptible to the effects of moisture absorption. This application is particularly unsuited to the use of the technique as experiments are conducted over a period of multiple days. As the quantity of moisture absorbed by the gear during the experiment would have been undeterminable, the technique of profile measurement was adopted. The process of scanning was, firstly, to take a tooth sample that had previously been prepared for the SEM work and then to use a profilometer to take measurements as a series of lines along the tooth from front to back. The gear tooth was mounted onto a pair of sliding tables arranged orthogonally so that the tooth could be moved in the x and z directions (Figure 68) to position the sample accurately for measuring. The profilometer used was Talysurf form measurement machine
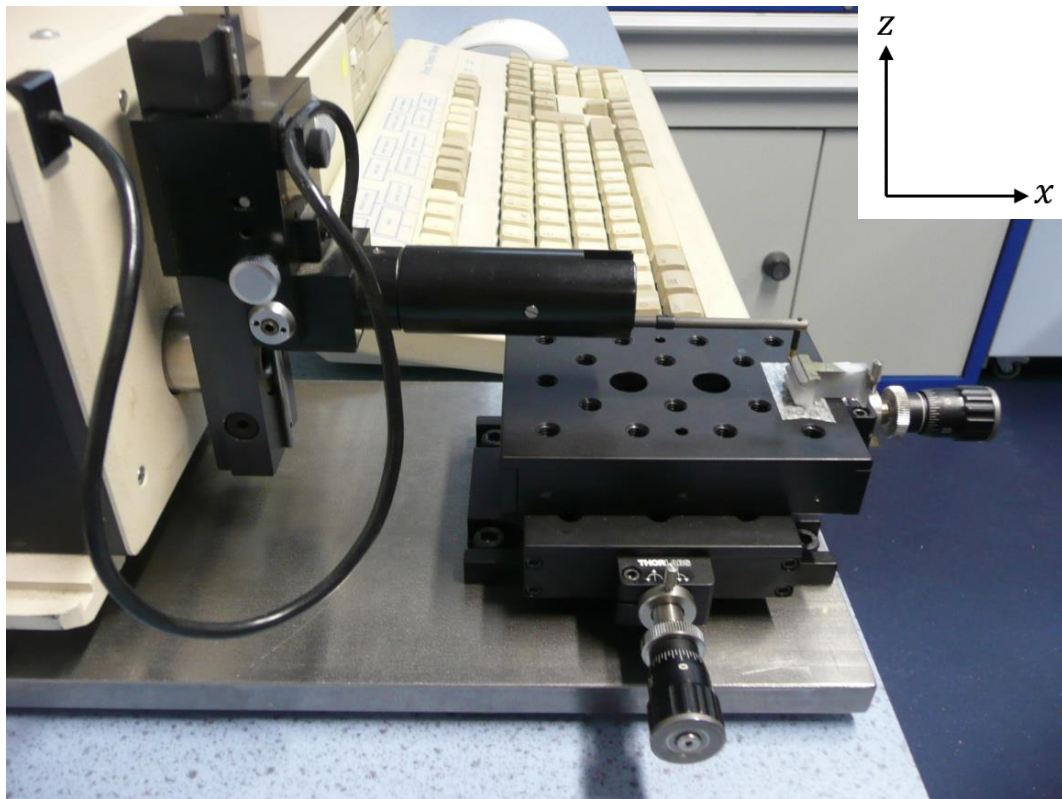
Figure 67: Talysurf form measurement and positioning of the sample gear tooth.

manufactured by Taylor-Hobson (a series 50 machine) and is shown in Figure 67. The profile measurement was undertaken along the x axis as depicted in the coordinate system in Figure 68 from the root of the tooth to the tip. The output from the Talysurf form measurement machine is in x and y Cartesian coordinates along the profile that the stylus had been moved. The profile length was 1.5 mm and 2, 000 data points were taken over this length. The profile data were then used to form the images of the three gear teeth that were scanned. A series of profiles were generated at distances of around 1 to 2 mm and were then swept together to form a solid model using the CAD system NX. The lighting has been manipulated to show more clearly the features on the surface of each of the gear teeth:

Tooth a) is from an unused gear tooth. The surface of this scan shows the machining marks from the manufacturing operation running in the y axis direction and it can be seen that the profile is consistent along the y axis.

Teeth b) and c) are scans of teeth that have been worn by 6 million cycles and the worn profile can be seen as markedly different from the unused gear tooth. There is a bias in the wear towards the left hand end of the teeth suggesting a slight misalignment in the mounting of the gears or deflection due to load.
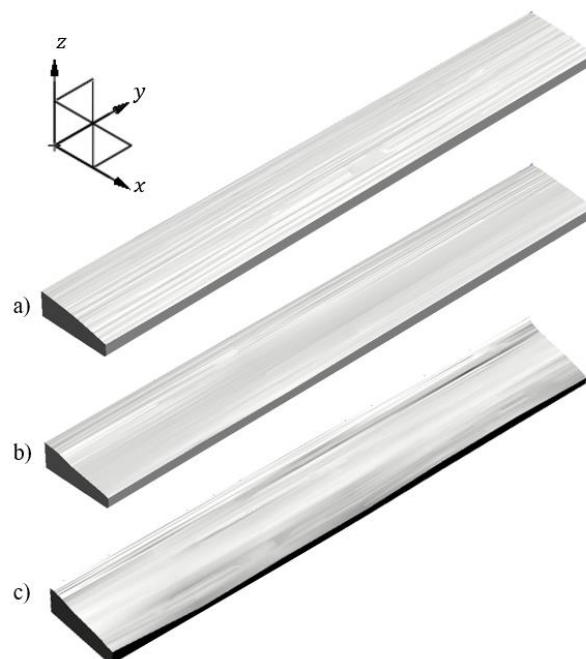
Figure 68: Scanned polymer gear teeth
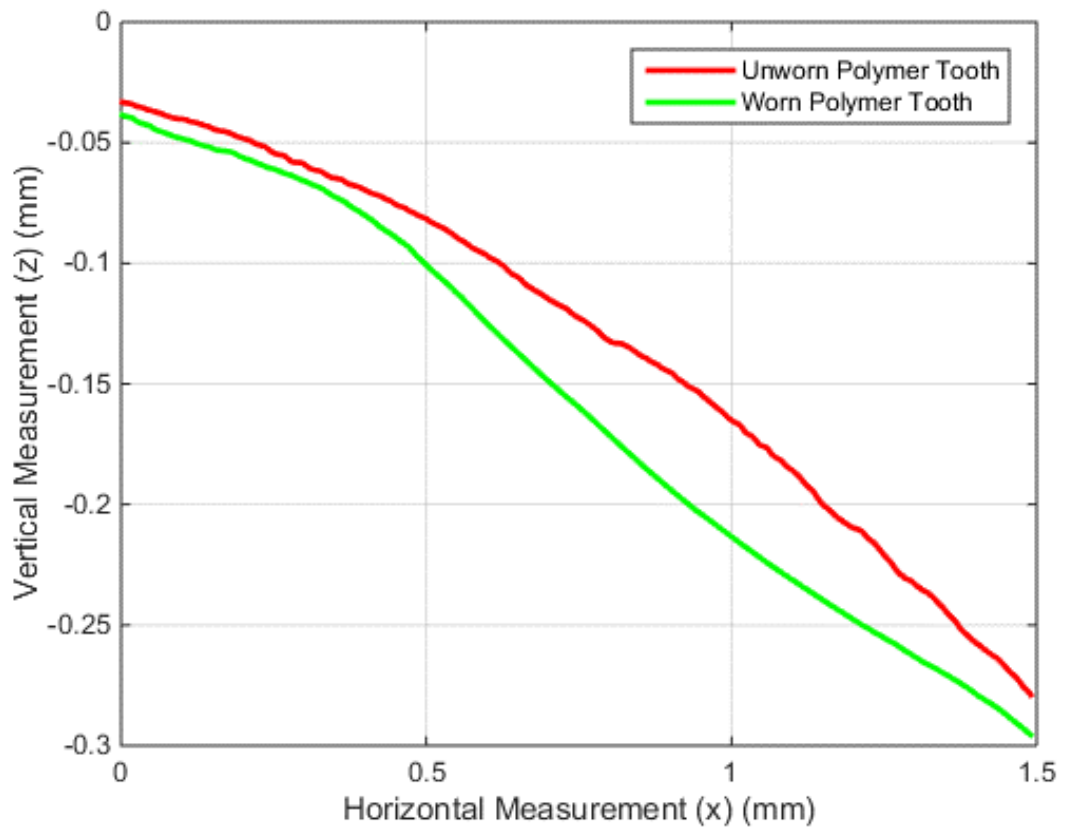
Figure 69: Polymer gear profile measurement results.

Figure 69 shows profilometer data taken of the worn and unworn polymer gear teeth. Four data sets have been averaged to give a normalised view of the wear across the teeth. These four samples were available from the sample preparation as described in Section 5.1.1. The red line shows the unworn, new teeth profile, while the green line shows data from teeth that have undergone the durability testing of around 6 million cycles. The traces were aligned at the left hand end where the tooth was untouched and therefore unworn. At the midpoint of the flank there is approximately 50 μm of wear and that the area between the 2 curves is approximately 0.035 mm^2. Given the contacting nature of the profilometer measurements a consideration of creep must be made. The profilometer stylus is designed in such a way as to produce a force as small as possible in order to maintain good contact with the work piece during the profile sweep. This being the case of this instrument, this is < 0.1 mN. The diameter of the stylus is 5 μm, therefore an assessment can be made of the likely pressure exerted on the polymer as the stylus is moved across the gear tooth. The radius of contact of the stylus is given by:

$$a = \sqrt[3]{\frac{3Fr}{4C_E}} \qquad (52)$$

where a is the radius of contact, F is the normal force of the stylus contacting the polymer, r is the radius of the stylus and C_E is the material property value previously calculated in equation (17). To a first order approximation, the stress developed can then be expressed as F/A from the calculation of a, which gives a value of 26.3 MPa. From the material table presented in Section 2.4 a value is given for the deformation under load of 0.7 % for a given pressure of 13.8 MPa. Therefore, there is a probable error of measurement using this method of approximately 1.3 %.

5.10.1 Steel Gear Profiles

The gear teeth of the steel pinion were also measured to ascertain whether wear had occurred. This was the case, although to a much lesser extent than that of the polymer gear teeth, particularly considering the ratio between the two gears makes the steel pinion act a multiple of 6.25 more cycles than the polymer. Figure 70 shows the profilometer data taken from a steel pinion that had been run in the product durability testing actuator. A series of 7 measurements were taken of both the worn side of a selection of teeth and the unworn side also in the same manner as was done for the polymer gears. These data sets were then averaged to make a single data set of the tooth profile. The two sets of data have been aligned such that the central part (where $x = 0.65$ mm) of the curves are coincident, which represents the pitch point line of the tooth flank. As there is no sliding and only pure rolling here, minimal wear only should occur. Thus, the wear at each end extents of the teeth is around 20 μm at a maximum and the area between the curves equates to approximately 0.008 mm². Taking into account the ratio between the pinion and gear, this means that the polymer has worn by a factor of around 27 more than the steel by comparison of the depth of penetration of wear between the polymer and the steel.
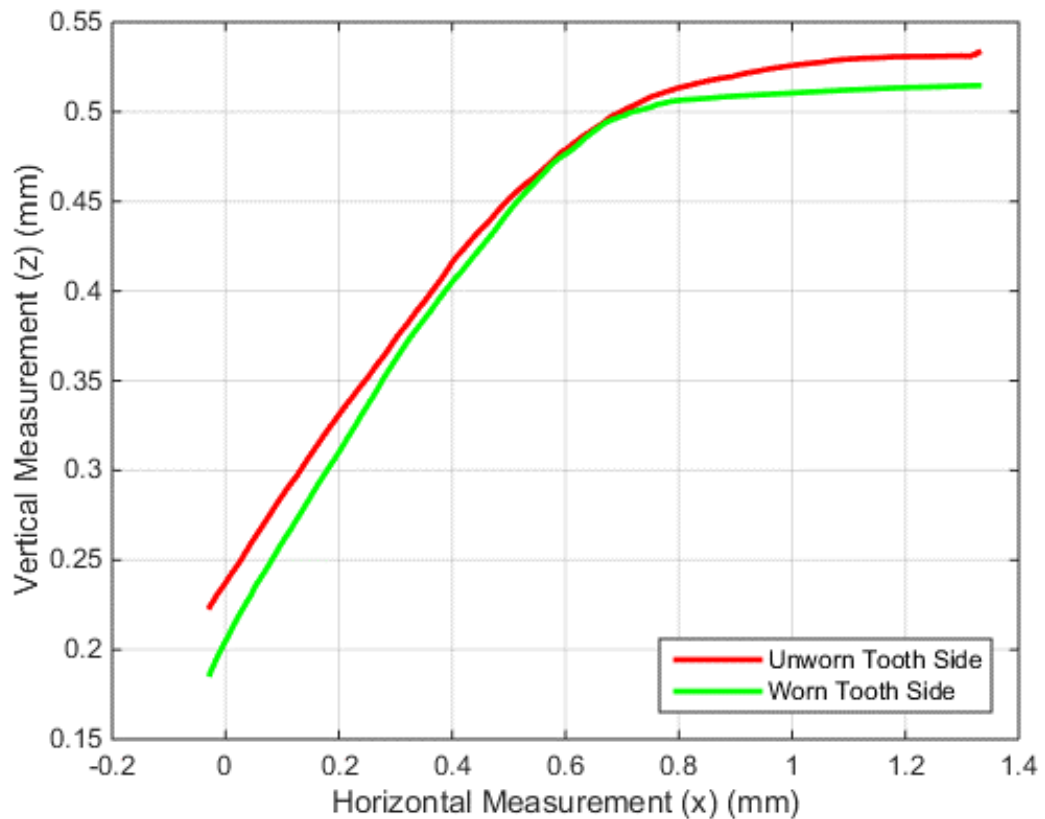
Figure 70: Steel gear profiles measurement results.

5.11 Discussion of Experimental Observations

A technique has been developed for preparing samples of polymer gear teeth in such a way that they can be imaged using the SEM and that their profile may be measured to assess the level of wear. During the development of this process a new mechanism of wear has been identified on an industrial product (the Rotork CVA), which was also replicated in the laboratory. This replication confirms that the wear mechanism was not an isolated event and also that it could be repeated independently of the product assembly and environmental conditions. The experiments conducted were done so in a systematic way as to capture the emergence and growth of this wear mechanism. The aim was that, by a gradual increase of the load and cycles, the instant at which the smears appear and then grow would be captured. In reality, this smear creation instant was not captured. However, the smears were observed many times, repeatable under different load conditions and cycle numbers.

The smears are produced by the action of the steel pinion running over the polymer gear surface. It is proposed that the smears are formed and are grown by the repeated cyclic action of the pinion running over the surface such that the smears become elongated and flattened to such an extent that the ends break away as small polymer debris particles. This has been captured in the laboratory and is seen quite clearly in Figure 64. The debris is small and, anecdotally, is seen as polymer dust that forms around the gears as they are used. This fine dust that has been removed from the polymer gear teeth will have been trapped between the steel and polymer teeth for a period of time before it was ejected from the mesh. It is likely that this debris is the cause of the small quantities of wear that have been measured on the steel gear teeth. Chapter 2 describes the geometry of the involute and how a variable slip speed across the contact sweep between the gears is developed. It also describes the rolling action in relation to this variable slip speed. The observations made in this chapter may now be described by a phenomenological model in the following chapter.

5.12 Consolidation of Chapter 5

The smears shown in Figure 54 have not previously been identified and documented in the open literature. As discussed in the opening chapter of this thesis, similar features have appeared in individual journal articles, but they are described as lateral cracks and are not treated as potential wear mechanisms. Certainly, the way that they are created, grown and subsequently result in wear material forming has not previously been investigated or developed.

It is proposed that these smears and the way that their failure removes material from the surface of the gear represent a new and previously unidentified wear mechanism specific to polymer spur gears.

The following and penultimate chapter of this thesis discusses the various methods that may be employed to model these features and so to predict their formation.

CHAPTER 6

Modelling of Polymer Smearing and Wear

In this chapter various techniques to explain the creation of polymer smears are presented. Numerical and analytical techniques are utilised, but a completely definitive model is beyond the scope of this thesis. This is partly because there are so many variables involved with the creation of the smear features. Also, there is disconnect between the micro scale at which the features are occurring and the macro or bulk scale strains that generate the smear features. Thus, at least two models are required.

Two modelling techniques are employed. Firstly, the stress distribution and profiles are investigated using finite element (FE) techniques. Secondly, a phenomenological model is developed that describes the creation of the smears and the quantity of material that is worn by them.

6.1 Discussion of Contact Modelling Techniques

Emphasis is made on the physical structure of the polymer and how this affects its performance under loaded contact. This approach has been taken in part due to the features observed on the surface of the worn polymer. When FE techniques are considered in the assessment of deformation of materials it is usually under the assumption that the material is homogenous and can be treated as a continuum. In that case, such as the treatment of static stress analysis of steels under elastic deformation, breaking the bulk material down into basic three dimensional elements makes sense. In fact, the tetrahedral three dimensional element type commonly used in FE analyses is actually quite closely matched to the body centred cubic crystalline formation of steel itself. For a polymer this is not the case. The bulk of the polymer is made of chains (not prism-like crystal formations) and they are interlinked in a semi-random semi-crystalline

way that means the chains must move together in an entirely different way to that used in traditional FE. Therefore, a new way of modelling these materials must be sought. The FE models investigate how the stress is distributed through the polymer in loaded contact, but do not give any indication of how the material is actually deforming. They are viewed in conjunction with the phenomenological models to more comprehensively describe how the material deforms under loaded contact.

In addition to the problem of how to model the bulk of the material there also exists disconnect between the large and small scale effects of contact and load. If a detailed model could be produced that accurately describes the material properties at the polymer chain level then the resolution would be too great to apply to a real scale large component. The approach taken is to investigate the stress distribution using FE tools (and by experimental observations as previously documented) and to develop phenomenological models to describe the micro scale deformations.

FE model assumptions:

The main assumption used during FE modelling was that the material bulk is homogenous and elastic.

Phenomenological model assumptions:

There are a number of assumptions made in the models, namely the percentage area of material that is really in contact and the percentage area that is a smear to be failed. Greenwood and Williamson (1966) provide a substantial theory on the statistical quantity of asperities in contact at a surface interface and they find that this value is very low in comparison to the perceived area of contact ($< 1\%$). The phenomenological model assumes this area to be 15% and although this is a much higher figure than determined by Greenwood and Williamson, their work was concerned entirely with hard metallic surfaces and in this case the polymer will deform significantly and plastically under the load to give a far greater real contact area. This constant value should be validated through further research, but due to the necessarily statistical nature of the work required to validate this constant, it is beyond the scope of this thesis.

6.2   Finite Element (FE) Models

It has been stated during the introduction that FE analysis has limited use when investigating the micro scale events that happen at a contact interface. This is due to the very different scales between the bulk material and asperity properties. However, the technique can still be used to inform on the stress distribution through the material due to contact. The following sections document various models that were constructed to do this, the strategy of which was to look first at the normal contact, then to investigate the inclusion of an asperity into that contact. An attempt was made to develop a dynamic model that could be used to model the complete system, but the computational time required to solve it would have been too great to complete in any reasonable time period.

The main problem encountered whilst developing a FE model to investigate the sliding of the steel tooth face against the polymer tooth face was one of constraints. Any FE solver requires a convergence of solution with respect to boundary and initial conditions. Unfortunately, with this problem there is not a convergent solution in that the steel continues to slide over the polymer. By definition, there is no convergence as the process is continual. However, various methods have been used that have yielded interesting results. In general, the models presented are dimensionless unless the specific stress values are of interest. The stress distribution is generally the important factor in these investigations.

6.2.1   Normal Contact

Three discrete points through the gear contact sweep have been chosen for the following FE analyses. They are approximately at the beginning, middle and end of the teeth contact sweep and show how the geometry changes over this travel and how the geometry affects the stress value and distribution in the polymer. The parameters for the analyses along with the maximum stress results from the models are shown in Table 9.

Table 9: Discrete points in the contact sweep for FE contact analysis

Steel Diameter (mm)	Polymer Diameter (mm)	Load (N)	Stress (MPa)
2.004	27.752	0.0282	78.71
4.504	25.252	0.0282	52.68
6.004	23.752	0.0282	46.08

The analyses were performed using the NX Nastran solver SESTATIC 101 and the models were identical apart from the differing radii. The models were constructed as an array of brick elements 0.0025 mm thick and so the load was adjusted down accordingly to give the correct pressures for the real gear pair at 12 mm thickness.
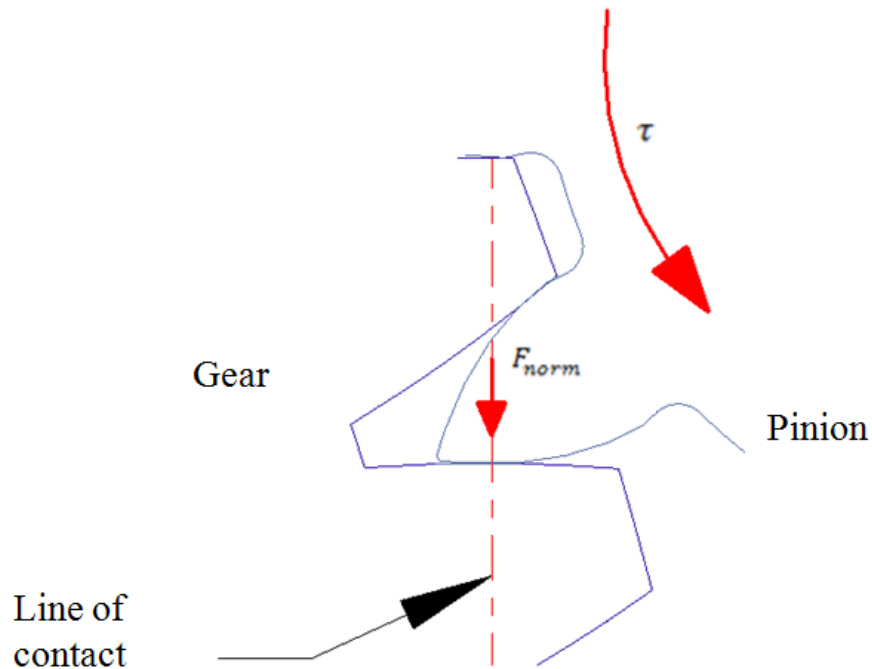
Figure 71: Basis of the FE model from the geometry of contact between the teeth.

Figure 71 shows the basis for the FE model. The steel pinion is driving the polymer gear with a given torque. This driving torque results in a force between the steel pinion and the polymer gear at the contact interface and is normal to the interface. The FE models were created to represent a small area just around the contact point with the upper portion being the steel and the lower being the polymer. The FE model is constrained in

such a way as to allow vertical motion of steel whilst the polymer portion is fixed at its base. A contact condition, including coloumb friction is set between the two faces.

Units = N/mm^2 (MPa)
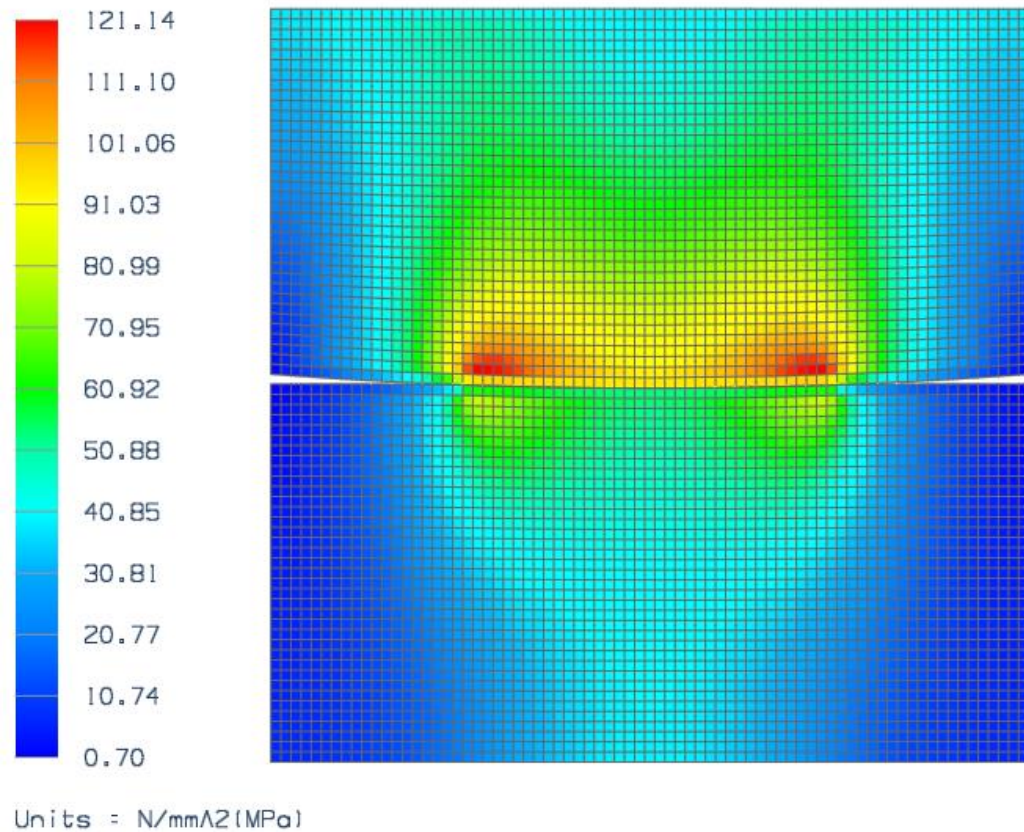
Figure 72: FE results of the contact model showing stress distribution (von Mises) due to loading contact between the steel tooth (upper part) and the polymer (lower part).

Figure 72 shows the von Mises stress developed between the steel pinion and polymer gear at a distance along the line of contact of 1.05mm due to normal load. This is when the steel pinion just comes into contact with the polymer and first starts to drive the tooth. The stress distribution can clearly be seen as concentrated in two separate areas symmetrical around the point of contact. The upper body represents the curvature of the steel pinion at this contact point and the lower body represents the polymer. Because of the large difference in stiffness of the two materials, there is a larger contact area than with standard Hertzian contact and so stress is developed at the edges.
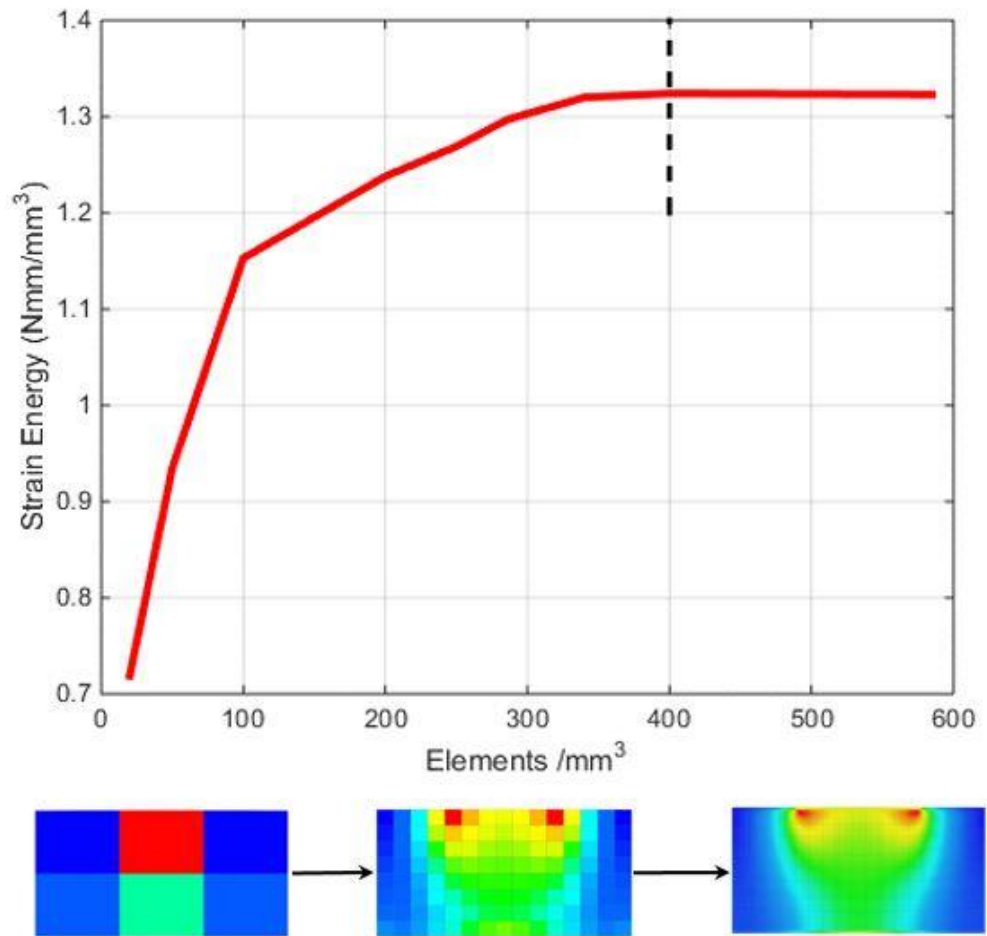
Figure 73: Solution convergence for a series of mesh densities for FE models shown in this section - black dotted line shows the final solution mesh density value

Figure 73 shows the results of a stress convergence study performed on the FE model shown in Figure 72. The solution convergence was determined by strain energy to ensure that an appropriate mesh size was used and it can be seen from the figure that the solution converges at around 350 elements/mm^3.Therefore 400 elements/mm^3 was the mesh density used for the following studies in the normal loaded case.
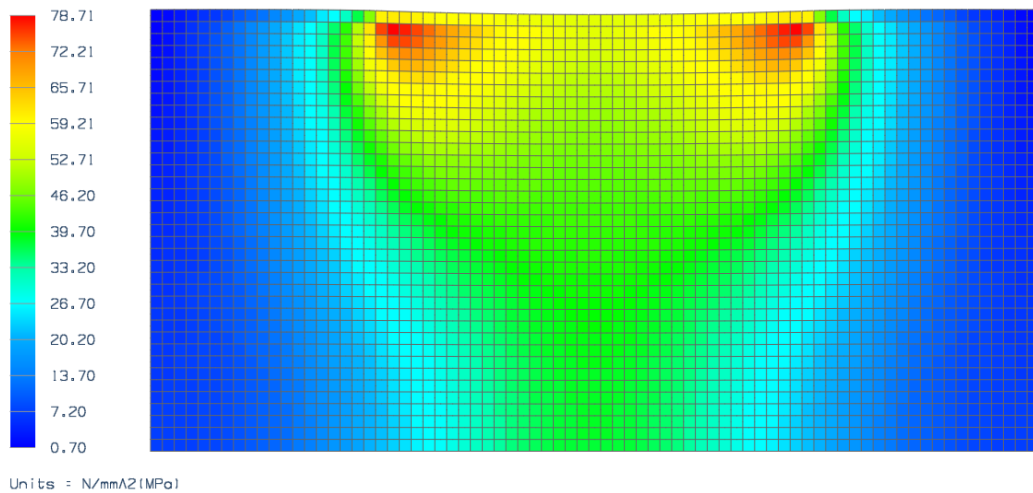
Figure 74: Stress distribution (von Mises) at the beginning of contact   - polymer only

Figure 74 shows the von Mises stress distribution in the polymer only at the beginning of contact, with the maximum stress is 78.7 MPa.
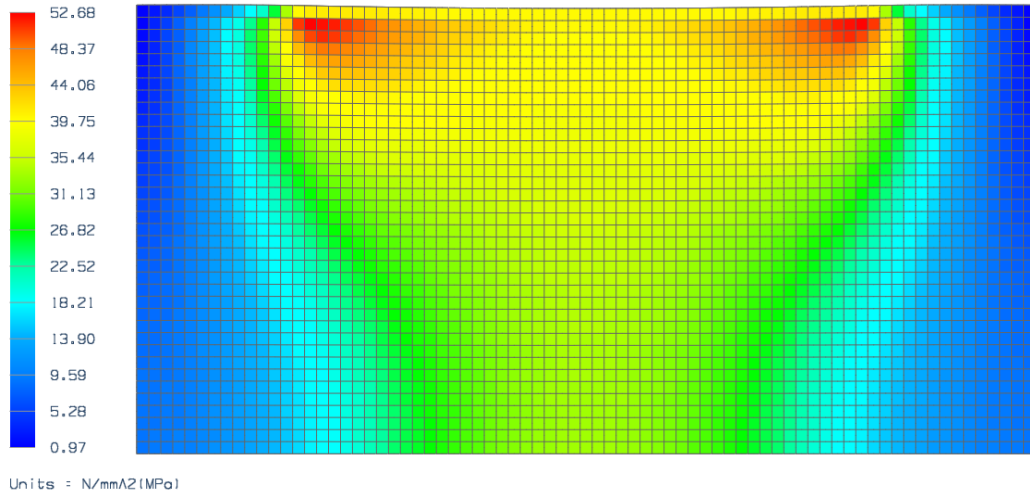
Figure 75: Stress distribution (von Mises) at the middle of the contact duration

Figure 75 shows the von Mises stress distribution when the teeth are in the middle of the contact sweep. Two distinct stress areas are again visible in the distribution; this is because the polymer is deflected heavily under the load. Deformation (and therefore strain) is large relative to neighbouring material that is not under the contact. The load

reaction is therefore highest at these points. Figure 76 shows the von Mises stress distribution when the pinion and gear are at the end of contact just as the steel pinion is about to lift off from the polymer gear. The two distinct stress areas are further apart now and so there must be a relative movement of the maximum stress areas as they move across the surface of the tooth through the contact sweep. As the polymer tooth is driven, the stress distribution changes to two distinct areas that move apart as the teeth move through the stroke. This must give rise a stretching of the material at the polymer surface. There is also a decrease in the maximum stress as the contact area increases as would be expected.
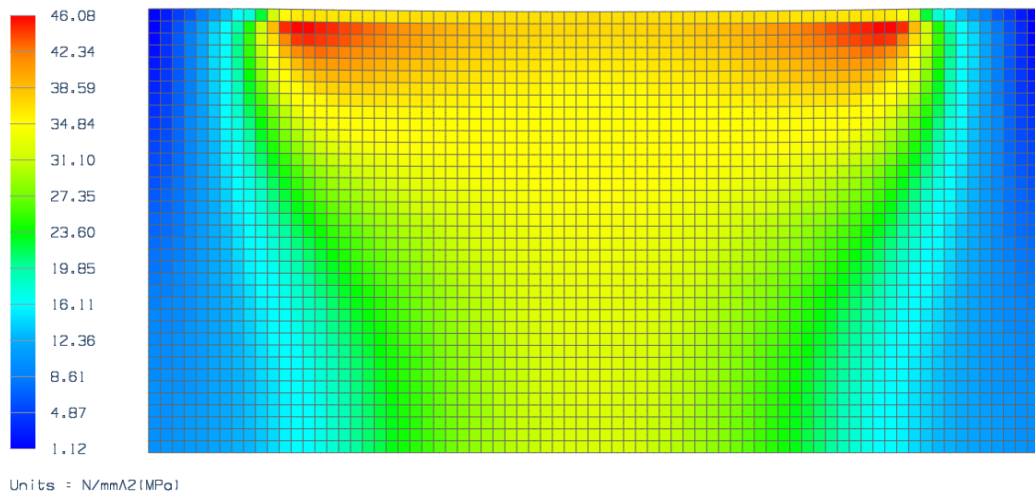
Figure 76: Stress distribution (von Mises) at the end of the contact duration

6.2.2 Speculative Stress Distribution Models

Various FE models were constructed to describe the contact conditions as the steel pinion slides against the polymer surface. However, the models are taken no further and are used only as an indication of how the stress is distributed in the polymer for a given contact scenario.

6.2.2.1 Normal and Tangential Loads
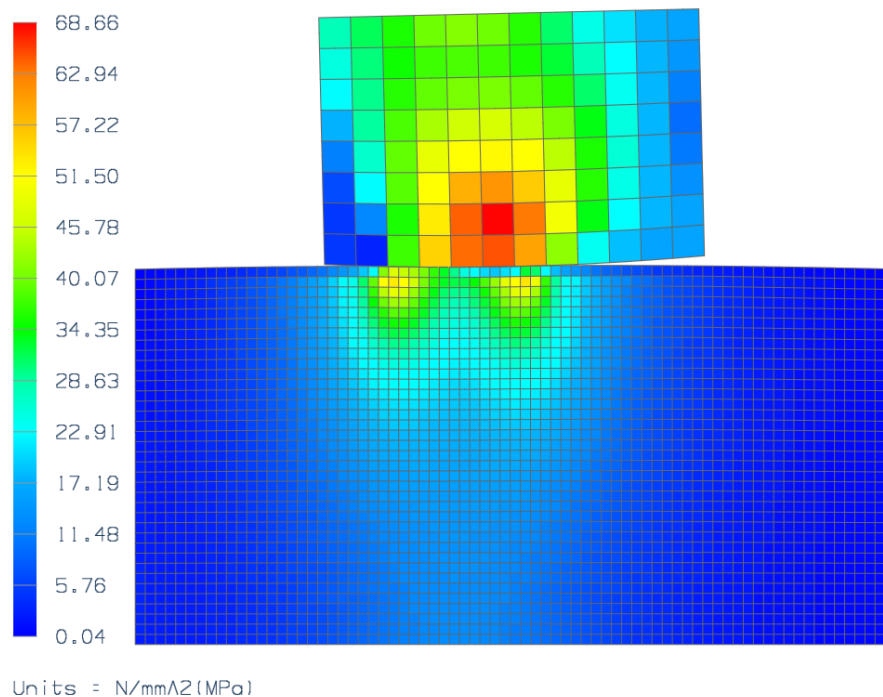
Figure 77: Stress distribution (von Mises) due to normal and tangential loads

In the model results shown in Figure 77, a load has been applied to the top of the steel upper part and a contact set is made between the two faces. For this scenario, the FE solver seeks a solution that satisfies the boundary and initial conditions. Time stepping is used as a way to find solutions between the start and end points of the analysis, but rather than being a dynamic solution this technique is simply a series of static solutions. There is also a load applied to the steel upper part in the direction from left to right, hence the steel

part has moved to the right. The mesh density used for the polymer is the same as in previous cases, however, the mesh density has been reduced for the part to save on computation time. This was necessary due to the number of time steps required for the solution. This action is justified as the steel is two orders or magnitude stiffer than the polymer and it is the deformation of the polymer that is under investigation. The model is solved as a series of time steps and Figure 77 shows the final solution step. The stress distribution in the polymer can be seen to be formed in the direction of the tangential load in addition to exhibiting the same double stress area distribution pattern as seen in the previous normal load only case.

6.2.2.2   Surface Energy Contour
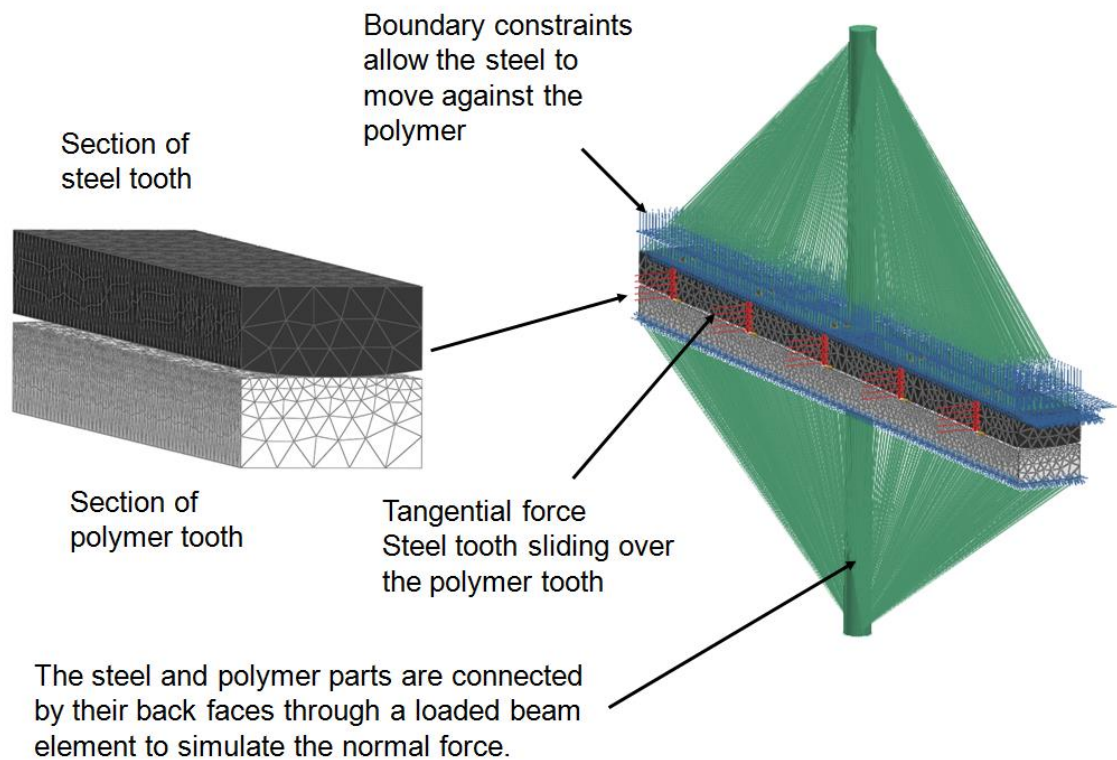
Figure 78: Surface contour stress model construction.

In Figure 78 the construction of a model is shown to investigate the surface stress across the tooth face as the steel rubs across the polymer. This was done to evaluate

whether stress is completely uniform across the width of the teeth or whether there is some distribution due to the width. The specific values of stress are unimportant in this case as it is the distribution that is under investigation.

The model is of the whole width of the tooth rather than a 2-dimensional representation to determine the stress across the whole length of the contact. Two solid sections of teeth can be seen, the black is steel and the white is polymer and they are connected by spider elements to a node above and below each. The spider element ends are then connected by a beam element to which a tensile load is applied and as there is a contact set between the faces of the steel and polymer this provides the contact pressure. The side load can be seen applied to the steel (in black) across the direction of the normal contact load. If the transverse load is not greater than the product of the normal contact and the coefficient of friction between the steel and polymer, then the solution of this model is stable and a convergence is found. Once the model was solved, the stress values along a line through the centre of the contact area were extracted from the FE results file for inspection.
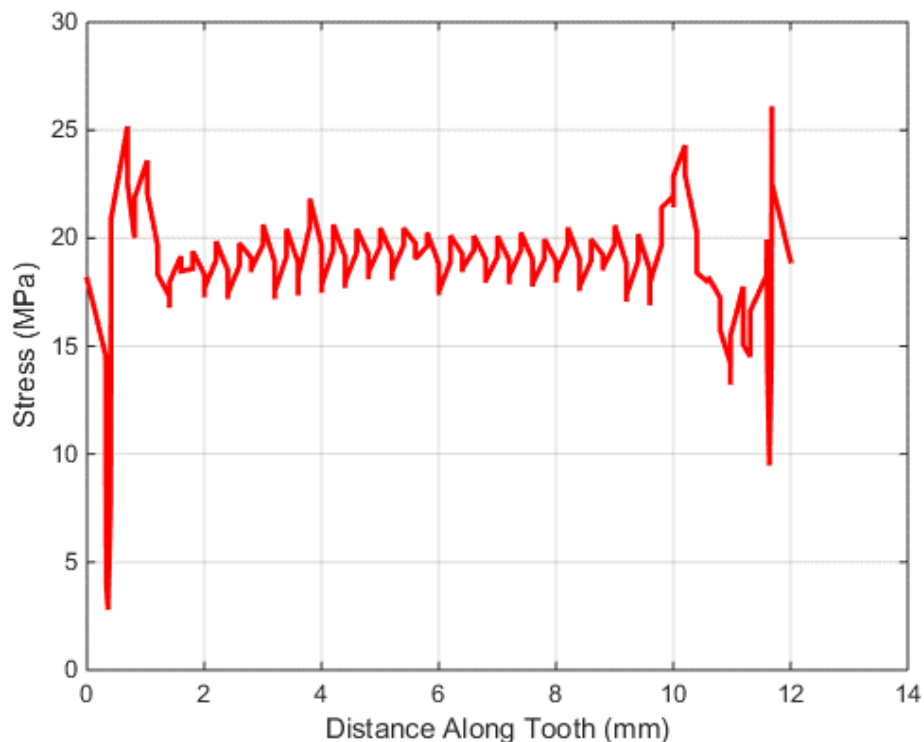
Figure 79: Stress values plotted for teeth contact

The plot shown in Figure 79 is of the stress values along the centre of contact on the surface of the polymer tooth from left to right. The data set is shown in red and a large

spike on the left hand and right hand extents is present, which is due to the edge effect in the model. As the elements at the left and right hand extents are not supported they experience much more strain than the elements inboard and so have a larger stress associated with them. This analysis was done to determine if there is a distribution of stress along the line of contact as this could affect the way the surface features are formed. Although the stress appears to be shown as higher at the edges, as discussed, this is due to edge effects of the model.

6.2.2.3   Polymer Chain Finite Element Model
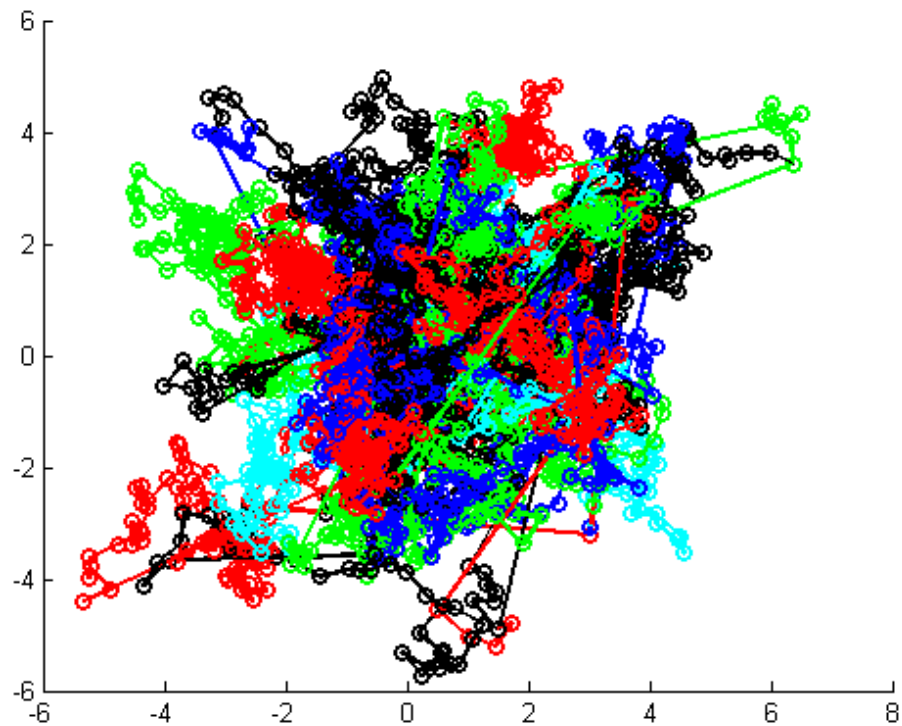
Figure 80: Polymer chain model: Random walks

A FE model to represent the real structure of the polymer chains can be conceived of that is constructed entirely of beam elements connected as pin-ended joints to represent the micro structure of the polymer. The pin-ended beam elements would be arranged in separate chains intertwined in a manner that replicates the pseudo-random semi-crystalline nature of the micro-structure of the polymer. This method of producing the basic geometry of the intertwined polymer chains has been adapted from the idea of random walks by Weiss (1983) where randomised functions are used to create systems or

processes that mimic naturally occuring phenomona. Figure 80 is a plot from a basic MATLAB model to generate a point cloud and then connects some of these points as individual chains of beam elements. Each individual coloured chain of elements represents a separate polymer chain. This representation could then be transferred to NX to be meshed as a FE model with appropriate boundary and initial conditions. It could then be solved for a variety of input loading conditions. However, although the initial joined up point cloud has been generated, to make the transfer to NX and do the other various meshing and connection tasks to make this a workable model would be a considerable undertaking. Also, the model would need to be very large containing many millions of chains to be capable of modelling a surface contact. In addition, the contact conditions of the solver would multiply the scale of the calculation further. It is an interesting idea that should be considered for the future.

6.2.2.4   Rotating Contact Iterative Model
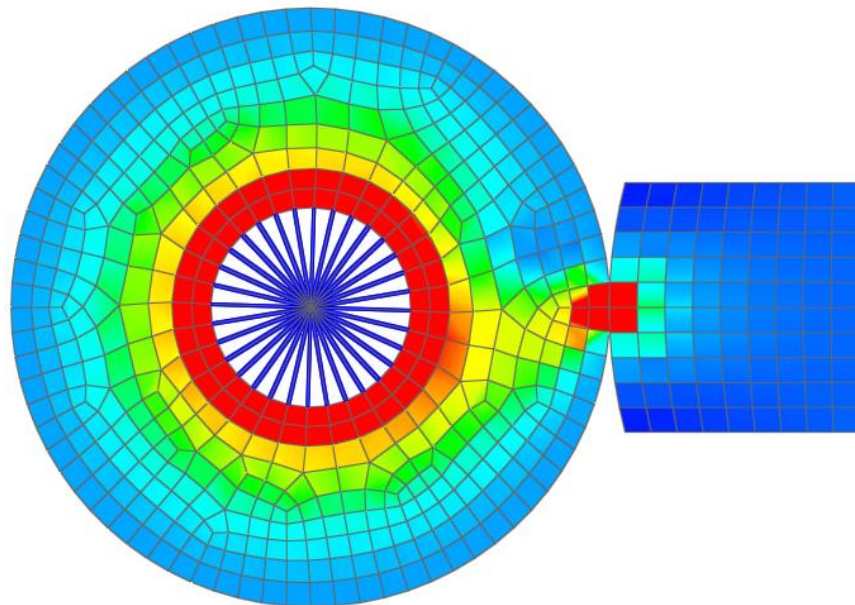
Figure 81: Stress distribution (von Mises) due to rotating contact

The model shown in Figure 81 should be considered as proof of concept alongside the polymer chain model described in Section 6.2.2.3. The mesh density is coarse but shows a method of driving one surface against another to simulate the contact conditions during the teeth contact. This model is too coarse to provide any useful information about the micro-contact mechanics at the interface between the steel on the right and the

polymer on the left (a disc). Time stepping has been used to rotate the polymer disc at a fixed speed; the steel block on the right has a load applied on the right forcing it onto the surface of the disc. A contact set is formulated at the interface with a coefficient of friction of 0.35. As the model uses time stepping it solves the contact problem at each interval. Due to the solver used (NX Nastran Non-linear 601), if the material is taken beyond its yield stress, the resulting deformation will remain as the disc surface has passed the contact point. As the disc is in constant rotation and a solution is found at each time step, then the solution is valid. In theory, the disc could be made to rotate as many times as required to simulate the real gear case (for instance many millions of cycles), however, the output file would be large beyond the capacity of the software. The input and solution files for the above model for a single rotation were 88 Mb in size, multiplying this by the 12 million cycles requires over 1 Gb of data. However, this does not account for any mesh refinement and the model element size is around 0.25 mm so would need a great deal of refinement. Even a conservative estimate of refinement would increase the file size by 1000, making the result and solution file 1 Tb, which is beyond the capability of the software.

In addition to this idea, the previous modelling concept of a random molecular chain as described previously could be combined with this rotating contact iterative model to produce a truly representative model of the contact mechanics of a polymer. The model was solved for a single rotation and was constructed with very coarse elements of around 0.25 mm^2, it took approximately 4 hours to solve using a modern single core processor computer. Given that the polymer chains are around 200 nm long the resolution of a single element within that chain must of the order of 1 nm and it would be necessary to solve millions of rotations to reach a representative solution.

6.3 Phenomenological Models

Models are presented in this section that are derived from the real physical phenomena observed through the SEM techniques. They are developed based on the real microstructure of the material and how the contact between the two surfaces is developed.

6.3.1 Polyoxymethylene (POM) Microstructure
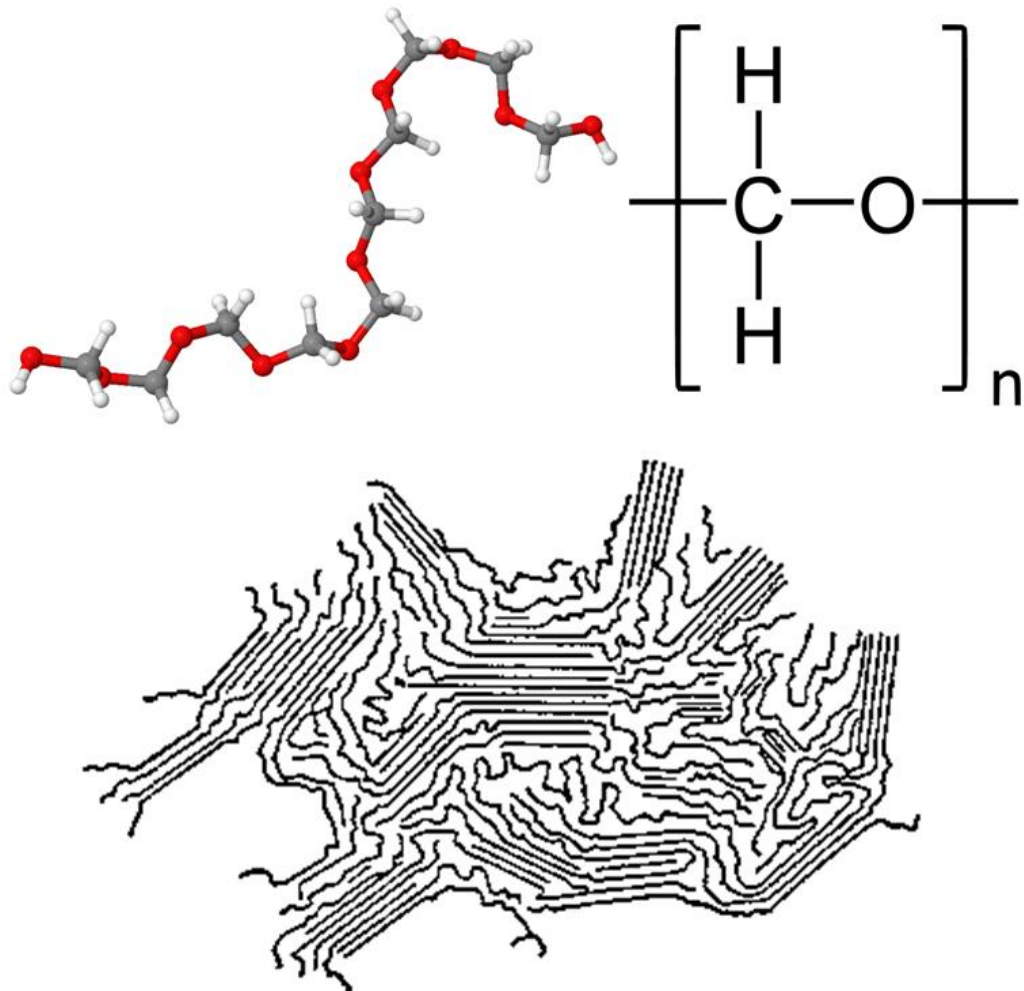
Figure 82: PolyOxyMethylene structure

The polymer used to manufacture the gear that has been focused on throughout this thesis. This is a thermoplastic semi-crystalline polymer with the name Polyoxymethylene (POM) and in the case of the particular gears studied is manufactured by DuPont. It is frequently used as an engineering polymer, is reasonably strong, inexpensive, and has good flow characteristics for injection moulding manufacturing. Its wear characteristics are not as good as some other polymers such as PEEK, but it does have a low coefficient of friction with steel. The bulk of the material is made up of polymer chains of around 200 nm in length, which are distributed throughout the material in a semi-random, semi-crystalline fashion, hence the descriptive name.

Figure 82 shows a graphical representation of part of a polymer chain, the chemical symbolic for POM, and also a schematic of how the chains are arranged in the material. They are semi-random with some chains in a crystalline shaping. The schematic is necessarily 2-dimensional, but clearly the chains are arranged like this in a 3-dimensional structure throughout the body of the material. The polymer therefore has a complex 3-dimensional construction on a scale that must affect the physical bulk properties and the way the material performs under loading and contact. This idea has been used to formulate techniques to model the wear, deformation characteristics, and smearing of the material. It is the subject of the remainder of this chapter.

6.3.2   Smear Creation Model
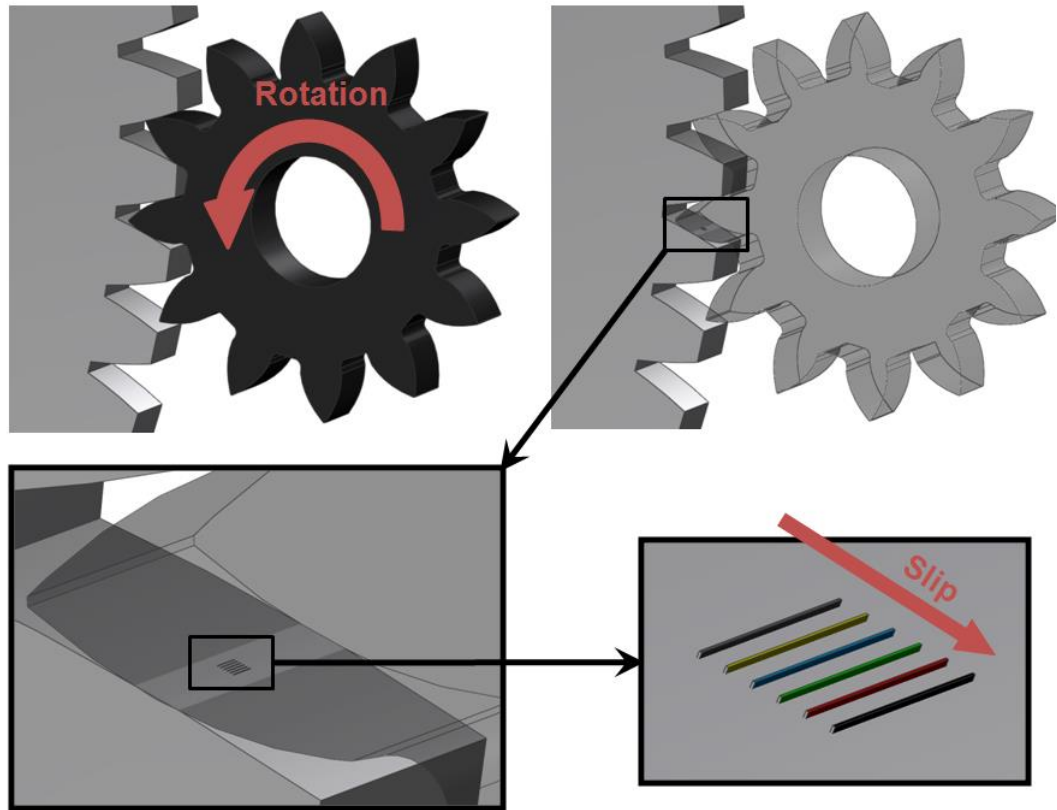
Figure 83: Polymer chain bunching smear model representation

As shown in Figure 83, the characteristic of the contact mechanics between the gear teeth mean that the steel pinion is rolling in one direction over the polymer gear, but that the sliding between them is in the opposite direction (Section 2.7 and Figure 14). Therefore, if a group of polymer chains were subjected to this action over many cycles and that the strain this action produces would be larger than the polymer could accept elastically, they would undergo a particular form of deformation. Figure 84 shows how rotation is translated into slip and shows a simplified and enlarged representation of a group of six polymer "chains" underneath the contact between the steel pinion and the polymer gear. They will be stretched in the direction of the slip and because of the rolling action in the opposing direction will be subjected to a differing force from the rear chain to the front chain.

The stress generated in the polymer can be evaluated from the force of the steel pinion pressing against the polymer gear flank due to torque transmission. In addition to the normal force directly due to torque, there will also be a tangential force. This tangential force is generated as a function of the normal force, the slip speed and the coefficient of friction between the steel and the polymer and is given by

$$F_T = \mu F_{norm} \tag{53}$$

As the material is loaded in this combination of normal and tangential forces a shear stress will be present. The stress components can be calculated as given by Johnson (1987):

$$\sigma_x = -\frac{2z}{\pi} \int_{-a}^{a} \frac{p(s)(x-s)^2 ds}{\{(x-s)^2 + z^2\}^2} - \frac{2}{\pi} \int_{-a}^{a} \frac{q(s)(x-s)^3 ds}{\{(x-s)^2 + z^2\}^2} \tag{54}$$

$$\sigma_z = -\frac{2z^3}{\pi} \int_{-a}^{a} \frac{p(s) ds}{\{(x-s)^2 + z^2\}^2} - \frac{2z^2}{\pi} \int_{-a}^{a} \frac{q(s)(x-s) ds}{\{(x-s)^2 + z^2\}^2} \tag{55}$$

$$\tau_{xz} = -\frac{2z^2}{\pi} \int_{-a}^{a} \frac{p(s)(x-s) ds}{\{(x-s)^2 + z^2\}^2} - \frac{2z}{\pi} \int_{-a}^{a} \frac{q(s)(x-s)^2 ds}{\{(x-s)^2 + z^2\}^2} \tag{56}$$

where $p(s)$ is the pressure distribution due to normal force, $q(s)$ is the pressure distribution due to the frictional force and a is the half width of the pressure distribution. x is the horizontal dimension along the face of the gear flank surface and z is the vertical dimension into the material. Note that the polymer gear flank is treated as an infinite half space. This approximation has been made as the radius of curvature of the polymer tooth flank is so much greater than that of the steel gear and in addition to this, the polymer is several orders of magnitude less stiff and so will conform to the shape of the steel pressing against it. These parameters are illustrated in Figure 84. The principal shear stress can then be found as

$$\tau_1 = \frac{1}{2}\{(\sigma_x - \sigma_z)^2 + 4\tau_{xz}^2\}^{1/2} \tag{57}$$
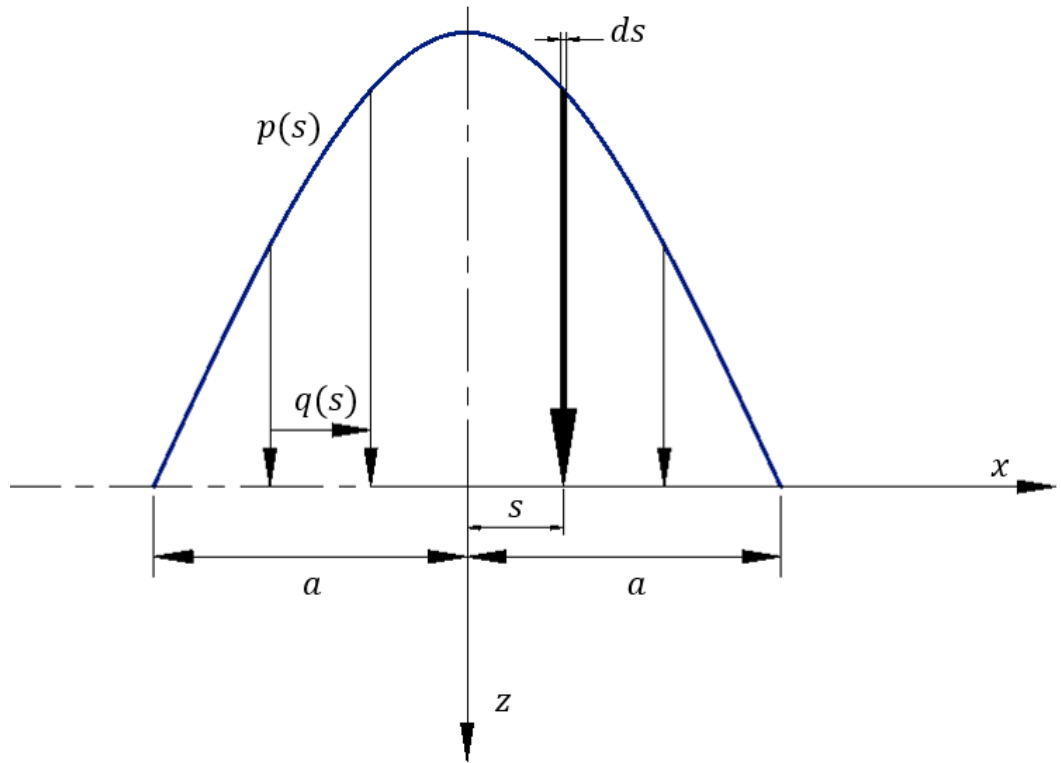
Figure 84: Pressure distribution of the contact between steel and polymer teeth.

The pressure distribution may then be evaluated as follows

$$p(s) = p_o(1 - \frac{x^2}{a^2})$$ (58)

being the conformal case as the polymer will be deformed by the steel, whilst the steel itself will remains un-deflected. Also,

$$q(s) = \mu p(s)$$ (59)

where a is the half width of the pressure distribution as shown in the Figure 84 and p_o describes the deformation of the material as a conformal contact between the steel and the polymer thus

$$p_o = \frac{(1 - v^2)}{(1 - 2v)} \frac{E}{(1 - v^2)} \frac{a^3}{r\delta}$$ (60)

where v is Poisson's ratio for the polymer, E is its Young's modulus, r is the radius of curvature of the steel and δ is the depth of penetration of the steel into the polymer and is calculated in chapter 4 equation 20.
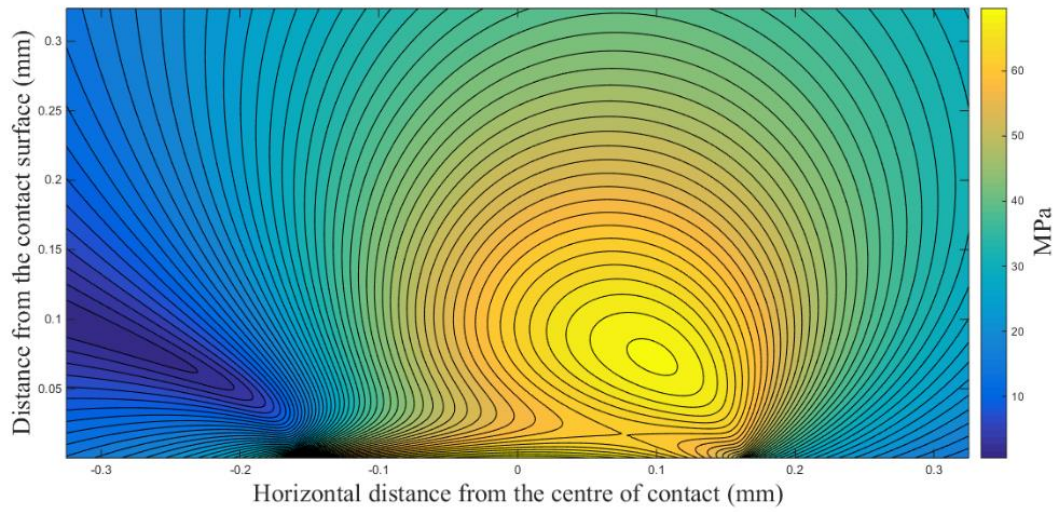
Figure 85: Principal shear stress contours – Conformal

These equations are then evaluated for a specific point along the line of contact $S = 1$ and are shown in Figure 85 and Figure 86. The contour plots show the principal shear stress in the polymer in a plane perpendicular to the axis of the gears local to the contact point.

A maximum stress of 71 MPa is found located on the surface at the contact interface. A separate concentration of stress is observed beneath the surface consistent with that found in Herztian contact theory. Figure 86 shows an enlarged view of the contour plot centred on the contact zone. A layer of material approximately 3 μm in depth occurs for the length of the conformal contact which is beyond the yield stress of the polymer given as 69 MPa in the material data Table 5.
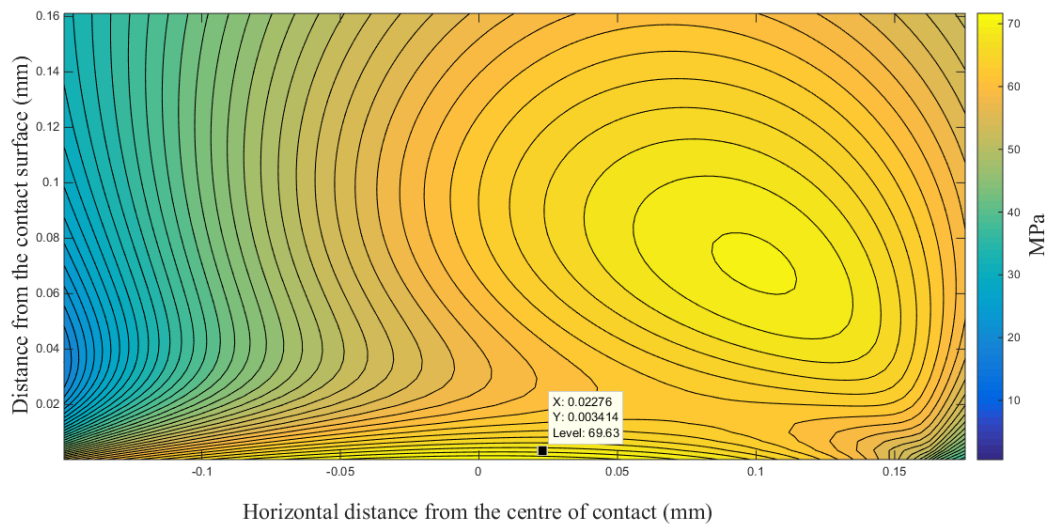
Figure 86: Yield point of the slip layer

For comparison, the Hertzian case is found using the same method with the variation of the pressure distribution p_o, the deflection δ and the pressure distribution half width a. They are found as

$$a = \left(\frac{3Pr}{4E}\right)^{1/3} \tag{61}$$

$$\delta = \frac{a^2}{r} \tag{62}$$

$$p_o = \left(\frac{6PE^2}{\pi^3 r^2}\right)^{1/3} \tag{63}$$
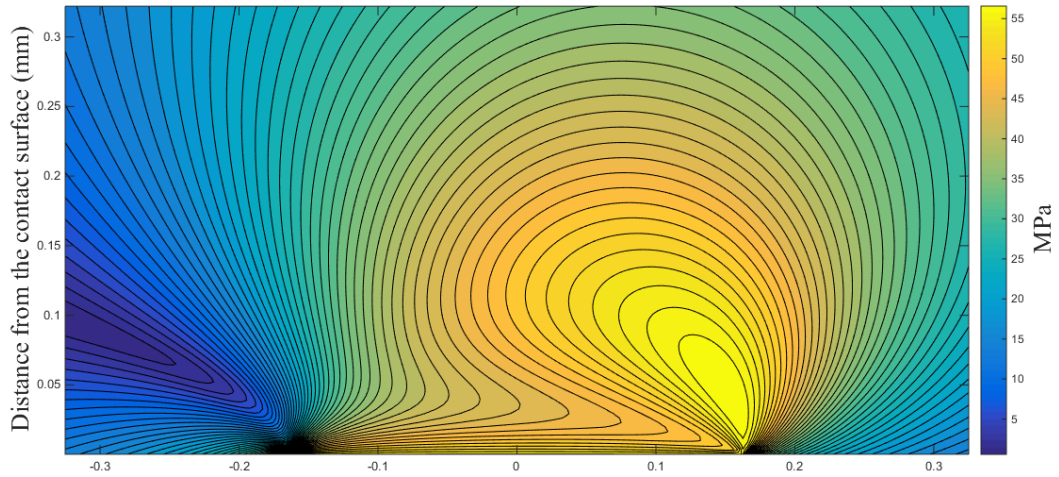
Figure 87: Principal shear stress contours - Hertzian

Figure 87 shows the principal shear stress in the polymer evaluated as a Hertzian contact rather than a conformal one. Although the Hertzian case is not appropriate for the polymer, as it is not behaving within its elastic limit, it is useful to compare the results. The maximum stress is found to be 57 MPa, considerably lower than the conformal case and within the yield stress limit of the material. Figure 88 shows an enlarged view of the Hertzian distribution and it is seen that the acute increase in stress at the edge of the contact must be less applicable than the conformal contacts shown in the previous figures.
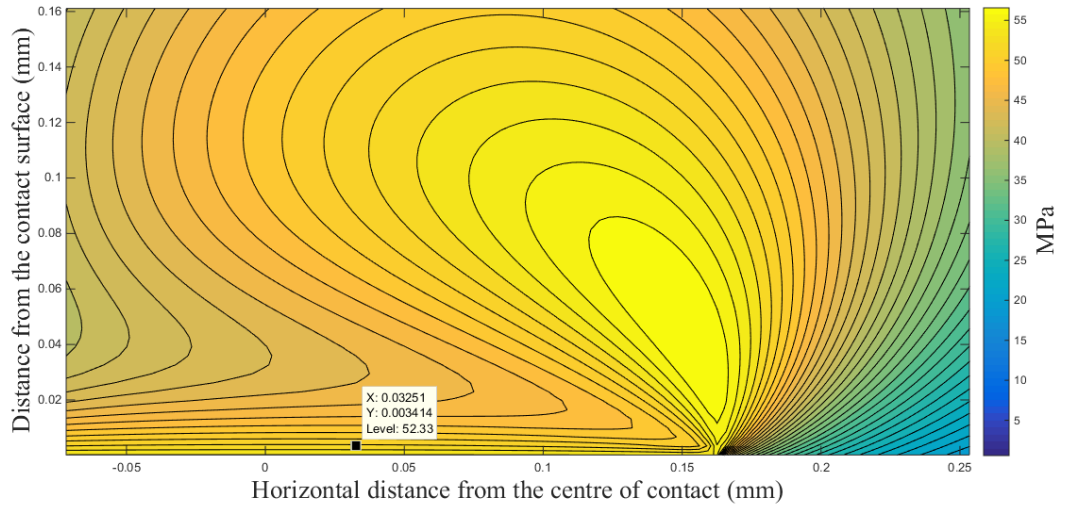
Figure 88: Hertzian distribution - enlarged
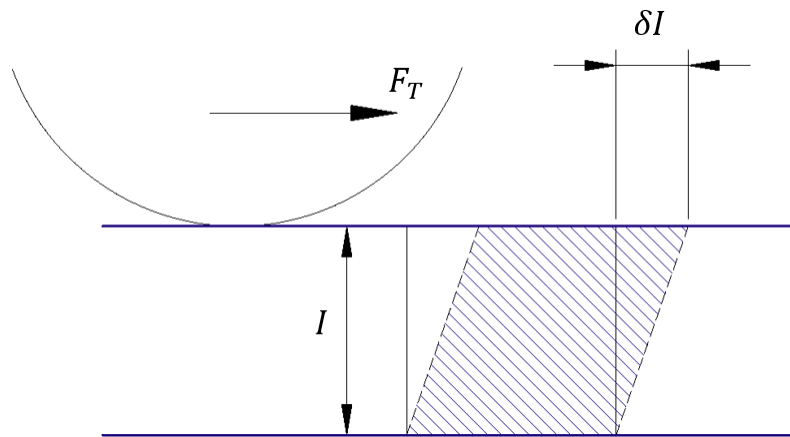
Figure 89: Slip layer definition

Given that the polymer has yielded around the contact zone to a depth of approximately 3 μm there will be a permanent deformation that persists after the gear tooth has passed. During each cycle of the gear this deformation will increase. Figure 89 illustrates the parameters for this where I is the slip layer depth, δI is the shear deflection due t strain in the polymer and F_T is the tangential force. The deflection is given as

$$\delta I = \frac{\sigma}{E} I \tag{64}$$

and may be evaluated as 6.77 x 10^{-5} mm.

This provides an evaluation of the strain in the material due to load. However, the power dissipated into the material is also a function of the slip velocity. The variable slip speed that is experienced through the line of contact between the gear teeth has previously been described and assessed. As the contact zone processes across the tooth flank this variation in speed will cause the power dissipated to also vary. It is proposed that this is the reason for the formation of the smears. Figure 90 shows a sketch of the principle. The upper portion of the sketch shows the slip speed decreasing from left to right and the lower portion shows a depiction of the smear. The faster slip at the left of the smear catches up the slow slip on the right and in this way the smear is created.
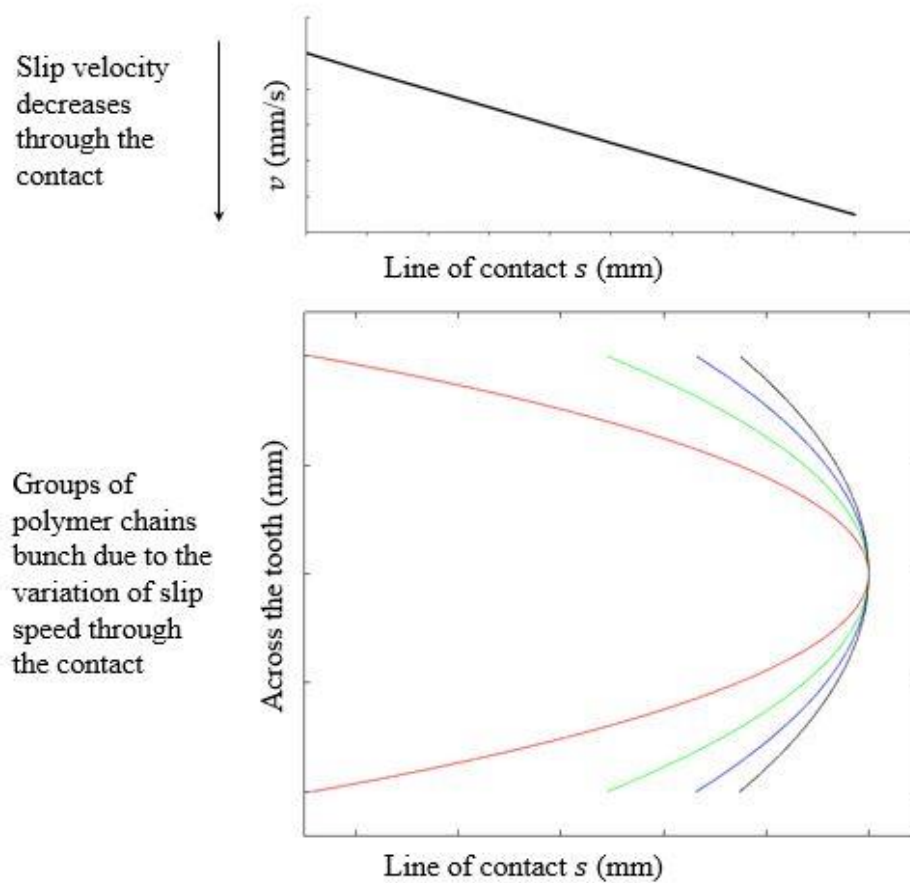
Figure 90: Grouping of polymer material to form smears –
Upper plot shows decreasing slip speed; lower plot shows polymer bunches
grouping due to the lowering slip speed.

Referring to Figure 66 it can be seen that a smear field has been created where smears have formed in lines and that they vary in pitch through the contact. Through the

model presented in this section it can be seen that the shear stress generated in the polymer will be along the full width of the contact of the teeth and so a linear relationship with the contact and the smears is established. Eventually, they form broken lines for the same reason that waves on a beach do not break in a continuous line. Small variations in contact and material parameters make breaks in the lines to produce the pattern shown in Figure 66. Given the general size of the smears, the model therefore predicts that smears will begin to form at around 300 cycles. Once they have begun to form, they are drawn out until material breaks away from the leading edge as described in the following section.
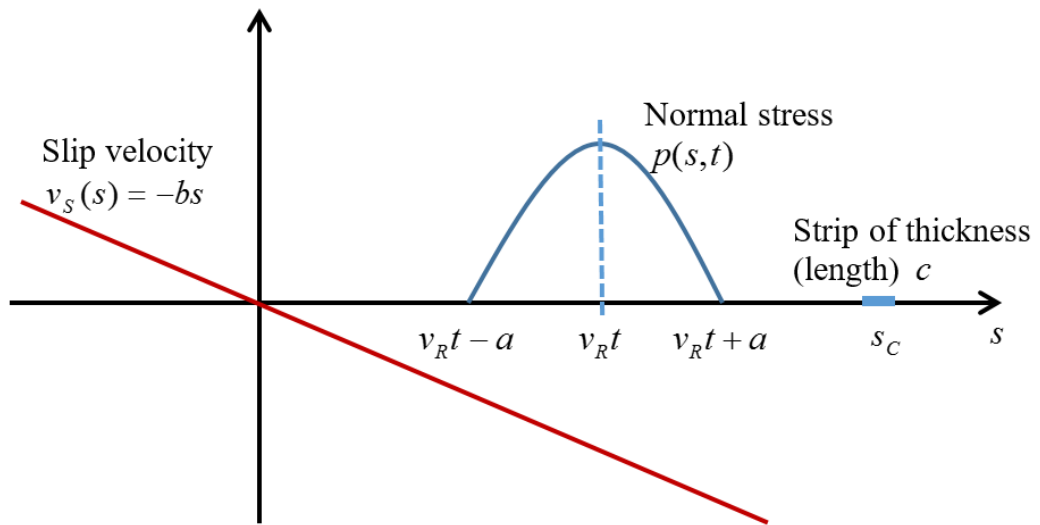
Figure 91: Moving contact zone pressure distribution.

Figure 91 shows the contact zone moving with a fixed velocity v_R due to rolling, with associated slip velocity $v_s(s)$ dependent on the position relative to the pitch point. The length of the contact zone, a, depends on the normal contact force. For cylinders in contact the normal stress is taken to be derived from the conformal case as given by equation (58):

$$p(s,t) = \begin{cases} p_o\left(1 - \left(\dfrac{s - v_R t}{a}\right)^2\right), & v_R t - a < s < v_R t + a \\ 0, & elsewhere \end{cases} \tag{65}$$

The normal force is

$$N = l \int_{v_R t - a}^{v_R t + a} p(s, t) \, ds \tag{66}$$

$$= p_o l \int_{v_R t - a}^{v_R t + a} \left(1 - \left(\frac{s - v_R t}{a} \right)^2 \right) ds \tag{67}$$

$$= p_o l a \int_{-1}^{1} (1 - z^2) \, dz \tag{68}$$

$$= \frac{4}{3} \pi p_o l a \tag{69}$$

where l is the width of contact of the gear tooth flank.

The area for consideration is a small stationary strip of length c under the contact and is relatively small in relation to that contact $2a$. The strip is the area that will undergo smearing. The rolling velocity component does not influence the slip velocity (v_R), which arises from the pinion/gear involute form and when $s = 0$ the pitch point of the gears is reached where no sliding occurs. The rolling velocity component v_R does not influence the slip velocity $v_s(s) = -bs$, which arises from the pinion/gear involute form. Here, $s = 0$ corresponds to the pitch point.

Consider a stationary strip of thickness c ($s_c - c/2 < s < s_c + c/2$) on the gear surface (see Figure 91), which is small compared to the length ($2a$) of the contact zone. The strip is swept by the contact from $t = (s_c - a)/v_R$ to $t = (s_c + a)/v_R$. Over a time increment δt, the work done by the friction force at $s = s_c$ is, to first order quantities is

$$\delta W = \mu p(s_c, t) l c |v_s(s_c)| \delta t \tag{70}$$

Hence the work done at $s = s_c$ from is $t = (s_c - a)/v_R$ to $t = (s_c + a)/v_R$

$$W = |v_s(s_c)| \mu l c \int_{(s-a)/v_R}^{(s+a)/v_R} p(s_c, t) \, dt \tag{71}$$

$$= |v_s(s_c)|\mu p_o lc \int_{(s-a)/v_R}^{(s+a)/v_R} \left(1 - \left(\frac{s_c - v_R t}{a}\right)^2\right) dt \tag{72}$$

$$= \frac{|v_s(s_c)|\mu p_o lc}{v_R} \int_{-1}^{1} (1 - z^2) dz \tag{73}$$

$$= \mu N |v_s(s_c)| \frac{c}{v_R} \tag{74}$$

A time period may be defined as $T_{cR} = c/v_R$, the time to traverse a distance c at the rolling velocity v_R, hence the work done on the smear is

$$W = \mu N |v_s(s_c)| T_{cR} \tag{75}$$

From this expression it can be seen that the work done on the material is a function of the slip speed. It is this relationship that gives rise the smear features depicted in Figure 90.

6.3.3   Smear Wear Model
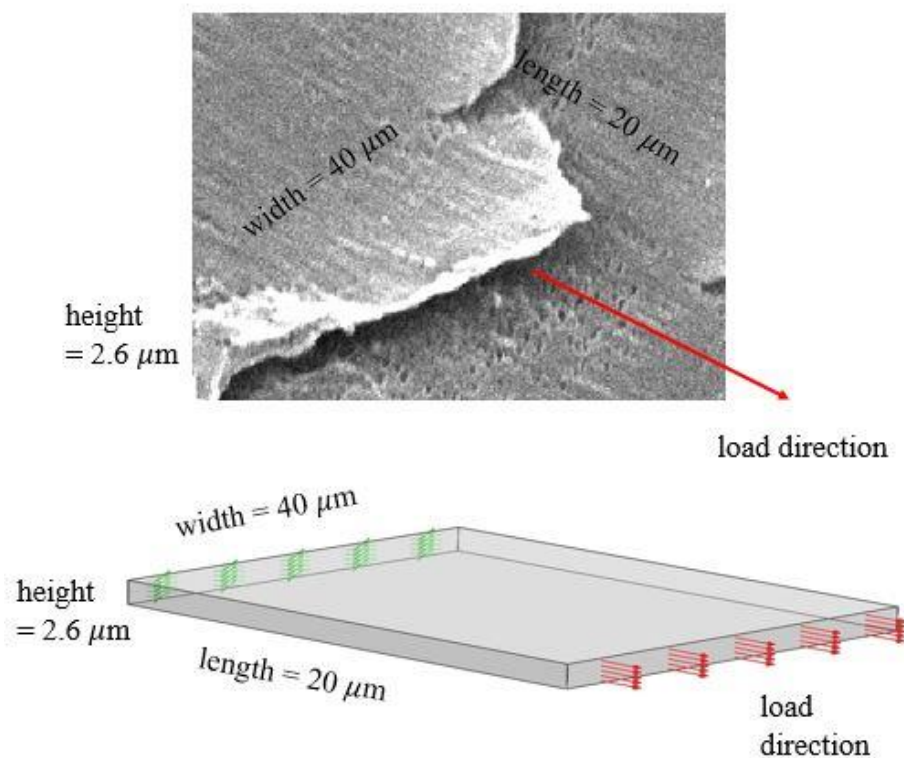
Figure 92: Comparison of a real smear and the analogous smear block model with dimensions taken from the observed mechanism.

An individual smear can be modelled as a block of material with dimensions corresponding to the smear sizes observed through the SEM images. If this analogous block were to be subject to a cyclic force of the same magnitude as the force applied due to the torque generated by the gear interaction, then it would be deformed. If the stress generated in the block exceeds its elastic limit then the block would not return to its original dimensions and given a sufficient number of cycles, would eventually fail. A mathematical model has been developed that applies this scenario to a simple block (see Figure 92) and uses a looping function to iterate until failure occurs.

The stress in the simplified smear block is given by

$$\sigma_p = \frac{F_p}{A_0} \tag{76}$$

where σ_p is the stress in the smear, F_p is the pull force and A_0 is the initial area of the smear. Figure 93 (upper series) shows the stress/strain curve for the POM as supplied by DuPont, the strain is interpolated from this curve and so the remaining strain in the smear is found when the load is removed:

$$\epsilon_r = \epsilon_{int} - (\frac{\sigma_p}{\nabla}) \tag{77}$$

where ϵ_r is the strain remaining in the smear when the load is removed, ϵ_{int} is the strain interpolated from the stress/strain curve of the material and ∇ is the slope of the elastic part of the material curve. This calculation follows the dotted line in Figure 93 (upper plot) back to zero stress. Therefore, the new height and width of the smear can be calculated using the strain the material has undergone:

$$h_1 = h_0 - (2h_0 \upsilon \epsilon_r) \tag{78}$$

where h_1 is the new height, h_0 is the initial height and υ is poissons ratio for the material (0.35). The width is calculated similarly and so the new area of the smear is found. This loop is repeated until an arbitrarily small value of the area is found, at which point the loop stops as it is assumed that the smear has finally failed.
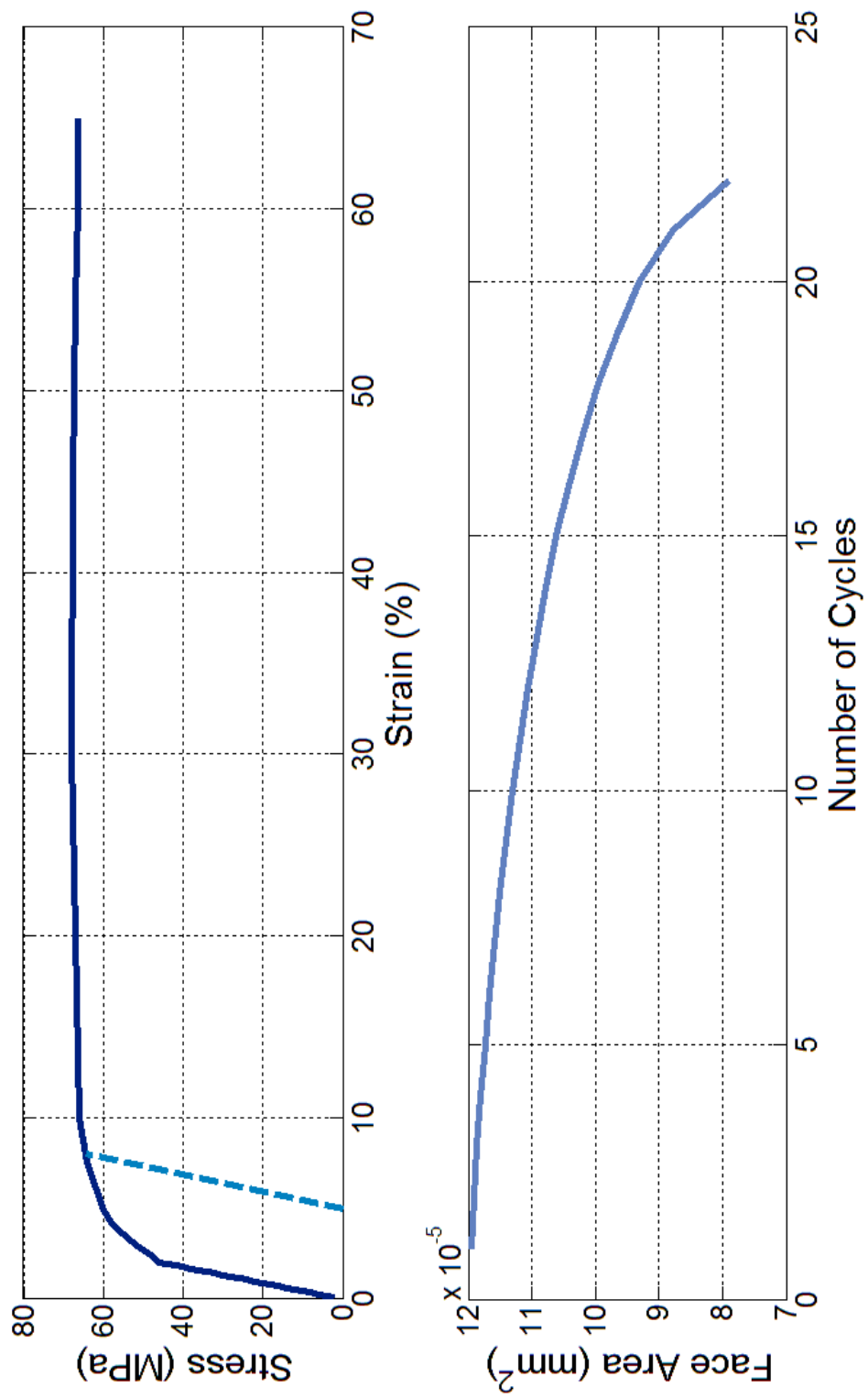
Figure 93: Stress/strain and face area reduction

The dimensions were chosen from inspection of the smear features observed through SEM. The manufacturer of the material used for the gears (POM) at the time of writing was DuPont and they provided an industry standard tensile tested stress/strain curve for the material which was used as the base material data for this analytical model. The stress/strain curve is plotted in the upper graph shown in Figure 93 and superimposed onto this curve for the polymer is a second series plotted in dotted light blue. If the material is stressed beyond its elastic limit it will plastically and permanently deform. From the load and dimensions of a smear the stress developed in the material is calculated at 64.4 MPa. As a result of this, when the load is released after the gear cycle has passed, there will be a residual deformation equivalent to the strain that was reached under loading. The secondary series on the Stress/Strain curve (in dotted light blue) shows this effect of how the material stress as the load releases follows a straight line back to zero whilst leaving a residual strain of a few percent, the model makes this calculation for each cycle of the gear and so evaluates the effect of the smear stretching out and finally breaking. Figure 93 (lower plot) shows the surface area of the face of the smear as the cycles progress; note how there is an exponential decrease in face area as the cycle numbers increase and there is a definitive drop-off point. This is the point at which the model assumes the smear has fractured and that some material has been removed. The size of the particle that has broken off from the smear is then evaluated as a percentage of the overall final smear cross-section and length.

For 6×10^6 cycles, the model returns a total wear mass for the whole gear of **67 mg**. This figure compares to **77 mg** of material worn away from the gear as measured experimentally using profile measurement as discussed in Section 5.10. The model developed has predicted the wear in the gear to within 13%, given the assumptions made on the real contact area and likely errors in measurement of the actual material worn away this figure shows that the model is robust and reasonably accurate.

6.4 Discussion of Model Outputs and Results

The phenomenological smear model predicts a worn volume of 67 mg against a measured value of 77 mg and describes how the smears are initiated based on real physical parameters rather than by using a constant derived from experimental data. This is a robust form of modelling which will yield reliable results once more validating data can be obtained by experimentation. The stress distribution in the contacting surfaces has been thoroughly investigated and it is seen that there is a twin stress point pattern (see Figures 85 to 89) that processes across the tooth sweep, separating as it goes. This must also add to the slip/roll action of the teeth during smear creation. The twin stress pattern is particular to the combination of a curved steel surface loaded against a curved polymer surface.

For the small scale, it is seen that it is possible to formulate a model that describes in detail how the polymer chains may interact with each other when acted upon by a contacting force. The model presented in Section 6.3 shows that setting simple mathematical relationships between the chains gives a result that is entirely consistent in relation to physical observations under the microscope. However, the limitations of the model in this case are that it only describes the material deformation in two dimensions. While it seems reasonable that the polymer chains are moving and bunching in the way the model predicts, there will also be a three dimensional mode to the interaction between chains. Some chains will be smeared across the surface from a start position on the surface, while other chains will have been partially buried at the initial start condition and will be extracted from the bulk of the material. Polymer chains are drawn from the bulk material in this way. Indeed, there will be a myriad of different deformation mechanisms at work during the contact of the hard steel gear surface against the softer polymer chain constructed material and the proposal of a three dimensional beam model in Section 6.2.2.3 could be used to do this not-with-standing the problem of computational power that would ensue.

This chapter has developed ideas about the how the structure of the polymer can be modelled that will describe how the material is really moving. A number of different models have been presented that describe different parts of the system. The ultimate goal would be to link all of these as a single mathematical model that could be used to assess the wear of a polymer due to contact and it would seem feasible to do this under a

separate research programme focused entirely on this model creation. It would be necessary to produce sub-routines that deal with the individual characteristics at particular scales that would be linked via an overall system analysis design interface, probably a purpose designed interface. The production of a model such as this could be the first true numerical wear model based on real physical principles that would ideally be validated by a robust experimental programme.

CHAPTER 7

Conclusions and Future Research

7.1 Conclusions

The research presented in this thesis splits broadly into two parts, the first has dealt with the heat rise in the running gear pair and the second has investigated an actual wear mechanism on the surface of the polymer gear. The novelty of the research is primarily in the smear wear mechanism that has been observed through scanning electron microscopy techniques which has been modelled using the assessment of the energy absorbed at the contact between the gear teeth. There is also novelty in the methodology for modelling the temperature rise in the gears, being a multi-disciplinary technique. It is to compare rod on axially aligned disc with real gear geometry using a technique of time averaging not previously seen in the open literature.

With respect to a steel pinion running on a polymer gear, studies have been made over the last 80 years that are relevant and these have been thoroughly reviewed and discussed. Many researchers have concerned themselves with the contact mechanics and wear mechanisms associated with hard-hard contacts but they have largely been restricted to hardened steels. There are a number of models presented in the body of literature around the area of non-metallic gears. However, they are based on empirical data gained through testing or on very generic assumptions based on the Archard wear equation. A specific and detailed description of a particular wear mechanism has not existed and this is the main contribution from this thesis to engineering science. That is not to say that the smearing wear mechanism that is shown here represents a complete view of the wear of a polymer gear. It does not, and in fact there are almost certainly many more different types of wear mechanism that contribute to the wear volume and steps should be taken in further research to finds other mechanisms using the techniques developed in this thesis.

Steps have been taken to validate the models that have been used to predict the wear volume and they correlate well with the experimental work.

The approach taken throughout the research was first to carefully observe and then to formulate a theory to explain the phenomenon seen. A detailed inspection and analysis of the basic geometry and contact properties of the involute spur gear form was conducted. From this initial inspection, the basis for the research germinated from the idea of the slip/roll action that is present between the two contacting faces of the teeth flanks. This slip/roll action is the core of the mechanism of the spur gear pair and from it the models of efficiency and wear mechanisms have been derived.

The smear features observed using scanning electron microscopy techniques prompted questions that have been at least partially answered by this thesis. When these features were first seen the question immediately was raised; How are they formed and do they contribute to wear? Through the modelling that has been presented, a credible process by which the smears are initiated, propagated and finally cause material to be removed from the surface of the polymer gear has been proposed. It has also been demonstrated that this new wear mechanism, or smearing, can be modelled and so the wear volume of the material due to this mechanism can be predicted. A specific wear rate has been both calculated and measured experimentally. For 6×10^6 cycles, the model returns a total wear mass for the whole gear of 67 mg, which compares to 77 mg as measured from the polymer gear. The steel gear was observed to have worn slightly which is likely to be caused by the wear debris from the polymer gear as it exits the mesh. In further research, the direction should be to attempt to validate the models by a more statistically significant sample size. In this thesis, the smears have been observed many times in both the industrial application and by experimentation and so it is clear that the process physically occurs. To completely validate the predictive abilities of the models with respect to wear volume it would be necessary to perform many more experiments than the scope of this thesis.

A method has also been developed for modelling the temperature rise in the polymer-steel gear pair. This method differs from any techniques to be found in the literature by using a number of approaches to eliminate the use of empirical constants derived from test data. The method can be used to predict the running temperature of the gears and also it can assess the efficiency of the gear pair as a useful and practical piece of information that would be used during the design of a gearbox. It is worthwhile using

this technique rather than relying on an entirely empirical formula such as the one supplied by British Standard 6168 as it gives more detailed information about the operating parameters of the gear pair in addition to the efficiency, which is of utmost importance to the performance of the gearbox.

In summary, the following has been found during the course of this research:

i. A new wear mechanism has been identified by which polymer smears are created by the action of the steel tooth upon the polymer tooth resulting in material removal from the trailing edge of the smears.

ii. Models have been presented that describe and predict this smear wear mechanism using the technique of evaluating the energy absorbed at the contact.

iii. A multidisciplinary model for predicting the running temperature of a polymer-steel gear pair has been presented and has been validated by experimentation.

iv. A method has been developed for directly equating the running temperature of a rod on axially aligned disc experiment to a real spur gear pair that, when used in conjunction with the modelling technique described in (iii), can be used by the gearbox design engineer to determine running temperatures with more confidence than previously possible.

7.2 Future Research

Future research should include a statistical study to validate the smear wear models. It would also draw together the differing techniques into a unified model run from a single user interface. The techniques used during this research have been many and varied from basic scientific principles to fully analytical and numerical computer models. Despite this complexity of analysis, in order to calculate the running performance of a polymer-steel gear pair and to predict the likely specific wear volume the user of such a unified model would need to know very little information about the running gear pair, namely, torque, speed, tooth number, tooth width and material. These parameters are well known and definable at the beginning of the design process, which makes such a unified model entirely achievable for the future.

In summary, the following research areas could follow:

i. The development of a single model and interface that draws together the individual parts of this thesis to provide basic gear parameters, efficiency and wear data for the gear pair.

ii. Analysis of the real contact area (in contrast to the apparent contact area) between a steel surface and a polymer surface. This would provide a more statistically sound basis to the power dissipated in the polymer due to the slip/roll action of the involute.

iii. Development of a realistic molecular scale polymer chain finite element representation in combination with a true contact model. This would allow the contact mechanics of the polymer-steel interface to be fully understood at both micro and macro scales through numerical simulation.

7.3   Aims and Objectives Answered

   i.   Involute gear tooth geometry was inspected and analysed in depth. Performing this initial investigation into the basic geometry helped to initialise the research ideas for the thesis.

  ii.   The information gathered and derived in (i) was used to develop a method for the analysis of a gear pair with respect to efficiency.

 iii.   Novel techniques have been developed to predict the running temperature of a gear pair from the basic parameters of geometry and material properties.

 iv.   A new wear mechanism has been identified that has not previously appeared in the open literature. This new wear mechanism has been extensively documented by way of scanning electron microscopy and a model has been developed to characterise its formation and growth.

7.4 Closing Statement

The original brief for this research was to find a method of calculating the running performance of a steel-polymer gear pair. Along the way, a new wear mechanism has been discovered and methods for predicting wear volume and other performance criteria have been also been developed. The base data of this research does indeed fulfil the original programme aims and it is hoped that work will continue to fully validate the assertions made here and to develop an industry friendly tool that could be used day-to-day by any gearbox design engineer.

At the time of submission of this thesis, a formal paper detailing the methodology for determining the running temperature and efficiency of a polymer-steel gear pair has been accepted for publication by a respected journal and can be found in the appendices. A second paper that documents a new mechanism of wear (smearing) with methods for characterising it by phenomenological models is approaching submission. It is felt that, through this research, new knowledge and understanding in the area of the tribology of polymer-steel gearing has been gained. It is hoped that both industry and the scientific community will benefit from it.

BIBLIOGRAPHY

Abdelbary, A., 2015. *Wear of polymers and composites.* Woodhead Publishing.

Abouelwafa, M. N., 1979, A study of the wear and related mechanical properties of silicone impregnated polyethylenes. Leeds, UK: University of Leeds.

Abramowitz, M. and Stegun, I., 1967. *Handbook of mathematical functions: with formulas, graphs, and mathematical tables.* US Government Printing Office.

Archard, J. F., 1953. Contact and rubbing of flat surfaces. *Journal of applied physics.* Volume 24(8), pp. 981 - 988.

Archard, J. F., 1957. The temperature of rubbing surfaces. *Proceedings of the International Conference on Gears.* Volume 2, pp. 438 - 455.

Barber, J. R., 1970. The conduction of heat from sliding solids. *International Journal of Heat Mass Transfer.* Volume 13, pp. 857 - 869.

Bassani, R., Di Pasquale, E. and Vitali, C., 1984. Probabilistic model for metal-polymer friction. *Wear.* 95(2), pp.177-191.

Beardmore, R., 2013. *RoyMech.* [Online]
Available at: http://roymech.co.uk/
[Accessed 28 February 2014].

Beerman, S., 2007. Estimation of lifetime for plastic gears. AGMA Conference Fall meeting.

Blok, H., 1963. The Flash Temperature Concept. *Wear.* Volume 6.6, pp. 483 - 494.

Boissonnet, L., Duffau, B. and Montmitonnet, P., 2012. A wear particle-based model of friction in a polymer-metal high pressure contact. *Wear,* Volume 286 - 287, pp. 55 - 65.

Bowden, F. P. and Tabor, D., 1966. Friction, lubrication and wear: a survey of work during the last decade. *British Journal of Applied Physics,* Volume 17, pp. 15 - 21.

Bowers, R. C., Clinton, W. C. and Zisman, W. A., 1954. Friction and lubrication of nylon. *Industrial and Engineering Chemistry,* 46(11), pp. 2416 - 2419.

Brainard, W. A. and Buckley, D. H., 1973. Adhesion and friction of PTFE in contact with metals as studied by Auger spectroscopy, field ion and scanning electron microscopy. *Wear.* 26(1), pp.75-93.

Breeds, A. R., Kukureka, S. N., Mao, K., Walton, D. and Hooke, C. J., 1993. Wear behaviour of acetal gear pairs. *Wear,* Volume 166, pp. 85 - 91.

Briscoe, B., 1981. Wear of polymers: an essay on fundamental aspects. *Tribolology International,* Volume 14.4, pp. 231 - 243.

Buckingham, E., 1949. *Analytical Mechanics of Gears.* Massachusetts Institute of Technology: Dover Publications.

Camnetics, 2014. *http://www.camnetics.com/.* [Online]
Available at: http://www.camnetics.com/geartrax/index.htm
[Accessed 2014].

Carslaw, H. S. and Jaeger, J. C., 1941. *Operational methods in applied mathematics.* Second ed. London: Oxford University Press.

Chang, L., 2008. Modeling of asperity collisions and their effects in a frictionless sliding contact of nominally flat metallic surfaces. *ASME Journal of Tribology,* Volume 130.3: 031403

Chen, Y. K., Kukureka, S. N., Hooke, C. J. and Rao, M., 2000. Surface topography and wear mechanisms in polyamide 66 and its composites. *Journal of Materials Science,* Volume 35, pp. 1269 - 1281.

Cheon, M., Chang, I., Koplik, J. and Banavar, J. R, 2002. Chain molecule deformation in a uniform flow - A computer experiment. *Europhysics letters,* Volume 58, pp. 215 - 221.

Chiu, P. Y., Barry, P. R., Perry, S. S., Sawyer, W. G. and Phillpot, S. R., 2011. Influence of the molecular level structure of polyethylene and polytetrafluoroethylene on their tribological response. *Tribological letters,* Volume 42, pp. 193 - 201.

Choong, 2006. Durability improvement method for plastic spur gears. *Tribology International,* Volume 39, pp. 1454 - 1461.

Chin, H. C., Khayat, G. and Quinn, T. M., 2011. Improved characterization of cartilage mechanical properties using a combination of stress relaxation and creep. *Journal of biomechanics*, *44*(1), pp.198-201.

Colbourne, J. R., 2006. *Gear Tooth Profile Curvature.* USA, Patent No. 11/016,029.

Cooper, J. R., Dowson, D. and Fisher, J. 1993. Macroscopic and microscopic wear mechanisms in UHMWPE. *Wear.* 162–4:378–84.

Cooper, J., Isaac, G. H. and Wroblewski, B. M. 1994. Observations of residual sub-surface shear strain in the ultrahigh molecular weight polyethylene acetabular cups of hip prostheses. *Journal of Material Science: Materials in Medicine.* 5:52–7.

Diab, Y., Ville, F. and Velex, P., 2006. Prediction of power losses due to tooth friction in gears. *Tribology Transactions,* 49(2), pp. 260 - 270.

Dontyne, 2014. *Dontyne Systems.* [Online]
Available at: http://www.dontynesystems.com/

Dudley, D. W., 1969. *The Evolution of the Gear Art.* Washington, D. C.: AGMA.

DuPont (2011). *DuPont Delrin Acetal Resin Design Guide*. [ONLINE] Available at: http://www.dupont.com/ [Accessed August 2011].

Duzcukoglu, H., 2009. Study on development of polyamide gears for improvement of load carrying capacity. *Tribology international,* Volume 42, pp. 1146 - 1153.

Evans, D. C. and Lancaster, J. K., 1979. The wear of polymers. *Treatise on Materials Science & Technology.* 13, pp.85-139.

Fisher, J., Dowson, D., Hamdzah, H. and Lee, H. L., 1994. The effect of sliding velocity on the friction and wear of UHMWPE for use in total artifical joints. *Wear,* Volume 175, pp. 219 - 225.

Flodin, A., 1997. Simulation of mild wear in spur gears. *Wear,* Volume 207, pp. 16 - 23.

Gagnadre, C., Caron, A., Guezenoc, H. and Grohens, Y., 2009. Electron microscopy pictures, mathematical model and approximate solution of the surface potential. *Kybernetes,* 38(5), pp. 780 - 788.

Giltrow, J. P. and Lancaster, J. K., 1967. Friction and wear of polymers reinforced with carbon fibres. *Nature*, 214(5093), pp.1106-1107.

Goda, T., Varadi, K. and Friedrich, K., 2001. FE micro-models to study contact states, stresses and failure mechanisms in a polymer composite subjected to a sliding steel asperity. *Wear,* Volume 251, pp. 1584 - 1590.

Greenwood, J. A. and Williamson, J. B. P., 1966. Contact of nominally flat surfaces. *Proceedings of the Royal Society of London. Series A. Mathematical and Physical Sciences,* Volume 295, pp. 300 - 319.

Hamrock, B. J., 2004. *Fundamentals of Fluid Film Lubrication.* :Marcel Dekker.

Holm, E., Holm, R. and Shobert, I. I., 1948. Theory of hardness and measurements applicable to contact problems. *Journal of Applied Physics.* Volume 20, pp. 319 – 327.

Hooke, C. J., Breeds, A. R., Kukureka, S. N., Mao, K. and Walton, D., 1992. Measurement and prediction of the surface temperature in polymer gears and its relationship to gear wear. *ASME Journal of Tribology,* Volume 115.1, pp. 119 – 124.

Hooke, C. J., Kukureka, S. N., Liao, P., Rao, M. and Chen, Y. K., 1996. The friction and wear of polymers in non-conformal contacts. *Wear,* Volume 200, pp. 83 - 94.

Kar, M. K. and Bahadur, S., 1974. The wear equation for unfilled and filled Polyoxymethylene. *Wear.* 30(3), pp.337-348.

Kar, M. K., and Bahadur, S., 1978. Micromechanism of wear at polymer-metal sliding interface. *Wear,* Volume 46, pp. 189 - 202.

Keogh, P. S., and Yong, W. Y., 2007. Thermal assessment of dynamic rotor/auxiliary bearing contact events. *Journal of Tribology* 129.1, pp. 143 - 152.

Kim, C. H., 2006. Durability improvement method for plastic spur gears. Tribology international, Volume 39.11, pp. 1454-1461.

Kleemola, J. and Lehtovaara, A., 2009. Experimental simulation of gear contact along the line of action. *Tribology International,* Volume 42, pp. 1453 - 1459.

Kukureka, S. N., Chen, Y. K., Hooke, C. J., and Liao, P., 1994. Surface failure mechanisms in polymer spur gears. *Proceedings of the International Gearing Conference, London.* pp. 13 – 18.

Kukureka, S. N., Chen, Y. K., Hooke, C. J., and Liao, P., 1995. The wear mechanisms of acetal in unlubricated rolling-sliding contact. *Wear,* Volume 185, pp. 1 - 8.

Kukureka, S. N., Hooke, C. J., Rao, M., Liao, P., and Chen, Y. K., 1999. The effect of fibre reinforcement on the friction and wear of polyamide 66 under dry rolling-sliding contact. *Tribology International,* Volume 32, pp. 107 - 116.

Lancaster, J. K., 1968. Relationships between the wear of polymers and their mechanical properties. *In Proceedings of the Institution of Mechanical Engineers, Conference Proceedings* (Vol. 183, No. 16, pp. 98-106). SAGE Publications.

Lancaster, J. K., 1969. Abrasive wear of polymers. *Wear.* 14(4), pp.223-239.

Lancaster, J. K., 1971. Estimation of the limiting PV relationships for thermoplastic bearing materials. *Tribology.* 4(2), pp.82-86.

Lin, A. and Kuang, J., 2008. Dynamic interaction between contact loads and tooth wear of engaged plastic gear pairs. *International Journal of Mechanical Science,* Volume 50, pp. 205 - 213.

Li, S., 2002. Gear contact model and loaded tooth contact analysis of a three-dimensional, thin-rimmed gear. *ASME - Journal of Mechanical Design,* Volume 124, pp. 511 - 517.

Liu, F., Galvin, A., Jin, Z., and Fisher, J., 2011. A new formulation for the prediction of polyethylene wear in artificial hip joints. *Proceedings of the IMechE Part H: Engineering in Medicine,* Volume 225, pp. 16 - 24.

Mao, K., Hooke, C. J., and Walton, D., 1996. The wear behaviour of polymer composite gears. *Journal of Synthetic Lubrication,* 12(4), pp. 337 - 345.

Mao, K., 2007. A numerical method for polymer composite gear flash temperature prediction. *Wear,* Volume 262, pp. 1321 - 1329.

Mao, K., Li, W., Hooke, C. J., and Walton, D., 2010. Polymer gear surface thermal wear and its performance prediction. *Tribology International,* Volume 43, pp. 433 - 439.

Mao, K., Li, W., Hooke, C. J., and Walton, D., 2009. Friction and wear behaviour of acetal and nylon gears. *Wear*, 267(1), 639 – 645.

MatWeb, L., 2014. *MatWeb - Material Property Data.* [Online]
Available at: http://www.matweb.com
[Accessed 23 January 2014].

Meng, H. C. and Ludema, K. C., 1995. Wear models and predictive equations - their form and content. *Wear,* Volume 181, pp. 443 - 457.

Michael, P. C., Rabinowicz, E. and Iwasa, Y., 1991. Friction and wear of polymeric materials at 293, 77 and 4.2K. *Cryogenics,* Volume 31, pp. 695 - 704.

Mulvihill, D. M., Kartal, M. E., Nowell, D. and Hills, D. A., 2011. An elastic-plastic asperity interaction model for sliding friction. *Tribology International,* Volume 44, pp. 1679 - 1694.

Myshkin, N. K. , Petrokovets, M. I. and Kovalev, A. V., 2006. Tribology of polymers: adhesion, friction, wear, and mass-transfer. *Tribology International.* 38(11), pp.910-921.

Nacy, S. M., Abdullah, M. Q. and Mohammed, M. N., 2007. Generation of crowned parabolic Novikov gears. *Engineering Letters,* Volume 15, pp. 1 - 4.

Olberg, E., Jones, F. D., Ryffel, H. H. and McCauley, C. J., 2012. *Machinery's Handbook (29th Edition).* Online: Industrial Press.

Parker, A., 1965. Gears that conform. *New Scientist*.

Porter, D., 1996. Materials modelling: A bridge from atoms to bulk properties. *Advanced Performance Materials,* Volume 3, pp. 309 - 324.

Quinn, T. M. and Grodzinsky, A. J., 1993. Longitudinal modulus and hydraulic permeability of poly (methacrylic acid) gels: effects of charge density and solvent content. *Macromolecules.* 26(16), pp.4332-4338.

Rabinowicz, E., 1953. A quantative study of the wear process. *Proceedings of the Physics Society. Section B 66.11*, pp. 929 - 936.

Ratner, S. B. , Farberova, I. I., Radyukevich, O. V. and Lure, E. G., 1964. Correlation between the wear resistance of plastics and other mechanical properties. *Soviet Plastics*;7:37–40 [in Russian].

Rotork, 2012. *Preliminary Results 2012.* Bath: Rotork.

Rotork, 2013. *Rotork Home Page - English.* [Online]
Available at: http://www.rotork.com/en/
[Accessed 9th October 2013].

Samyn, P. and Schoukens, G., 2008. Calculation and significance of the maximum polymer surface temperature T* in reciprocating cylinder-on-plate sliding. *Polymer Engineering Science,* Volume 48.4, pp. 774 - 785.

Samyn, P. and Schoukens, G., 2008. Experimental extrapolation model for friction and wear of polymers on different testing scales. *International Journal of Mechanical Sciences.* 50(9), pp.1390-1403.

Scholz, C. W. R., 2013. Stick-slip and wear behaviour of ceramic and polymer materials under reciprocating sliding conditions. Turin, World Tribology Congress.

Senthilvelan, S. and Gnanamoorthy, R., 2009. Efficiency of injection moulded polymer composite spur gears. *Proceedings of the IMechE Part J: Journal of tribology,* Volume 223, pp. 925 – 928.

British Standards, 1987. *BS6168 - Specification for non-metallic spur gears.*

British Standards, 2006. *BS ISO 6336-2 - Calculation of Load Capacity of Spur and Helical Gears.*

Taburdagitan, M. A. M., 2006. Determination of surface temperature rise with thermo-elastic analysis of spur gears. *Wear,* Volume 261, pp. 656 - 665.

Tanaka, K., Uchiyama, Y. and Toyooka, S., 1973. The mechanism of wear of polytetrafluoroethelene. *Wear,* Volume 23(2), pp. 153 – 172.

Tsukamoto, N. and Terashima, K., 1986. Development of plastic gears for power transmission (various methods of lengthening the life of plastic gears and their effect). *Bulletin of JSME,* Volume 29, pp. 249 - 255.

Tworzydlo, W. W., 1998. Computational micro and macroscopic models of contact and friction: formulation, approach and applications. *Wear,* Volume 220, pp. 113 - 140.

Unal, H., Sen, U. and Mimaroglu, A., 2004. Dry sliding wear characterisitics of some industrial polymers against steel counterface. *Tribology International,* Volume 37, pp. 727 - 732.

University of Cranfield, 2009. *A Short Course in Spur Gears.* Cranfield.

Van De Velde, F. and De Baets, P., 1997. The friction and wear behaviour of polyamide 6 sliding against steel at low velocity under very high contact pressures. *Wear,* Volume 209, pp. 106 - 114.

Vick, B. F. M., 2001. A basic theoretical study of the temperature rise in sliding contact with multiple contacts. *Tribology International,* Volume 34, pp. 823 - 829.

Vinogradov, G. V., Mustafaev, V. A. and Podolsky, Y. Y., 1965. A study of heavy metal-to-plastic friction duties and of the wear of hardened steel in the presence of polymers. *Wear,* Volume 8.5, pp. 358 – 373.

Walton, D. and Shi, W., 1989. A comparison of ratings for plastic gears. *Proceedings of the IMechE,* Volume 203, pp. 31 - 38.

Walton, D. and Shi, Y. W., 1994. Load sharing in metallic and non-metallic gears. *Proceedings of the IMechE,* Volume 208, pp. 81 - 87.

Walton, D., Cropper, A. B., Weale, D. J. and Meuleman, P. K., 2002. The efficiency and friction of plastic cylindrical gears. Part 1: Influence of materials. *Proceedings of the IMechE. Part J: Journal of Engineering Tribology,* Volume 216, pp. 75 - 92.

Weiss, G. H., 1983. Random walks and their applications. *American Scientist,* Volume 71, pp. 65 - 71.

Williams, J. A., 1999. Wear modelling: analytical, computational and mapping: a continuum mechanics approach. *Wear,* Volume 225, pp. 1 - 17.

Wright, N. A. and Kukureka, S. N., 2001. Wear testing and measurement techniques for polymer composite gears. *Wear,* Volume 251, pp. 1567 - 1578.

Xiao, L., Björklund, S. and Rosén, B. G., 2007. The influence of surface roughness and the contact pressure distribution on friction in rolling/sliding contacts. *Tribology International,* Volume 40, pp. 694 - 698.

Xie, Y. and Williams, J., 1996. The prediction of friction and wear when a soft surface slides against a harder rough surface. *Wear,* Volume 196, pp. 21 - 34.

Yakut, R., Dozcukoglu, H. and Demirci, M. T., 2009. The load capacity of PC/ABS spur gears and investigation of gear damage. *Archives of Material Science,* Volume 29.1-2, pp. 84 – 92.

Yamaguchi, 1982. The limiting pressure-velocity (PV) of plastics under unlubricated sliding. *Polymer Engineering and Science,* Volume 22, pp. 248 - 253.

Yi, J. and Quinonez, P. D., 2005. Gear surface temperature monitoring. *Proceedings of the IMechE Part J: Engineering Tribology,* Volume 219, pp. 99 - 105.

Young and Budynas, 2011. *Roark's Formulas for Stress and Strain.* 8th ed. : McGraw-Hill.

Zhang, H. Q., Sadeghipour, K. and Baran, G., 1999. Numerical study of polymer surface wear caused by sliding contact. *Wear,* Volume 224, pp. 141 - 152.
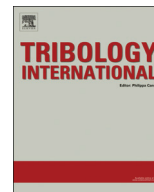
APPENDIX

8.1 Journal Publication 1

Evans, S. M. and Keogh, P. S., 2016. Efficiency and running temperature of a polymer–steel spur gear pair from slip/roll ratio fundamentals. *Tribology International*, *97*, pp.379-389.

Efficiency and running temperature of a polymer–steel spur gear pair from slip/roll ratio fundamentals

S.M. Evans [a,b,*], P.S. Keogh [a]

[a] Department of Mechanical Engineering, University of Bath, Bath BA2 7AY, UK
[b] Rotork plc, Brassmill Lane, Bath BA1 3JQ, UK

ABSTRACT

A new methodology to predict the transient operational temperature of a polymer–steel gear pair under loaded running is presented. For the involute gear form, rolling and sliding leads to a loss of gear efficiency and generation of heat in the contact zone. The power dissipated is used to set the conditions for a series of rod on disc experiments. The rod-on-disc data are processed in a time averaging procedure, which allows prediction of the complete gear temperature. This is assessed with analytical and finite element models to validate the predicted temperature rise against the experimental data. The significance is that the experimental procedures may be used to assess gear thermal performance without testing full gear pairs.

© 2016 Elsevier Ltd. All rights reserved.

1. Introduction

Spur gears that are machined or injection moulded from polymers are becoming increasingly prevalent in geared systems since they can be manufactured cost effectively, especially when moulded. They also have a lower inertia than metallic gears, which can be advantageous in terms of the dynamic response of a gear train used in low power transmission applications. In addition, as the number of polymer gears manufactured per year rivals that of metallic gears there is a desire to utilise them in higher power applications. Metallic spur gears have been well-researched and developed and it is now possible to design them with a high degree of confidence, taking account of strength and wear. However, it is less straightforward to calculate the strength of polymer spur gears due to the nonlinear properties of polymers and the limited work that has been done to investigate their wear mechanisms. This paper investigates the contact mechanism between two straight cut spur gear teeth (one metal and one polymer) and how it results in heat generated in the zone of contact.

The contact in a straight cut involute spur gear pair has both rolling and sliding elements as first documented by Breeds et al. [1]. Pure rolling occurs at the point at which the contact is in line with the centres of both the pinion and the gear; however, this occurs only at an instantaneous point. As the contact approaches

this point and then moves away from it the sliding velocity decreases and then increases, respectively. This action can be modelled using the concept of equivalent cylinders, as reported by Hamrock et al. [2] who associates, for each point in the contact sweep, two cylinders of differing radii in contact with relative velocities determined by the rotation of pinion and gear. The sliding velocity can then be calculated through the contact sweep, which will vary through the stroke.

The geometry of a gear is such that fine details of the size and shape of the teeth are superimposed upon the overall diameter of the circular gear. A full thermal analysis of the complete gear geometry would therefore be complex and an alternative predictive model based on the equivalent cylinders analogue would be preferable. This alternative model would also require experimental validation, for example, from an axially aligned steel rod in sliding contact with a polymer disc. The manner in which experimental and predicted results are compared would be critical for the validation process and this provides a focus for the procedures described in this paper.

The works of Hooke et al. [3] and Breeds et al. [1] make substantial inroads into understanding how spur gears run together and what the contact mechanics are of the gear teeth. In particular, the actions of rolling and sliding between the driven and driving gear are described. Furthermore, they indicate how this geometry driven contact, so particular to involute spur gears, may influence the efficiency of any given gear pair as well as resistance to wear, which are both instrumental in temperature rise. With reference to polymer–steel contact in involute gears a study was conducted using a Bowden–Leben stick-slip machine, which is a conventional

---

tribometer utilising a pin sliding against a flat surface (Bowers et al. [4]). For steel running against nylon, values of 0.37 and 0.34 for static and dynamic friction, respectively, were published. Clearly, the materials chosen for the gears will have a large effect on the friction and associated efficiency, which were measured by Walton et al. [5]. The efficiency ranged between 88% and 98% depending on material, load and speed. Overall, the material is a driving factor in the increase or decrease of efficiency, but the geometry, hence slip ratio is also important. Xie and Williams [6] made progress in predicting the coefficient of friction and wear between a randomly rough hard surface and a softer surface. They used a technique developed by Greenwood and Williamson [7] and expanded it to include specific plastic microcutting of the softer material by the harder. Although progress has been made in the link between this and the actual contact mechanism, much is still to be done to quantify it completely. Indeed, in medical prosthetics, there has been much experimentation to validate a particular geometry of ball and cup of defined materials. Fisher et al. [8] found that surface roughness contributes greatly to the wear of a polymer in contact with a metal. They also concluded that the wear was not dependent on sliding velocity, however, the maximum sliding speeds used were 240 mm/s, which are lower than those generally experienced by gear teeth.

Blok [9] describes the concept of flash temperature, which provides a method for estimating the likely temperature between two contacting and sliding surfaces. If the flash temperature for a polymer–steel spur gear pair is above the melting point of the polymeric material, failure of the component will clearly be imminent. This has been expanded and improved upon on by Samyn and Schoukens [10] and also by Conte et al. [11] with inclusion of thermal diffusivity for the material in question. A numerical solution has been developed specifically for the application to spur gear teeth by Mao [12], who accounts for the effects at the tooth tip as the mesh starts and finishes, but it is considerably more complex than the Blok model. Attempts to reduce the running temperature to see if that materially affects the wear rate of the gears were carried out by Kim [13] and Duzcukoglu [14] by drilling small holes through the base of the root of the tooth to let air circulate more freely across the tooth flank. These studies found that reducing the running temperature of the gears also reduces the wear rate. Other experiments include loaded running of gears for temperature measurement and wear measurement, as in the work of Hooke et al. [15].

Another test method uses a back-to-back apparatus with one electric motor driving through the gear pair under investigation to the driven motor, which acts as a generator and so provides the load. This was undertaken by Senthilvelan and Gnanamoorthy [16] and surface features were observed that are relevant. However, no further analysis or conclusions for wear mechanisms or temperature rise were given. Hooke et al. [15] used a four-square rig with a single electric motor to drive two sets of spur gears connected across two parallel shafts. The driven gears were manufactured from case hardened steel, whilst the others were test polymer gears, as reported by Mao et al. [17,18]. The load was applied to the system through a lever arm, even as the gears became worn. These studies were concerned with how temperature and differing materials affect the wear of the gears. Acetal was used as the gear test material and it was concluded that it has a critical limit in terms of slip/roll beyond which complete failure of the material occurs due to thermal effects.

Analytical models have been constructed that predict the temperature rise around a contact area such as in the work of Vick and Furey [19] who used a Green's function approach. For steel running against a polymer the temperature rise should not exceed the polymer softening or melting temperature as this would clearly result in a catastrophic failure. This is the basis for a concept of the pressure–velocity limit for a polymer as proposed by Archard [20]. In a study by Walton et al. [21], load sharing of polymer gears was investigated using computational finite element techniques. They were concerned only with the loading between the gear teeth. A thermoelastic model can be created using finite element techniques as done by Taburdagitan and Akkok [22]. It is of interest as it illustrates some of the difficulties associated with producing this type of model. The model mesh was refined around the gears and the driven gear was considered loaded via a torsional spring at its centre. The conclusion was that tip relief of the gear teeth is important to the temperature rise as applying it can help to reduce the slip speed when the driving gear initially touches the driven gear and load transfer occurs. In a study by Unal et al. [23] of extremely high pressures of steel rubbing against a polymer, it was found that the wear rate of a polymer in this case is not strongly dependent on the pressure applied.

In this paper, an experiment involving an axially aligned steel rod applied to the circumference of a polymer disc is described. This experiment was augmented to run a full gear pair, of which the running temperatures were also measured. An analytical thermal model is formulated to predict the temperature rise in the axially aligned rod on disc experiment. A finite element model was also employed as an alternative method for prediction, though limited to a fixed heat source on the disc. This simplification is used to reduce the complexity of a full gear model and the mesh density required at the contact. Lee et al. [24] present a case in which a high mesh density is implemented for asperity–asperity interaction. Finally, a novel method of time averaging is presented to directly correlate the aligned rod on disc experiment with full the gear pair experiment.

2. Geometry, flash temperature, loadings and heat flux evaluation

In this section, pertinent evaluations are made that are appropriate for geometric and material parameters associated with the experimental system and gears considered in Section 3.

2.1. Geometry

A feature of the involute profile that is known, but not generally considered significant, is that slip occurs between the teeth flanks. This results in a reduction in efficiency of around 1–2% [5]. However, in an unlubricated polymer–steel gear pair it gives rise to heat generation. In the line diagram shown in Fig. 1, two contacting surfaces are represented by two separate cylinders of radii r_a and r_b. The rotational speeds of these cylinders are equal to those of the gears, respectively. This technique is described by Hamrock et al. [2] and the slip speed is

$$v = (r_{bg}\sin\alpha + s)\omega_b - (r_{ag}\sin\alpha - s)\omega_a \qquad (1)$$

where r_{ag} is the pinion pitch radius, r_{bg} is the gear pitch radius, α is the pressure angle (rad), s is the distance of the point of contact from the centre line, ω_a is the rotational speed (rad/s) of the pinion, and ω_b is the rotational speed (rad/s) of the gear. Accordingly, $r_a = r_{ag}\sin\alpha - s$ and $r_b = r_{bg}\sin\alpha + s$.

2.2. Flash temperature

Blok [9] proposed that if two surfaces are rubbed together, heat will be generated at the interface giving rise to a flash temperature. Because of the transient and constrained nature of the contact, this temperature rise will be higher than expected for the load and speed conditions of a gear pair. The flash temperature is

given by

$$T_f = A \frac{q_{av}}{\sqrt{kc}} \sqrt{\frac{b}{v}} \tag{2}$$

where v is the sliding velocity, b is the length of the heat source in the sliding direction, k is the thermal conductivity of the material, c is the specific heat per unit volume, A is a form factor offered by Blok, which is specific to the distribution of the heat flux, and q_{av} is the average heat flux input over the length b. Fig. 2 shows a typical evaluation of T_f for a gear, where v has been evaluated from Eq. (1) for $-2 \leq s \leq 2$ (mm). However, T_f is only a transient parameter and takes no account of the gradual accumulation and cyclic

Fig. 1. Equivalent cylinders.

Fig. 2. Flash temperature profile. Data used: $A = 1.1$, $k = 0.25$ W/m/K, $c = 500$ J/kg/K (steel), $c = 1670$ J/kg/K (nylon), b, v and q_{av} vary through stroke according to geometry of contact.

nature of the heat generation in a continuously rotating power driven gear pair. Hence the flash temperature alone cannot provide the final operating temperature of the gears.

2.3. Loadings and heat flux evaluation

The force generated between the driving and driven gear acts normal to the two gear teeth curvatures at their instantaneous point of contact and can be calculated from the driving torque, the acting radius and the pressure angle of the involute. The force normal to that point of contact is given by

$$F_{cn} = \frac{\tau}{r_a} \cos \alpha \tag{3}$$

where τ is the input torque and r_a is the reference radius of the pinion (Fig. 1). In the case of the studied gear pair, $\tau = 0.85$ Nm and $r_a = 6$ mm, which yields a normal force of 133 N. The materials investigated are steel (EN 1.1186, EN8) for the pinion and a polymer (POM Delrin 100) for the gear. The dynamic coefficient of friction between these materials is taken as 0.34 from Bowers et al. [4]. Since polymer–steel gears are generally unlubricated, the losses arising from a potential increase in friction need to be assessed. It is important to analyse the resulting temperature increase in order to be able to ensure that the polymer is able to operate within its temperature limit. It follows that as the equivalent cylinders change to represent the contacting radii through the tooth stroke and the normal force remains constant, the penetration of the steel gear into the polymer gear changes. Hence the area onto which the heat input is applied also changes. To this end, the deflection must be calculated to determine the heat flux for any given point in the contact between the teeth.

The maximum stress and circumferential length of contact area for a cylinder pressing against a cylinder is given by Hertzian contact stress theory [25]. Let subscript a denote the steel pinion material and subscript b the gear polymer material. Then

$$C_E = \frac{1 - v_a^2}{E_a} + \frac{1 - v_b^2}{E_b} \tag{4}$$

where E is the Young's modulus and v is Poisson's ratio. The maximum Hertzian stress is

$$\sigma_{max} = 0.798 \sqrt{\frac{F_{cn}(r_a + r_b)}{2C_E w r_a r_b}} \tag{5}$$

and the circumferential length of contact due to penetration is

$$b = 1.6 \sqrt{\frac{2F_{cn}C_E r_a r_b}{w(r_a + r_b)}} \tag{6}$$

where w is the gear width and F_{cn} is the normal load. For completeness, the penetration depth is

$$\delta = \frac{2F_{cn}C_E}{\pi w} \left[\frac{2}{3} + \ln \frac{4r_a}{b} + \ln \frac{4r_b}{b} \right] \tag{7}$$

Given a disc width of 10 mm, Table 1 shows evaluated variation of parameters with variation of distance along the line of contact s as the teeth move through a contact cycle.

Table 1
Contact stress at points along the line of contact s.

s (mm)	0.0	0.1	0.2	0.3	0.4	0.6	0.9	1.1	1.4
σ_{max}(MPa)	74.5	73.1	71.7	70.5	69.3	67.2	64.5	62.9	60.9
b (mm)	0.73	0.73	0.73	0.72	0.72	0.71	0.71	0.70	0.69
r_b (mm)	12.83	12.73	12.63	12.53	12.43	12.23	11.93	11.73	11.43
r_a (mm)	2.05	2.15	2.25	2.35	2.45	2.65	2.95	3.15	3.45
v (mm/s)	0	61	121	182	243	364	547	668	850

The instantaneous power dissipated into the polymer follows as

$$P_T = \phi F_{cn} \mu v \qquad (8)$$

where ϕ is a fractional coefficient and μ is the coefficient of friction (0.34). The precise value of ϕ will thermal conductivity values and the relative size of the disc compared to the rod. For the experimental system, $\phi \approx 1$ is a good approximation. The heat flux into the polymer is

$$Q_T = \frac{\phi F_{cn} \mu v}{wb} \qquad (9)$$

Using the previous data, this is evaluated as 0.848 W/mm² for $s = 0.2$ mm. This is purely the heat generated between the two contacting surfaces. The relative proportions of that heat transport that are shared between the polymer and the steel are accounted for in the models presented in the later sections.

3. Experimental thermal assessment

The assessment of temperature rise was made in two separate experiments. The first was designed to emulate the equivalent cylinders (Fig. 1) and consisted of a disc rotating against a loaded, but stationary and axially aligned rod. The second experimental arrangement measured the temperature rise in a complete gear. The purpose of the axially aligned rod-on-disc experiments is to replicate the range of slip and torque conditions expected from a complete gear design. In Section 5.1 it is shown how the rod-on-disc results may be used to predict the temperature rise for a complete gear. This avoids the problem of redesign of a complete gear and/or gear train should excessive temperature rise become evident.

3.1. Steel rod axially aligned on disc

The polymer discs were made from Delrin 100 (Poly-oxymethylene, POM). The experimental hardware (Fig. 3) consisted of a 100 W brushless DC electric motor driving a small 5:1 reduction epicyclic gearbox. The gearbox was connected, via a flexible coupling, to a steel shaft. The polymer disc was keyed to this shaft and so could be rotated up to a maximum speed of 800 rev/min. Motor speed was measured by way of a Hall Effect surface mount encoder sensing the angular position of a small

magnet attached to the rear of the motor shaft. The steel rod was held by an aluminium block, which was bolted to the load transducer. This consisted of a mild steel bar that had been machined to amplify the strain at a specific point. A full bridge strain gauge was adhered to the steel bar in the position of the maximum strain. The surface temperature of the disc was measured using an infra-red sensor, the positioning of which in relation to the disc surface is shown as an inlay to Fig. 3. It was approximately 5 mm from the disc and was adjusted for an emissivity value of 0.91 for the device calibration, as provided by Beardmore [26].

The speed of rotation of the disc and the load applied through the rod were both calibrated using external measurements and were found to be within a 0.5% tolerance band. An investigation was made as to the magnitude of any fluctuations that may be present in the temperature data resulting from manufacturing tolerances. Fig. 4(a) shows the temperature of the disc surface, measured with maximum time resolution. Starting from a thermally heated state, the temperature decays for around 8 s at which point the disc was rotated at approximately 1 Hz. The fluctuation of the surface temperature can be seen clearly as the bulk of the material continues to cool, which is attributable to load variations between the aligned rod and disc caused by slight out of concentricity of the disc (Fig. 4(b)). The ± 1 °C variations were considered to be within bounds for follow-on experimental investigations.

The aim was to measure surface temperature rise in the disc at a variety of speeds that would correspond with a series of positions along the line of contact in a real gear. Fig. 5 shows a trial run of the experiment at full speed and load for 1 h. The detailed view between 30 and 40 min shows the temperature fluctuations caused by the varying load. The temperature rise in the disc is initially steep, but the rate of temperature rise decreases with time. An overall bulk increase of temperature of the experimental hardware (aluminium housing, plate, motor and gearbox) also gave rise to an additional increase in surface temperature. There are two distinct knee points of the data at 700 s and 2800 s. These represent conditions of saturated bulk heating and a limit to the experimental time was therefore set at 1800 s.

In association with Table 1, the corresponding disc rotational speeds, ω, are given in Table 2. Fig. 6 shows the measured temperature corresponding to slip speeds associated with s over the range 0.1–1.1 mm. Surface temperatures of the disc increase as the slip speed increases until it is seen that the data sets for 0.9 mm
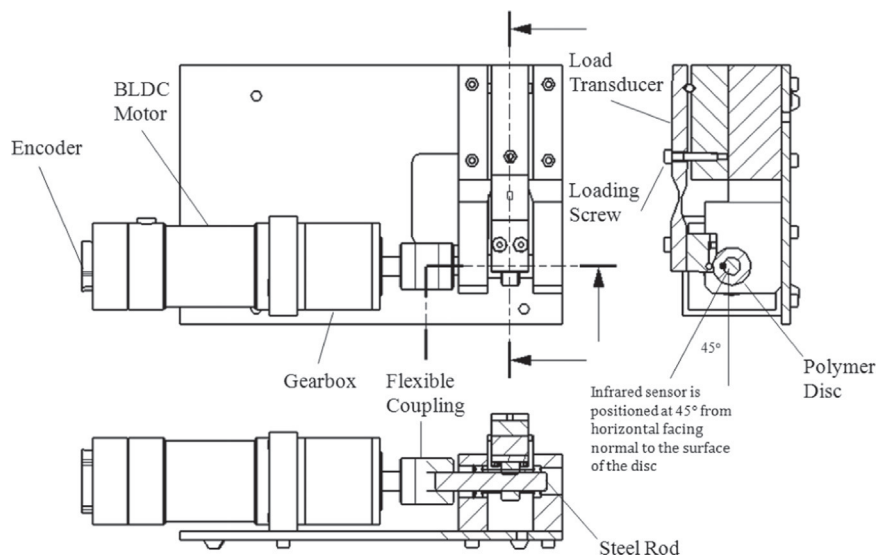

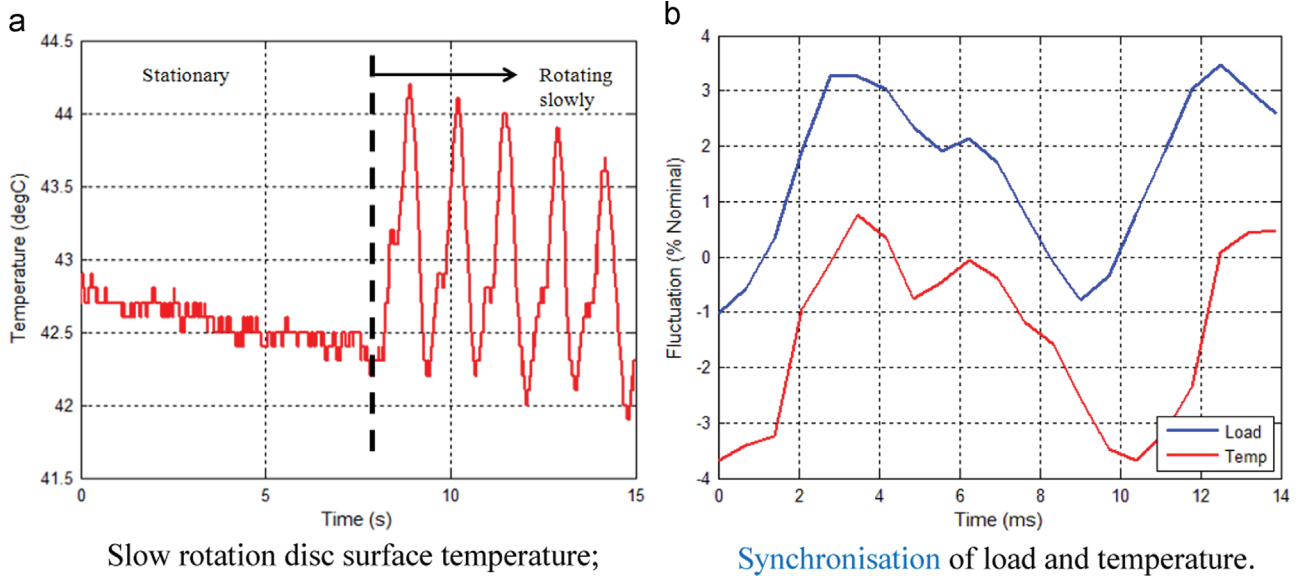**Fig. 3.** Axially aligned steel rod-on-disc facility.

Fig. 4. (a) Slow rotation disc surface temperature; (b) synchronisation of load and temperature.
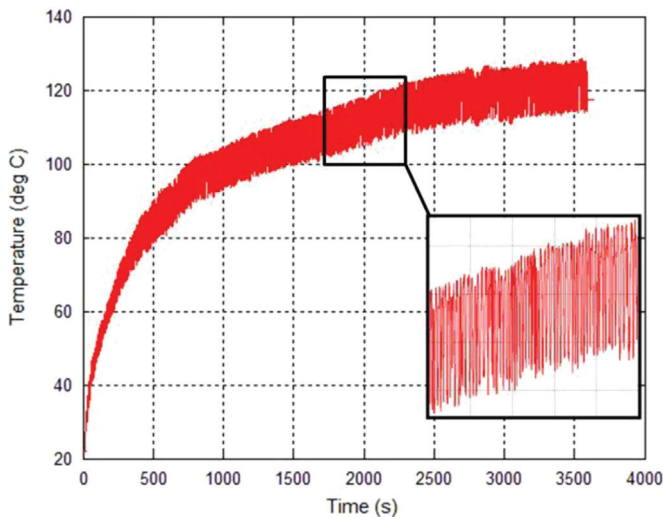

Fig. 5. Trial run of measured disc surface temperature to determine the required measurement time.

Table 2
Correspondence of speeds with gear contact position.

s (mm)	0.0	0.1	0.2	0.3	0.4	0.6	0.9	1.1	1.4
v (mm/s)	0	61	121	182	243	364	547	668	850
ω (rev/min)	0	45	91	138	184	275	414	505	643

and 1.1 mm overlap. Also, the 1.1 mm set exhibits a higher level of temperature fluctuation as time increases, which is attributable to amplified load variations.

3.2. Temperatures for a gear pair

This experiment used the same motor, load transducer assembly and control electronics as in the previous axially aligned rod on disc setup. This arrangement, however, drives a pair of gears together under a constant load and speed. Fig. 7 shows the experimental hardware. Pertinent data are given in Table 3.

The motor drives the steel pinion, which is supported in two concentric bearings; the first allows the pinion to rotate and the second allows the frame in which the pinion is mounted to also rotate. This frame holds the polymer gear. The output shaft from the polymer gear is connected to a magnetic particle brake. When a voltage is applied to the brake it provides a resistive load to the rotation of the output from the gear, which in turn attempts to rotate the frame. The frame is reacted back to the support structure through the load transducer and so the torque generated by the output shaft from the gear is measured directly. Gear temperature was measured using the same infra-red sensor as in Fig. 3. This was positioned facing the polymer teeth directly as they exited from the gear mesh. The system torque and speed were set using a trial gear, which was then replaced with the experimental gear and the experiment was started. The speed and torque of the input pinion was 168 rev/min and 0.85 Nm, respectively. Each run lasted for 1 h to ensure that the temperature rise due to teeth contact had been captured. Four runs were undertaken and labelled in order as: G1, followed by G2 after 2.5 h, followed by G3 after 1 h, followed by G4 after 1 week. Fig. 8 shows the measured temperature profiles. The second profile, G2, is slightly higher by approximately 2 °C than the first, G1, while G3 is higher by around 4 °C. The final profile, G4, was taken after a delay of a week so that all latent heat in the system had dissipated and it lies below G1. The ambient temperature data sets were also recorded and are presented in Fig. 8. The gear temperature data were then adjusted to account for the ambient temperature during each of the experiment runs. The data were adjusted with respect to the first run G1 in the following manner:

$$G2_{Adj} = G2 - (G2_{Amb} - G1_{Amb})$$

$$G3_{Adj} = G3 - (G3_{Amb} - G1_{Amb})$$

$$G4_{Adj} = G4 + (G1_{Amb} - G4_{Amb})$$

Fig. 9 shows the adjusted data. Runs G1, G2 and G4 are nearly coincident. However, G3, which was run with only a 1 h delay after G2, is approximately 4 °C higher in temperature than the others. Table 4.
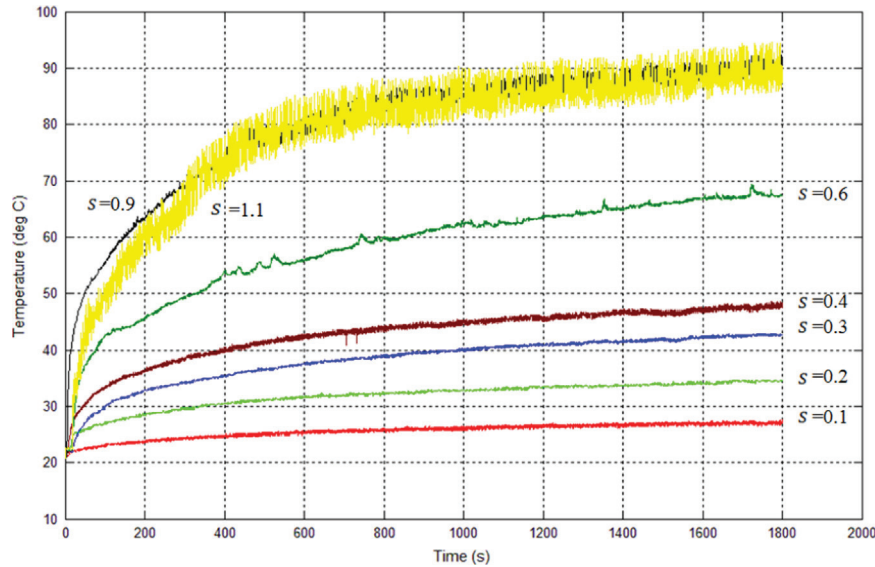
Fig. 6. Aligned rod on disc temperature results.
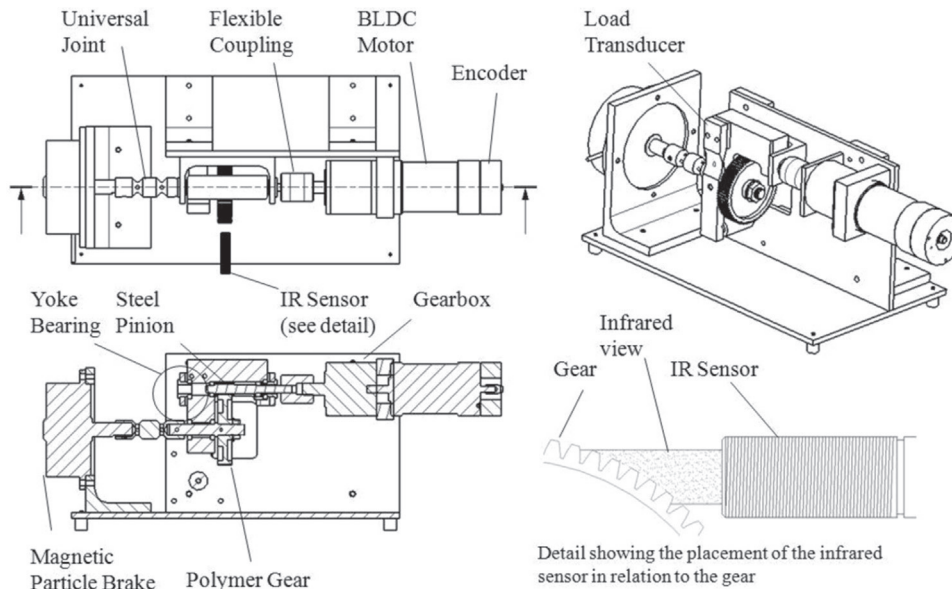
Fig. 7. Gear running experimental hardware.

4. Thermal modelling for the axially aligned rod on disc

4.1. Finite element (FE) model

A solver was used and the following heat transfer coefficients were applied:

(a) 200 W/m²/°C between the shaft and the disc.
(b) 12 W/m²/°C shaft to the environment.
(c) 1.9 W/m²/°C the disc to environment.

The heat load of 0.13 W was uniformly distributed on the outer circumferential surface of the polymer disc.

A FE model of the aligned rod and disc arrangement, without rotation, was established to provide an initial assessment of the thermal response. Fig. 10 shows the meshed shaft and disc. The finite element model has been developed as a design environment alternative to the full analytical model described in Section 4.2. A series of these models should be used in conjunction with the time

Table 3
Pinion/gear data.

	Pinion	Gear
No of teeth	12	75
Torque	0.85 Nm	5.3 Nm
Speed	168 rev/min	26.7 rev/min
Power	15 W	< 15 W
Module	1	1
Pressure angle	20°	20°
Reference diameter	12 mm	75 mm
Material	Steel 1.0511	POM
Profile shift	+0.5	−0.5
Method of manufacture	Hobbed	Hobbed

averaging technique described in Section 5.1 to determine the heat rise in a gear. A heat flux distribution is applied to the outer diameter of the polymer disc and convection boundary conditions to the environment were set up on the flanks of the disc and also on the external surfaces of the steel shaft. Since the model was non-
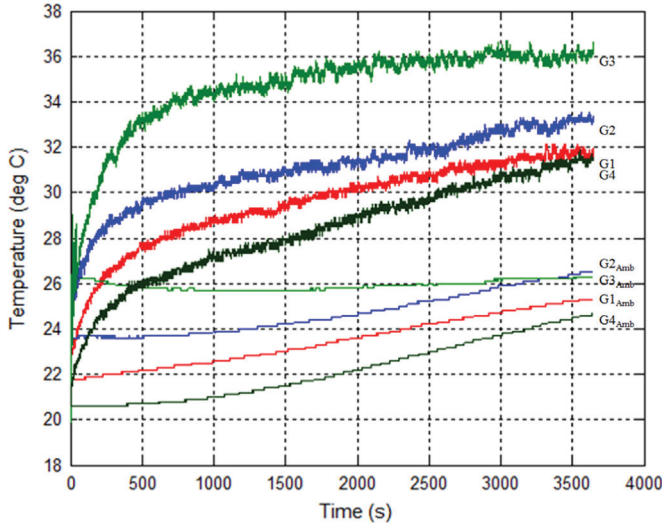
Fig. 8. Measured gear running temperatures.
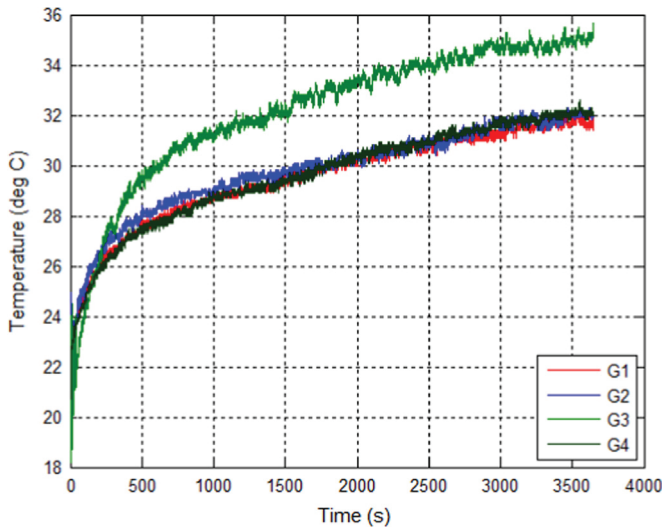
Fig. 9. Gear running temperatures – adjusted for ambient.

Table 4
Model parameters.

	Disc	Shaft
Element type	20 node hexagonal	20 node hexagonal
Element number	3080	572
Element size	1 mm	3.4 mm
Element material	POM	Steel

rotational, an averaged heat flux was applied over the circumferential surface of the polymer disc. Firstly, a heat flux from the aligned rod to the polymer disc was evaluated according to Eq. (9). This was then scaled to distribute it over the complete circumferential surface according to

$$Q_{FET} = Q_T \frac{A_i}{A_d} \tag{10}$$

where Q_{FET} is the heat flux value of the circumferential distribution applied in the FE model, Q_T is heat flux generated under the aligned rod (Eq. (9)), A_i is the area of indentation of the rod on disc, and A_d is the circumferential area of the modelled disc. The heat flux was applied in a step-like manner and a time dependent solution was obtained for a point on the centreline of the disc, as

shown in Fig. 11. Although the general trend is similar to the experimental measurements of Fig. 9, a more accurate dynamic thermal analysis from the rod heat flux is appropriate.

4.2. Analytical dynamic thermal model

Flash temperature predictions such as in Fig. 2 indicate behaviour in the immediate vicinity of contact between the two surfaces. However, cyclical thermal response due to rotation is not predicted. Higher order analytical modelling is possible, for example, to determine temperature rise generated in magnetic bearing touchdown events (Keogh and Yong [27]). Consideration is therefore given to the interaction of the steel rod in contact with the rotating polymer disc. The model is based around the heat transfer equation in polar coordinates (Fig. 12), which may be axially averaged across the width of the polymer disc:

$$\frac{\partial^2 T}{\partial r^2} + \frac{1}{r}\frac{\partial T}{\partial r} + \frac{1}{r^2}\frac{\partial^2 T}{\partial \theta^2} - \frac{1}{\alpha}\frac{\partial T}{\partial t} - \beta T = 0 \tag{11}$$

where T is the axially averaged disc temperature relative to the ambient temperature, T_a, (r, θ) are polar coordinates, and

$$\alpha = \frac{k}{\rho c_p}, \beta = \frac{2h}{Lk} \tag{12}$$

where k is the thermal conductivity of the polymer, ρ is its density, c_p is the specific heat capacity, L is the disc width, and h is a convection heat transfer coefficient. The boundary condition at the outer surface of a cylinder of radius $r = R_I$ is

$$k\frac{\partial T}{\partial r}\bigg|_{r=R_I} = q_I(\theta, t) \tag{13}$$

where $q_I(\theta, t)$ is the axially averaged circumferential heat flux into the disc. Taking the Laplace transform of Eq. (11) yields

$$\frac{\partial^2 \overline{T}}{\partial r^2} + \frac{1}{r}\frac{\partial \overline{T}}{\partial r} + \frac{1}{r^2}\frac{\partial^2 \overline{T}}{\partial \theta^2} - \frac{p}{\alpha}\overline{T} - \beta\overline{T} = 0 \tag{14}$$

where p is the Laplace transform variable. Expanding transformed temperature and heat flux as a Fourier series in the circumferential coordinate gives

$$\overline{T}(r, \theta, p) = \sum_{-\infty}^{\infty} \overline{T}_n(r, p)e^{in\theta}, \overline{q}_I(\theta, p) = \sum_{-\infty}^{\infty} \overline{q}_{In}(p)e^{in\theta} \tag{15}$$

The equation of heat conduction becomes

$$\frac{\partial^2 \overline{T}_n}{\partial r^2} + \frac{1}{r}\frac{\partial \overline{T}_n}{\partial r} - \left(\frac{n^2}{r^2} + \frac{p}{\alpha} + \beta\right)\overline{T}_n = 0 \tag{16}$$

The Bessel function solution that is finite as r tends to 0 is

$$\overline{T}_n(r, p) = A_n I_n(\lambda r) \tag{17}$$

where $\lambda = \sqrt{\frac{p}{\alpha} + \beta}$. The boundary condition of Eq. (13) is satisfied by

$$A_n = \frac{1}{k\lambda I'_n(\lambda R_I)}\overline{q}_{In}(p) \tag{18}$$

Hence

$$\overline{T}_n(r, p) = \frac{I_n(\lambda r)}{k\lambda I'_n(\lambda R_I)}\overline{q}_{In}(p) \tag{19}$$

The following recurrence relation (Abramowitz and Stegun [28]) applies:

$$I'_n(z) = I_{n+1}(z) + \frac{n}{z}I_n(z) \tag{20}$$
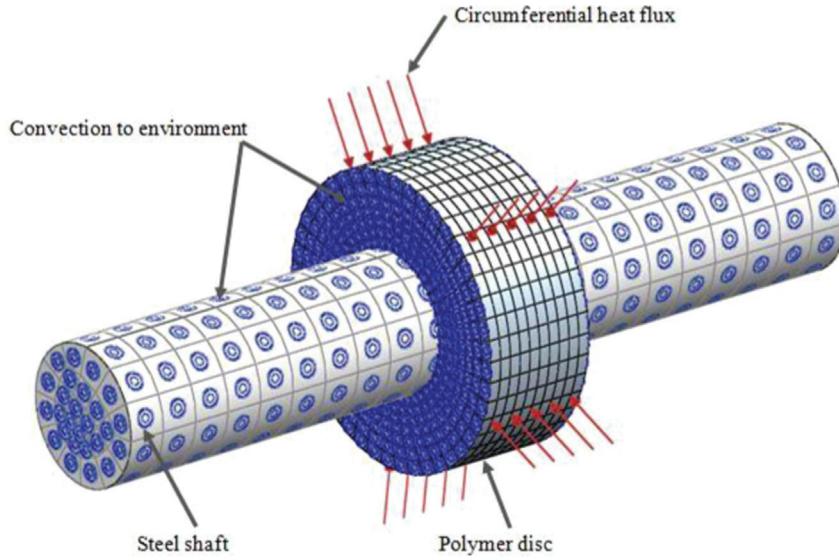
Fig. 10. Circumferential heat flux FE model.
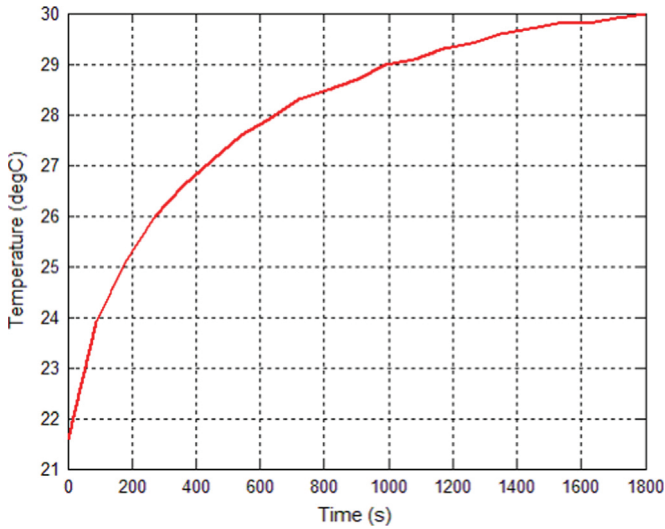
Fig. 11. Disc centreline surface temperature prediction from FE model.

Eq. (19) can then be inverted to give a solution in the time domain as

$$T_n(r,t) = \frac{1}{2\pi i} \int_{c-i\infty}^{c+i\infty} \frac{I_n(\lambda r)}{k\lambda \left(I_{n+1}(\lambda R_I) + \frac{n}{\lambda R_I} I_n(\lambda R_I)\right)} \overline{q}_{In}(p) e^{pt} dp \qquad (21)$$

The temperature response may be obtained using the convolution integral

$$T_n(r,t) = \int_0^t H_n(r, t-\tau) q_{In}(\tau) dt \qquad (22)$$

where

$$H_n(r,t) = \frac{1}{2\pi i} \int_{c-i\infty}^{c+i\infty} \frac{I_n(\lambda r)}{k\lambda \left(I_{n+1}(\lambda R_I) + \frac{n}{\lambda R_I} I_n(\lambda R_I)\right)} e^{pt} dp \qquad (23)$$

Because $I_n\left(v e^{\pm \frac{1}{2} \pi i}\right) = e^{-\frac{1}{2} n \pi i} J_n(\mp v)$ has poles on the real axis it is appropriate to complete the contour of integration as shown in Fig. 13. In general, $p = z_\gamma \alpha x^2 / R_I^2$ on the angled lines where $x > 0$ and $z_\gamma = e^{i\gamma}$ on the upper line. Hence

$$dp = 2 \frac{z_\gamma \alpha}{R_I^2} x dx, \quad \lambda_\gamma = \sqrt{\frac{z_\gamma x^2}{R_I^2} + \beta} \qquad (24)$$
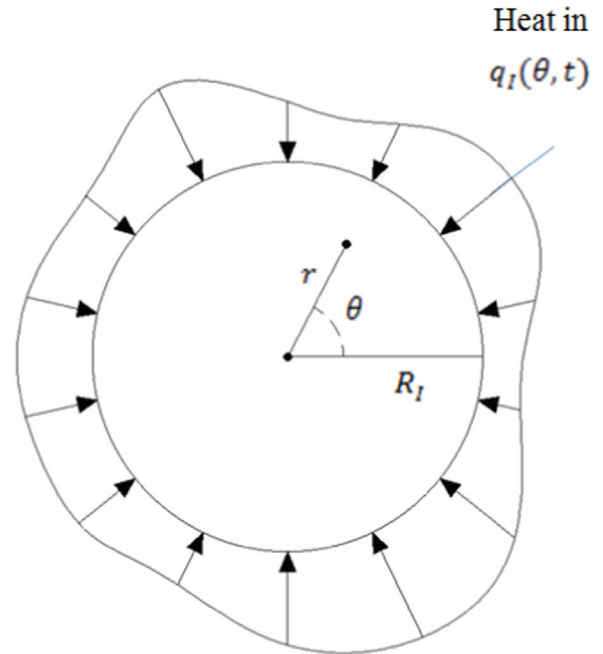
Fig. 12. Geometry and coordinates associated with the polymer disc analytical thermal model.

It now follows that

$$\frac{1}{2\pi i} \int_{c-i\infty}^{c+i\infty} f(\lambda) e^{pt} ds = \frac{z_\gamma \alpha}{\pi i R_I^2} \int_0^\infty f(\lambda_\gamma) e^{\frac{z_\gamma \alpha x^2 t}{R_I^2}} x dx - \frac{z_{-\gamma} \alpha}{\pi i R_I^2} \int_0^\infty f(\lambda_{-\gamma}) e^{\frac{z_{-\gamma} \alpha x^2 t}{R_I^2}} x dx \qquad (25)$$

Since the second term is the complex conjugate of the first term, it follows that

$$\frac{1}{2\pi i} \int_{c-i\infty}^{c+i\infty} f(\lambda) e^{pt} dp = \mathrm{Re}\left(\frac{2 z_\gamma \alpha}{\pi i R_I^2} \int_0^\infty f(\lambda_\gamma) e^{\frac{z_\gamma \alpha x^2 t}{R_I^2}} x dx\right) \qquad (26)$$

In this expression

$$z_\gamma f(\lambda_\gamma) x = \frac{2 R_I^2}{Lk} h_n(x, \rho, \gamma)$$

$$h_n(x,\rho,\gamma) = \frac{z_\gamma x I_n\left(z_\gamma^{0.5}\rho x\right)}{\left(z_\gamma^{0.5}x I_{n+1}\left(z_\gamma^{0.5}x\right) + n I_n\left(z_\gamma^{0.5}x\right)\right)} \tag{27}$$

where $\rho = r/R_I$. It now follows from Eqs. (22) and (23) that

$$H_n(r,t) = \frac{\alpha}{\pi i k R_I}\int_0^t\int_0^\infty\left\{h_n(x,\rho,\gamma)e^{\frac{z_\gamma\alpha x^2(t-\tau)}{R_I^2}} - h_n(x,\rho,-\gamma)e^{\frac{z_{-\gamma}\alpha x^2(t-\tau)}{R_I^2}}\right\}q_{In}(\tau)dxd\tau \tag{28}$$

Considering the axially aligned rod and disc, the heat flux can be regarded as rotating at frequency ω about the circumference of the disc, which is considered to be stationary:

$$q_I(\theta,t) = Q_I(\theta-\omega t) \tag{29}$$

Hence

$$q_I(\theta,t) = \sum_{-\infty}^\infty Q_{In}e^{-in\omega t}e^{in\theta} \tag{30}$$

Then

$$q_{In}(\tau) = Q_{In}e^{-in\omega\tau} \tag{31}$$
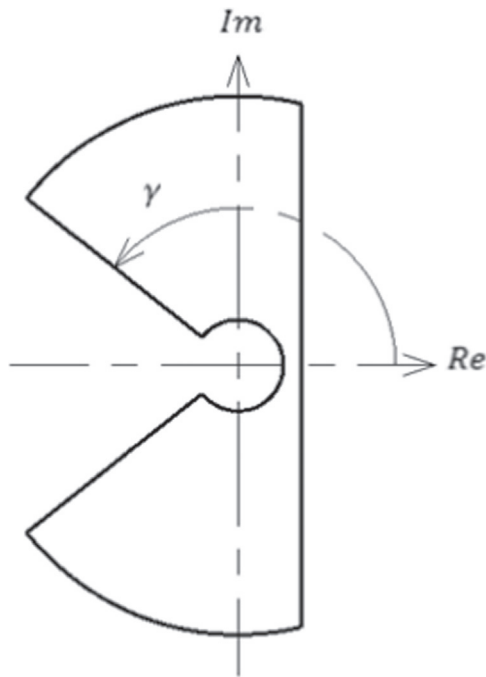
Fig. 13. Completion of the inversion contour.

Substituting into Eq. (28) and performing the time integration yields

$$T_n(r,t) = \frac{1}{2i}(T_{n,\gamma}(r,t) - T_{n,-\gamma}(r,t)) \tag{32}$$

where

$$T_{n,\gamma}(r,t) = \frac{2\alpha}{\pi k R_I}\int_0^\infty h_n(x,\rho,\gamma)\frac{e^{z_\gamma\alpha x^2 t/R_I^2}}{\left(z_\gamma\alpha x^2/R_I^2 + in\omega\right)}dx Q_{In} \tag{33}$$

For a heat flux arising from a Hertzian pressure distribution between the aligned rod and disc, an appropriate expression for the heat flux into the polymer is

$$Q_I(\theta) = \begin{cases} Q_0\sqrt{(\theta_0^2-\theta^2)}, & |\theta| < \theta_0 \\ 0, & |\theta| > \theta_0 \end{cases} \tag{34}$$

where $Q_0 = \phi\mu R_I\omega$ and $2\theta_0$ is the angular extent of the contact zone. The implication of Eq. (34) is that the Fourier coefficients follow as

$$Q_{In} = \begin{cases} \frac{Q_0\theta_0}{2n}J_1(n\theta_0), n \neq 0 \\ \frac{Q_0\theta_0^2}{2}, n = 0 \end{cases} \tag{35}$$

The complete expression for the axially averaged disc temperature is

$$T(r,\theta,t) = \sum_{-\infty}^\infty T_n(r,t)e^{in\theta} \tag{36}$$

This expression was evaluated for the parameters matching the case when $s = 0.2$ mm. Time dependent contour plots of the disc temperature are shown in Fig. 14. The heat source moves in an anti-clockwise sense starting from the right hand side of the disc. After the second rotation it can be seen that the wall is starting to cool as the leading edge of the heat approaches the heat source for the third time. In the 10 rotation plot, the temperature is nearly uniform around the circumference of the disc.

Fig. 15 shows the temperature variation at a fixed point on the circumference at 45° clockwise from the top of the disc. The initial step-like variation is due to the cyclic heating as the heat source (aligned rod) passes the observation point. The steps persist, though are not resolvable on the macroscale of the lower plot.

5. Comparison and analysis of measured and modelled temperatures

The purpose of this section is to assess the level of correlation between the aligned rod on disc temperature measurements, the gear temperature measurements, and the predicted temperature measurements.
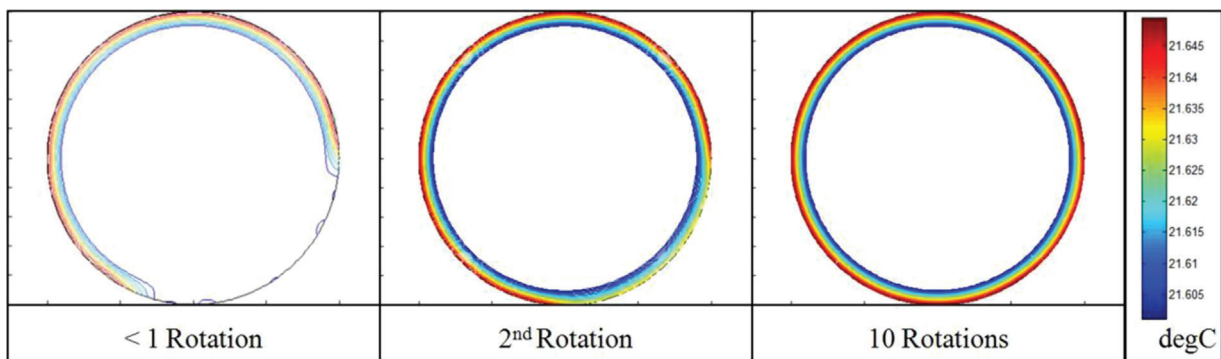
Fig. 14. Disc temperature contours for up to 10 rotations.
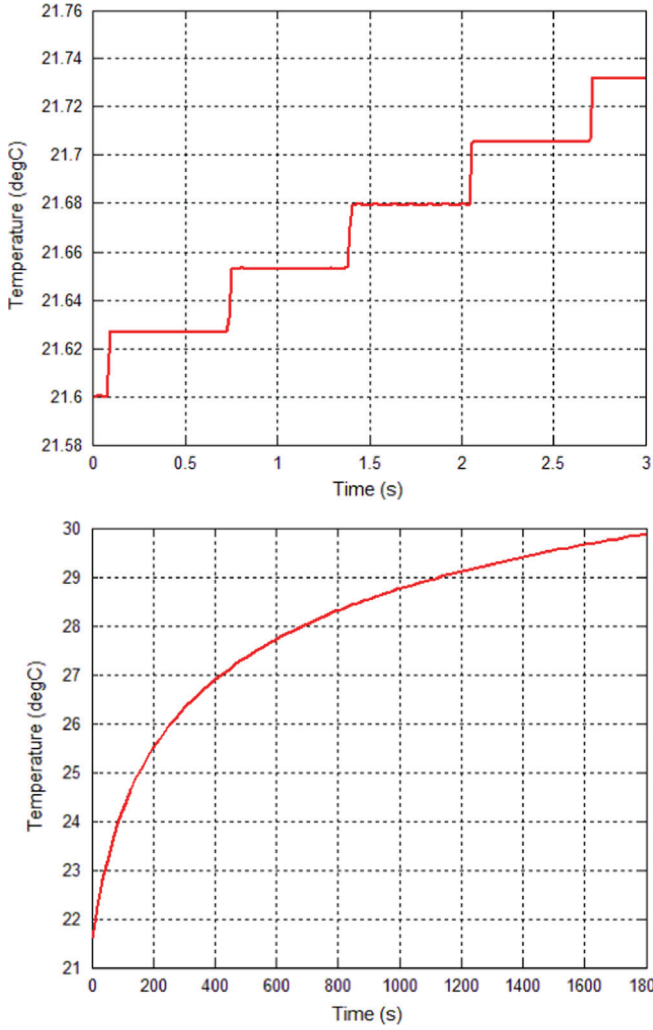
Fig. 15. Fixed point temperature variation with time.

5.1. Aligned rod on disc and gear temperature measurement correlation

The temperature data for the aligned rod on disc need to be transformed so as to be useful to compare with the measured gear temperatures. The issue is that gear tooth slip speeds are variable during operation, while aligned rod on disc slip speeds are constant for each condition of test. The rod on disc measurements are therefore amalgamated to apportion results with appropriate to gear tooth slip speeds at each point of the tooth sweep. The temperature generated at a given point in the tooth contact sweep is a function of both time and distance along the line of contact:

$$T_s = T(t, s) \tag{37}$$

where T_s is the temperature at the point along the line of contact s at time t. As the slip speed, v, varies through the contact sweep, the time increment spent in contact is given by

$$\delta t = \frac{1}{v}\delta s \tag{38}$$

Each aligned rod on disc temperature set ($i = 1, ..., N$) is then averaged according to the time spent in contact to estimate the gear temperature as

$$T_{ave}(t) = \frac{1}{s_0}\sum_{i=1}^{N} T(t, s_i)\delta s_i \tag{39}$$

where s_0 is the length of travel along the line of contact. As the gear and pinion run together, heat flows into the polymer and the steel.

As the teeth share contact, the heat generation will also be shared in the proportion given by the contact ratio, which is given by

$$R_C = \frac{\sqrt{\left(R_{go}^2 - R_{gb}^2\right) + \left(R_{po}^2 - R_{pb}^2\right)} - \sin\alpha}{d\cos\alpha} \tag{40}$$

where R_{go} is the outer radius of the gear, R_{gb} is the base radius of the gear, R_{po} is the outer radius of the pinion, R_{pb} is the base radius of the pinion, α is the pressure angle of the tooth form and d is the circular pitch of the teeth. Incorporating this factor of contact ratio into the summation of the data sets gives the correlated temperature as

$$T_{cor}(t) = \frac{R_C}{s_0}\sum_{i=1}^{N} T(t, s_i)\delta s_i \tag{41}$$

5.2. Comparison of gear temperatures with time averaged rod on disc temperatures and modelled temperatures

Fig. 16 (a) shows the comparison of the summation of the averaged aligned rod on disc and gear temperature measurements. There is an offset between the two series of approximately 2.5 °C. In Eq. (41), the contact ratio depends on the depth of the teeth and, in the case of the real product gear and pinion combination, a

Fig. 16. Comparison of gear and disc temperature data. (a) Without correction. (b) With 70 μm correction.

Fig. 17. Comparison of rod on disc temperatures with the model.

correction of 0.5 mm has been applied. This is to the addendum and dedendum of the gear teeth, which effectively moves the contact towards the gear centre. This is don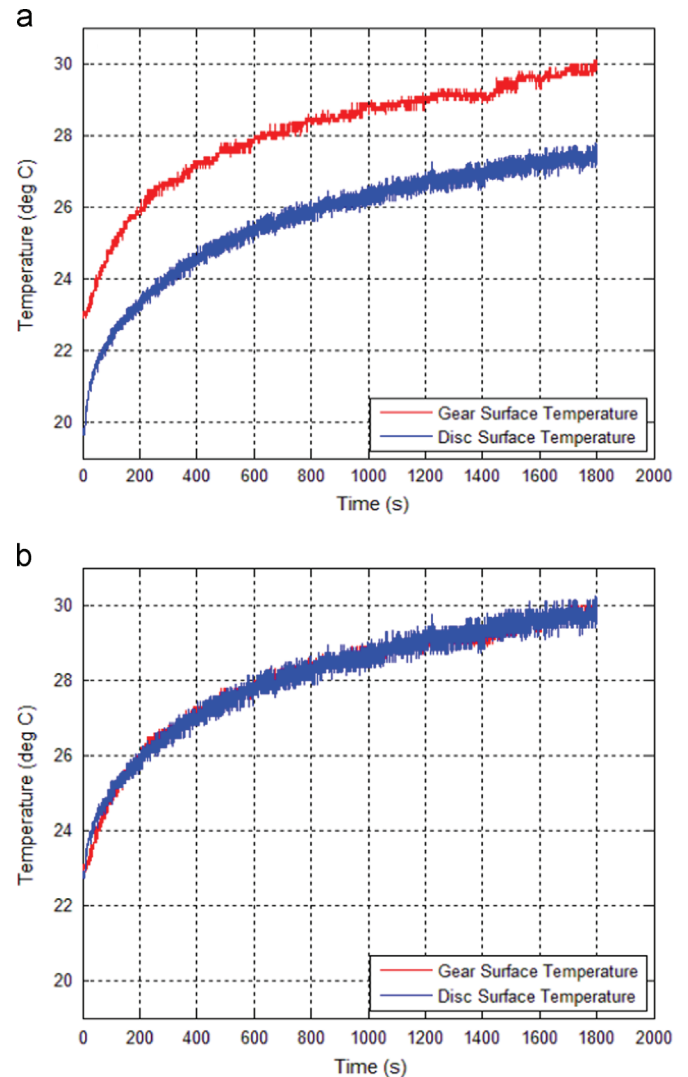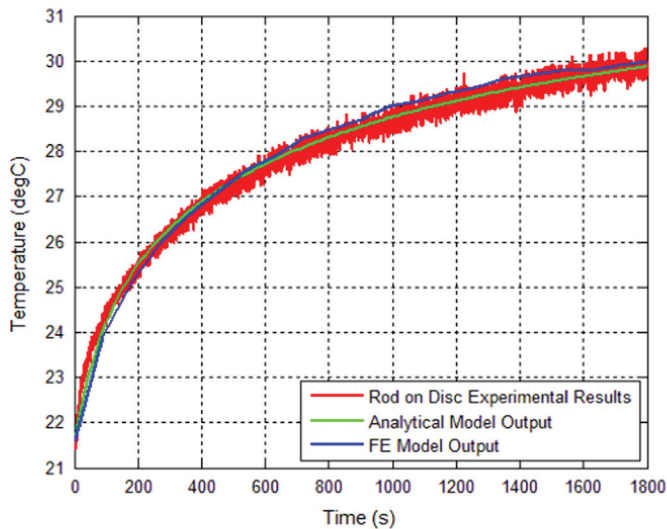e to avoid undercutting and therefore weakening the teeth of the pinion during manufacture. The time averaging was repeated, including a 70 μm adjustment (reduction) to the contact radius. This was achieved by altering the values R_{go}, R_{gb}, R_{po} and R_{pb} in the contact ratio expression given in Eq. (40). The corrected averaged rod on disc temperature is shown in Fig. 16(b), which now aligns closely with the measured gear temperatures. It is therefore possible to use aligned rod on disc experimental data to evaluate the likely temperature rise in a real gear pair to within a tolerance determined by the accuracy of the manufactured gears.

Finally, the temperatures measured and time averaged from the rod on disc experiment can be compared to both the analytical and finite element models that have been presented. These data are also shown in Fig. 17 and good correlation exists between the three data sets. It is therefore possible to predict the running temperature of a polymer–steel spur gear pair using a simple aligned rod on disc model, either in analytical of finite element form. This is useful and convenient because, as previously discussed, a model that accurately represents the geometry and contact conditions of a spur gear pair would be excessively complex to construct and run.

6. Conclusions

An axially aligned steel rod on a polymer disc system is proposed for the prediction of the thermal response of a steel pinion and polymer gear, which is important for the assessment of gear efficiency. Losses arise from slip between the teeth. An experiment was therefore devised to measure thermal response of the polymer disc, with heating equivalent to local zones of contact between the gear teeth. The experiment was then augmented to enable the real gear pair to be run and the dynamic temperature of the polymer gear to be measured. The polymer disc and gear temperatures were then correlated through a novel technique of time averaging of the rod on disc results to integrate each temperature data set with respect to the gear contact sweep load profile. The initial correlation under-predicted the gear temperature results by around 9% or 2.5 °C. This difference was attributed to manufacturing tolerance of geometric offsets, commonly introduced to prevent weakening of the pinion teeth during manufacture. A reduction of the reference radius from

the gear centre 70 μm was considered appropriate and was shown to give rise to the under-prediction of 2.5 °C.

Two models were also presented to predict the temperature rise in the aligned rod on disc experiment. The FE model considered an averaged circumferential heat input, whilst the analytical model included the rotational and cyclic nature of the heat input to the polymer disc. There was good correlation between both models and the experimental data, which provides a degree of validation. It is therefore concluded that the combination of aligned rod on disc modelling and experimentation, together with time averaging over a gear contact load profile is sufficient to predict the running temperature of a spur gear pair. This avoids the need for complex transient analysis of the multiple interactions of teeth in a gear pair, which would be excessive if undertaken by FE modelling. Hence the methodology is appropriate for the design of new gear pairs in terms of the defined contact load profile.

References

[1] Breeds AR, Kukureka SN, Mao K, Walton D, Hooke CJ. Wear behaviour of acetal gear pairs. Wear 1993;166:85–91.
[2] Hamrock BJ, Schmid SR, Jacobson BO. Fundamentals of fluid film lubrication. 2nd ed.. CRC Press: Marcel Dekker; 2004.
[3] Hooke CJ, Kukureka SN, Liao P, Rao M, Chen YK. The friction and wear of polymers in non-conformal contacts. Wear 1996;200:83–94.
[4] Bowers RC, Clinton WC, Zisman WA. Friction and lubrication of nylon. Ind Eng Chem 1954;46:2416–9.
[5] Walton D, Cropper AB, Weale DJ, Meuleman PK. The efficiency and friction of plastic cylindrical gears. Part 1: influence of materials. Proc Inst Mech Eng Part J: J Eng Tribol 2002;216:75–8.
[6] Xie Y, Williams JA. The prediction of friction and wear when a soft surface slides against a harder rough surface. Wear 1996;196:21–34.
[7] Greenwood JA, Williamson JBP. Contact of nominally flat surfaces. Proc R Soc Lond A: Math Phys Eng Sci 1966;295:300–19.
[8] Fisher J, Dowson D, Hamdzah H, Lee HL. The effect of sliding velocity on the friction and wear of UHMWPE for use in total artificial joints. Wear 1994;175:219–25.
[9] Blok H. The flash temperature concept. Wear 1963;6:483–94.
[10] Samyn P, Schoukens G. Calculation and significance of the maximum polymer surface temperature T* in reciprocating cylinder-on-plate sliding. Polym Eng Sci 2008;48:774–85.
[11] Conte M, Pinedo B, Igartua A. Frictional heating calculation based on tailored experimental measurements. Tribol Int 2014;74:1–6.
[12] Mao K. A numerical method for polymer composite gear flash temperature prediction. Wear 2007;262:1321–9.
[13] Kim CH. Durability improvement method for plastic spur gears. Tribol Int 2006;39:1454–61.
[14] Duzcukoglu H. Study on development of polyamide gears for improvement of load carrying capacity. Tribol Int 2009;42:1146–53.
[15] Hooke CJ, Mao K, Walton D, Breeds AR, Kukureka SN. Measurement and prediction of the surface temperature in polymer gears and its relationship to gear wear. ASME J Tribol 1992;115:119–24.
[16] Senthilvelan S, Gnanamoorthy R. Efficiency of injection moulded polymer composite spur gears. Proc Inst Mech Eng Part J: J Tribol 2009;223:925–8.
[17] Mao K, Li W, Hooke CJ, Walton D. Friction and wear behaviour of acetal and nylon gears. Wear 2009;267:639–45.
[18] Mao K, Li W, Hooke CJ, Walton D. Polymer gear surface thermal wear and its performance prediction. Tribol Int 2010;43:433–9.
[19] Vick B, Furey MJ. A basic theoretical study of the temperature rise in sliding contact with multiple contacts. Tribol Int 2001;34:823–9.
[20] Archard JF. The temperature of rubbing surfaces. Wear 1959;2:438–55.
[21] Walton D, Tessema AA, Hooke CJ, Shippen JM. Load sharing in metallic and non-metallic gears. Proc Inst Mech Eng Part C: J Mech Eng Sci 1994;208:81–7.
[22] Taburdagitan M, Akkok M. Determination of surface temperature rise with thermo-elastic analysis of spur gears. Wear 2006;261:656–65.
[23] Unal H, Sen U, Mimaroglu A. Dry sliding wear characterisitics of some industrial polymers against steel counterface. Tribol Int 2004;37:727–32.
[24] Young WC, Budynas RG. Roark's formulas for stress and strain. 8th ed.. New York: McGraw-Hill; 2011.
[25] Lee Y, Liu Y, Barber JR, Jang YH. Thermal considerations during transient asperity contact. Tribol Int 2016;94:87–91.
[26] Beardmore R. RoyMech [Online] Available at: ⟨http://roymech.co.uk/⟩; 2014 [accessed 28.02.14].
[27] Keogh PS, Yong WY. Thermal assessment of dynamic rotor/auxiliary bearing contact events. ASME J Tribol 2007;129:143–52.
[28] Abramowitz M, Stegun IA. Handbook of mathematical functions: with formulas, graphs, and mathematical tables. US Government Printing Office, Courier Corporation; 1967.

8.2 Journal Publication 2

Currently in process of submission - August/September 2016

Wear Mechanisms in Polyoxymethylene Spur Gears

8.3 Conference Publication

Presented at the 5th World Tribology Congress in Turin, September 2013

Evans, M., Akehurst, S. and Keogh, P., 2014. Wear mechanisms in polyoxymethylene (POM) spur gears. In *5th World Tribology Congress, WTC 2013* (pp. 2591-2594). University of Bath.

Wear Mechanisms in Polyoxymethylene (POM) Spur Gears

Mike Evans[1]*, Sam Akehurst[1] and Patrick Keogh[1]

1)   Department of Mechanical Engineering, University of Bath,
Claverton Down, Bath BA2 7AY, United Kingdom

*Corresponding author: smme20@bath.ac.uk

1. Introduction

The involute gear form is a gear tooth profile that allows constant and smooth power transmission from the driving gear to the driven gear. The involute profile is generated by sweeping an arc from the base circle of the gear out beyond the outer diameter of the gear, which produces the characteristic involute shape. This gear form is often described as being extremely efficient at transmitting power as it involves mainly a rolling contact between the teeth. However, there also exists sliding motion between the teeth. This sliding motion gives rise to a particular contact mechanism between the teeth, and in the case of a steel pinion driving a plastic gear, several distinct wear mechanisms. This paper identifies one of these mechanisms through Scanning Electron Microscopy images and provides a model to predict the quantity of material that is removed from the bulk of the gear by it during continuous operation of the gear pair under load. *Figure 1* illustrates how the sliding between the two faces occurs, the small opposing arrows at the contact interface show the driving gear flanks sliding direction with respect to the driven gear.
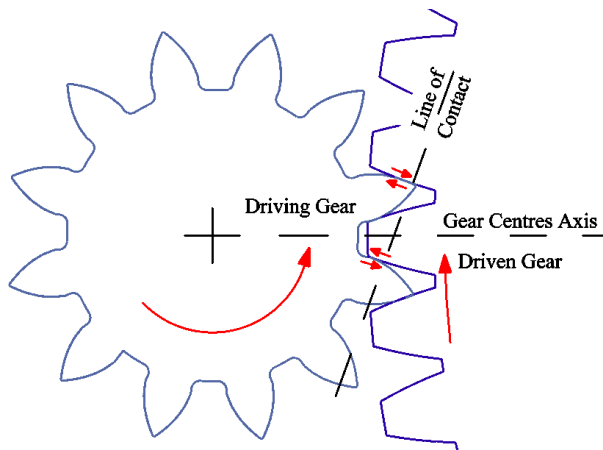

Figure 1: Gear Contact and Sliding

The contact between the two gear teeth can be thought of as analogous to a pair of contacting equivalent cylinders whose diameters vary through the line of contact as described by Hamrock *et al* [1]. The rotational speed of these equivalent cylinders varies through the line of contact and so the slip speed can be calculated as the difference between their speeds thus:

$$\beta = \left[((r_b \, sin\psi + S) \times 2\pi) \times \omega_1 \right] \\ - \left[((r_a \, sin\psi - S) \times 2\pi) \times \omega_2 \right] \quad (1)$$

where:

β = Slip speed (mm/s)
r_a = Pinion radius (mm)
r_b = Gear radius (mm)
ψ = Pressure angle (radians)
ω_1 = Rotational speed of gear (rev/s)
ω_2 = Rotational speed of pinion (rev/s)
S = Distance along the line of contact from the gear centre axis

From equation (1) it can be seen that the slip speed β will be positive until the S becomes zero, at which point there will be no slip speed. The slip speed then becomes increasingly negative as the contact point moves away from the gear centre axis along the line of contact.

The contact and wear of a polymer gear has been identified as a complex mixture of material characteristics and contact mechanics. Breeds *et al* [2] have identified that the driving and driven gears are moving in opposing directions and Kukureka *et al* [3] present images of a wear mechanism between the gear teeth that is described as lateral cracking. However, these works were concerned predominantly with wear rates rather than the specific wear mechanism that is operating on a microscopic level. The wear mechanism identified by this research has been observed in Polyoxymethylene (POM - Delrin 100, a type of nylon) gears that have been operated for many cycles in an industrial product. The product was undergoing durability testing, hence the large number of cycles. The wear mechanism has also been replicated in the laboratory by the use of purpose built equipment. The mechanism itself consists of distinct areas of asperities that appear to have been generated by the operation of the gears under load. These areas can be large or small in relation to the tooth flank area, but appear consistently across the flank of the tooth.

2. Observed Smearing Mechanism

Figure 2 shows a POM gear tooth flank that has been in continuous operation for ~ 6×10^6 cycles and then has been sectioned, processed and imaged using a Scanning Electron Microscope. As the imbedded footer shows, the image is at 600 times magnification and is tilted at an angle of 40° to show the surface structures more clearly. The direction of slip is from the top right of the image to the bottom left. In the centre of the image

several smears are seen as created by the contact conditions as the gears are driven together. They range in size and are approximately 10-40 μm in length and are in the order of 1-3 μm high. The swept forms of the features would appear to be a function of the sliding contact between the gear teeth.
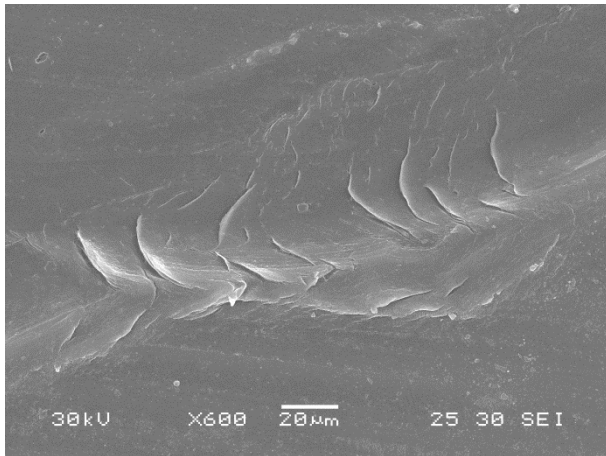

Figure 2: Smearing of Gear Flanks 6x10^6 Cycles

These smears are evident on all teeth observed from the industrial product that was tested, but in order to determine that they had not been produced by some other effect of the products system (rather than the contact between the teeth) an experiment was devised to attempt to reproduce these features in the laboratory. *Figure 3* shows the experiment arrangement, which consists of a steel pinion running against a POM gear. The pinion is driven by an electric motor and the POM gear reaction load is controlled by an electric magnetic particle brake, which can be seen at the far left of the image. The assembly is mounted in such a way that the reaction to loading is directed though a thin steel beam that is strain gauged and calibrated to measure the torque delivered through the POM gear to the magnetic particle brake. The speed of rotation is also measured accurately by way of an encoder mounted to the rear shaft of the motor. Using this hardware it was possible to run the gears together for a known period of time at an accurately measurable torque and speed.
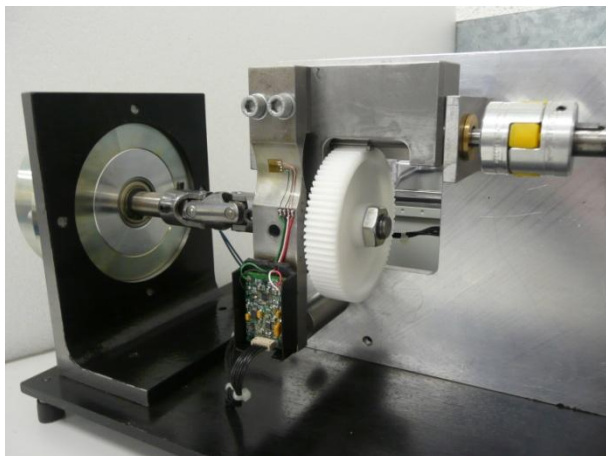

Figure 3: Gear Wear Experiment Hardware
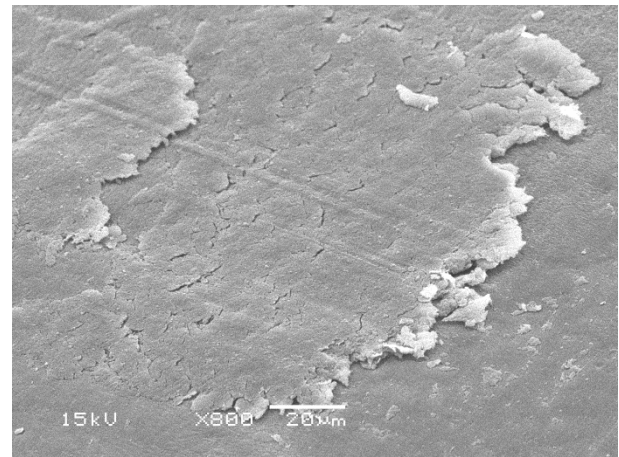
Figure 4: Smearing Created by Experiment

Figure 4 shows a smear feature that was created by this experimentation. The structure of the feature is different from the previous image in that it is approximately 5 times longer and has a rougher leading edge than the 6x10^6 cycle gear. However, due to the extremely long timescales that the 6x10^6 cycles gear had endured (1 year), it was necessary to attempt to accelerate the process somewhat. The smear created by experiment was run at around 4 times the pressure seen on the long timescale running gear. However, smearing is seen to be taking place in the gear surface and in addition to this, small pieces of material can be seen in the process of being ejected from the leading edge of the smear. It is proposed that this is indeed the process by which material is worn away from the surface of the gear. The smear is initiated and as the gear runs, this feature is then augmented by the repeated action of the steel gear sliding and rolling over it again and again. After many operations the smear becomes elongated and more pronounced until it reaches the point where the material finally fails and breaks away from the leading edge of the smear, thus removing material.

3. Prediction of Wear Volume

An individual smear can be modelled as a block of material with dimensions corresponding to the smear sizes observed through the SEM images. If this analogous block were to be subject to a cyclic force of the same magnitude as the force applied due to the torque generated by the gear interaction then it would be deformed to a certain degree. If the stress generated in the block exceeds its elastic limit then the block would not return to its original dimensions and given a sufficient number of cycles, then would naturally fail. A mathematical model has been developed that applies this scenario to a block of dimensions 20×40×3 μm (length, width, height) and uses a looping function to iterate until failure has occurred. *Figure 5* shows the output from this model for the single smear block. As the area is diminished by the cyclic loading, the stress increases at each iteration and so the area reduces rapidly to failure. The number of cycles to fail an individual smear is small (~25) in this model. However, the smear must also have been created in the first place and so the actual number of cycles to initiate, grow and ultimately fail the smear will be greater than this.

Figure 5: Single Smear Failure Model
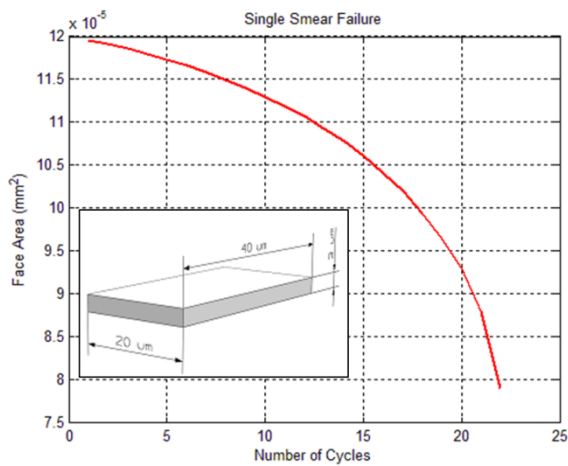
There are a number of assumptions made in the model, namely the percentage area of material that is actually in contact and the percentage area that is actually a smear to be failed. Greenwood and Williamson [4] provide a substantial theory on the statistical quantity of asperities in contact at a surface interface and they find that this value is very low in comparison the perceived area of contact.

The product of the variables used in the proposed model is 15% and although this is a much higher figure than determined by Greenwood and Williamson, their work was concerned entirely with hard metallic surfaces and in this case the polymer will deform significantly and plastically under the load to give a far greater real contact area. This value should be validated through further research. For $6x10^6$ cycles, the model returns a total wear mass for the whole gear of 67 mg.

4. Measurement of Wear Volume
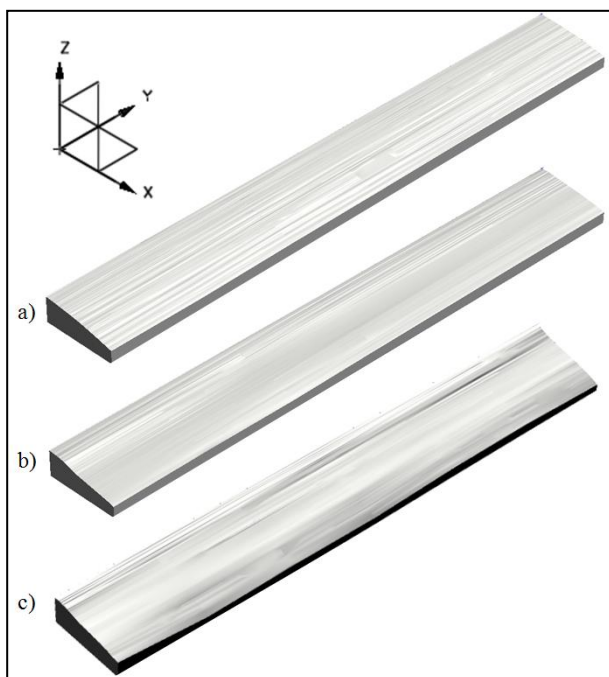
Figure 6: Scanned Gear Teeth

The gear teeth were scanned to find the exact shape and the quantity of material that had been worn away during operation of the $6x10^6$ cycle gears. *Figure 6* shows 3 gear teeth that have been scanned. The process of scanning was first to carefully cut the gear tooth away from the gear wheel and then to use a profile measurement machine to measure the tooth profile as a series of lines along the tooth from front to back. The profile measurement was done along the *x*-axis as depicted in the coordinate system in the figure. These profile data were then used to build a computer model from whence the images in *Figure 6* came. A series of profiles along the *y*-axis were generated at distances matching the measurement planes and were then swept together to form a solid model. The lighting has been manipulated to more clearly show the features on the surface of each of the gear teeth. Tooth a) is from an unused gear tooth, the surface of this scan shows the machining marks from the manufacturing operation running in the *y*-axis direction and it can be seen that the profile is consistent along the *y*-axis. Teeth b) and c) are scans of teeth that have been worn by $6x10^6$ cycles of operation and the worn profile can be seen as markedly different from the unused gear tooth.
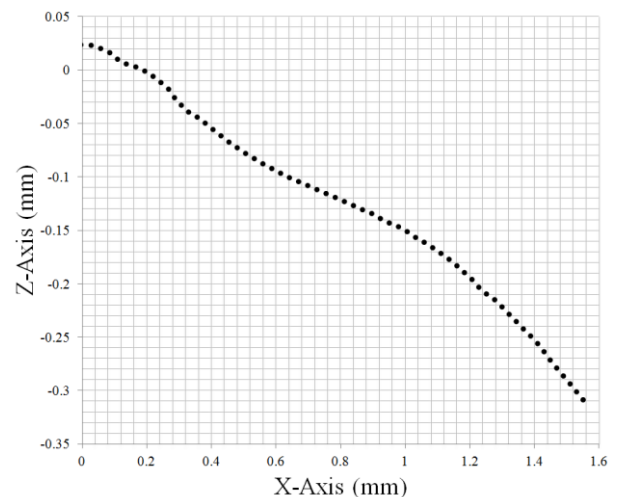
Figure 7: Tooth Profile Measurement Data

Figure 7 shows one set of measurement data taken during the scanning process. A dip in the profile is seen at $x = 0.4$ mm, this is as the steel tooth is slipping in the positive *x* direction. The slip speed reduces to zero as the contact point moves through the gear centre axis on the line of contact, which is $x = 1.1$ mm and then alters direction so slip in the negative x direction to the tip of the tooth at $x = 1.6$ mm.

The models allow the analysis of the surface of the gear teeth to measure the quantity of material removed by wear. An average of the worn teeth was taken in terms of volume and was then subtracted from the unworn tooth volume and multiplied by the number of gear teeth in the complete gear (75). This figure came to 77 mg of material worn away from the complete gear.

5. Conclusions

A wear mechanism in POM spur gears has been identified by Scanning Electron Microscopy. A simple modeling has been presented which can be used to predict the quantity of material removed by that process of wear, although the premise of the model must be validated. The mass of material removed from the gears during realistic operational conditions has been measured using the technique of profile measurement and the modeled wear mass has shown to be of a similar order as that of the physical measurements taken. The profile measured mass of worn material value was 77 mg, while the modelled value was 67 mg. Although superficially there appears to be a good correlation between the model and experimental results, this is dominated by the constants used to describe the real contact area and number of smears on the gear tooth surface. In the continuation of this research, this value will be confirmed by further experimentation. Further validation of this technique will now be undertaken by repetition of the experimental results and by analysis. In particular, a statistically significant number of measurements of the size and quantity of smears found on the surface of a worn gear should be taken. This will allow a more accurate assumption to be made for the model inputs.

6. References

[1] Hamrock, B. J. *et al*, "Fundamentals of fluid film lubrication". Vol 169. CRC Press, 2004.

[2] Breeds, A.R. *et al*, "Wear behavior of acetal gear pairs", Wear, **166**, 1993, 85-89.

[3] Kukureka, S. N., Y. K. Chen, C. J. Hooke, and P. Liao. "Surface failure mechanisms in polymer gears." Proc. Int. Gearing Conf., London, 1994, 13-18.

[4] Greenwood, J.A. and Williamson J.B.P., "Contact of nominally flat surfaces", Proc. R. Soc. Lond. A 1966 **295**, 300-319.

[5] Bowden, F.P. and Tabor, D., "Friction, lubrication and wear: a survey of work during the last decade", Br. J. Applied Physics **17**, 1966, 1521

[6] Hooke, C.J. *et al*, "The friction and wear of polymers in non-conformal contacts", Wear, **200**, 1996, 83-94.

[7] Mao, K. *et al*, "Friction and wear behavior of acetal and nylon gears", Wear, **267**, 2009, 639-645.

8.4 Rotork Polymer Gear Manufacturing Drawing
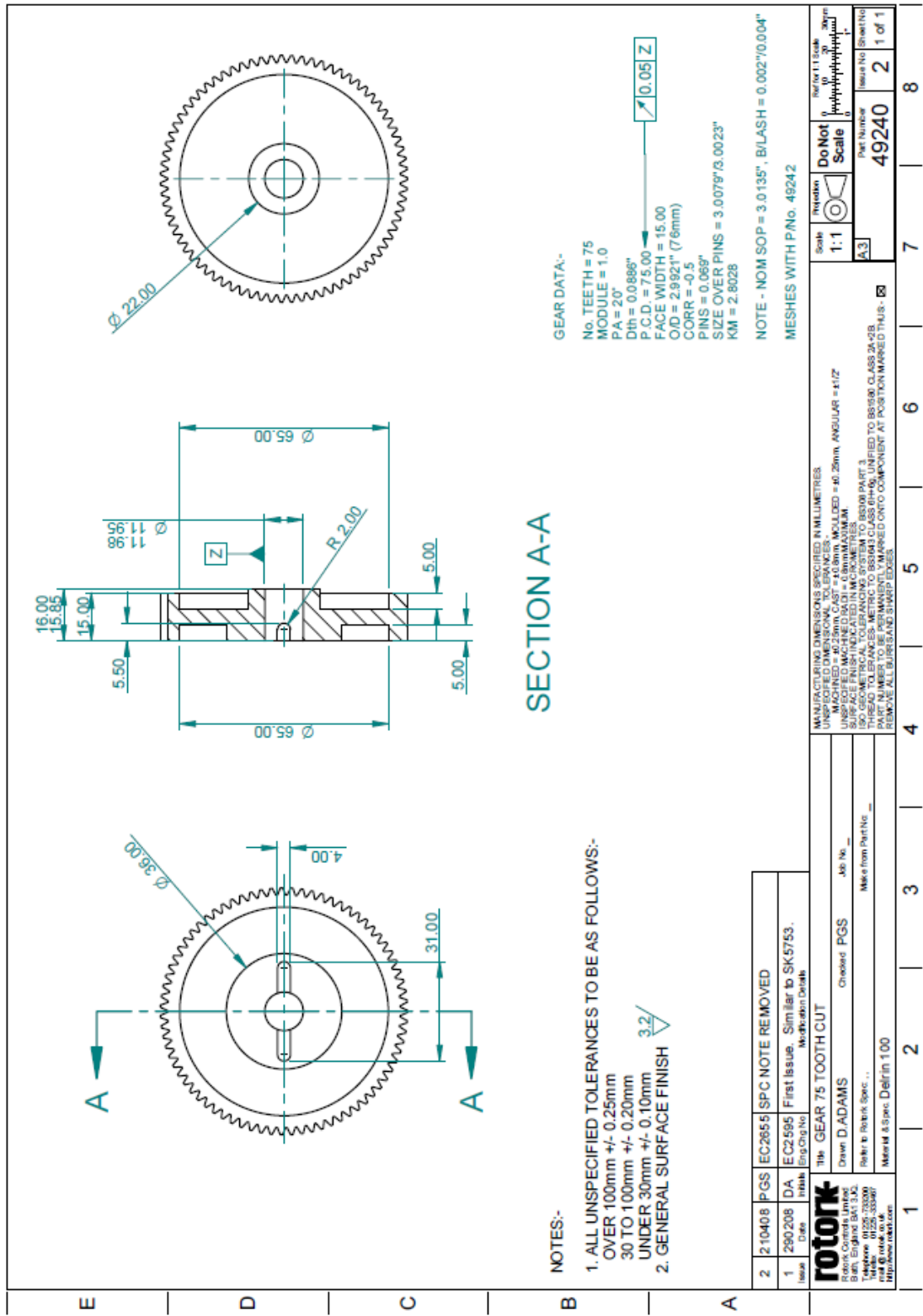
8.5 Rotork Steel Pinion Manufacturing Drawing

ISOMETRIC VIEW

SECTION A-A

EXTERNAL GEAR DATA;

No. TEETH = 12
MODULE = 1.0
PA = 20°
P.C.D = 12.00
Dth = 0.0886"
O/D = 0.5906" (15mm)
CORR = +0.5
PINS = 0.087"
SIZE OVER PINS = 0.6416"/0.6385"
KM = 1.5524

NOTE - NOM SOP = 0.6447", B/LASH = 0.002"/0.004"

MESHES WITH P/No. 49240

∅ 7.99 / 7.97

⌀ 2.10 / 2.00

21.00
2.00
48.00
19.50 / 19.40

0.05 Z

R 0.30 MAX TYP 2 POS'NS

C 1.00 x 20° TYP 2 POS'NS

SEE EXTERNAL GEAR DATA

∅ 7.99 / 7.97

NOTES:-

1. GENERAL SURFACE FINISH 3.2
2. TOOTH SURFACE FINISH 3.2
3. MACHINING CENTRES PERMISSIBLE IN BOTH ENDS OF ∅7.99/7.97 SHAFTS. REMOVE MINIMAL MATERIAL. ENSURE NO SHARP EDGES.

MANUFACTURING DIMENSIONS SPECIFIED IN MILLIMETRES.
UNSPECIFIED DIMENSIONAL TOLERANCES:-
UNMACHINED - MEDIUM CAST - ±0.6mm, MOULDED - ±0.25mm, ANGULAR - ±1/2°
UNSPECIFIED MACHINED RADII - 0.8mm MAXIMUM.
SURFACE FINISH INDICATED IN MICROMETRES.
ISO GEOMETRICAL TOLERANCING SYSTEM TO BS308 PART 3.
THREAD TOLERANCES:- METRIC TO BS3643 CLASS 6H-6g, UNIFIED TO BS1580 CLASS 2A+2B.
PART NUMBER TO BE PERMANENTLY MARKED ONTO COMPONENT AT POSITION MARKED THUS:- ⊠
REMOVE ALL BURRS AND SHARP EDGES.

Issue	Date	Initials	Eng.Chg No	Modification Details
2	210408	PGS	EC2655	TOOTH SURFACE FINISH ADDED
1	290208	DA	EC2595	First Issue. Similar to SK5754.

rotork
Rotork Controls Limited
Bath, England BA1 3JQ.
Telephone 01225-733200
Telefax 01225-333467
mail @ rotork.co.uk
http://www.rotork.com

Drawn D. ADAMS   Checked PGS
Title PINION 12 TOOTH CUT GEARS
Refer to Rotork Spec:_   Make from Part No:_   Job No:_
Material & Spec. Mild Steel BS EN 10083-2, 1.0511, C40 (080M40)

Scale 5:1   Do Not Scale   Projection
A3
Part Number 49242   Issue No 2   Sheet No 1 of 1

180

8.6 Polyoxymethylene (Delrin 100) Data

The following material data for Delrin 100 was compiled from the DuPont website and correspondence with them to find the data points for the stress-strain curve.

Tensile Stress versus Strain ISO 11403 — DuPont™ Delrin® 100P, 100 and Copolymer
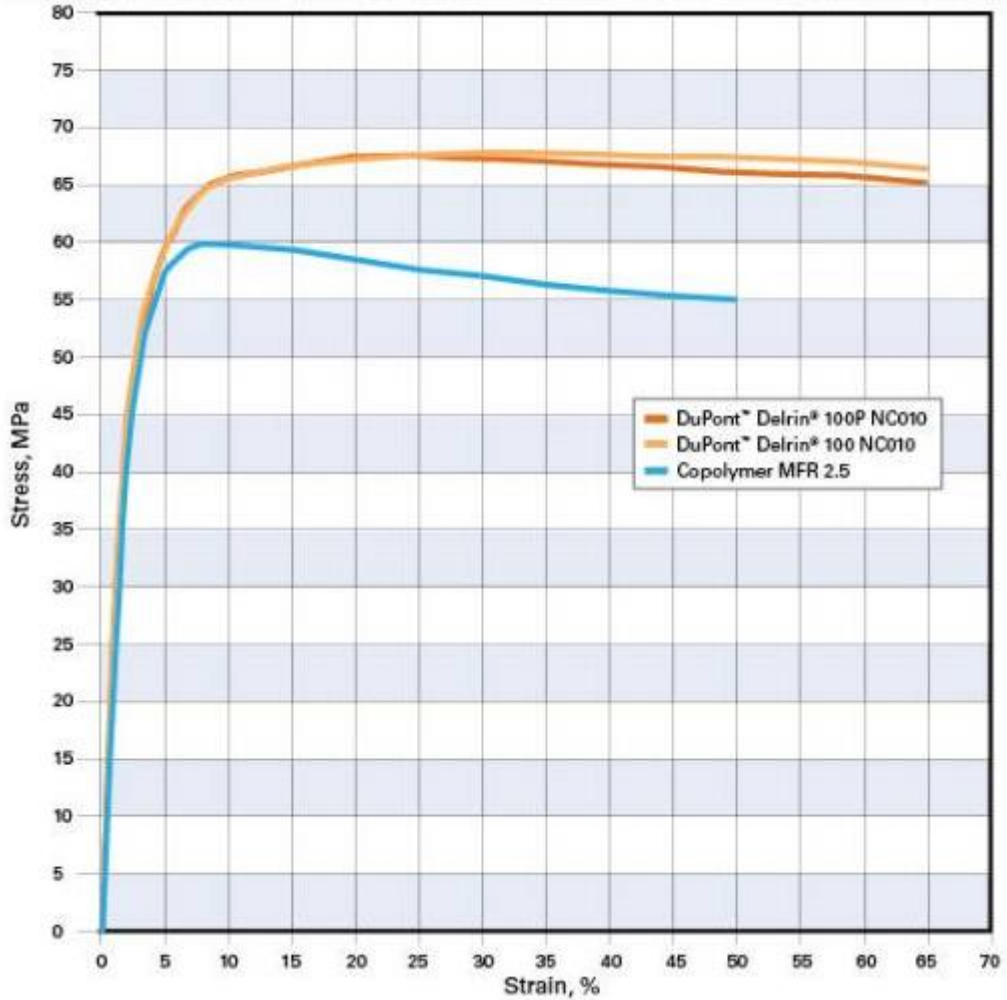
x [%]	y [MPa]
0	0
1.11	30.9
2.22	46
3.12	51.7
4.67	58.8
6.24	62.1
7.8	64.1
9.35	65.4
10.9	66.2
12.5	66.6
14	66.8

8.7 Brushless DC Motor Drawing

LEAD WIRE	MOTOR			HALL SENSOR			
SERIAL NUMBER	V	U	W	HU	HV	HW	GND	VCC+
PCB WELDING	yellow	green	blue	orange	white	brown	black	red(+)
							(-)	
LEAD WIRE SPC	UL1007 AWG20#			UL1007 AWG24#				
LEAD WIRE LENGTH	300mm							
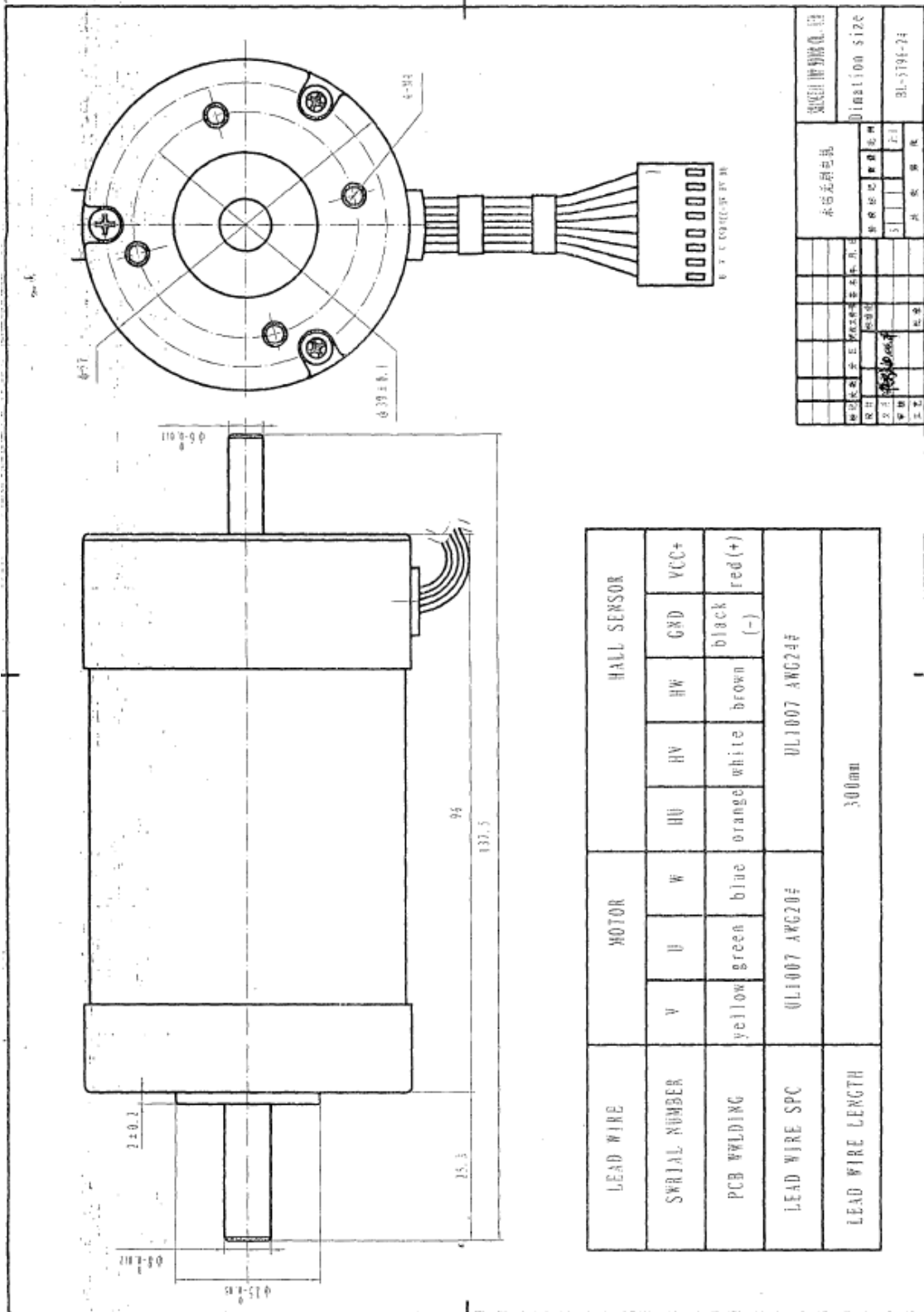
8.8 Gearbox Data Sheet

Industrial Planetary gearheads

IP series

Ratio Options:

IP series gearheads are available in a wide range of ratios, many of which being from stock as shown below:

Single stage units	2 stage units	3 stage units
• 5:1	• 25:1	250:1
• 10:1	• 50:1	500:1
	• 100:1	1000:1

• **Standard ratios:**

Gear ratio options shown in **bold** are usually available from stock.

Dimensions:

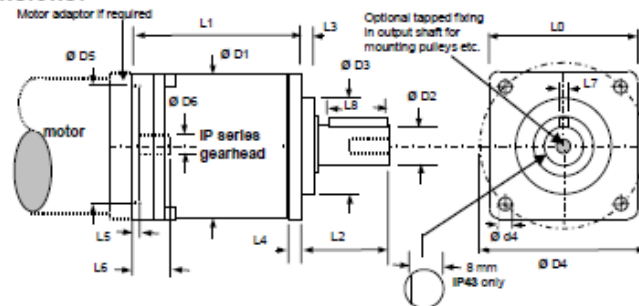## Table of dimensions: mm

Gearhead model		IP43			IP 57		
		MO1	MO2	MO3	MO1	MO2	MO3
Gearhead flange square	L0		42.8			57.2	
Gearhead Length	L1	47	56	66			
Ratios 3:1 4:1 **5:1**					54		
10:1					67.75		
25:1						66	
50:1 100:1						79.75	
250:1 500:1 1000:1							92.75
Shaft length from flange	L2		20			25.4	
Output Register length	L3		1.5			1.6	
Flange thickness	L4		4.3			5.2	
Input register length	L5		2.0			2.5	
Max. input shaft length	L6		To be advised			Dependent on adapter length	
Output shaft Key width	L7		See shaft flat details on IP43			3.2	
Output shaft key length	L8		Shaft flat length 15 mm			19.0	
Diametric dimensions							
Gearhead diameter	D1		42.8			57.2	
Output shaft diameter	D2		9.5 / 9.52 *			12.67 / 12.69 *	
Output register diameter	D3		22.2 / 22.225			38.05 / 38.10	
Mounting hole PCD	D4		50.8			66.68	
Mounting hole diameter	D4		3.78			5.1	
Input register diameter	D5		22.22 / 22.24			38.10 / 38.12	
Max. motor shaft dia.	D6		5			8 .	

Specification

Gearhead	Number of stages	Maximum Continuous Torque * (Nm)	Max. Peak Torque* (Nm)	Typical Backlash (arc min.)	Efficiency	Max. Input Speed (rpm)	Max. Radial Load (N)	Max. Axial Load (N)
IP043-M01	1	3.3	6.0	20	92%			
IP043-M02	2	6.7	12	30	84%	6000	500	350
IP043-M03	3	10.0	20	40	78%			
IP057-M01	1	6.0	12	20	92%			
IP057-M02	2	12	24	30	84%	5000	500	350
IP057-M03	3	20	40	40	78%			

Note * De-rate by 10% for gear ratios 10:1 & 100:1

Mclennan Servo Supplies Ltd.   Tel: +44 (0)8707 700 700 www.mclennan.co.uk   Mclennan   Issue 001

8.9 Optris IR Thermometer Data Sheet

optris
infrared thermometers

optris® CS LT

Simple access into multiple sensor installations:
Smart, safe and easy for -40 to 1030°C

FEATURES

- Temperature range: -40°C to 1030°C
- Response time: 25 ms
- Optical Resolution 15:1
- Green LED alarm indication, aiming support, selfdiagnostic or temperature code indication
- Usable up to 80°C ambient temperature without cooling
- Scalable analog output:
  0-10 V or 0-5 V + alarmoutput or digital output
- USB programming interface, direct serial 9.6 kBaud interface
- Power supply: 5-30 V DC

General Specifications

Environmental rating	IP 63
Ambient temperature	-20°C to 80°C
Storage temperature	-20°C to 85°C
Relative humidity	10 - 95%, non condensing
Vibration	IEC 68-2-6: 3 G, 11-200 Hz, any axis
Shock	IEC 68-2-27: 50 G, 11 ms, any axis
Weight	58 g

Electrical Specifications

Output/analog	0-5 V or 0-10 V free scalable or alarm with adjustable voltage levels
Output/alarm	0-30 V/50 mA (open collector)
3-state alarm output	adjustable threshold values and voltage level for: no alarm, pre-alarm, alarm
Output/digital	uni/bidirectional, 9.6 kBaud, 0/3 V digital level/USB optional
Input (0-10V)	programmable functional input for external emissivity setting/ambient temperature adjustment, triggered signal output or peak-hold function
LED-functions	alarm indication, automatic aiming support, self diagnostic, temperature indication (via. temp.code)
Cable length	1 m (standard), 3 m, 8 m, 15 m
Power supply	5-30 V DC
Current draw	4 mA (ohne LED)/10 mA

Measurement Specifications

Temperature range (scalable via software)	-40°C to 1030°C
Spectral range	8 to 14 µm
Optical resolution (90 % energy)	15:1
CF-lens (optional)	0.8 mm @ 10 mm
System accuracy (at ambient temp. 23 ± 5°C)	± 1.5% oder ± 1.5°C[1]
Repeatability (at ambient temp. 23 ± 5°C)	± 0.75% oder ± 0.75°C[1]
Temperature coefficient	± 0.05 K/K oder ± 0.05 % K[3]
NETD	0.1 K[2]
Response time (90%)	25 ms (adjustable up to 999 s)
Emissivity/Gain (adjustable via 0-10 V DC input or software)	0.100 - 1.100
Transmissivity (adjustable via software)	0.100 - 1.100
Signal processing (parameter adjustable via software)	peak hold, valley hold, average; extended hold function with threshold and hysteresis
Software	optris Compact Connect

[1] objecttemperature > 0°C; whichever is greater
[2] at time constant 100 ms and T_{obj} 25°C
[3] for ambient temperatures <18°C and >28°C; whichever is greater

Innovative Infrared Technology

8.10 Magnetic Brake Data Sheet

THE MAGNETIC IMPACT OF SG TRANSMISSION

SG TRANSMISSION

MAGNETIC PARTICLE CLUTCHES & BRAKES

OP SERIES
MAGNETIC PARTICLE CLUTCH BRAKE

FEATURES

FAST RESPONSE
The OP series has been designed to provide fast response. Response rates can be further quickened through overexcitation circuits.

STABLE TORQUE
The OP series produces consistent and repeatable torque. Torque is independent of speed and proportional to voltage applied to the field.

LONG LIFE
The OP series sturdy construction and precise formulation of the magnetic particles combine to provide extended life.

SLIP CAPACITY
OP series clutches and brakes are designed to deliver high performance under constant slip conditions.

Clutch Type 51 -OPC
Size 5, 10 & 20

Clutch Type 51 -OPC
Size 40 & 80

Brake Type OPB
Size 5, 10, 20, 40 & 80

8.11 Strain Gauge Data Sheet

Full Bridge Patterns

Micro-Measurements

Transducer-Class® Strain Gages

Actual sizes shown. Enlarged when necessary for definition.

inch
millimeter

Low-cost full-bridge gage for bending-beam transducers.

†BAL is balanced to ± 0.4mV/V, but RG is 350 ohms ± 15%

GAGE PATTERN				GAGE DESIGNATION See Note 1	RES. IN OHMS	STANDARD CREEP CODE	ENCAPSU-LATION OPTION AVAILABLE
DIMENSIONS				J2A-XX-S1425-35B	BAL ± 0.4†	N/A	

	GAGE LENGTH	OVERALL LENGTH	GRID WIDTH	OVERALL WIDTH
	0.050	0.260	0.050	0.220
	1.28	6.66	1.28	5.64
MATRIX SIZE	0.32 L x 0.25 W			8.2 L x 6.4 W